Artificial spin ice : from statistical physics to stochastic computing

Maryam Massouras

Université de Lorraine, Collegium Sciences et Technologies

Ecole doctorale C2MP « Chimie - Mécanique - Matériaux – Physique »

THESE DE DOCTORAT

pour l'obtention du titre de

DOCTEUR DE L'UNIVERSITE DE LORRAINE

SPECIALITE : PHYSIQUE ET CHIMIE DES MATERIAUX

Présentée par :

MARYAM MASSOURAS

ARTIFICIAL SPIN ICE: FROM STATISTICAL PHYSICS TO STOCHASTIC COMPUTING

Thèse soutenue publiquement le 16 / 03 / 2021 devant le jury composé de :

M. André Thiaville	Directeur de recherche CNRS, LPS, HdR	Rapporteur
M. Joo-Von Kim	Chargé de recherche CNRS, C2N, HdR	Rapporteur
Mme Agnès Barthélémy	Professeur, CNRS/Thalès, Paris Saclay	Examinatrice
M. Bruce B. Doris	Chercheur, IBM Watson	Examinateur
M. Nicolas Rougemaille	Chargé de recherche CNRS, IN, HdR	Examinateur
M. Dragi Karevski	Professeur, LPCT, UL	Président
M. Daniel Lacour	Chargé de recherche CNRS, HdR	Co-directeur
M. François Montaigne	Professeur, IJL, UL	Directeur

RÉSUMÉ:
Depuis leur introduction en 2006, les systèmes de spins artificiels ont suscité un large intérêt autant pour leur similarité avec des systèmes frustrés tels que la glace d'eau ou certains pyrochlores. Ces réseaux de nano-aimants sont observables par des techniques de microscopie simples et modifiables à volonté. Dans ce travail, nous avons étudié des modifications de géométries classiques pour l'étude de l'évolution des interactions et pour l'élaboration d'un dispositif. Dans un premier temps, nous avons étudié la modification des interactions par la rotation des éléments d'un système carré. Pour un système dans l'état brut de croissance, l'état de fondamental évolue d'ordre antiferromagnétique à ferromagnétique suivant les prédictions de calculs dipolaires. En considérant les interactions longue portée dans nos simulations Monte Carlo, nous avons décrit l'énergie dipolaire totale ainsi que les populations de vertex de notre système. Cette description a mené à une étude de la thermodynamique du système et la détermination d'une température effective unique. Ensuite, nous nous sommes intéressés à la possibilité de « tailler sur mesure » ces systèmes de spins artificiels pour des applications de calcul. Nous avons commencé par montrer que ces systèmes sont plus adaptés en exploitant de la propagation de paroi plutôt que le couplage. Nous avons ensuite établi que le défi dans de grandes structures connectées est le compromis entre champ de nucléation et champ de piégeage du haut de la structure. Par une optimisation fine de sa forme, nous avons observé la propagation d'une paroi injectée à un endroit choisi. Cette propagation a été caractérisée en termes de champs de propagation, de types de renversements et a montré que notre système optimisé permet des propagations en majorité unidimensionnelles qui sont stochastiques. Ce comportement aléatoire a pu être décrit par un poids moyen décrivant l'ensemble des choix réalisés, ces derniers ne présentant aucune corrélation entre eux. Notre étude a démontré que les systèmes de spins peuvent être utilisés pour de la génération de nombres aléatoires au même titre qu'une planche de Galton. Cette thèse a donc montré la versatilité des systèmes de spins artificiels en qualité de glace de spin pour la compréhension de la modification des interactions dans leur thermodynamique. Ce travail a aussi démontré leur versatilité pour des applications de génération de nombres aléatoires grâce à une optimisation de leur géométrie.

MOTS-CLES : systèmes de spins artificiels, logique aléatoire, glace de spin artificielle, physique statistique

ABSTRACT:
Since their introduction in 2006, artificial spin ice systems have sparked an interest for their similarity with frustrated systems such as water ice or some pyrochlores. These networks of interacting nanomagnets can be observed using simple microscopy techniques and be tailored at will. In this work, we have studied customised geometries in order to observe the evolution of dipolar interactions and develop a device. First, we have studied the tuning of the dipolar interactions induced by rotation of the elements of the square geometry. For an as-grown system that the ground state evolution from antiferromagnetic to ferromagnetic orders observed is consistent with dipolar computations. Taking into account the long-range interactions in our Monte Carlo simulations, we have described the total dipolar energy along with the vertex populations of our system with all its tilted networks. This has led to a study of the thermodynamics of our system and a unique effective could be ascribed. Secondly, we have taken an interest into the possibility of tailoring these artificial spin systems for applications in random number generation. We have seen that these systems are a better fit exploiting domain wall propagation rather than reversals by coupling. We have then established that the main challenge to overcome in large connected structures is the trade-off between nucleation field from the outputs and depinning field of the upper part of the nanostructure. Indeed, it is necessary to ensure than the domain wall propagating in the structure is indeed the injected one and that no parasitic nucleation occurs which is overcome this issue. The domain wall propagation has been characterised in terms of propagation fields and types of reversals. We have shown that our optimised system exhibits reversal induced by the injected domain wall mainly in unidimensional fashion with clear stochastic behaviour. The characterisation of this behaviour has shown that a mean weight value describes the choices observed which do not exhibit any correlation. Our artificial spin system therefore behaves as a Galton board, the prime device for random number generation. This PhD work has shown the versatility of artificial spin systems as spin ice for understanding the influence of tuned interactions in their thermodynamics. This work has also demonstrated their versatility for an application with the characterisation of their stochastic behaviour through an optimisation of the geometry.

KEY-WORDS: artificial spin systems, stochastic logic, artificial spin ice, statistical physics

Acknowledgments

"Control your life before domain walls"
K. Ait Oukaci

I would like to sincerely thank Dr. André Thiaville and Dr. Joo-Von Kim for having accepted the heavy task of reviewing this work. I would also like to thank Prof. Agnès Barthélémy, Dr. Nicolas Rougemaille, Dr. Bruce B. Doris for being part of review committee and Prof. Dragi Karevski for agreeing to be the president. It sincerely was a great honour to have people that I admire on this such important event for me. I have a special thought for Bruce who has been following me since 2016, coming to a full circle from Masters degree to PhD, I am convinced it is not nearly the end.

I would like to thank Prof. François Montaigne and Dr. Daniel Lacour for advising and trusting me with this PhD project. I am more than grateful for the countless things they have taught me and for having the opportunity to work with such incredible scientists.

I would like to acknowledge the people that have contributed to this work: Sandrine Mathieu (CC 3M) for the EDS measurements, Dr. Charles Guillemard for the FMR measurements, Dr. Kosseila Ait Oukaci for the VSM measurements.

A particular thought to Dr. Laurent Badie (CC MinaLor) who has performed the optimisations for the material deposition, I would like to thank him for his help and benevolence both during and after the PhD on matter both related and not related to the PhD. His help has been precious on numerous occasions.

I would also like to thank Dr. Rachid Belkou, Dr. Kosseila Ait Oukaci and Prof. François Montaigne for the experiments at Soleil, their help has been more than precious. I would like to thank Rachid, for his insight and kindness but also for making the Hermes beamline such a warm place. I was told that synchrotron experiments are an experience and indeed I will remember our discussions on presidential campaign, zero-field, focus and aborted acquisition in between sleepless nights. I am grateful that I could share this time with them.

I would like to sincerely thank Dr. Karim Bouzehouane (CNRS/Thalès) for the MFM experiments at low temperature I am forever grateful for his time and help but also to have been able to see in action such an impressive scientist although he told me that I do not have to since he is doing "*Pour la science !*". I also have to thank Dr. Aymeric Vecchiola for making my time at Thalès so pleasant.

I would like to sincerely thank Dr. Sébastien Petit-Watelot, Dr. Olivier Copie, Dr. Stéphane Andrieu for their insight and the numerous helpful discussions.

I would like to thank our team manager Prof. Stéphane Mangin who in exchange for only a couple of presentations has been a caring boss and colleague. I would also like to thank the members of the Nanomagnetism and Spintronics team: Julius, Jon, Karine, Thomas, Michel, Aurore, Isabelle. and the others for the pleasant environment they have created. I would also like to thank the PhD students who

are not students anymore: Gauthier, Anton, Charles, Thibault, Vincent, Boyu, Yassine and all the others; and the ones that are still students: Anna, Maxime, Quentin, Jean-Loïs, Valentin, Boris, Danny and wish them all the best. I will not forget about the post-docs: Elmer, Claudia, Elodie, Ibrahim and the others. I would also like to thank Fahad, Dorra, Alejandro, Sébastien G. and Alexis for the time together. I also need to thank the people of the CC Daum: Danielle, Ludovic, Olivier L. along with of course Sébastien, Olivier, Carlos and Stéphane for the wonderful times inside and outside the lab and for becoming more than co-workers. However, I have to admit that the thing I will miss the most is the periodic loudest laugh of history in the hallway, this person does not need to be named.

I would like to sincerely thank François, Stéphane A. and Carlos for having invited me into their homes, some on numerous occasions. Their generosity moved me more than I can say, I feel very privileged and I hope that I will be able to return the favour sooner than later.

With all of them, I will keep cherished memories and I cannot thank them enough for the time I have spent with them. I hope they understand in these few words that I am forever grateful for making the difficult exercise of the PhD a wonderful experience.

There is one last person that I have met during my time at the Institut Jean Lamour, he has begun as my co-worker and became later my dear friend, Kosseila. I am not sure that in the future I will meet someone with whom I will build such a friendship. I wish him all the best and I can only hope that he will meet someone as kind and caring as him because I can talk from experience, they bring you much more joy that you could hope for.

My last thought is for my family, to whom I would like to dedicate this work particularly my parents who have contributed so much in their own way to this PhD by either reassuring me or telling me what I needed but did not want to hear. I owe them everything and more, there are no words to express my gratitude but I will try with this: *merci pour tout*.

Table of contents

Chapter 1. Introduction

"It is clear that there will be plenty more opportunities
to put the drinks on ice in order to celebrate future breakthroughs."
C. H. Marrows

Introduced 15 years ago to mimic the behaviour of water ice and rare-earth titanate pyrochlores, artificial spin ice systems have been presented ever since as a playground for competing interactions. The frustration they exhibit have allowed emerging collective phenomenon. In this chapter, we will first present the basis of geometrical frustration and the repercussion in natural and synthetic materials as well as the artificial spin systems that have been introduced relying mainly on Refs. [1–3].We will then present the outline of this PhD work.

1.1. Geometrical frustration: From water ice to spin ice materials

Frustration in physics as well as in life, arises from the incapacity to simultaneously satisfy interactions at play. The prime example is to consider three spins equally spaced as shown in Fig.1-1.

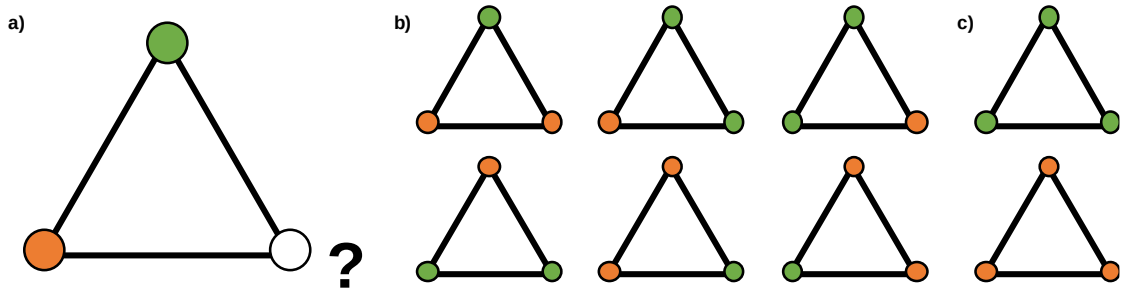

Fig.1-1: Three-spin located at the vertex of a triangle; a) if two of them are antiferromagnetically coupled, the third that can be either antiferromagnetically coupled to one and ferromagnetically coupled to the other; b) the six possible low-energy configurations and c) the two high-energy configurations. Green disk is taken as out-of-plane going out and orange out-of-plane going in.

If two of the three spins are taken in their low-energy configuration hence with antiferromagnetic coupling, there will be inevitably frustration with the third one (Fig.1-1.a)). Indeed, the remaining spin

will be antiferromagnetically coupled with one of the spins and ferromagnetically coupled with the other. There are six possible configurations that match these interactions that are of same energy shown in Fig.1-1.b). This obvious frustration brings along the concept of degeneracy. Among the $2^3 = 8$ possible configurations, six of them are low-energy configurations and the last two are of high-energy configurations with exclusively antiferromagnetic couplings or ferromagnetic couplings (Fig.1-1.c)).

In nature, the prime example of a frustrated material is water ice, one of its numerous enigmas was its residual entropy at low temperature. Experimentally measured by Giauque and Ashley [4] in the 1930s, Pauling explained this result by the arrangement of the protons around the oxygen atoms at the vertices of a diamond lattice [5]. Protons are not centred on the oxygen-oxygen bond but rather close(far) of one(other) forming a two-in/two-out configuration as shown in Fig.1-2.a), baptised the ice rules.

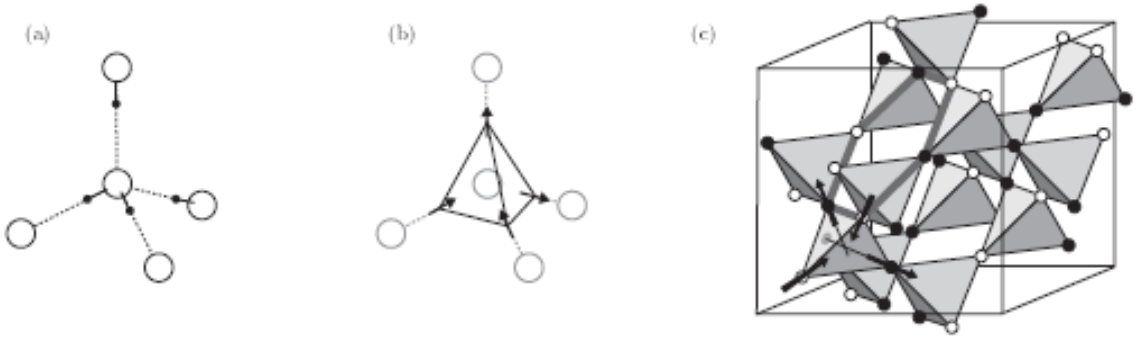

Fig.1-2: From Ref. *[6]*, (a) the arrangement of the molecule H_2O and the asymmetry in the protons baptized as the ice rules; (b) the translation of the ice rules in spin configuration with a two-in/two-out configuration and (c) the disorder resulting from the ice rules in rare-earth titanate pyrochlores.

These fascinating properties of frustration got a further impulse in the 1990s with the discovery of rare-earth titanate pyrochlores such as $Ho_2Ti_2O_7$ and $Dy_2Ti_2O_7$ magnetic materials with icelike behaviour [7]. Due to both ferromagnetic coupling and anisotropy that force the spins to align along the centre of corner-sharing tetrahedra, the ice rule arises among the spins (Fig.1-2.b) and c)). These materials with their two-in/two-out spin configurations, found to have residual entropy at low temperature [8], were baptised spin ice materials.

1.2. Artificial spin ice

Artificial spin ice has been introduced for the first time in 2006 by the pioneering work in Schiffer's group by Wang *et al.* [9]. The goal was exactly as suggested by the name: mimic the properties of icelike materials with a novel class of metamaterial. Ever since, new geometries for various studies have emerged.

Wang *et al.* created networks of nano-magnets in interaction of thin Permalloy films fabricated using semiconductors fabrication processes, with dimensions allowing Ising-like behaviour. These elements are arranged according to a square lattice where 4 meet at the vertices as shown in Fig.1-3.

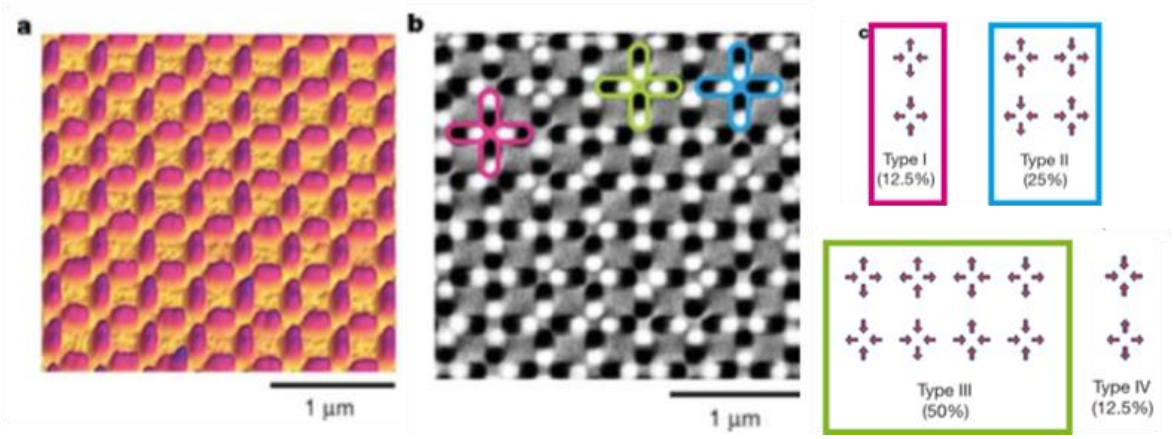

Fig.1-3: Adapted from Ref. [9], a) atomic force microscopy (AFM) image of the array of elongated nanoislands; b) corresponding magnetic force microscopy (MFM) image and c) the 16 possible vertex configurations, Type I, Type II and Type III vertices are observed experimentally.

There are 2^4=16 possible vertex configurations, six of them obeying the 2-in/2-out ice rules. The translation from the three-dimensional pyrochlore, where all six pairwise interactions are equal, to the 2-dimensional artificial spin ice loses the degeneracy. In square ice, perpendicular spin pairs have stronger interaction than collinear pairs. In the conventions set by Wang *et al.* -that the community still uses today- it means that Type I vertices are of lower energy than Type II. They have shown that using a field-demagnetized protocol -later studied in Ref. [10]- an experimental system exhibits both types and vertices with ice rules violations with spin flips creating pairs of Type III vertices. In 2011, it has been shown by Morgan *et al.* [11] that observing these systems after deposition and lift-off, in the a-grown state, that long-range low energy states can be reach.

The second geometry of artificial spin ice was introduced within months after the work of Wang *et al.* by Tanaka *et al.* [12] with continuous honeycomb geometry shown in Fig.1-4 and disconnected geometry by Qi *et al.* and Mengotti *et al.* [13,14].

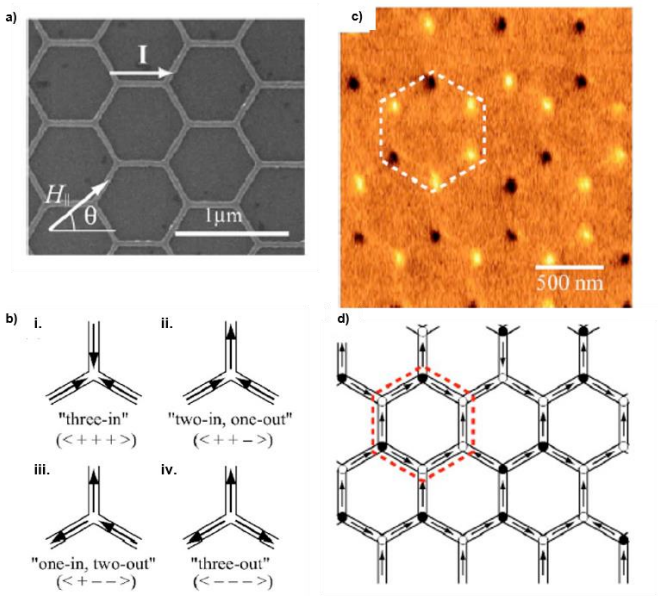

Fig.1-4: Adapted from Ref. [12], a) SEM image of continuous honeycomb network; b) the four possible arrangements of the 3-spin vertex; c) corresponding MFM image and d) extracted spin configuration.

In this geometry, 3 spins point toward the vertex and all interactions are equal. This geometry exhibits two types of vertex configurations that are 2-in(out)/1-out(in) obeying the pseudo-ice rules and 3-in(out) configurations. These two types carry either a ±q and ±3q charge, no uncharged vertices is allowed.

Artificial spin ice have proven their flexibility of tailoring through nanofabrication processes and ease of observation of individual elements by various techniques (magnetic force microscopy (MFM), photoemission electron microscopy (PEEM), Lorentz Microscopy, scanning transmission x-ray microscopy (STXM), Kerr-Microscopy, …). Various geometries have emerged as shown in Fig.1-5.

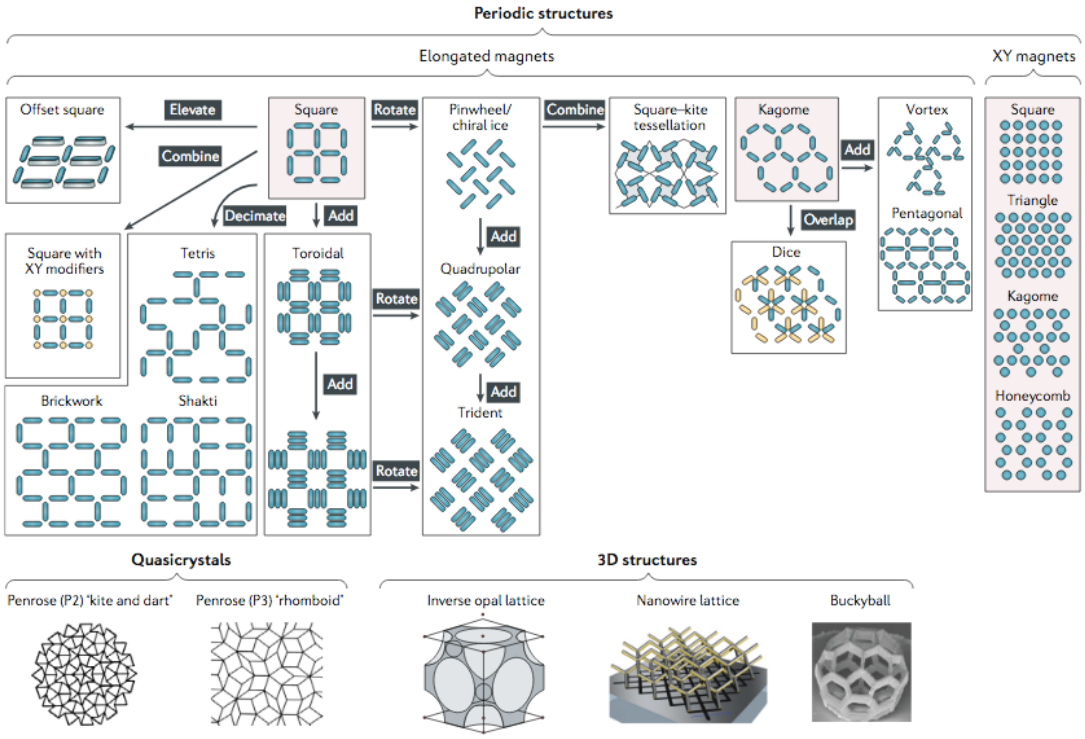

Fig.1-5: From Ref. [3], reported artificial spin systems inspired by the square and honeycomb/kagomé artificial spin ice.

The properties of artificial spin ice have been exploited to study various intersecting phenomena such as phase transitions [15] or magnetic monopoles [16,17]. This last point has been of particular interest since it has been an easy demonstration of similar behaviour as Dirac strings with reversals under magnetic field [18,19]. This first systems inspired by Wang *et al.* were athermal in the sense only temperature of 10^4-10^5 K would induce any fluctuations of the magnetic configuration. It has been shown that these systems can be thermally active first on the square ice [20]. Collective behaviour below blocking temperatures have been studied by precise optimisation of the element dimensions [21,22]. Our listing is far from exhaustive.

There are many possible device applications for artificial spin ice and artificial spin systems in general such as computation, data storage but unconventional logic such as reservoir computing [23,24]. It has been enabled mainly by the potential of tuning the interactions for the desired applications as shown in Fig.1-6.

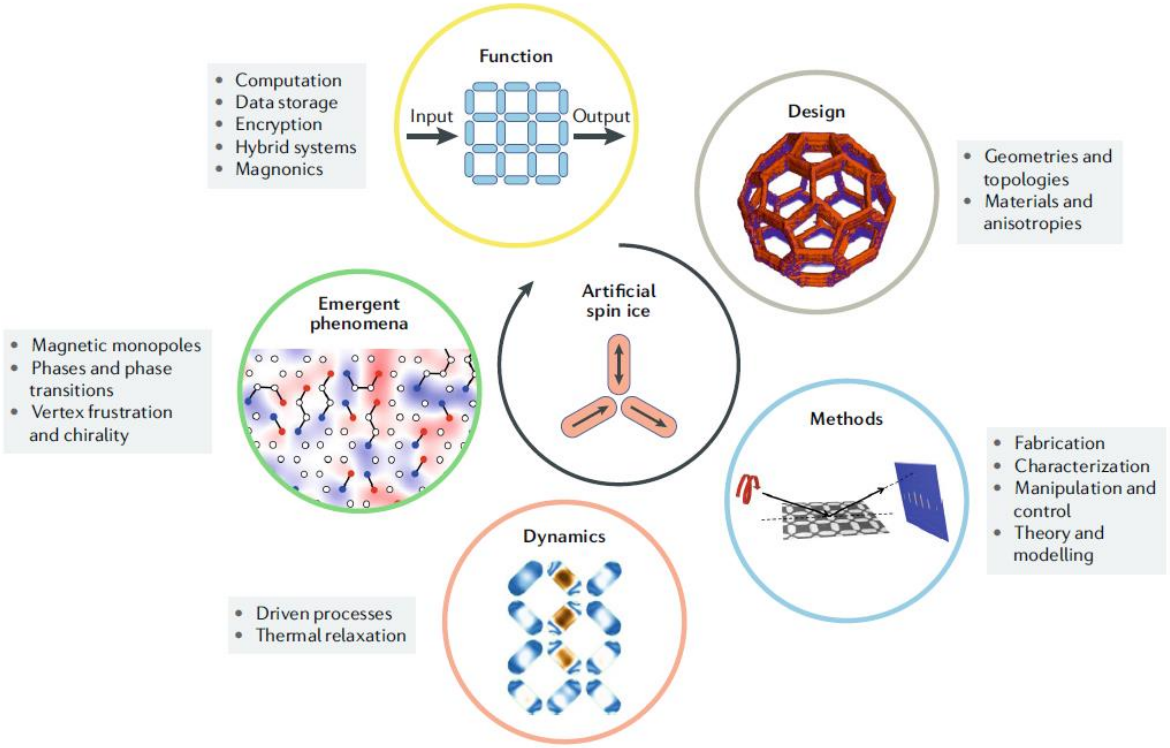

Fig.1-6: From Ref. [3], artificial spin ice, "the key directions for future research" as presented by Skjærvø et al.

It should also be mentioned that artificial spin system are not limited to nanomagnets but also coloids [25], superconductors [26] and buckled-polymer nanostructures [27].

1.3. Motivations and overview

In this work, we present a study of artificial spin ice systems as a playground for competing interactions. Tailoring of the geometry of classical geometries will be presented with two ambitions: first, the study the thermodynamics and the ground state evolution with rotation angle and second, for random generation number with the development of nanoscale Galton board.

We will first present the methods and techniques used for the fabrication of the samples presented in this work. We will compare the two main fabrication processes and discuss the issues that we had to take into consideration for our artificial spin systems. We will also detail the magnetic characterisation that we performed using mainly magnetic force microscopy (MFM). In this part, the reader shall find our approach to understand the spin configurations extracted from the MFM images of our systems.

The following chapter is dedicated to the study of a modified classical square ice through the rotation of the elements. We will first study the evolution of the dipolar interactions that suggest a transition from antiferromagnetic order (Type1 vertices) for the square ice to ferromagnetic order (Type2 vertices) for the pinwheel ice. Our computations will show the necessity to consider interactions beyond first neighbours to obtain an accurate description of the system total energy and ground state. We will then confront dipolar computations to experiments with two low-energy samples: as-grown state and field-demagnetized state. The as-grown state, the lowest-energy system, will be studied in terms of magnetic

structure factor that will give a characterisation of the system order evolution according to rotation angle. Using Monte Carlo simulations, we will establish the phase diagram of our frozen system. We will demonstrate that describing our system energy with a dipolar Hamiltonian, both energy and vertex populations are described by a unique effective temperature.

The last part of this work will focus on the application of artificial spin systems as potential devices notably stochastic computing applications. This work exploits the properties of reversals under magnetic field in honeycomb artificial spin system. We will show that with a precise study of reversals in both disconnected and connected geometries that reaching avalanche-like behaviour from a chosen starting point is actually quite complex. Our development of such a system is in need of particular features to obtain unidimensional propagation from one end to the other end of the structure. After the optimisation is completed, we will make a detailed study of the experimental domain wall propagations extracting several scenarios. We will show that the propagations are stochastic and the structure resembles a Galton in both design and behaviour. We will explain that we have achieved the development of a system for random number generation, slightly biased. The absence of memory effect between successive choices while propagating emphasises the randomness of the device. We will also show that this stochastic behaviour is robust at low temperature. We will also explain a few leads on the origin of the stochastic behaviour of our artificial spin system.

Chapter 2. Methods and techniques

"Une bonne mesure, ça se mérite !"
D. Lacour

Artificial spin systems are a class of metamaterials that are tailor-designed and can be directly visualised. These two-dimensional arrays of nanomagnets in interaction are fabricated using standard nanofabrication processes and observed by atomic-scale microscopy. This thesis essentially focuses on experimental studies of artificial spin ice systems in which nanofabrication and magnetic characterisation are crucial steps. In this chapter, we will present our method to fabricate and observe our designed systems. First, we will present the steps of our nanofabrication process and the challenges overcome to ensure accuracy between design and sample. Then, we will detail our method for their magnetic characterisation to determine the spin configurations. This last part aims for the reader to understand the magnetic force images presented in this work on our various structure types.
I have made the choice to present the processes and techniques that I have performed myself. Other techniques were used by or with the help of colleagues which will not be detailed here. If details are needed, we refer to Dr. K. Ait Oukaci's PhD thesis for Scanning Transmission Microscopy and Vibrating Sample Magnetometer [28], to Dr. C. Guillemard's PhD thesis for the Ferromagnetic Resonnance [29] and to Dr. D. Louis' PhD thesis for Monte Carlo simulations [30].

2.1. Nanofabrication

Artificial spin ice systems are arrays of nanoislands with lateral dimensions a few hundreds of nanometres long and wide, tens of nanometres thick. The first introduced system by Wang *et al.* [9] was fabricated using a lift-off process but artificial spin ice systems have also been elaborated by etching process [20,30–32]. In this section, we will compare both nanofabrication processes, explain the challenges of the e-beam lithography and show the characterisation of the deposited Permalloy.
All nanostructures presented in this work were elaborated in the MinaLor platform, cleanroom of the Institut Jean Lamour.

2.1.1. Process flows

All nanofabrication processes for the elaboration of artificial spin systems have in common the use of a high-resolution patterning technique. Electron-beam lithography -also called e-beam lithography- is widely use because of its versatility, reproducibility and ease of use [33]. Around it, one has many possible ways to obtain the designed magnetic nanostructures. Here, we will present two process flows among all available that we used to fabricate our samples: magnetron sputtering combined with etching

and e-beam evaporation combined with lift-off. From now on, we will refer to the former as etching process and the latter as lift-off process for simplicity purposes. We emphasise that these appellations are somewhat imprecise since evaporation and lift-off is used for both processes.

In our processes, we start with Ta(3nm)/NiFe(20nm)/Pt(3nm) stack (Ta and Pt act as adhesion and capping layers respectively) on top of Si substrate for the etching process and with a plain Si substrate for the lift-off process as shown in Fig.2-1.

Fig.2-1: a) Ta(3nm)/NiFe(20nm)/Pt(3nm) deposited with magnetron sputtering on top of Si substrate for the etching process and b) plain Si substrate for the lift-off process.

For both fabrication processes, the next step is to shape a mould of nanoarrays by e-beam lithography. After cleaning the surface with solvents, we spin-coat and bake a bi-layer of Poly(methyl methacrylate) (PMMA) positive electrosensitive resist, diluted 33% (PMMA/MA) and 2% (PMMA) as bottom and top layers respectively. We then draw onto it the design with the electron focused beam of the e-beam lithography. This has the effect to change the chemical properties of the resist whose exposed regions are then dissolved in a resist developer bath (Methyl Isobutyl Ketone (MIBK) and Isopropanol (IPA) 1:3). The three described steps, spin-coating, exposition and development, are shown in Fig.2-2.

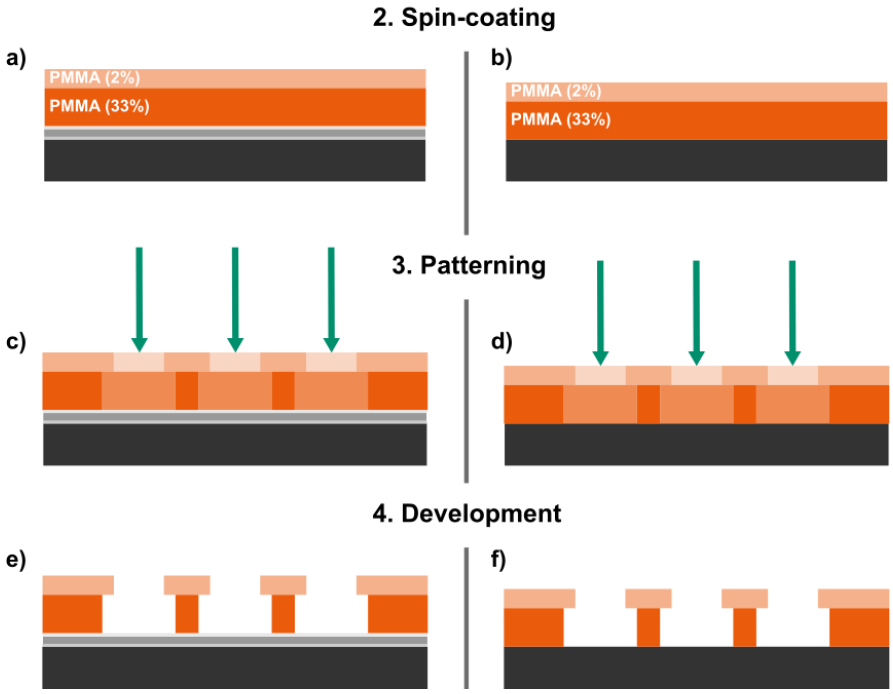

Fig.2-2: On the left etching process and on the right lift-off process, a)-b) spin-coating and baking of bi-layer PMMA/MA (33%) and PMMA (2%), overall resist thickness is 300 nm measured by profilometer; c)-d) patterning by e-beam lithography, exposed resist is represented with a lighter colour; e)-f) development of the exposed resist in MIBK/IPA (1:3) and IPA baths.

As can be seen in Fig.2-2.e)-f), now the two fabrication processes differ: for the etching process, the mould needs to be used for protection whereas for the lift-off process the mould needs to be filled. For the etching process, a thick-enough hard mask layer for the etching step is needed to reveal the structures, here we choose to use Al. One could suggest negative resist or having patterned all around the nanostructures for the remaining resist could act as a hard mask but PMMA is not suitable for the Ion Beam Etching (IBE). For the lift-off process, we need to deposit the magnetic material and a capping layer to prevent oxidation. The depositions of the 100 nm-thick Al layer for the hard mask and the NiFe(20nm)/Al(3nm) stack are performed by e-beam evaporation, thickness is surveyed using a quartz crystal microbalance. The next step is to remove the surplus of material that is the resist and the material onto it. To do so, we leave the sample in a Remover 1165 hot bath (two hours at least) then get it sonicated. This procedure is repeated twice before rinsing the samples with water. The bath dissolves the resist beneath the material which is then removed from the sample's surface. The described steps are shown in Fig.2-3.

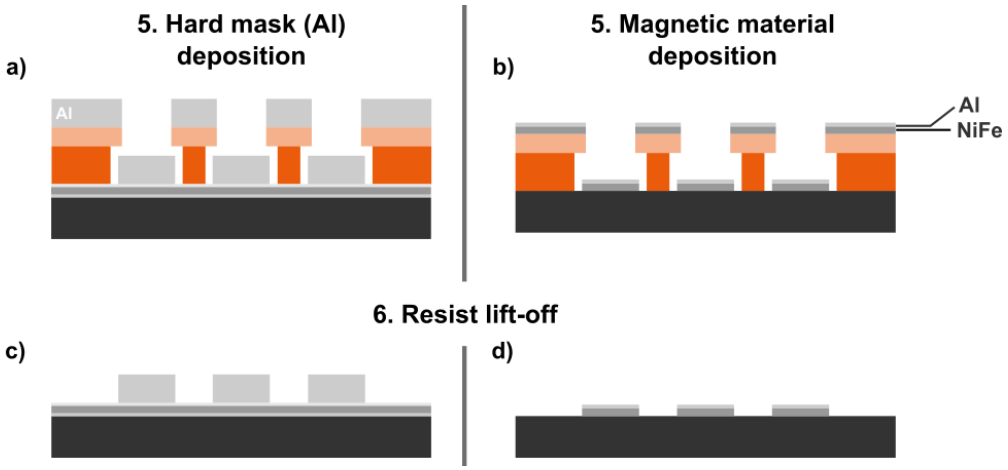

Fig.2-3: a) Deposition by e-beam evaporation of 100 nm-thick Al layer acting as hard mask in order to perform IBE and b) NiFe(20)/Al(3) also by evaporation for the lift-off process; c)-d) result of lift-off of the remaining resist and surplus of material by Remover1165 hot bath and sonication.

We mention here that the lift-off is the reason we use a bi-layer resist. While exposing, the less the PMMA is diluted the bigger will be the area where the electrons will be diffused hence the shape of the mould (Fig.2-2.e)-f)). Deposition by evaporation is directional leaving lateral and vertical gaps between resist the material deposited. These spacings make it easier for the remover to reach the resist all around the patterned areas.

On one hand, the lift-off process is now over since as shown in Fig.2-3.d) the nanostructures in NiFe are revealed. On the other hand, the etching process requires another one last step that is the etching strictly speaking. We etch the sample and survey the materials evolution using secondary ion mass spectrometry (SIMS). The hard mask thickness is chosen high enough to ensure that the magnetic material beneath is protected while the uncovered material is etched up to the substrate. The final sample is similar to the lift-off one except for the Ta and Pt thin layers and the Al left after IBE.

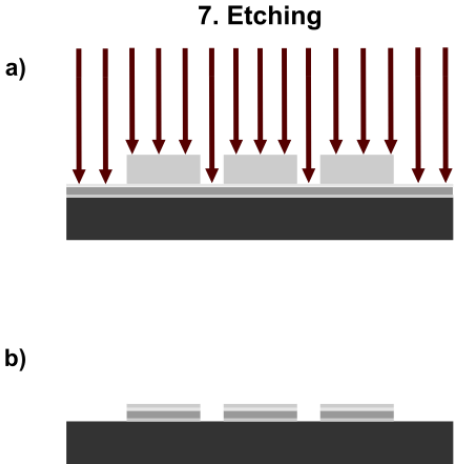

Fig.2-4: a) Etching step and b) final sample of the etching process.

The lithography and evaporation will be explained in the following sections but before, we will stress the pros and cons of both presented process flows.

2.1.2. Pros and cons of both fabrication processes

The etching and lift-off processes described before are in fact the prime examples of what one could name an industrial process and a research process (apart from e-beam lithography that is too slow for industrial process). Although the described lift-off process is widely used to elaborate artificial spin systems both methods present pros and cons. To make a comprehensive comparison, there are several aspects to consider.

The first concern is the magnetic material deposition. We have the choice between sputtering and evaporation for the etching and lift-off processes respectively. We emphasise here that it may be an issue only in a particular case of observation the so-called as-grown state [11]. Explained in a few words, the as-grown state purpose is the observation of long-range ground state of lithographically patterned nano-arrays. Because of shape anisotropy by constraining the growth inside the mould, the system is supposed to arrange by itself according to neighbouring dipolar couplings. This is achievable only if the magnetic material is not exposed to any strong fields during deposition. Thus for this particular case, evaporation is more suitable than sputtering that is our previously described lift-off process. However in our etching process, NiFe is deposited before patterning which adds another concern, the non-constrained growth. We will show in the next chapter the effect of both sputtering and not using the mould leads to no reasonable low-energy configuration in its as-grown state.

The second concern is the potential redeposition during lift-off and etching. On one hand lift-off, possibly non-reproducible process step, is a very good chance to witness redeposition. It also becomes more challenging when closed shapes are patterned as in connected kagomé artificial spin ice for example. On the other hand while etching, redeposition may also occur as collars on the edges of the nanostructures but it can be overcome by tilting the sample or by using another hard mask material for example Ti as explained in Ref. [28]. Although this was not observed in our samples by etching process, other aspects are to consider before choosing one process over the other. Etching by IBE is an added step compared to the lift-off that could require optimisation. Lift-off with the bi-layer resist is quite easy to perform and fulfils most of the time its purpose. Since we do not have the time-issues of the microelectronic industry and we cannot perform its star technique (Reactive Ion Etching (RIE)) because we handle magnetic materials, we choose to mainly perform lift-off.

The last concern is the magnetic characterisation. Our etching process leaves a hard mask that is most likely thicker than the capping layer of the lift-off process. This added thickness of material could make the observation by magnetic force microscopy more challenging. Indeed the topography can be more difficult to follow and the signal could be reduced.

All samples presented in this manuscript are fabricated using evaporation and lift-off unless otherwise mentioned.

2.1.3. Patterning by e-beam lithography

We have used a Raith 150-TWO equipment to perform the e-beam lithography. We use its software combined with a Python program to design our –sometimes complex- artificial spin systems. We present our approach for the design and the patterning parameters used. Information about its working principal can be found in Ref. [33].

One needs to understand the beam trajectory onto the sample in order to obtain the designed nanostructures (Fig.2-5.a)): the less the beam moves the better should be the resolution. We also need to keep in mind that features below 20 nm are very difficult to achieve. For the design of our nanostructures, we try -as much as possible- to cut the nanostructures in elementary elements and control the patterning order. The aim is twofold: small identical features should be patterned in similar way (Fig.2-5.b)) and the ordering in pattern (Fig.2-5.c)) should decrease the beam displacements or deflections. Both are considered in order to increase precision.

We design our nanostructures using the Graphic Database System II (GDSII) software. We set the write field dimensions to 100 µm × 100 µm, area where only the beam moves and its deflections are in focus. We manage the design so our structures do not cross write fields in order to avoid stitching issues.

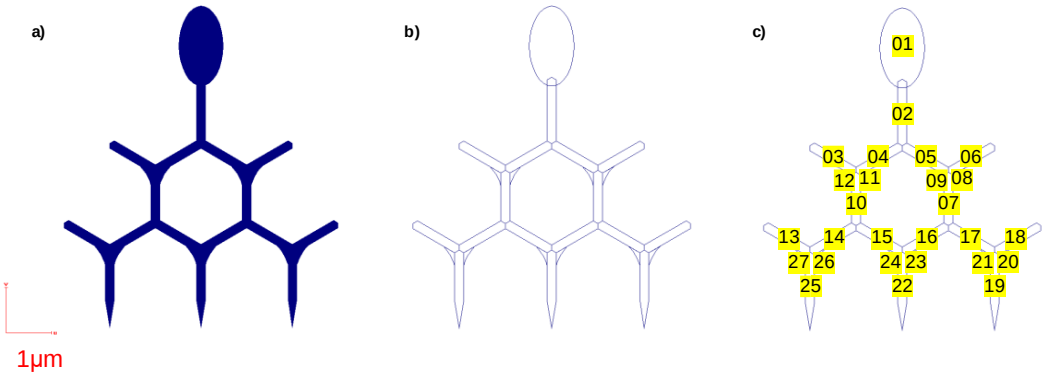

Fig.2-5: a) The design of an optimised connected kagomé-like artificial spin system; b) composition of the design in identical elements and c) their patterning order.

The next step is to pattern the design onto the resist. For resolution purposes, we set the acceleration voltage to 20 kV and the aperture to 10 µm of column. The reference area dose is taken at 120 µC/cm^3 with an area step size set at 10 nm (sometimes 20 nm) and for curved elements a curve step size at 20 nm. We make sure that the area step size is indeed a multiple of our elements width to ensure their symmetry. Different doses factors are patterned simultaneously in all samples so we can choose the right dimensions. With these parameters, we then have to choose a suitable patterning mode, responsible for the beam trajectory of a given feature. Because our design can be complex with small features (as shown in Fig.2-5) we have tested various modes. We show in Fig.2-6 the patterning of the ellipse and two of different patternings for our rectangular-like elementary elements as computed by the Raith Software.

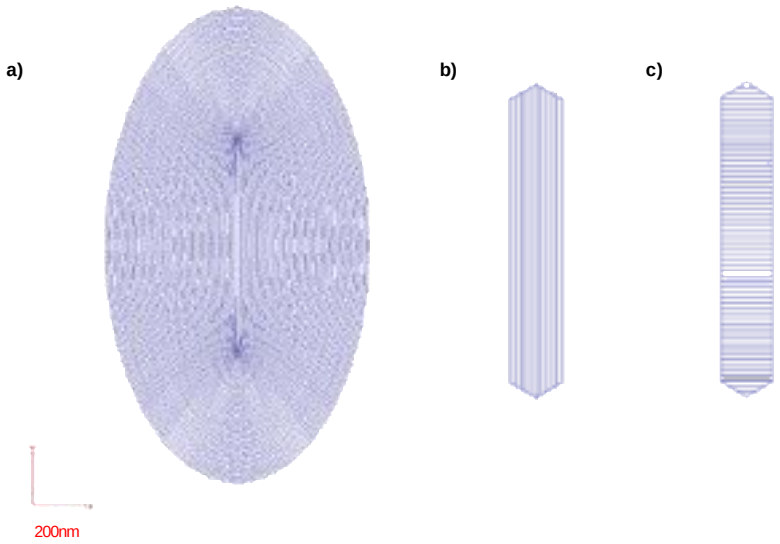

Fig.2-6: a) Curved element patterned inwards; elementary element shown previously patterned using b) Longitudinal Meander mode where lines are patterned along its long axis in one and the opposite directions successively and c) Transversal Line mode where lines are patterned along its short axis each time in the same direction. Area step size of 10 pixels (20nm) is shown here for simplicity purposes.

Longitudinal mode (Fig.2-6.a)), with its efficient speed pattern, is the most commonly used. However, in our connected honeycomb nanostructures it raises an intractable issue. We show in Fig.2-7.a) the longitudinal patterning of an intersection computed by the software.

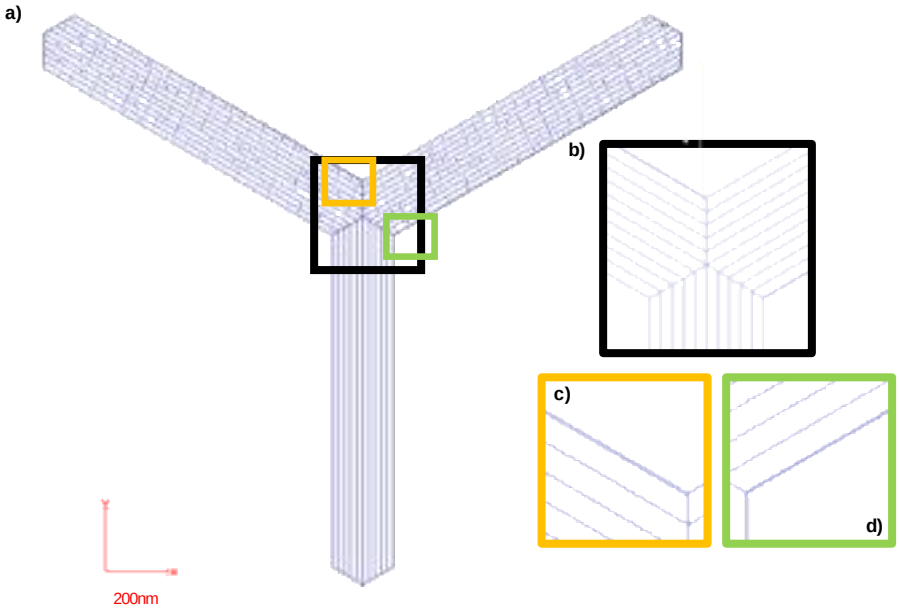

Fig.2-7: a) Longitudinal patterning of an intersection of connected kagomé structure; b)-d) close-up views.

We see on the close-up view of the intersection (Fig.2-7.b)) that the division in patterning lines is not identical for all three elements, there are additional lines in both tilted elements as shown in Fig.2-7.c) and d). For the left tilted element (Fig.2-7.c)), we observe on its upper edge that the last patterned line is close to the element edge. A similar feature is observed in the right tilted (Fig.2-7.d)) element at its

lower edge. This shows that the subdivision of our rotated elements in equally spaced patterning lines is not well handled by the software. These additional patterning lines could overexpose the specified edges of our elements and in turn be responsible not only for a widening of the dimensions but also an asymmetry in the intersection. In connected artificial spin systems used for domain wall propagation, any lithographic asymmetry [34] or roughness on our nanowires [35,36] can modify the propagation characteristics which is highly unintended.

To overcome the last-mentioned issue, we choose to use a different patterning strategy, less efficient in terms of speed: the Transversal Line patterning (Fig.2-6.c)). We show the computed patterning lines of an intersection in Fig.2-8.a).

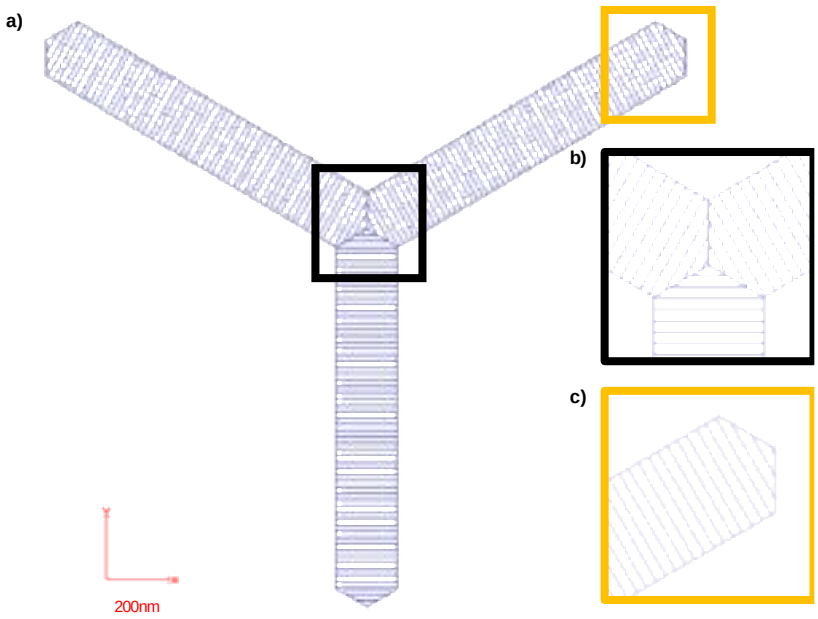

Fig.2-8: a) Transversal Line patterning of an intersection of connected kagomé structure; b)-c) close-up views.

Looking closer at the patterning lines at the intersection (Fig.2-8.b)) we observe again a mismatch between patterned lines of the elements at the centre of the intersection. This feature is also observed at the ends of the elements as shown in Fig.2-8.c). Both observations show the unequal subdivision in patterned lines of the elements by the software. However in this case, any over-exposition will occur around the centre of the intersections thus without creating any asymmetry at the edges.

We show Scanning Electron Microscopy (SEM) images for samples using both Longitudinal Line and Transversal Line generated patternings in Fig.2-9.

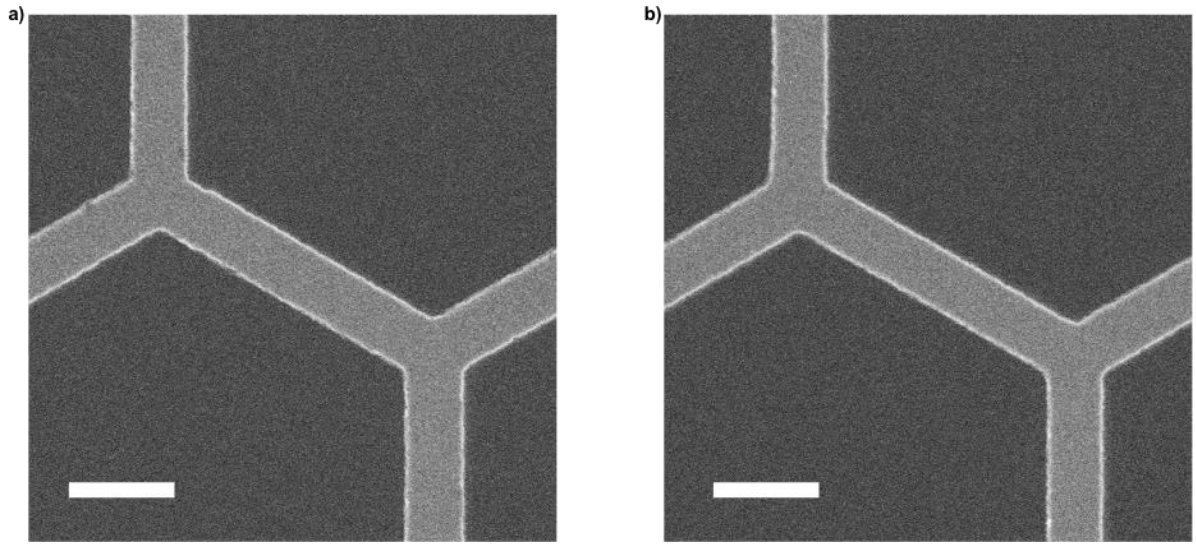

Fig.2-9: SEM images of vertices patterned using a) longitudinal line patterning (5 pixels of 2 nm) and b) transversal line patterning (5 pixels of 2 nm). Scale bars are 400 nm.

In our patterned structures, we observe smooth edges but a small widening of the dimensions of a few tens of nanometres. Looking carefully at the intersections, we observe an asymmetry with the Longitudinal Line mode (Fig.2-9.a)) that is absent in the Transversal Line mode (Fig.2-9.b)) as expected. As observed on Fig.2-9.b), the over-exposition at the centre of the intersections is not an issue to obtain smooth and symmetric features.
We mention that these issues could have been overcome using specific software allowing fine control of the patterning strategy but was not accessible for this work.
All features detailed here were taken into account when patterning samples. This has led to the fabrication of numerous samples. We show SEM images of our square artificial spin ice (detailed in Chapter 3) and our optimised honeycomb connected artificial spin system (detailed in Chapter 4) in Fig.2-10.

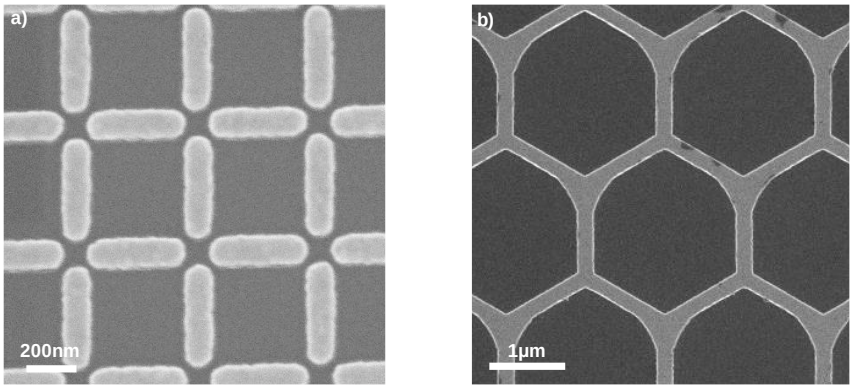

Fig.2-10: SEM images of a) square ice network and b) optimised connected honeycomb nanostructures elaborated.

2.1.4. Permalloy deposition by e-beam evaporation

We performed the thin-film deposition with a Plassys MEB400S ebeam evaporator (thanks to Dr. L. Badie). As mentioned in the previous section, we used the lift-off and evaporation approach for the

fabrication of most of our samples. We want to deposit 20 nm-thick Permalloy ($Ni_{80}Fe_{20}$) layer and 3 nm-thick Al cap layer to prevent the magnetic one from oxidation.
We have performed Scanning Electron Microscopy/Energy Dispersive X-ray Spectrometry (SEM/EDS) to determine the stoichiometry of our material (performed by S. Mathieu). We find that our NiFe is composed by 80% of Ni and 20% of Fe. This result is consistent with the expected stoichiometry of Permalloy.
We have verified the in-plane magnetisation by Vibrating Sample Magnetometer (VSM), the hysteresis loops are plotted in Fig.2-11.

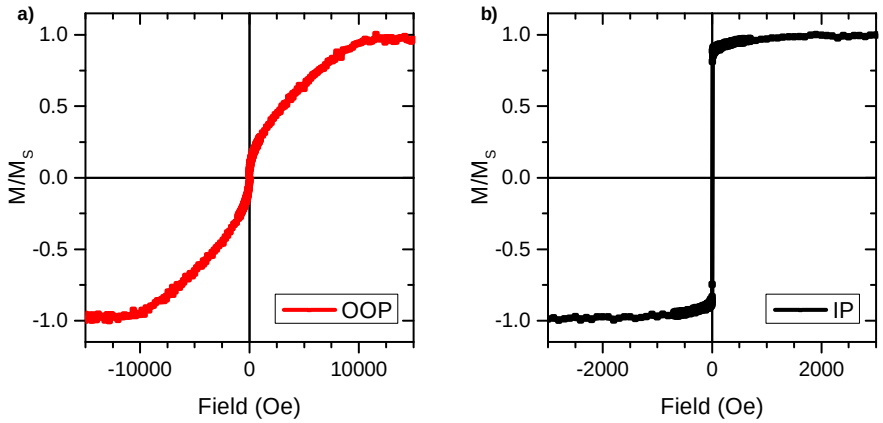

Fig.2-11: a) Out-of-plane (OOP) and b) in-plane (IP) hysteresis loops on 20 nm-thick Permalloy full film (performed by Dr. K. Ait Oukaci).

We find a coercivity of 7.35 Oe and a saturation magnetisation of 835 emu/cm^3, consistent with literature. We have verified the homogeneity of our material by ferromagnetic resonance and determined its damping and its effective magnetisation. Our Permalloy follows Kittel's law, the measurement have returned a damping value of $\alpha = 4.4 \,.\, 10^{-3}$ and M_{eff}=836 emu/cm^3 and confirmed that the magnetic material is magnetically uniform. Results are shown in Fig.2-12.

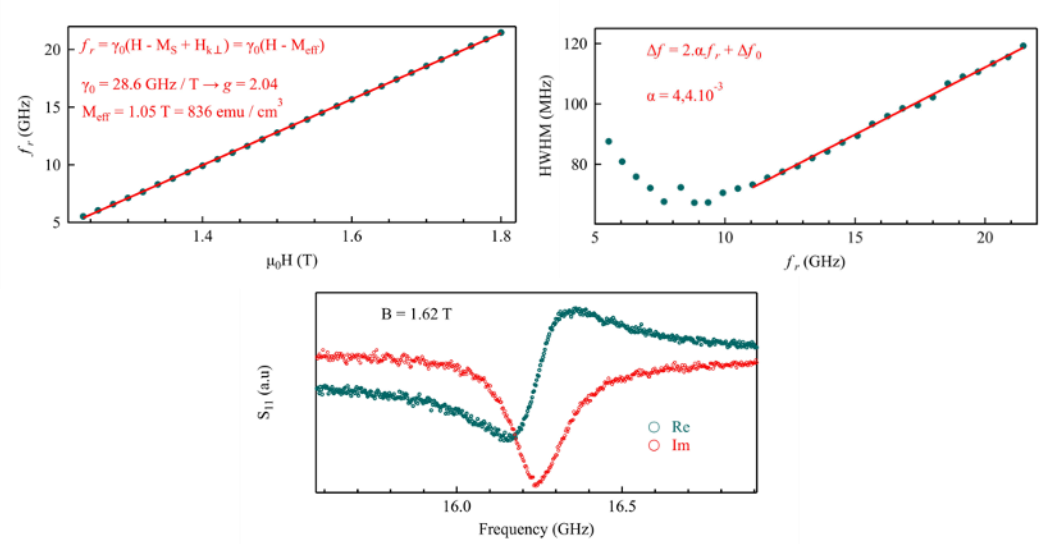

Fig.2-12: Ferromagnetic resonance measurement (performed by Dr. C. Guillemard).

2.2. Characterisation by Magnetic Force Microscopy

For this work, we have mainly used magnetic force microscopy (MFM) for the characterisation of our artificial spin systems [37]. The aim of this section is twofold: to present the possibilities of our equipment and to give keys to understand the images presented in this manuscript.
All images presented were processed using WSxM 5.0 Develop 9.0 software [38].

2.2.1. The microscope and its use

The magnetic force imaging using an atomic force microscope is performed with a sharp tip coated with magnetic material (typically Co alloy). The forces of interest are the tip-magnetic sample interactions which are detected with the probe trajectory shown in Fig.2-13. Further information about its working principle can be found in Prof. M. Hehn's PhD thesis [39].

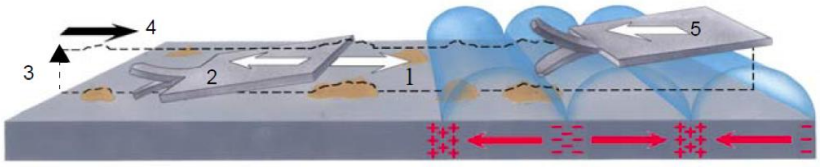

Fig.2-13: From the Vecco Dimension 3100 Manual: 1st and 2nd step, the probe traces and retraces the surface to get the topography in tapping mode; 3rd step: the probe ascends in the Lift Scan Height or Nap Height; 4th and 5th steps: probe traces and retraces the topography.

Our magnetic force microscope is an Asylum Infinity microscope in MFM mode. This equipment was used for all the MFM images presented in this manuscript unless otherwise mentioned. A picture of our setup is shown in Fig.2-14.

Fig.2-14: MFM set up used for this work.

It is equipped with a Variable Field Module 3 (VFM) for the application *in situ* of magnetic field. For our work, especially on domain wall propagation. This module was used in planar configuration. We show its schematics in Fig.2-15.

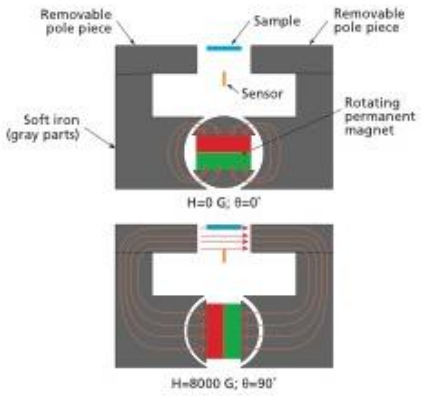

Fig.2-15: From Oxford Instruments Brochure: schematics of the VFM module in planar configuration.

The removable pole pieces are placed by hand onto the holder as well as the sample onto the VFM module. Therefore an imprecision in the field alignment according to the sample can be expected. The poles are always placed with great care and the nanostructures to be observed disposed as much as possible centred in between the pole pieces. To further prevent any misalignment issue, we patterned our nanostructures with several tilts (in steps of 0.5°) and measure the ones aligned with the scan. This method has the advantage to leave an uncertainty only on a possible misalignment of the pole pieces. Tilted design patterned is shown in Fig.2-16.

Fig.2-16: Example of multiple tilted patterns for MFM observation in order to find the right alignment according to the scanning direction. Structures are patterned on 90 µm x 45 µm.

The microscope comes also with automation software MacroBuilder for the control of scanning parameters and field application. An example of field procedure used in this work is shown in Fig.2-17.

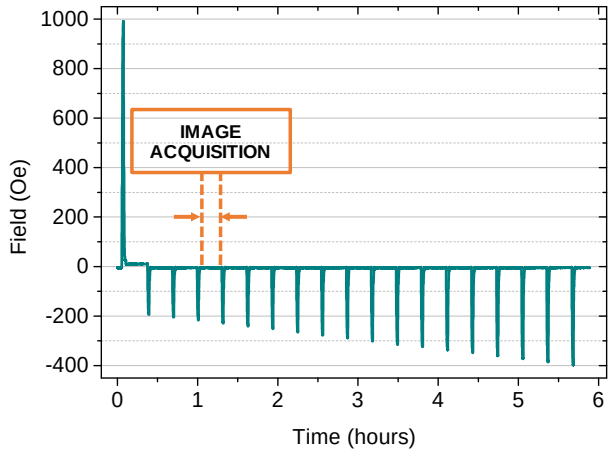

Fig.2-17: Example of field protocol used: saturation at 1000 ± 10 Oe then starting from –200 ± 2 Oe the field is decreased in steps of 12 ± 10 Oe. Typical time to reach field setpoint is 2-3 s. Here, and as well in all our under-field experiments, the images are taken at remanence and image is acquired in about 17 minutes.

This automation of the acquisition can be repeated as long as the probe holds. It allows to stay in identical conditions and has been of great interest when large amount of data is required. We will discuss the optimisation acquisition later (section 2.2.3).

2.2.2. Interpretation of the contrasts

In this section, we will present typical MFM images of the systems of interest in this work. The goal is to give the reader keys to determine the spin configurations of our artificial spin systems from their contrasts. We will first show our MFM data on frozen disconnected networks and then on connected kagomé-like systems.

2.2.2.1. Frozen systems disconnected

We focus here on disconnected geometries in a square-like geometry which will be the topic of Chapter 3. Images were acquired using Standard Asylum tips. We scan in both upward and downward directions to verify that the tip does not alter the magnetic configuration.

The goal is to determine the individual configuration of the nanomagnets composing the networks. Due to their elongated shape, the elements will exhibit opposite contrasts at their ends that are easily identified as shown in Fig.2-18.

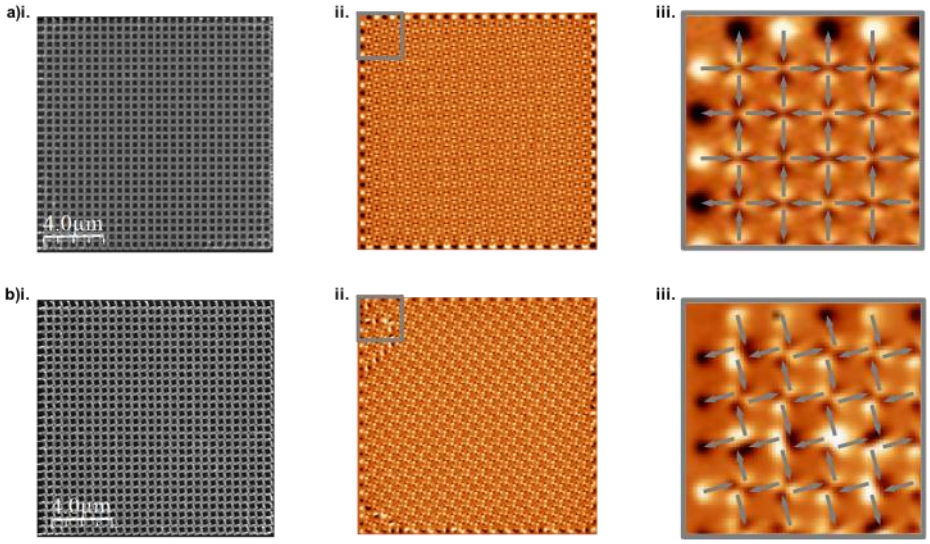

Fig.2-18: a) Square network and b) 15°-tilted network and their i. AFM image, ii. MFM image and iii. the corresponding spin configuration.

The geometry -square or 15°-tilt - matters little and the spin configuration is determined unambiguously. This is true as long as the same convention of contrasts is kept (here the spin is pointing to a black contrast).

For these systems, configurations were extracted manually and results obtained are in good adequacy with the ones observed in literature.

2.2.2.2. Domain wall propagation in connected systems

We will now present the interpretation of the MFM data for connected honeycomb geometries acquired with low moment (LM) and high coercive (HC) Asylum tips and also LM NanoSensors tips. We have verified that scanning more than once the same area does not exhibit different contrasts.

In this section, we will focus on two small geometries (SEM images are shown in Fig.2-19) to explain how we extract from the MFM images the spin configurations.

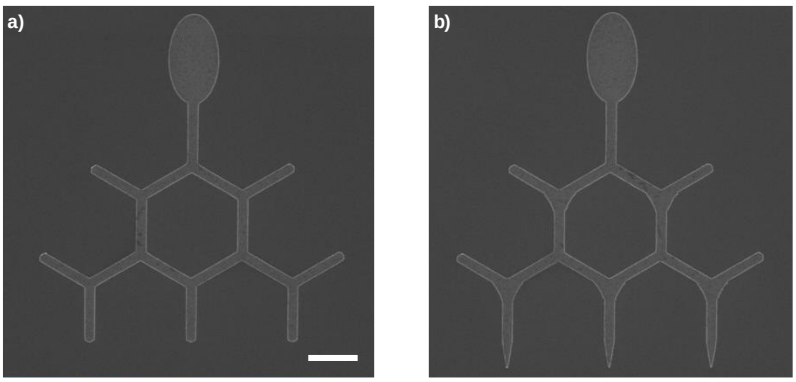

Fig.2-19: SEM images of a) nanostructure with symmetric intersections and b) with funnel-shaped intersections. Scale bar is 1 µm valid for both images.

On these structures, we aim to observe that reversals induced by a nucleated domain wall from the elliptic pad to the end of the structure. The field protocol used for these structures is as shown previously in Fig.2-17.

We begin with the MFM images of our structure with symmetric intersections (SEM image in Fig.2-19.a)). First, we apply +1000 Oe to saturate the sample along the length of the structure (see the black arrow in Fig.2-20.a)i.) and go back at remanence. After relaxation spins are oriented in the same direction defined arbitrarily upwards, as shown in Fig.2-20.a)ii.. The corresponding MFM image exhibits contrasts at its edges and vertices. From only the edges, contrast convention can be identified and we can deduce the colours associated to each vertex configuration. In our case, using the contrasts at the edges at saturation (Fig.2-20.a)i.) we find that the spin is pointing to a black contrast yielding our contrast convention. In turn, we can extrapolate contrasts for the possible vertex configurations as shown in Fig.2-20.b)-c).

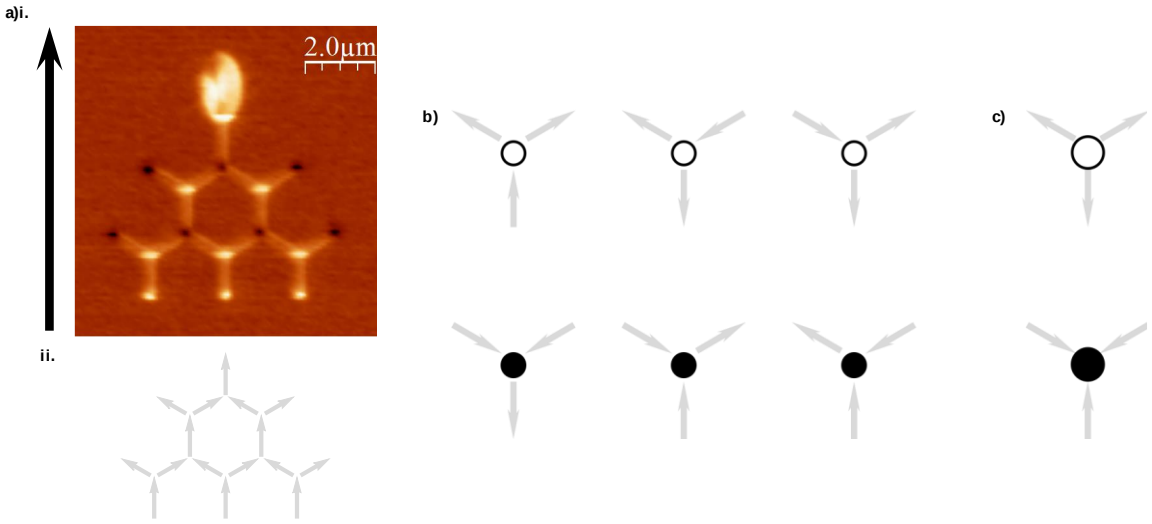

Fig.2-20: a)i. MFM image at saturation after applying field according to the black arrow and ii. corresponding spin configuration arbitrarily oriented upwards, spin pointing to a black contrast as contrast convention; b) corresponding contrasts of 2-out/1-in and 2-in/1-out and c) 3-out and 3-in vertex configurations.

The next step is to apply a lower field in the opposite direction and to keep track of any contrast change compared to saturation. We show an example of MFM image where –176 Oe was applied along with its saturation in Fig.2-21. In this case, the reconstruction of the spin configuration using Fig.2-20.b) gives the reversals. The example shows that the domain wall nucleated from the pad is pinned in the right upper part of the structure. We note that no forbidden state (3in/3out in Fig.2-20.c)) is observed.

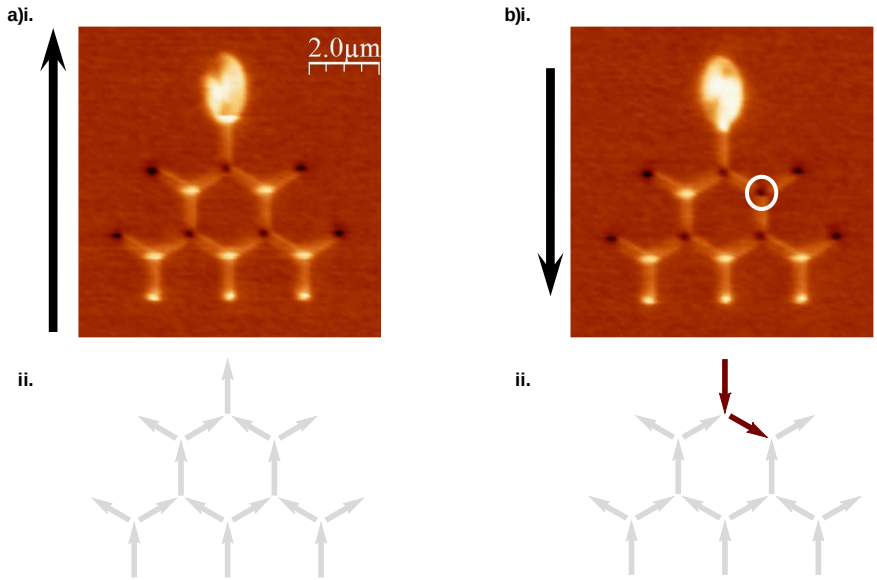

Fig.2-21: a)i. MFM image at saturation and ii. its corresponding spin configuration; b) –176 Oe is applied nucleating a domain wall that has propagate according to the red arrows shown in ii.

In Fig.2-21, we have shown a case of MFM image that yields unambiguous reversals using only the vertex colours. However, this approach sometimes gives way to doubt for the determination of the spin configuration. A typical example is when the 2nd output changes contrast as shown in Fig.2-22.b)ii. returning two possible scenarios (Fig.2-22.b)ii.-iii.). If the resolution is chosen high enough, the shape of the contrasts can be used to determine the path of the domain wall propagation. In this example shown, comparing the close-up views of the contrasts allows to say that the reversals are according to Fig.2-22.b)iii.

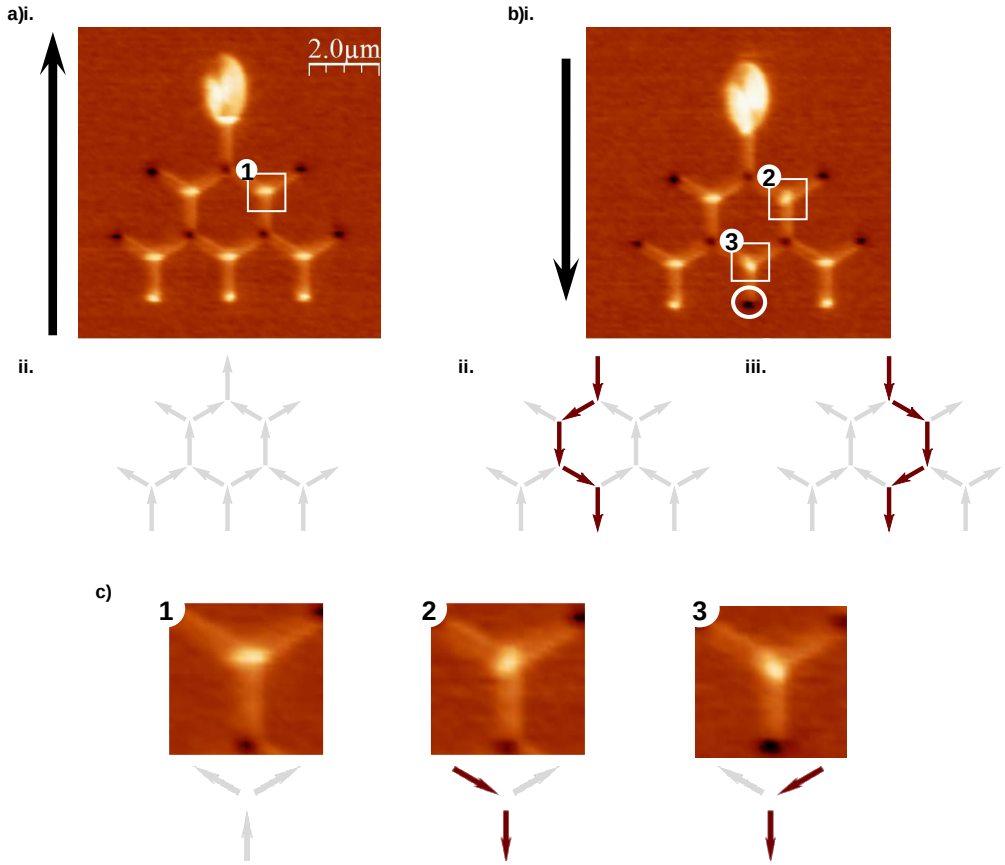

Fig.2-22: a) Nanostructure after applying +1000 Oe i. MFM image and ii. corresponding spin configuration; b) nanostructure after applying –248 Oe i. MFM image and ii.-iii. two possible corresponding spin configurations; c) magnification of the contrasts to assign a shape to a vertex configuration.

On the examples shown here, the spin configurations are easy to reconstruct but it becomes more challenging for larger structures. To help us determine the spin configurations, we have elaborated a program on Mathematica Wolfram Software. The code contains image processing for reading the contrasts of the images and returns all possible spin configurations corresponding. An example for one MFM image is shown in Fig.2-23.

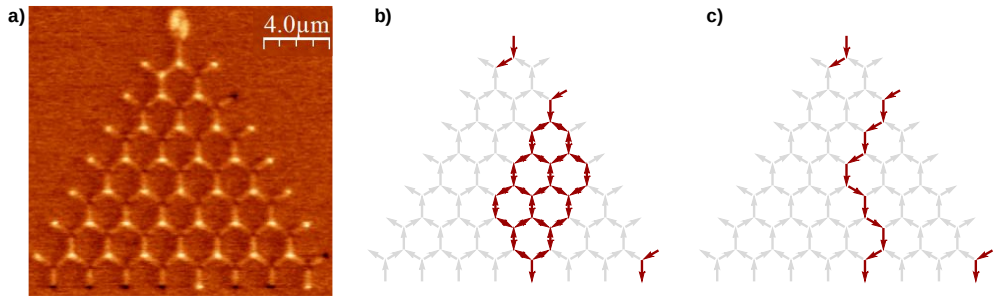

Fig.2-23: a) MFM image of an 8-output structure with symmetric intersections after applying –248 Oe; b) the returned spin configuration by our code, with an uncertainty in the middle propagation and c) determined reversals by observation of contrast deformations. Here the contrast convention is the spin pointing to a white contrast.

According to the image in Fig.2-23.a), the code returns: (i) the domain wall has been injected and has passed the first intersection on the left; (ii) the 8th output is returned and the next edge element and (iii) chain-like reversals between the 5th output and the second edge element on the right side of the structure which could have taken more than one path (Fig.2-23.b)). A further look at the distortion of the contrasts shows that reversals explained in (ii) followed the path shown Fig.2-23.c). the combination of both our program and observations has led to unambiguous determination of spin configurations.

Now, we present the interpretation of the MFM contrasts of another honeycomb-like with rounder intersections and tapered ends (SEM image in Fig.2-19.b)). The same field procedure is applied with images acquired at remanence (Fig.2-17). The approach of using the contrasts colours and shape is made easier with the funnel shape at the intersections. Contrasts at saturation and undergone domain wall propagation can be identified without difficulty (squares 1, 3 and 5 in Fig.2-24 respectively): the former is symmetric and the latter elongated to the element underneath. Their shape is consistent with the vertex configuration and the contrast convention (spin pointing to a black contrast). However, the contrasts observed when the domain wall is pinned is not as straightforward because of the funnel shape. But by construction, we can assert that when a domain wall is pinned travelling from one side or the other the contrasts are 2nd and 4th configurations shown Fig.2-20.b)-c) magnified in Fig.2-20.e).

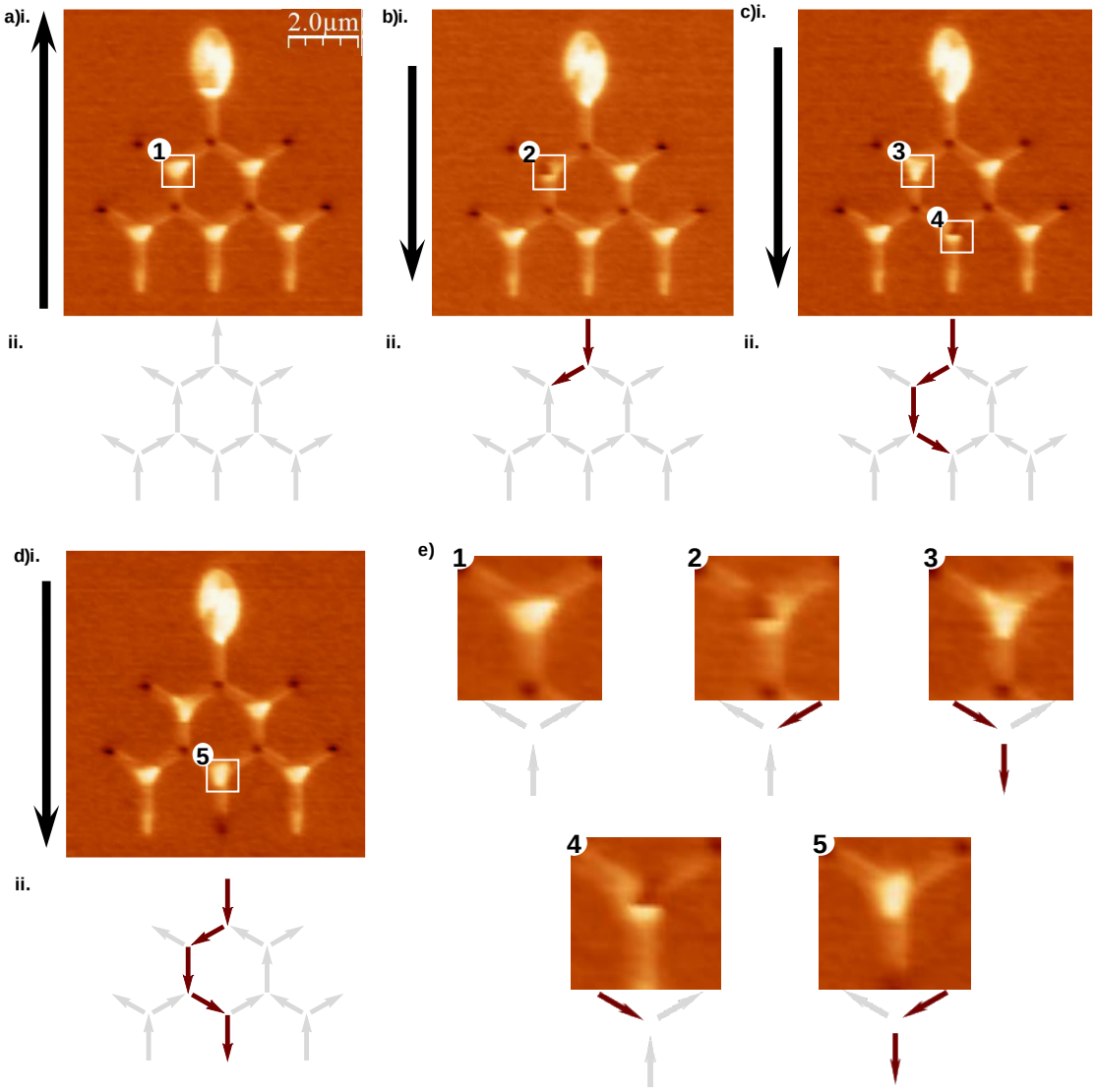

Fig.2-24: Data for kagomé-like nanostructure with funnel shape; a)i. MFM image and ii. corresponding spin configuration at saturation; b) after applying –176 Oe i. MFM image and ii. spin configuration corresponding to domain wall pinned at after the first intersection; c) after applying –248 Oe, i. MFM image and ii. spin configuration showing a second pinning before reaching the output and d) after applying –260 Oe, i. MFM image and ii. spin configuration showing a propagation from the pad to the 2nd output; e) close-up views of contrasts at intersection according to their configuration.

For this particular geometry, the funnel allows a systematic and unambiguous determination of the reversals with little regard to the resolution. An example of the "worst" resolution acquired on an 8-output structure is presented in Fig.2-25.

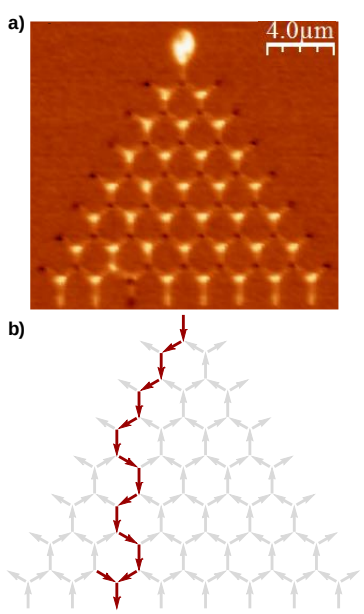

Fig.2-25: After applying –236 Oe a) MFM image and b) its corresponding spin configurations using only the contrasts and using their shape.

For these large structures, using both contrasts and their shape as established in Fig.2-24.e), we are able to identify unambiguously the reversals without any image processing.

2.2.3. Optimisation of acquisition time

As we will emphasise in Chapter 4, we needed to perform as many times as possible the field experiment shown in Fig.2-17. This field history takes hours to perform, this transposed to dozens or hundreds of experiments is obviously time-consuming. The parameters of acquisition were therefore critical and we have thought of several ways to decrease the duration of the experiments. Beyond making sure that the protocol turned in a loop in order to not waste any time, we have used studied two other aspects of the acquisition. We mention that we have chosen to keep the field increment (12 Oe ±2 Oe) in all our field experiments.

The first lead was to decrease the number of images scanned while observing all the steps of the reversal process. Whenever introducing a new design, the first thing we have done is to identify the fields at which an output is activated and for safety, a few (3-4) images were added. Studying the reversals up to this event is indeed enough to determine if the reversals form an avalanche. This method has shown all steps of the propagations and their characteristics (injection and depinning fields, multiple pinnings, …) along with their statistical behaviour (statistical weights, correlation between successive choices, …).

The second lead was to decrease the time of the individual images, the main reason why some images are of poorer resolution than others. Scan rate could not be increased because we observe 20 nm-thick nanostructures and was therefore kept at 0.5 Hz. This way, the probe would not at any time touch the structures thus preserving the tip. When necessary and possible, multiple structures were observed simultaneously (maximum scan size with the microscope is 90 µm). We typically took 512 points (sometimes 1024 points) by line which yields for a square scan about 34 (68) minutes for each image. The last trick we used was to divide the number of lines by two decreasing by the same factor the scan time yielding 17 or 34 minutes per image for 512 and 1024 points respectively. Samples were designed and patterned so that structures to be observed are kept within a 90 µm × 45 µm (as shown in Fig.2-16).

All of the points stated before were taken into account when performing the field experiment of our honeycomb artificial spin systems. The final optimised acquisition was about 4 hours for one field experiment using the probing technique that is MFM. In the end for our optimised structure, we were able to acquire a total of 229 field experiments. We believe that we have attained an honest trade-off between domain wall characterisation and statistics with our “slow” but high-resolution technique.

Chapter 3. Tuning the interactions in an artificial spin ice system

"La Nature il ne faut pas essayer
de la contrôler, il faut savoir l'écouter »
O. Copie

This chapter of the manuscript focuses on the study of artificial spin ice systems in which elements are rotated around their central point. This tuning of the interactions induces a change from antiferromagnetic order for the square ice to ferromagnetic order for the pinwheel ice. Using vertex populations, dipolar energy and magnetic structure factor, we will show that it is experimentally the case with a coexistence for rotation angles in between. We will then study the thermodynamics of the system and show that the dipolar energy can be described by an energy-based effective temperature. This temperature is unique for the entire system if all interactions are taken into account. This result shows that rotating the elements of an artificial square ice does not affect the thermodynamics of the system.

3.1. Motivations

Originally introduced to mimic the spin behaviour of rare-earth titanate pyrochlores [9], artificial spin ice systems have raised countless potential studies of emergent phenomena. Over the years, they have proven to result in exotic or elegant collective phenomena -as some like to describe it- with the simple dipolar/exchange interactions among the elements.

A variety of geometries has emerged [40] mainly in order to recover the manifold degenerate ground state hardly reachable with the original square lattice. One can think about: the kagomé lattice [13,41], highly degenerate with 3-spin vertices; more complex geometries with new levels of degeneracy and reduced dimensionality with the Shakti [40,42,43] -degeneracy within a unit cell of the array-, tetris [40,44] –staircases within the array- lattices respectively or the Santa Fe geometries. Studied geometries are summarised in the recent review of Skjœrvø and collaborators [3]. The lifting of degeneracy of the square geometry has been overcome notably in the work of Perrin *et al.* [45] by offsetting elements one direction from the other. At a critical height, degenerate ground state was recovered along with Coulomb phase features.

In 2017, a novel modification of the classical square lattice was introduced [46]: rotation of the nanomagnets around their central point of 45°, soon after baptized the pinwheel lattice [47]. We mention that this rotation of magnetic elements has also been studied in another metasystem for 4-state Potts artificial spin system [48]. Using X-ray photoemission microscopy, Gliga *et al.* [46] have shown that it

exhibits a preferred rotation during thermal relaxation under a small bias field. They qualified this customised square lattice as a new chiral ice with a ratchet behaviour promising for nanoscale devices. Later, they have explained this behaviour by the stray field distribution of the nanomagnets [49]. The edge bending of the magnetisation under applied field measured using superconducting quantum interference device (SQUID) were consistent with micromagnetic simulations. In 2018, Macêdo *et al*. [47] realised jointly theoretical studies of the pinwheel ice using Monte Carlo simulations. They have established the phase diagram of the rotation of the elements showing the ground state transition from antiferromagnetic to ferromagnetic ordering. In addition, they have shown the effects of the edges shape and size array in the ferromagnetic behaviour of the pinwheel ice. Following this work, it has been found that under an applied field, this geometry exhibits a superferromagnetic behaviour with coherent domain wall nucleation and propagation [50].

Our work is in line with this simple way of modifying the dipolar interactions by rotation of the elements from square ice to pinwheel ice (rotation is as shown in Fig.3-1). Our goal is to characterise the ground state transition due to the rotation experimentally.

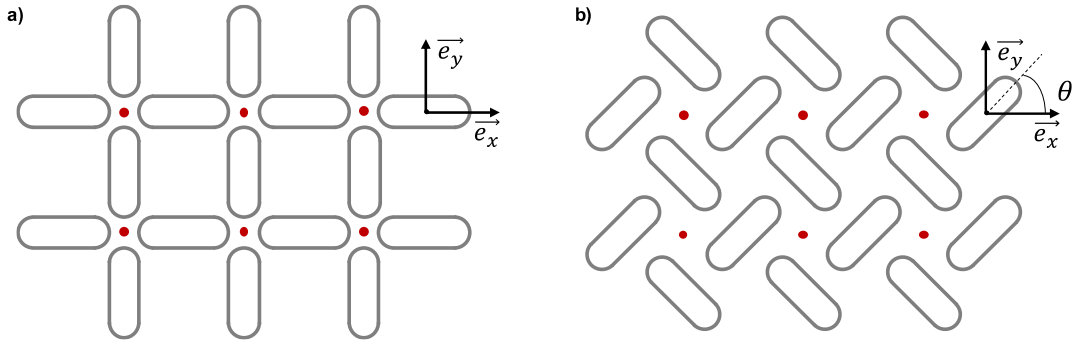

Fig.3-1: Tilting a) a square array through θ up to b) the pinwheel array ($\theta = 45°$), red dots stand for the vertices.

We characterise this tuning of the interactions using the dipolar approximation from square ice to pinwheel ice for an athermal system. Adapting the thermodynamic approach of Macêdo *et al.* and using the protocol of the as-grown state by Morgan *et al.* [11], we show that the characteristic parameters of the rotated arrays of a sample are described by a unique energy-based effective temperature.

We will first compute the dipolar energies as a function of rotation angle. We will show that an accurate description requires an all-interactions approach throughout the entire array. With the calculations of various ordered spin configurations energies, we will determine the ground state that can be expected. We will confront the computations with experimental systems in terms of vertex populations and dipolar energies. Then on the lowest energy system that is the as-grown one, we will study the networks orders by magnetic structure factor. Finally, we will study its thermodynamics using first the vertex model and second Monte Carlo simulations. We will show that the latter allows ascribing a unique effective temperature of the entire system.

3.2. Tuning the dipolar interactions

Since their introduction, there have been several attempts to describe accurately the energy of artificial spin ice systems. With both vertex and all-interactions approaches, the system energy has been computed using several approximations or models (point-dipole, micromagnetic model, dumbbell model [51],

finite magnetic bodies [52]). In this work, we choose to consider exclusively the dipolar approximation compute the interactions of our artificial spin ice system with rotated elements. We will show that this tuned system because of its geometry requires long-range interactions for an accurate description. Using this all-interactions approach, we will compute the energies of various ordered spin configurations and determine the ground state as a function of rotation angle. The aim of this section is to yield insight about the potential behaviour of experimental systems.

$$E_{ij} = -\frac{\mu_0}{4\pi}\frac{3(\vec{\mu}_i \cdot \vec{e}_{ij})(\vec{\mu}_j \cdot \vec{e}_{ij}) - \vec{\mu}_i \cdot \vec{\mu}_j}{r_{ij}^3}$$

3.2.1. Dipolar energy of spin pairs and vertices

Within the dipolar approximation, relevant interactions are considered punctual magnetic moments $\overrightarrow{\mu_i}$ and $\overrightarrow{\mu_j}$. The energy between spin pairs is then expressed as:

$$E_{ij} = -\frac{\mu_0}{4\pi}\frac{3(\vec{\mu}_i \cdot \vec{e}_{ij})(\vec{\mu}_j \cdot \vec{e}_{ij}) - \vec{\mu}_i \cdot \vec{\mu}_j}{r_{ij}^3} \quad \textit{(Eq.1)}$$

where $\vec{e}_{ij}$ is the unit vector between ith and jth magnetic moments and r_{ij} the distance between them two. Beyond two moments, one computes the system energy as the sum of all spin pairs hence the following normalized dipolar Hamiltonian (Eq.2):

$$\mathcal{H}_{dip} = \frac{1}{N} D a^3 \sum_{<i,j>} \left[\frac{\vec{S}_i \cdot \vec{S}_j}{r_{ij}^3} - \frac{3(\vec{S}_i \cdot \vec{r}_{ij}) \cdot (\vec{S}_j \cdot \vec{r}_{ij})}{r_{ij}^5} \right] \quad \textit{(Eq.2)}$$

where $D = \frac{\mu_0 \mu^2}{4\pi a^3}$ is the dipolar coupling constant[1], a the lattice spacing and ${r_{ij}}^2 = \left[\overrightarrow{e_x} \cdot (\overrightarrow{r_i} - \overrightarrow{r_j})\right]^2 + \left[\overrightarrow{e_y} \cdot (\overrightarrow{r_i} - \overrightarrow{r_i})\right]^2$ the distance between spins i and j as in Refs. [47,53]. In this chapter, the energy is computed and plotted is normalized by the number of spins composing the array N.

In order to tune the interactions, we rotate the spins around their central point of an angle θ. The 0° rotation corresponds to the classical square lattice. The modification on a vertex is shown in Fig.3-2.

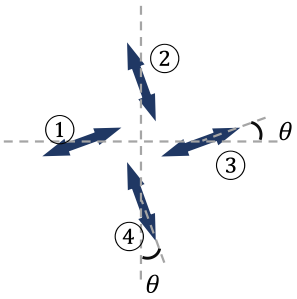

Fig.3-2: Schematics of four magnetic moments of a square lattice undergoing a rotation of θ.

[1] D is taken homogenous to an energy as in Ref. [53].

Due to the anisotropic nature of the dipolar interaction, the tuning of pairwise spin interaction is expressed as a function of rotation angle θ. This modulation for perpendicular spins (1 and 2, 1 and 4, 2 and 3, 3 and 4 in Fig.3-2), spaced $a/\sqrt{2}$ is expressed for ferromagnetic and antiferromagnetic coupling as:

$$E_{\perp_{FM}} = -D \cdot 3\sqrt{2}\cos(2\theta)$$
$$E_{\perp_{AFM}} = +D \cdot 3\sqrt{2}\cos(2\theta)$$

and between collinear spins (1 and 3, 2 and 4 in Fig.3-2), spaced a, the interaction is expressed as:

$$E_{\parallel_{FM}} = -D/2 \cdot (3 \cdot \cos(2\theta) + 1)$$
$$E_{\parallel_{AFM}} = +D/2 \cdot (3 \cdot \cos(2\theta) + 1)$$

Energies are plotted in Fig.3-3.

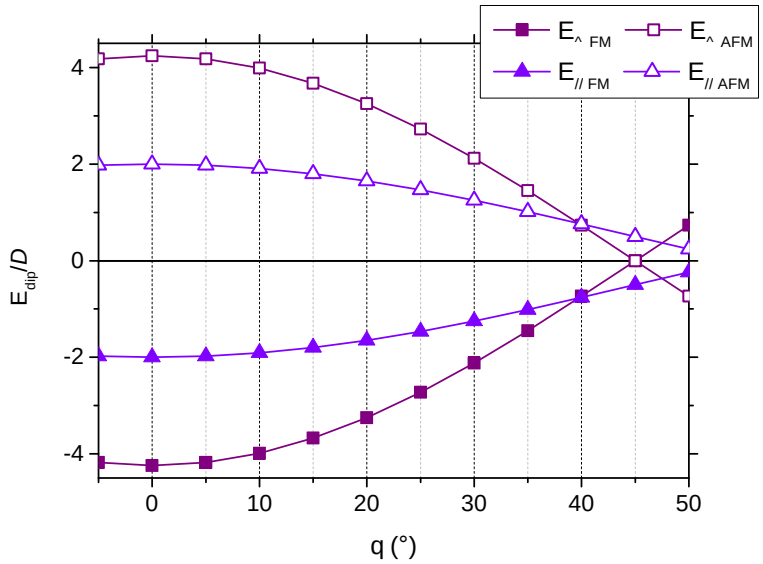

Fig.3-3: Evolution of the dipolar energy between perpendicular and collinear spins in tilted lattices. Solid and open symbols are for ferromagnetic and antiferromagnetic couplings respectively.

As can be expected, from 0° to 45°, both spin pairs favour ferromagnetic coupling. We see that above ~47.4°, due to geometry, perpendicular spins favour antiferromagnetic coupling. For the well-known square ice, or 0°-tilt, ferromagnetic coupling is of lower energy for both spin pairs. This is valid as long as rotation angle is lower than ~39.7°[2] at which ferromagnetic coupling of both perpendicular and collinear spins are of same value. Increasing the rotation angle, the trend between the two couplings reverses. We find that at 45°-tilt, or pinwheel ice [47], the interaction between collinear spins is null. This last comment will be of great interest later in our study of wider arrays.

A vertex, as shown in Fig.3-2, has $2^4 = 16$ possible configurations. They were initially divided in four types with increasing magnetostatic energy for the square ice [9]. Type1 and Type2 vertices are the two-in/two-out ice rule configurations, Type3 vertices are 3-in(out)/1-out(in) configurations and Type4 vertices are 4in(out) configurations (Fig.3-4.a)). Their energy is expressed by summing all six interactions into play ($4\times E_{\perp_{(A)FM}}$ and $2\times E_{\parallel_{(A)FM}}$). Each vertex energy is computed using the coupling

[2] Rounded angle value for which $E_\perp = E_\parallel \implies \theta = \tan^{-1}\left(\sqrt{\frac{3\sqrt{2}-2}{3\sqrt{2}-1}}\right)$ $[2\pi]$.

expressions between perpendicular and collinear spins according to their configuration. Expression are given below and plotted in Fig.3-4.b):

$$E_{T1} = -E_{\perp_{FM}} + 2E_{\parallel_{AFM}} = D \cdot (3 \cdot \cos(2\theta) \cdot \left(1 - 4\sqrt{2}\right) + 1)$$

(Eq.3)

$$E_{T2} = -2E_{\parallel_{FM}} = -D \cdot (3 \cdot \cos(2\theta) + 1)$$

(Eq.4)

$$E_{T3} = 0$$

(Eq.5)

$$E_{T4} = +4E_{\perp_{AFM}} + 2E_{\parallel_{AFM}} = D \cdot (3 \cdot \cos(2\theta) \cdot \left(1 + 4\sqrt{2}\right) + 1)$$

(Eq.6)

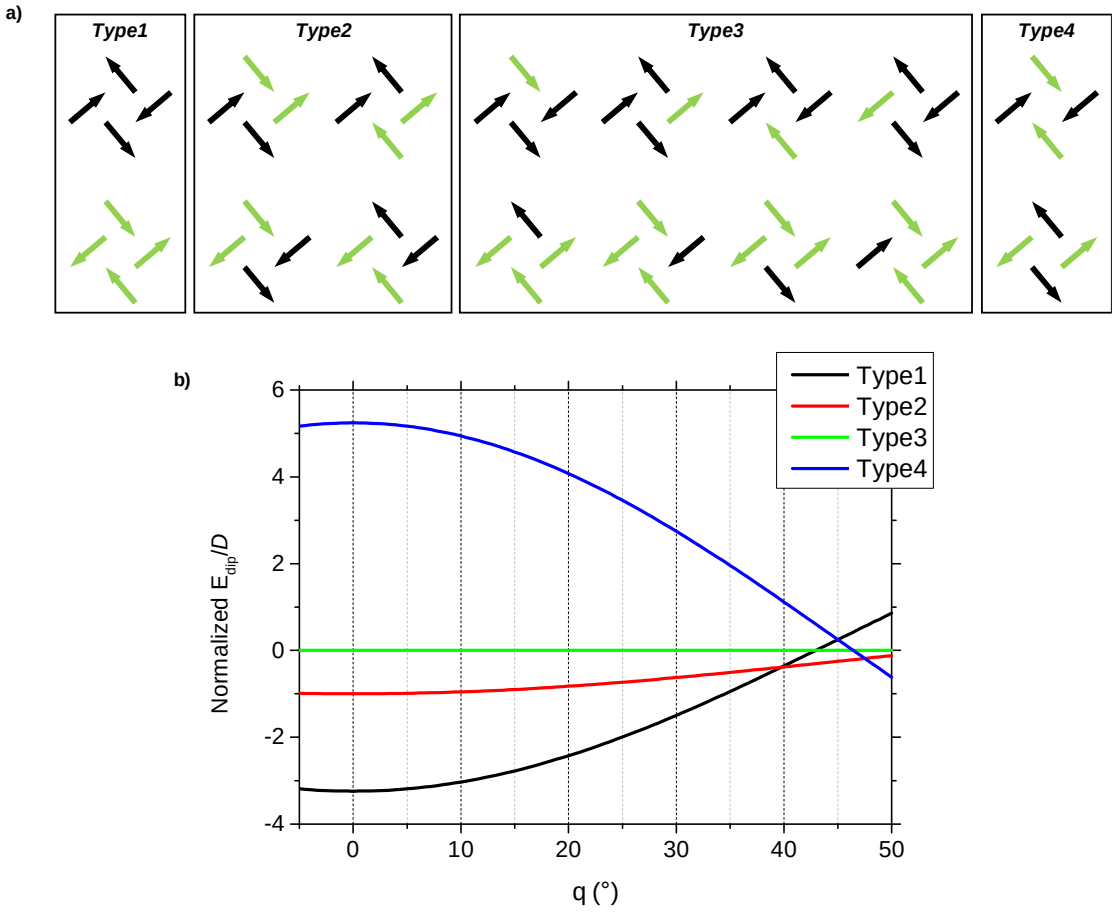

Fig.3-4: a) The 16 possible vertex configurations: Type1 is two-in/two-out configuration where collinear spins are antiferromagnetically coupled, Type2 is also a two-in/two-out configuration but collinear spins are ferromagnetically coupled, Type3 is a three-in(out)/one-out(in) configuration and Type4 a 4out(in) configuration; b) normalised vertex energy according to rotation angle. Vertex configurations are represented at an arbitrary angle. Green and black colours are chosen according to position and angle, colours highlight the coupling between collinear spins: same colour is used if there are antiferromagnetically coupled.

Using Fig.3-4.b), we find that Type1 vertex is the lowest energy configuration up to ~39.7°, same value as for the spin pairs. Above that threshold, Type2 vertex becomes of lowest energy up to ~47.4° then Type4 is. As before, the features are due to geometry because above 45°, the position of the vertices changes. The change in ground state from Type1 to Type2 vertices is due to the change in trend between ferromagnetic coupling of collinear and perpendicular spins. Indeed since $|E_\perp| < |E_\parallel|$ for $\theta > \sim 39.7°$, the sum of the interactions of the two types changes. We also note the at $\theta = 45°$, the contribution for Types1 and 4 are equal and all vertex types are very close in energy.
We remark upon that at ~39.7°, Type1 and Type2 vertices are of same energy. This result translates in the sixfold degenerate ground state following the ice rule lifted in the original square ice.

We conclude that in its smallest size, the ground state of our artificial spin system with rotated elements evolves from Type1 to Type2 vertex. However the very interest of these systems lays in large arrays especially for the study of collective phenomena [54]. The next step is therefore similar only on a wider array: computing the energy of various configurations to determine the ground state of the system according to rotation angle. With the vertex energies studied, one could suspect orders with Type1 and/or Type2 vertices.

3.2.2. Dipolar energy for a network: beyond first neighbours

Among the studies of artificial spin ice systems, some have made the argument that only predominant interactions –the nearest neighbouring coupling- can be considered for the energy. But with our tuning of the dipolar interactions, this quite crude approximation cannot be made. As seen with the 45°-tilted lattice, because the interaction of first-nearest neighbouring spins is null, long-range interactions are necessary for an accurate description [47].

Dipolar coupling constants J between any spin pairs of the array can be computed as:

$$E_{dip} = -J \cdot \vec{S_i} . \vec{S_j},$$

where $\vec{S_i}$ and $\vec{S_j}$, the spin-pair considered. With this convention, ferromagnetic (antiferromagnetic) coupling between the spin pair of interest will be of positive (negative) value. We demonstrate our point using the first-four-neighbouring spins of an array taken as shown in Fig.3-5.a) using (Eq.1). Expressions are given below.

$$J_1 = D \cdot 3\sqrt{2}\cos(2\theta)$$
$$J_2 = D \cdot 3\cos^2\theta - 1$$
$$J_3 = D \cdot 1 - 3\sin^2\theta$$
$$J_4 = D \cdot \frac{1}{4\sqrt{2}}(1 - 3\sin 2\theta)$$

Only first-four couplings are considered for simplicity purposes but interactions all over the array can be computed the exact same way. Curves are given in Fig.3-5.b).

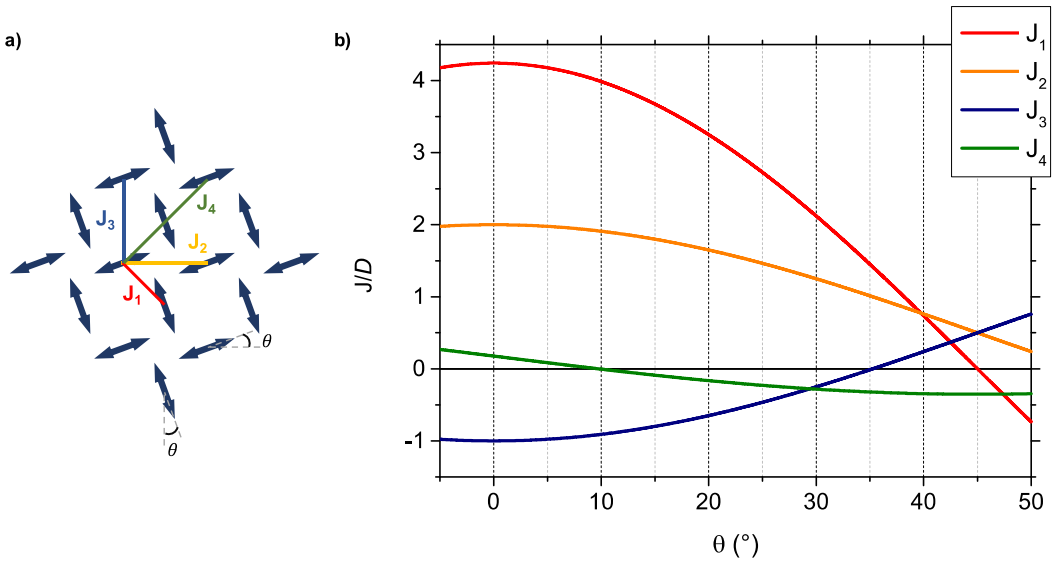

Fig.3-5: a) Schematics of the first-four neighbouring spins listed with increasing distance and b) the associated dipolar coupling constants evolution according to angle.

First-two dipolar couplings constants J_1 and J_2 -the $E_\perp$ and $E_\parallel$ presented in section 3.2.1- are the predominant up to $\sim 42.5°$, at which first- and third-nearest, J_1 and J_3, become equal. Above this rotation angle, second- and third-nearest neighbouring interactions, J_2 and J_3, are predominant and at 45° they become equal. For low rotation angles, the first-two nearest neighbouring interactions are higher of at least a factor 2 but as the rotation angle is increased, the difference between all four interactions becomes smaller. For the 45°-tilt, we find that the first-nearest neighbouring interaction is null but also that second- and third-nearest neighbouring interactions are equal and very close in strength to the fourth one, J_4. These results are strongly in favour of an all-interactions approach. We also mention that between $\sim 28.8°$ and $\sim 42.4°$, third-nearest neighbouring interaction is lower in amplitude than the fourth one.
In order to compute the energy of an array, one could choose to compute the energy of the network differently for each rotation angle by considering only the *n*-most predominant ones as in Ref [43]. But due to the interactions and geometry, the predominant interactions change and should be carefully selected according to rotation angle. Rather than that, we choose to compute of each tilted array of the system energy taking into account all spin-pairs in the defined Hamiltonian in (Eq.2). The benefit is twofold: accuracy and consistency between all tilted arrays.

In addition to have confirmed the importance of an all-interaction approach, these computations have also brought out the determining parameters for the system energy: size array and configuration. We now compare orders composed by Type1 vertices and identical Type2 vertices as shown in Fig.3-6.a)-b) respectively. From now on, we will refer to the former configuration as antiferromagnetic order and to the latter as ferromagnetic order, because of the coupling between colinear spins. Energies according to size array are shown for three rotation angles 0°, 30° and 45° in Fig.3-6.c). We chose these two orders because vertex energy has shown that ground state evolves from Type1 to Type2 vertices.

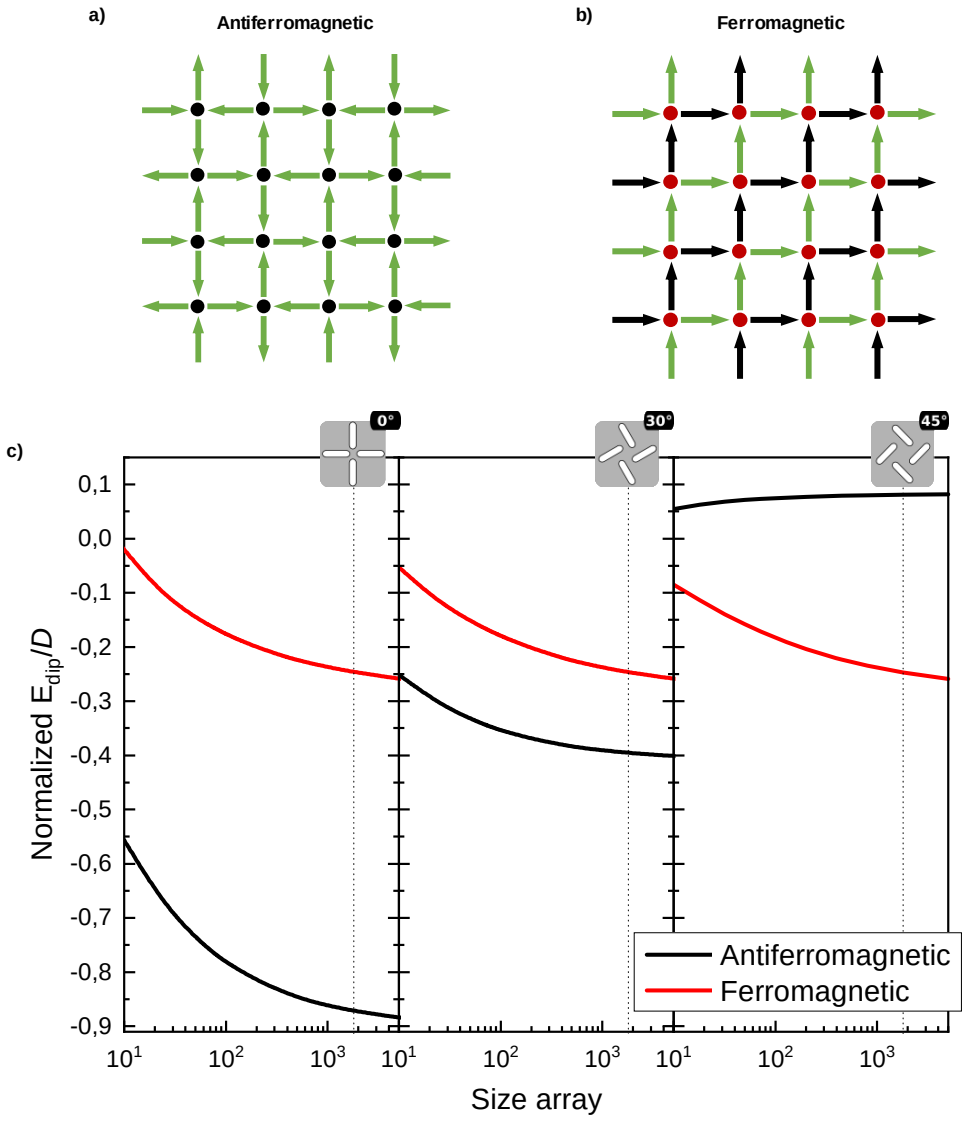

Fig.3-6: a) Antiferromagnetic configuration; b) Ferromagnetic configuration (Type2 vertices can be arranged in various but we define this order with lines of ferromagnetically coupled spins); c) the evolution of energy in dashed line the 1800-spin-square size array used for our experimental systems. Black and red circles in the spin configurations stand for Type1 and Type2 vertices respectively. Colour code is as Fig.3-4.a) highlighting coupling between colinear spins: same (different) colour if antiferromagnetically (ferromagnetically) oriented.

For the dipolar Hamiltonian used, the sum on an infinite bidimensional converges according to similar computations performed in Ref [30]. We find that for all orders no matter the rotation angle, energy decreases with increased size array except for the antiferromagnetic order at 45°. Therefore -most of the time-, the wider is the array the lower the energy.

For our experimental size array (1800 elements, vertical dashed lines in Fig.3-6.c)), we find that lowest-energy state changes from antiferromagnetic for the 0° and 35° rotation angles and to ferromagnetic for 45°. However, here we have considered only two configurations for only three rotation angles. The next step is to explore more potential spin configurations and compute their energies with rotation angle.

3.2.3. Dipolar energy of various ordered configurations

In order to determine the ground state, we need to study various configurations and compare their energies as a function of rotation angle. Only then, it is possible to have an expectation about the ground state of a system. For our tilted system, we add to the antiferromagnetic and ferromagnetic orders presented before, the four following configurations:

- *Manhattan* order [55]: another arrangement of Type2 vertices where lines of ferromagnetically coupled spins are antiferromagnetically placed one next to the other (Fig.3-7.a));
- Types1/3 order: alternating vertex lines of Type1 and Type3 vertices (Fig.3-7.b));
- Types2/3 order: alternating vertex lines of Type2 and Type3 vertices (Fig.3-7.c))
- Type3 order: Type3 vertices where in one direction lines of spins are ferromagnetically coupled and in the other direction lines of spins are antiferromagnetic coupled (Fig.3-7.d);
- Type4 order: as named, composed exclusively by Type4 vertices.

Typical examples of corresponding arrangements are shown in Fig.3-7 but others can be imagined respecting the stated conditions. We plot in Fig.3-7.f) their dipolar energies in an all-interactions approach for a square array of $2\times30^2=1800$ spins.

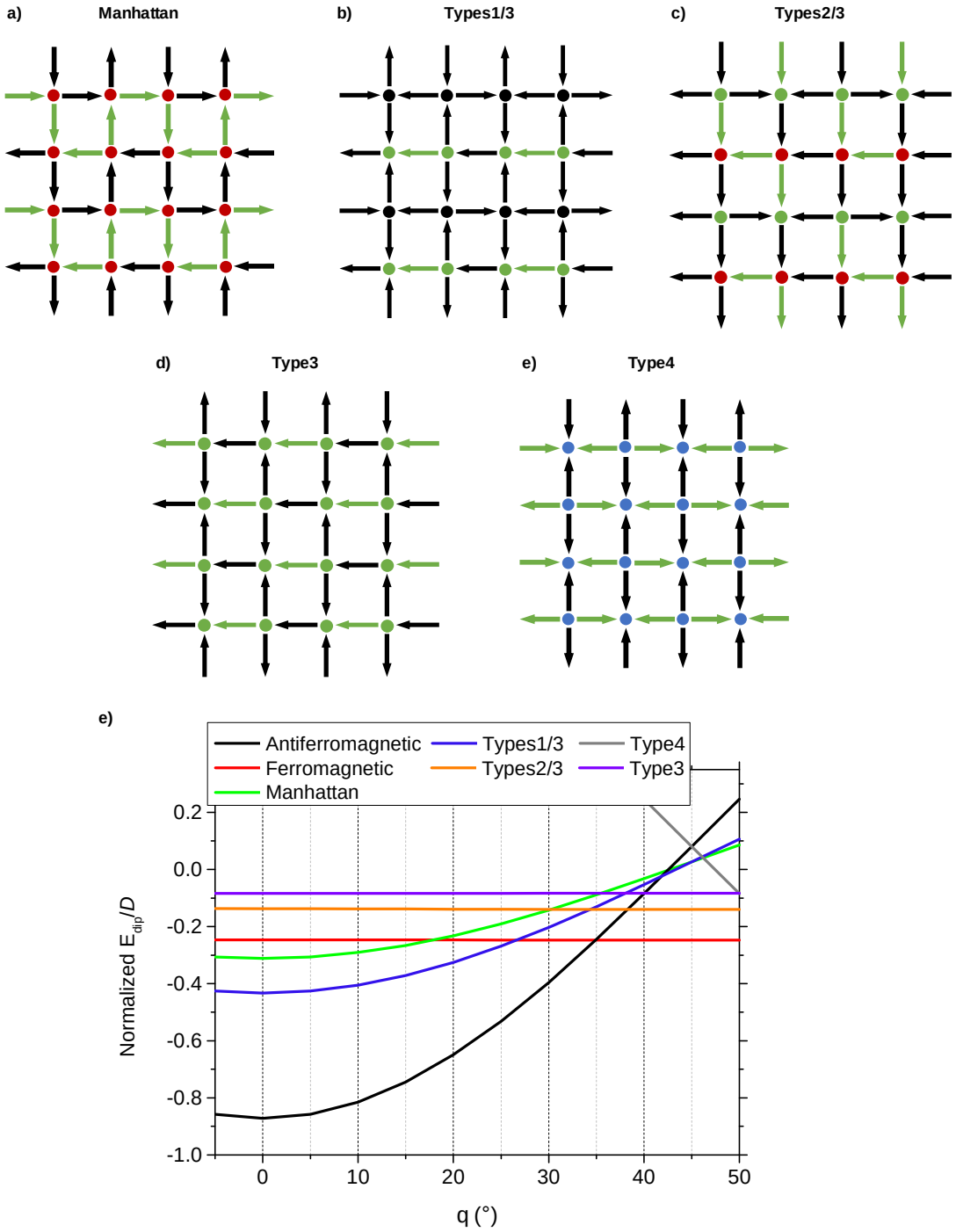

Fig.3-7: Typical arrangements of a) Manhattan, b) Types1/3, c) Type2/3, d) Type3 and e) Type4 orders, lines of spins can toggled at will; f) Normalized energy of the presented orders along with the antiferromagnetic and ferromagnetic orders. Black, red, green and blue circles stand for Type1, Type2, Type3 and Type4 vertices respectively. Colour code highlights coupling between colinear spins: same (different) colour if antiferromagnetically (ferromagnetically) oriented.

We demonstrate that, with increasing rotation angle, ground state changes from antiferromagnetic -antiferromagnetically coupled colinear spins, Type1 vertices- to ferromagnetic -ferromagnetically coupled colinear spins, same Type2 vertex repeated all over the array- order with a transition at ~34.9°. All other presented configurations are of higher energy for the range angle of interest but it is worth mentioning a few other observations.

We find the other configurations next in line: the Types1/3 is the next low-energy state after the antiferromagnetic one up to $\sim 26.6°$; then up to $\sim 34.9°$, it is the ferromagnetic order. Above this transition, the second lowest-energy state becomes again the antiferromagnetic order up to $\sim 38.3°$ to the benefit of the Types2/3 order. We also observe that energies of the Type2 arrangements (ferromagnetic, Types2/3) and the Type3 order do not change with rotation angle. This feature was already observed in Refs. [30,48] while computing the dipolar energy of a 2D Potts systems in ferromagnetic configuration. Also, we confirm what was observed in vertex energy that is antiferromagnetic and Type4 orders are of same energy at 45°. We find as already stated in Ref. [55] about the Manhattan order -a different arrangement of Type2 vertices-, which is of lower energy than the ferromagnetic but only up to $\sim 17.8°$. With this observation, we stress that Type2 vertices can be arranged in various manners but their energies do depend on the final spin configuration.

3.2.4. Conclusion

Through this section, we have seen how to compute the energy of an artificial spin system in the dipolar approximation. The calculations on vertex types show that the rotation of the elements induces a change of ground state from Type1 vertex to Type2 vertex, consequently tuning the interactions. We have also raised the question about long-range interactions and show that our modification of the square lattice makes it necessary to consider beyond first-two-nearest neighbours. Otherwise, the pinwheel lattice would not be described accurately since the interaction between perpendicular spins is null. Therefore, we use the dipolar Hamiltonian taking all interactions throughout the array into account. Using this approach, we have shown that the normalised energies of two ordered spin arrangements indeed depend on the size of the network. Exploring the energies of possible ordered arrangements, we have been able to predict the ground state evolution with rotation angle: a transition from antiferromagnetic order (Type1 vertices) to ferromagnetic order (Type2 vertices with same net magnetisation). We have found that there are several ways two arrange Type2 vertices (*e.g.* ferromagnetic and Manhattan orders) and in an all-interactions approach their energies are distinct. The same configurations in a vertex approach would have same energy emphasising the limitations of this model. Therefore, such a tuned system cannot be adequately described by a vertex approach.

The next step of our study is to observe this transition experimentally and verify the dipolar computations made so far.

3.3. Experimental study

Having computed the dipolar interactions of arrays with rotated elements and studied various spin arrangements, we test these models experimentally. We choose to work on frozen systems (20 nm-thick Permalloy) to study our tuned system.
In this section, we will present the different preparation protocols used to bring our samples into a low energy state. We will then characterise their magnetic configurations in terms of vertex populations and dipolar energy in order to determine the lowest-energy system. We will end our study on our best candidate with a characterisation beyond first neighbours yielding a fine estimation of their disorder.

3.3.1. Reaching a low-energy state

In this section, we address one of the main challenges of artificial spin ice that is experimentally reaching the ground state. We will first present the protocols presented in reported works on artificial spin ice to reach a low-energy state and then present our experimental systems based on them.

3.3.1.1. Protocols established in the literature

For their establishment and long after, the protocol to prepare the artificial spin systems consisted in an ac field demagnetization. The oscillatory in-plane field, starting above the coercive field of the islands, is stepped down to zero while rotating the sample. Optimisations had shown that a small field step size yields a lower energy state [56]. The goal of this protocol is to decrease the magnetisation as much as possible close to zero. This approach was expected to either result in arrangement in antiferromagnetic order (Type1 vertices) or in a highly disordered state. The former being the lowest energy state and the latter a higher energy state but with the hope of recovering the manifold degenerate ground state expected from the ice rules [57]. Using a field demagnetization, the best ground state reported years later was with a linear demagnetization while rotating the sample [58]. But this protocol returned merely 60% of Type1 vertices. The main drawback of the field demagnetization as Marrows [2] explained it, is that it starts from a high-energy configuration and allows only steps back unlike a real anneal process.
There have been other attempts to reach the ground state of the square artificial spin ice by a true anneal process, but the patterned structure can hardly undergo heating above blocking or Curie temperatures. However annealing was achieved by changing the material for the islands [59,60] and/or adding additional layers [20,41].
The quest of a quality ground state has been of great interest ever since. Its only true demonstration of an as-grown state after a lift-off fabrication was realised by Morgan *et al.* [11] in 2011. This approach allows to pass through every thickness while depositing the magnetic material. Fluctuations take place when the volume is low enough and reaches a thickness threshold: the magnetic state become arrested. This process was explained theoretically in Ref [61]. This approach has shown to result in large antiferromagnetic domains with isolated defects and proven to be reproducible [62]. The sole drawback of this process is that it cannot be reached again unless performing the fabrication since applying a magnetic field would be somewhat fatal.

For this work, we choose both the most common and the "simplest" methods to reach the ground state for our tuned system. We work on frozen systems (20 nm-thick Permalloy) and try three different approaches: (i) as-grown state after a lift-off process; (ii) ac field-demagnetization protocol and (iii) as-grown state after an etching process.

3.3.1.2. Samples and selected protocols

In order to study the tuning of the interactions through rotation, we fabricated sets of arrays tilted from 0° to 45° by steps of 5°. The square arrays have 1800 nanomagnets (2×30^2) with a lattice constant of 500 nm (centre to centre), elements are 400 nm-long, 100 nm-wide with circular ends so they behave like Ising spins. The samples were fabricated using the lift-off and etching process flows described in section 2.1. We perform the characterisation using magnetic force microscopy. An atomic force microscopy image of the 15°-tilted network is shown in Fig.3-8.

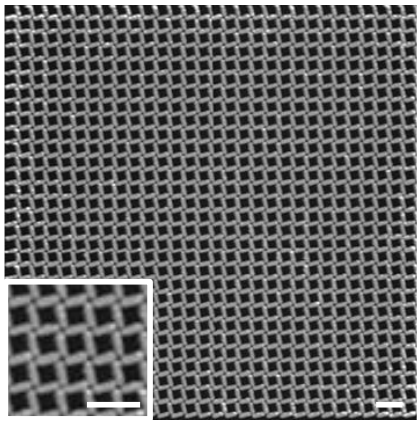

Fig.3-8: Observation by atomic force microscopy of the 15°-tilted network. Scale bars are 1 µm.

We tested three of the previously presented protocols to reach the ground state: as-grown states of both lift-off and etching processes and field-demagnetized state[3]. The field-demagnetizing protocol we use is an oscillatory sinusoidal field with an amplitude decreased by 3.3 Oe per period –small enough according to Ref. [56]- starting at 1000 Oe. Using the square lattices of the three approaches (Fig.3-9), we have a rather good insight about the quality of the reached ground state.

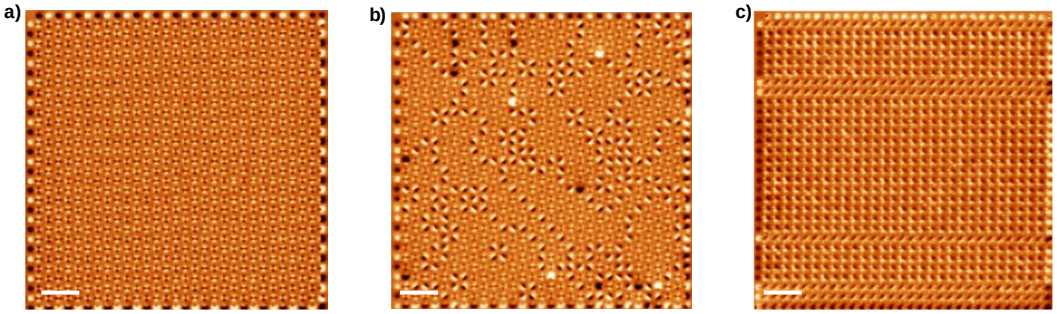

Fig.3-9: The three states of the square geometry used to approach the ground state: a) as-grown after lift-off, b) field-demagnetized and c) as-grown after etching. Scale bars are 1 µm.

We observe that samples in the as-grown state and after the field-demagnetizing protocol (Fig.3-9.a)-b)) exhibit the chequerboard aspect[4] of the antiferromagnetic ordering. The as-grown state has a perfectly ordered spin configuration whereas the field-demagnetized one is cut off in small domains separated mainly by Type2 vertices and a few pair of Type3 vertices (recognisable with the larger brighter/darker contrasts). Unlike them, the as-grown state after an etching process (Fig.3-9.c)) exhibits alternating horizontal domains of Type2 and Type3 vertices.

Obviously, the observation of the MFM images gives only a clue of the potential ground state reached, one should study the entire system to be conclusive. However, we can already take the etching one out since no Type1 vertices are observed. As can be expected, the absence of shape anisotropy during the growth is critical since the magnetisation similar to the one of a blanket film only on individual elements. Now, we will see if the trend observed on the square lattice of the as-grown state after lift-off and the field-demagnetized state is similar through a more quantitative study.

[3] Also after a lift-off process but the fabrication process is not relevant in a field-demagnetizing protocol.
[4] One should look at section 2.2.2.1, where the chequerboard aspect is shown in detail.

3.3.2. Comparison as-grown and field-demagnetized states

In the previous section, we have established that among the three protocols the best candidates are the as-grown state after lift and the field-demagnetized states. We will compare them in a quantitative manner using vertex populations and dipolar energies.

3.3.2.1. Vertex populations

From dipolar computations, we expect an evolution from antiferromagnetic to ferromagnetic ordering with increasing rotation angle translating in a change from Type1 to Type2 vertices. We will now see if it is experimentally observed for the as-grown and field-demagnetized states. Vertex populations have been extensively used to describe artificial spin ice systems because it is an unambiguous and easy to quantify their ordering. In this section, we will first show the MFM images and the vertex types for each tilted lattice of our as-grown and field-demagnetized systems. Then we will compare the systems vertex populations.

We will first focus on rotation angles from 5° up to 25° for which the system should exhibit a majority of Type1 vertices. MFM images and corresponding vertex populations are given in Fig.3-10.

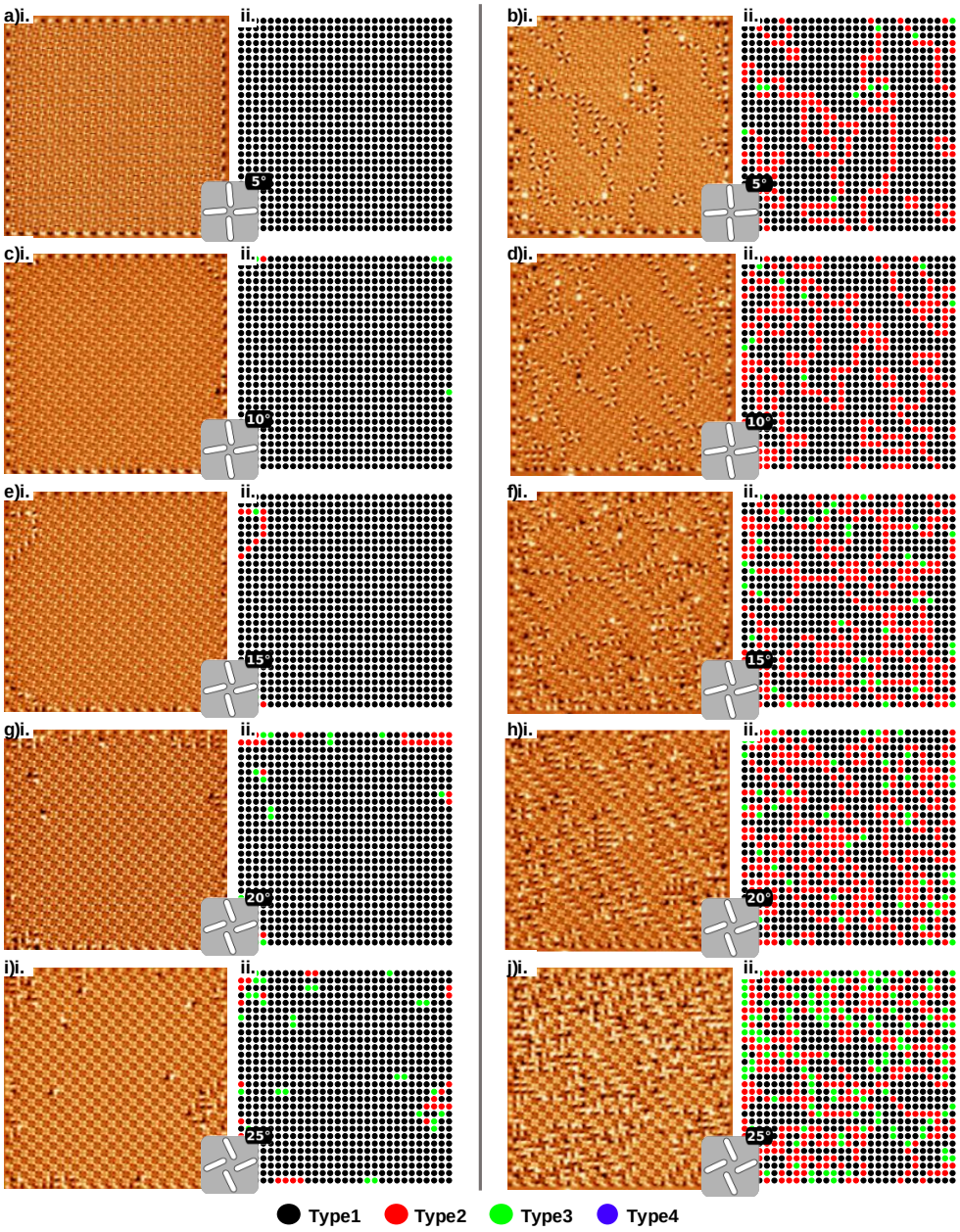

Fig.3-10: MFM images (i.) and corresponding vertex populations (ii.) of as-grown state (left column) and field-demagnetized (right column) state from 5° to 25°.

To the extent of the MFM images, the as-grown system through $\theta = 10°$ (Fig.3-10.a)i. and c)i.) exhibits an almost perfect chequerboard aspect with a few spins flipped on the edges of the network creating monopole-antimonopole pairs [16,63]. A rough count of the vertices (Type1, Type2, Type3 and Type4 vertices are represented by black, red, green and blue disks on vertex populations) results in a clear majority of Type1 vertices (Fig.3-10.a)ii. and c)ii.). On the other hand, for the same angle range, the field-demagnetized state is arranged in domains of Type1 vertices. Type2 vertices and a few Type3 vertices (behaving as defects for linking two boundaries pieces) compose the boundaries between them. We find that both states are rather similar to their square lattices shown in Fig.3-9.a) and b) respectively. For $\theta \in [15°; 25°]$, the as-grown state still exhibits an almost perfect chequerboard aspect (Fig.3-10.e)-g)i.). An increased number of defects, compared to lower rotation angles, are scattered mostly at the edges of the arrays. The 15°-tilted network is composed by three Type1 domains: one covering most of the array and two small domains located at the upper and lower left part of the network (Fig.3-10.e)ii.).

Type2 vertices and one Type3 vertex separate the domains, the latter again behaving as a defect created between the two parts of the boundary. Increasing the rotation angle to 20°- and 25°-tilt (Fig.3-10.g) and i)ii.), this state arranges itself with few Type2 vertices on the edges of the array and pairs of Type3 vertices because of spin flips. The field-demagnetized state shows, for 10°- and 15°-tilts (Fig.3-10.d) and f)), numerous Type1 domains separated by Type2 and Type3 vertices (Fig.3-10.d)ii. and f)ii.). At 20°- and 25°-tilts (Fig.3-10.h) and j)), the arrays are arranged smaller Type1 domains and domains of Type2 vertices start to appear (Fig.3-10.h)ii. and j)ii.). We also observe an increased number of Type3 vertices especially at 25°, significantly higher than in the as-grown state.

The remaining tilted networks of the as-grown and field-demagnetized systems are shown in Fig.3-11.

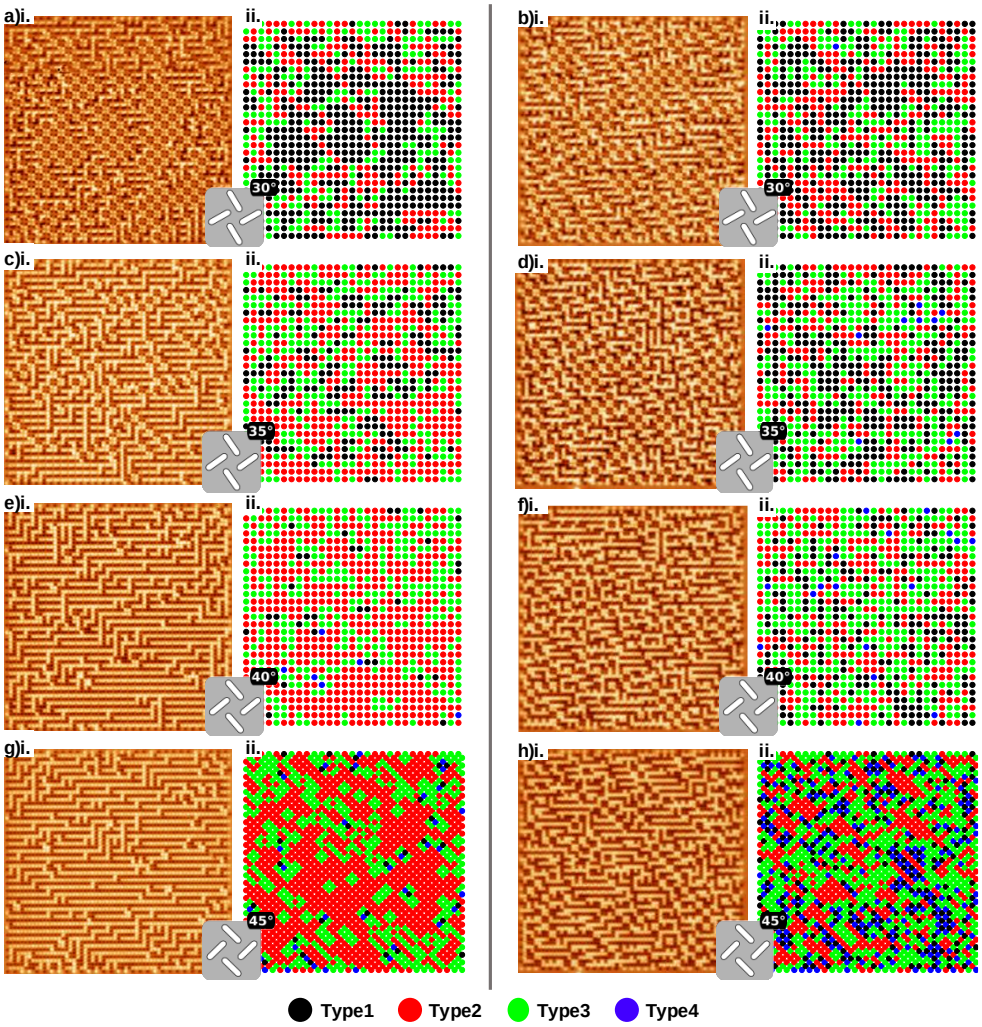

Fig.3-11: MFM images (i.) and corresponding vertex populations (ii.) of as-grown state (left column) and field-demagnetized (right column) state from 30° to 45°.

For 30° and 35° rotation angles (Fig.3-11.a) and c)), the as-grown system reveals a change in ground state. The 30°-tilted network is arranged in mainly domains of Type1 vertices and small domains of Type2 vertices and a greater number of Type3 vertices (Fig.3-11.a)ii.). The 35°-tilted network is arranged with mainly domains of Type2 vertices, a few domains of Type3 vertices and fewer Type1 vertices (Fig.3-11.c)ii.). On the other hand, the field-demagnetized state at 30° exhibits numerous domains of Type1 and Type2 vertices and an increased number of Type3 vertices compared to lower

rotation angles (Fig.3-11.b)). For the 35°-tilted array, the domains of Type1 vertices shrink to the benefit of domains of Type3 (Fig.3-11.d)).
Increasing the rotation angle to 40°, the as-grown state is arranged with clear domains of Type2 vertices and what seems to be domains of Type3 vertices rather than boundaries (Fig.3-11.e)). The arrangement of the field-demagnetized state is quite different with more domains of Type3 vertices than domains of Type2 vertices that seem rather small (Fig.3-11.f)). For both states, we observe that Type1 and Type4 vertices now compose the defects. For the 45°-tilted array, the number of vertices is doubled because of the geometry, all of them are represented in Fig.3-11.g) and h). The as-grown state is arranged mainly in domains of Type2 vertices that could be considered as unique with small domains of Type3 vertices that seem trapped into it (Fig.3-11.g)). A few number of pairs Type1/Type4 vertices are present within the domains of Type3 vertices. The field-demagnetized state is showing in domains of Type2 and Type3 vertices and a greater number of pairs of Type1/Type4 vertices compared to the as-grown state (Fig.3-11.h)).

We count each vertex type for both systems for all tilted networks and plot them in Fig.3-12.

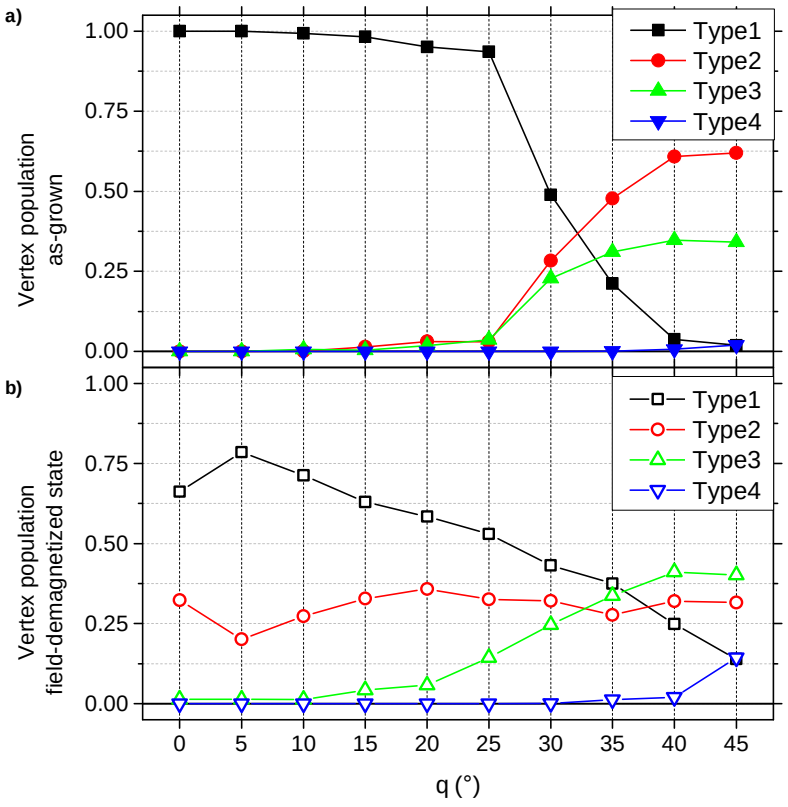

Fig.3-12: Vertex populations in proportions of a) in the as-grown system after lift-off and b) the field-demagnetized one.

We find that that for tilted arrays up to 25°, the vertex population of the as-grown state shows more than 95% of Type1 vertices (Fig.3-12.a)). For the same angle range in the field-demagnetized state, Type1 vertices represent merely 50-80%, mainly to the benefit of Type2 vertices. We note that for this state, the square lattice exhibits more domains than the following two rotation angles. This result emphasises that the observation of a single network does not allow any conclusion about the actual ground state of the system.
For 30°-tilt, vertex populations are similar for both systems: the as-grown system is composed by 48.9% of Type1 vertices, 28.3% of Type2, 22.8% of Type3 and no Type4 vertices; the field-demagnetized

system has 43.2% of Type1 vertices, 32.1% of Type2, 24.6% of Type3 and 0.1% of Type4 vertices. However for the 35°-tilt, the as-grown system has inversed its trend in Type1 and Type2 vertices with 21.2% and 47.7% proportions respectively whereas the field-demagnetized one has not with 37.5% of Type1 vertices and 27.7% of Type2. Both systems exhibit a similar proportion of Type3 vertices (31.0% and 33.7% for as-grown and field-demagnetized systems respectively). Only a low proportion of Type4 vertices is counted.
For the 40°- and 45°-tilted arrays, we find that the main difference between the two states is their majority: Type2 vertices for the as-grown state against Type3 vertices for the field-demagnetized one. We count for the 45°-tilted in the as-grown system 62.0% of Type 2, 34.1% of Type3 vertices and the rest are Type1 and Type4 vertices equally distributed while in the field-demagnetized state 40.2% of Type3 vertices, 31.6% Type2 vertices and the rest are composed Type1 and Type4 vertices again equally distributed. For pinwheel lattices, equal proportions of Type1 and Type4 vertices because they come in pair as seen on the MFM images.

On one hand, the field-demagnetized state evolves from a majority of Type1 to Type3 vertices with increasing rotation angle. We note that up to 30°-tilt, the system has higher proportions of Type2 and Type3 vertices than could expected with vertex energies (Fig.3-4). For higher rotation angles, all three types are close in proportions, although Type2 is of lower energy (Fig.3-4), all vertex types are close in energy. This last observation nuances the inadequacy between computations and experiments. On the other hand, the as-grown state exhibits for rotation angles up to 25° only a few vertices other than Type1. The transition from Type1 to Type2 majority occurs between 30° and 35° and above the system exhibits a higher proportion of Type2 vertices than Type3 and very few Type1 and Type4.
Vertex populations of the as-grown state are consistent with dipolar computations better than the field-demagnetized system. This result suggests that the as-grown state is the most suitable system for our study. This has yet to be confirmed with total dipolar energy of the systems.

We remark upon the 35°-tilted network of the as-grown system exhibits twofold its proportion of Type1 vertices in Type2 vertices translating in sixfold degenerate ground state to the extent of vertex population. However, as can be seen on the MFM image (Fig.3-11.a)i. and c)i.), the system is arranged in domains of both Type1 and Type2 vertices rather than in a disordered arrangement expected from the ice rules. This result emphasises the point made before about the lack of spatial representation of the vertex populations. However, associating MFM images with their arrangements yields only a qualitative conclusion since there is no quantification of the disorder.

3.3.2.2. Dipolar energy

We now compare our as-grown and field-demagnetized states by computing their dipolar energy. To do so, we use the dipolar Hamiltonian shown in (Eq.2) taking into account all pairwise spin interactions of the arrays. Normalised energies are plotted in Fig.3-13.

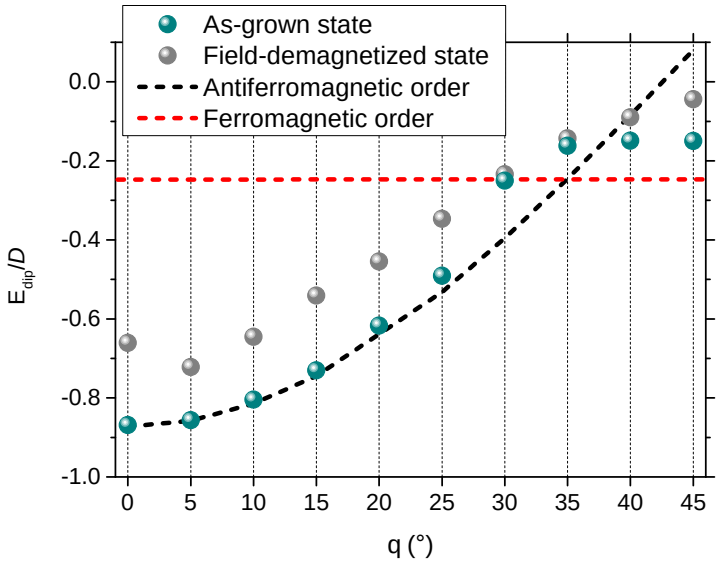

Fig.3-13: Normalised dipolar energies in an all-interaction approach for experimental as-grown and field-demagnetized systems.

We find that for the square lattice the field-demagnetized system is of higher energy than the as-grown one. This could have expected from the MFM images (Fig.3-9) where we observed in the former an arrangement in numerous domains and in the latter a perfect arrangement in Type1 vertices. We conclude that the arrangement in domains is energetically unfavourable for this tiling.
Increasing the rotation angle from 5° to 25°, we observe that the systems energies have roughly the same trend within an offset. The as-grown state is still of lower energy for this angle range. We note that the 5°-tilted array of the field-demagnetized state is of lower energy that its square array most likely due to the greater number of domains as noticed in vertex population (Fig.3-12.b)).
For the next two rotated networks, 30° and 35°, both systems have about the same energy although very different vertex populations and arrangements were observed. This feature is most likely due to rotation which we have seen bring closer in energy very different spin configurations (Fig.3-7).
For the 40° and 45° tilings, we observe that the field-demagnetized state is of higher energy than the as-grown one especially for the 45°-tilt. According to their vertex population, this could be due to the very different proportions in Type2 and Type3 vertices.

With the comparison of the as-grown and field-demagnetized energies, we conclude without doubt that the as-grown exhibits a lower-energy ground state. This result can be further underlined by the comparison with the antiferromagnetic (Type1 vertices) and ferromagnetic (Type2 vertices with same net magnetisation) orders (black and red dashed lines in Fig.3-13). Indeed, we have shown in the previous section with dipolar computations that our system is expected to undergo a transition from antiferromagnetic to ferromagnetic order with a transition at ~39.7°. Unlike the field-demagnetized state, the as-grown system follows closely the antiferromagnetic order up to 25°. The small deviations observed are most likely due to its increasing number of defects appearing with rotation angle. The gap between the antiferromagnetic ground state and the field-demagnetized state is apparently due to the arrangement in domains. Increasing the rotation angle, the as-grown state is only within a constant to the ferromagnetic order apart from the 30°-tiling. The field-demagnetized however increases in energy with rotation angle that could be explained by the increased number of defects and the Type1/Type4 pairs.

For all enounced arguments, we choose to carry on our experimental study on the as-grown system. Both vertex populations and total dipolar energy however suggest that our system is not in the lowest-

energy possible. From 35° and above, the system is of higher energy than the ground state it can be expected to lie, most likely due to the higher proportion of Type3 vertices. We now need to understand the actual transition observed in our as-grown state.

3.3.3. Lowest-energy state: beyond first neighbours

We have seen that out of the low-energy states elaborated, the lowest-energy is the as-grown state. We have found that to the extent of vertex populations, there is a transition from antiferromagnetic to ferromagnetic ordering but not following the ground state. We will now study the actual ordering of the arrays using magnetic structure factor.

3.3.3.1. Magnetic structure factor

As Rougemaille *et al.* [54] explained, counting the vertex types gives only a partial view of a spin configuration, so it is for the overall magnetisation. These approaches do not yield any certainty about the disorder present or not in the array. This issue has been of particular interest while trying to recover degenerate ground state. One solution is to perform a Fourier transform of the spin-pairs correlations of the configuration. Correlation between S_i and S_j spins is expressed by:

$$C_{ij} = < S_i . S_j >$$

This transformation from real to reciprocal space gives the magnetic structure factor or the diffraction pattern of the spin configuration. The intensity in the q direction is computed as:

$$I(\boldsymbol{q}) = \frac{1}{N} \sum_{i,j=1}^{\frac{1}{2}N} \sum_{\alpha,\beta=1}^{2} \boldsymbol{S}_{i\alpha}^{\perp} \boldsymbol{S}_{j\beta}^{\perp} \exp\left(-i\boldsymbol{q}.\boldsymbol{r}_{i\alpha,j\beta}\right)$$

where i and j are the nodes of the network and α, β both sites of the unit lattice as explained in Ref [55]. The features are well-known: Bragg peaks at specific locations (centre and/or edges of the Brillouin zones) and specific so-called pinch-points specific of the Coulomb Phase. But one can compute the magnetic structure factor of any spin configurations and conclude about the ordering of its unambiguously magnetic configuration beyond nearest neighbours.
For further information about this characterisation, we refer to Dr. Y. Perrin's PhD thesis (Ref. [55]).

3.3.3.2. Ideal orders

In order to understand our experimental results, we first compute the magnetic structure factor of ideal antiferromagnetic and ferromagnetic spin configurations. The size array used is the same as our experimental networks. All magnetic structure factors presented in this work are symmetrised and the colour code of Fig.3-14 is used for the spin configurations.

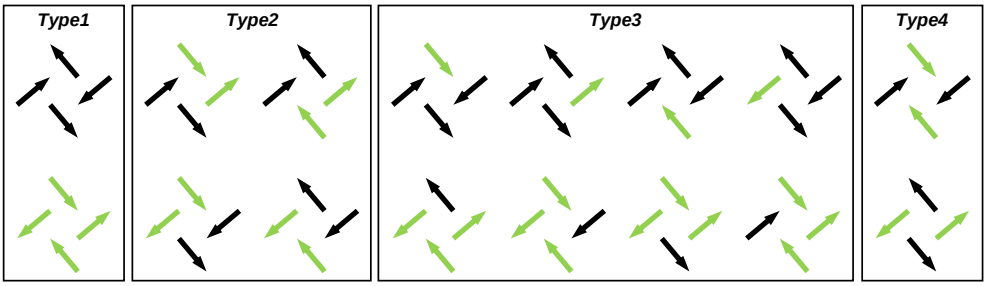

Fig.3-14: The 16 possible vertex configurations. Colour code, chosen according to position and rotation of the spins, emphasising the antiferromagnetic (same colour) and ferromagnetic (different colours) coupling between collinear spins.

Antiferromagnetic order translates in spin configuration (with antiferromagnetic coupling between colinear spins) hence exclusively Type1 vertices (appearing in a unique colour black or green over the array). Ferromagnetic order (with ferromagnetic coupling between colinear spins) translates in Type2 vertices with same net magnetisation (appearing in diagonals of alternating black and green spins). Spin configurations of the orders and their corresponding magnetic structure factor are plotted for 0°-, 35°- and 45°-tilted arrays in Fig.3-15.

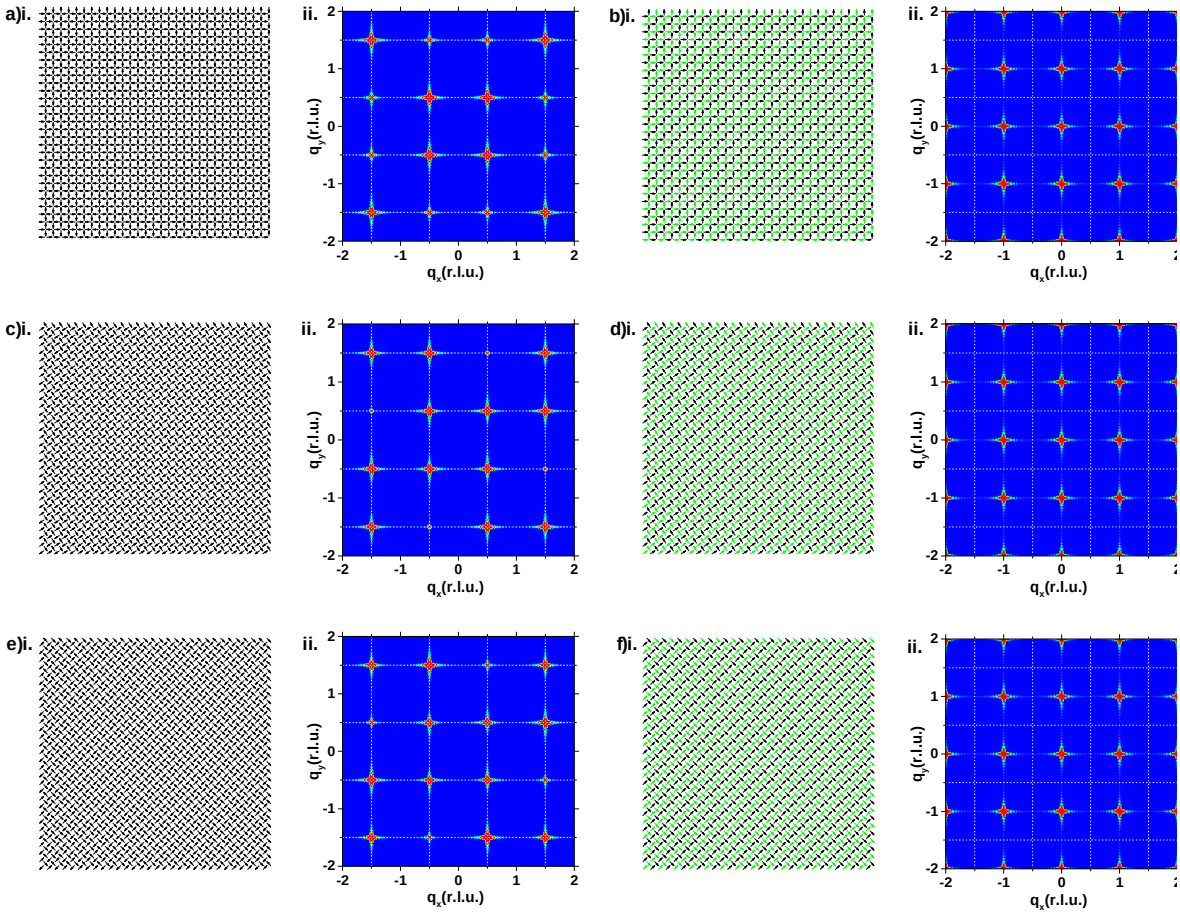

Fig.3-15: Ideal antiferromagnetic orders (two left columns) and ferromagnetic orders (two right columns) spin configuration and magnetic structure factors for a)-b) 0°-, c)- d) 35°- and e)-f) 45°-tilts. Same colour scale is used for magnetic structure factors.

For the square array, the ideal antiferromagnetic order translates in magnetic structure factor in sharp Bragg peaks located at the corners of the Brillouin zones (Fig.3-15.a)). We observe that the peaks do not have same intensities at points $(\pm 0.5, +1.5)$, $(\pm 0.5, -1.5)$, $(\pm 1.5, +0.5)$ and $(\pm 1.5, -0.5)$.
The same lattice arranged in a ferromagnetic order results in magnetic structure factor by sharp Bragg peaks located at the centres of the Brillouin zone (Fig.3-15.b)). No variation of intensity is observed here.
We find that rotating the spins of 35° and 45° does not change the locations of the peaks: for the antiferromagnetic order they are located at the centres of the Brillouin zones and for the ferromagnetic ones they are at the edges. However, we observe that for these two tilings peak intensities of only the antiferromagnetic order change: they are now located at points $(\pm 1.5, \mp 0.5)$ and $(\pm 0.5, \pm 1.5)$.

We also applied the same approach for the Manhattan, Types2/3, Type3 and Types1/3 orders (see section 3.2.3). Spin configurations and magnetic structure factors for 35°-tilted arrays are shown in Fig.3-16.

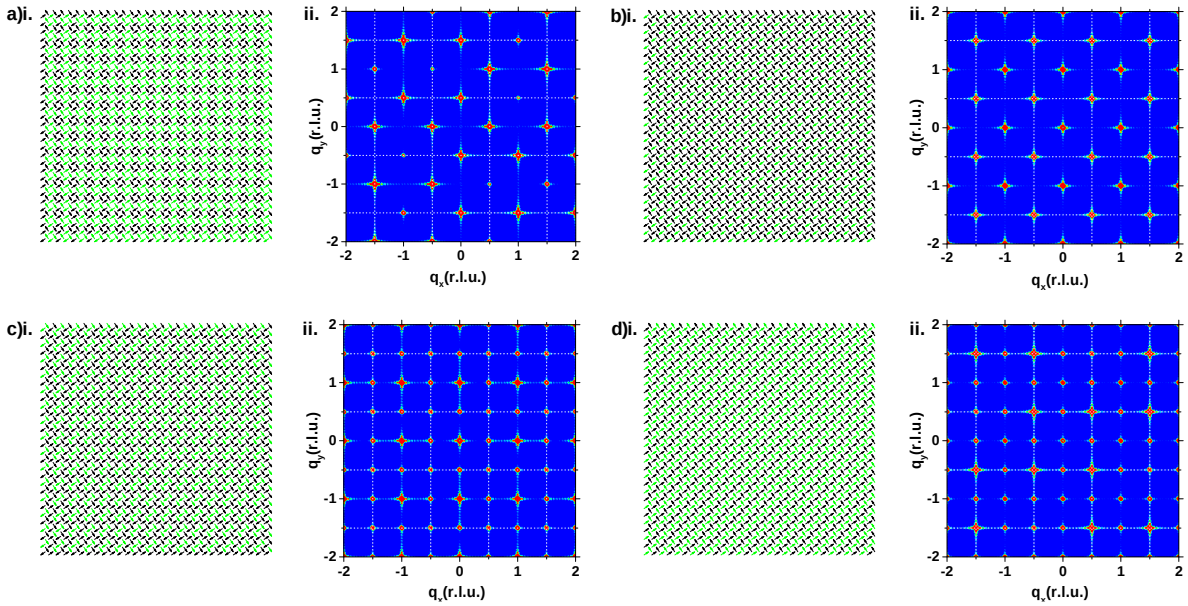

Fig.3-16: Spin configurations and magnetic structure factors of a) Manhattan order; b) Type3 order; c) Types2/3 and d) Types1/3.

We find that the Manhattan order -its spin configuration characterised by alternating chiralities between vertices- results in Bragg peaks seen at the middle of the edges of the Brillouin zones (Fig.3-15.a)). Weak peak intensities are located at $(\pm 1, \pm 1.5)$ and $(\pm 1.5, \mp 1)$, also even weaker peaks at $(\pm 0.5, \mp 1)$ and $(\pm 1, \pm 0.5)$. The Type3 order –with a spin configuration of alternating-coloured spins along both diagonals- exhibits Bragg peaks located at both centres and corners of the Brillouin zones (Fig.3-16.b)). Here no variation of the peak intensities is seen. Types2/3 and Types1/3 both show Bragg peaks located at the centres and corners in addition to the ones in the middle of the edges of the Brillouin zone. We observe no obvious extinctions only in the former that peaks at the centres and in the latter peaks at the corners of the Brillouin zone. We remark that these features are specific of the ferromagnetic and antiferromagnetic orders shown previously.

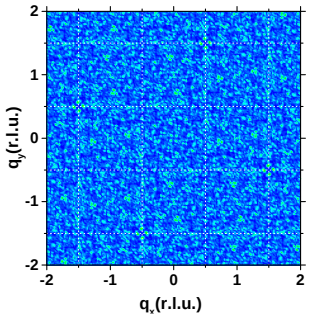

Fig.3-17: Magnetic structure factor of a random spin configuration

We have also computed the magnetic structure factor of a random spin configuration (Fig.3-17). The total absence of order translates in magnetic structure factor in a diffuse moderately intense pattern.

3.3.3.3. Experimental orders

Now that we have identified the specific signatures of various orders on magnetic structure factor, we use them as references for our experimental as-grown system. With the vertex populations we have seen two main trends: up to 25°-tilt a majority of Type1 vertices arranged in a wide domain and above 40°-tilt Type2 vertices arranged in (smaller) domains. We compute the experimental magnetic structure for each tiling, we show the spin configurations (using the colour code of Fig.3-14) and magnetic structure factors of the two tilings mentioned in Fig.3-18.a) and b).

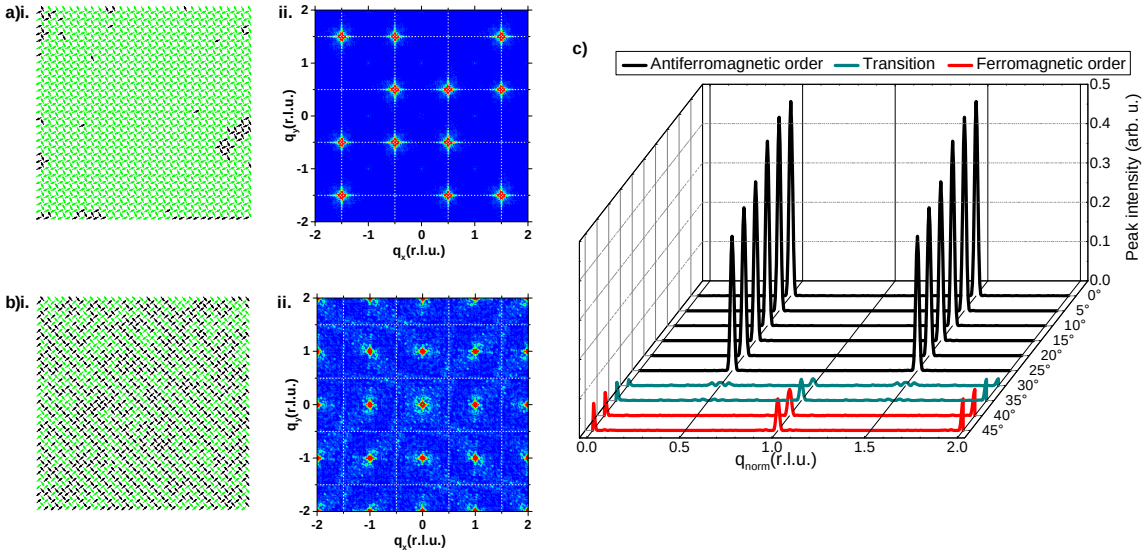

Fig.3-18: Spin configurations and magnetic structure factors of a)i. and ii. 25°-tilted and b)i. and ii. 40°-tilted networks and c) cross-sections along the diagonal on magnetic structure for the entire tilted system.

The 25°-tilted array is arranged in a wide domain with antiferromagnetic coupling (in green) with defects such as spin-flips and small antiferromagnetic domains located at the edges of the network. We note here that this representation of the spin configuration is indeed more precise since domains this small cannot be seen on vertex population. This configuration translates in magnetic structure factor in sharp Bragg peaks located at the corners of the Brillouin zones. Weak peaks are also observed at the centres of the Brillouin zones. This very small contribution is most likely due to the sparse defects seen on the

spin configuration. We conclude that the tiling is arranged in a clear antiferromagnetic order and that the few defects observed have little effect.
The 40°-tilted array is arranged with apparently less order, but ferromagnetic domains can be identified with scattered small domains or defects of both antiferromagnetic and ferromagnetic couplings. Its magnetic structure factor exhibits Bragg peaks located at the centres of the Brillouin zones suggesting a ferromagnetic ordering. We find that a very light diffuse background surrounds the features so this time the inhomogeneous the spin configuration affects more significantly the pattern.

We now verify that the pattern observed for the 25° and 40° are similar to the ones up to 20° and 45° respectively. To do so, we look at cross-sections along the diagonal of magnetic structure factor (Fig.3-18.c)). We find that the antiferromagnetic order observed at 25° is also present from 0° to 20° rotation angles. All the same for 40°, the 45°-array exhibits the same features of the ferromagnetic order seen for the previous tiling. This emphasises the conclusions made previously about the antiferromagnetic-ferromagnetic order transition with increasing rotation angle.
A striking feature also observed here is about the 30° and 35° tilts, the cross-sections show Bragg peaks of both the antiferromagnetic and ferromagnetic orders. Their spin configurations and corresponding magnetic structure factors are shown in Fig.3-19.a) and e).

The 30° and 35°-tilted arrays indeed exhibit peaks at both the corners and the centres of the Brillouin zones with extinctions as seen in Fig.3-15.a)ii. and b)ii.. In the former, the peaks result of an arrangement in antiferromagnetic domains (green and black ensembles) separated by domain walls with ferromagnetic coupling (Fig.3-19.a)i.). In the latter, it is the result of small antiferromagnetic and ferromagnetic domains (Fig.3-15.e)i.). These results again raise the question about the actual nature of the observed order. Peak positions are consistent with a Type3 order (Fig.3-16.b)) but also with both antiferromagnetic and ferromagnetic orders together. We suspect a coexistence of both antiferromagnetic and ferromagnetic orders rather than a Type3 order for two features of the real and reciprocal spaces. First, non-negligible proportions of Type1 and Type2 vertices compared to the Type3 vertices compose the spin configurations. Second, the extinctions observed in magnetic structure factors are consistent with the ones on antiferromagnetic order at 30°-tilt. However, we will verify this hypothesis by studying the contribution on magnetic structure factor of both the antiferromagnetic and ferromagnetic couplings. To do so, we choose to assimilate the Type1 vertices to the antiferromagnetic order. Thus, we discriminate the Type1 vertices from all others and compute the resulting magnetic structure factor (Fig.3-19.b)-d) and f)-h)).

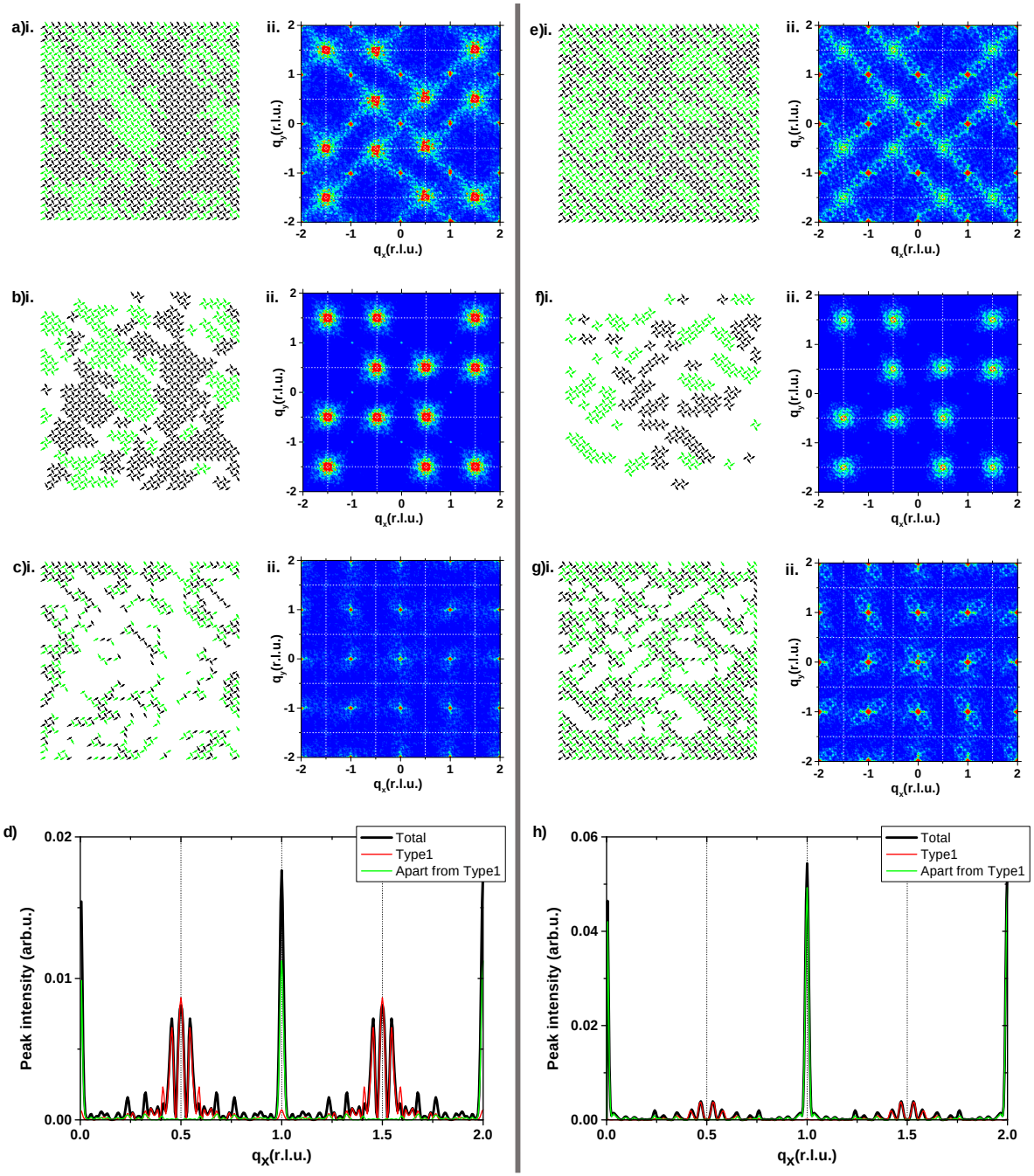

Fig.3-19: For 30°-tilted network (left column) a).i. spin configuration and ii. magnetic structure factor, discrimination of Type1 vertices on b).i. spin configuration and ii. resulting magnetic structure factor from all others c)i. on spin configuration and ii. magnetic structure factor, d) cross-section on magnetic structure comparing the array and both contributions. Same analysis for the 35°-tilted network (right column) e)-h).

For the 30°-tilted array, we find that the contribution of the Type1 vertices on magnetic structure shows wide intense and weak peaks located at the corners and the centres of the Brillouin zones respectively (Fig.3-19.b)). This antiferromagnetic signature is the result of various sizes and shapes of antiferromagnetic domains of both configurations (green and black ensembles). The weak signature of the ferromagnetic order is most likely due to the boundaries of ferromagnetic coupling between antiferromagnetic domains of both configurations juxtaposed. The remaining spins mainly forming thin ferromagnetic domains ensue the ferromagnetic signature of magnetic structure factor (Fig.3-19.c)). From this, we conclude that antiferromagnetic domains and the boundaries between them are mainly

responsible for the antiferromagnetic and ferromagnetic contributions on magnetic structure factor. Looking at the cross-sections of the two contributions compared to the total one (Fig.3-19.d)) we find a good agreement.
The observations are similar for the 35°-tilted array. The small antiferromagnetic domains result in wide peaks at the corners of the Brillouin zones and the boundaries between juxtaposed domains are –most likely- responsible for the weak peaks at the centres of the Brillouin zones (Fig.3-19.f)). The rest of the spins translate in peaks specific of the ferromagnetic order (Fig.3-19.g)). Using the cross-sections, we find that the ferromagnetic peak intensities are higher for the 35°- than for 30°-tilted array. Conversely, the antiferromagnetic peaks are more intense for the 30°- than the 35°-tilted one. This observation is consistent with the results explained up to now.

We conclude that our system evolves from antiferromagnetic to ferromagnetic order for low and high rotation angles respectively as shown by the magnetic structure factors. Although the antiferromagnetic order is clear, it is not as clear for the ferromagnetic one considering the diffuse background observed. Nevertheless, the cross -sections on magnetic structure factor gives an unambiguous proof in spite of the disorder. We conclude that the transition between the two strongly suggests a coexistence of antiferromagnetic and ferromagnetic orders.

3.3.4. Conclusion

The goal of this section was to study experimentally the evolution of the magnetic configuration due to the rotation of the islands of a square array.
Among the protocols established in the literature, we have chosen to try reaching a low-energy state with an ac field-demagnetized state and with an as-grown state. The study of their vertex populations has shown that the as-grown state is more consistent with the vertex energies evolution according to rotation angle. The observations made suggested that the as-grown state was of lower energy than the field-demagnetized one. This result was confirmed by the comparison of their total energy, the as-grown state being, for all rotation angles, of lowest energy. This study has revealed that for high rotation angles, despite a majority of Type2 vertices, the high proportion of Type3 vertices cannot allow ascribing any order to the tilings. In addition, we have seen that the corresponding energy is higher than the ground states expected. Therefore, we needed to perform a characterisation beyond first-neighbours that could give insight about the actual order of the arrays. We chose to compute spin-spin correlation, an all-interaction approach, and compute magnetic structure factor.
Using reference patterns of magnetic structure factor, we have observed that low rotation angles exhibits features of the antiferromagnetic order and high rotation angles of the ferromagnetic order. We unambiguously concluded that the ground state evolves from antiferromagnetic to ferromagnetic ordering as predicted by dipolar computations in an all-interactions approach.
This study has also shown that the transition between the antiferromagnetic and ferromagnetic orders is characterised by a magnetic structure factor with specific features suggesting a coexistence of both orders. We have shown by splitting the spin configurations in relevant groups that it indeed results from the contribution of both the antiferromagnetic and ferromagnetic domains.

3.4. Thermodynamics of the system: antiferromagnetic-paramagnetic transition

We have shown using magnetic structure factor that our as-grown system evolves from an antiferromagnetic to a ferromagnetic order with increasing rotation angle. For tilted arrays in between

the two (rather) clear orders, we have found features on magnetic structure suggesting a coexistence of both orders rather that an abrupt transition. Our ambition is to now study the thermodynamics of our low-energy system. We would like to see if this evolution with the tuning of dipolar interactions we chose can be described by an effective temperature.
We will first use a vertex approach often used in the literature but, as we will show the mean-field approximation it relies on is inaccurate to describe our system. So then, we will use an all-interactions approach, established, more accurate and actually describing closely our experimental system dipolar energy and vertex population.

3.4.1. 16-vertex model

Artificial spin systems are athermal due to the large magnetostatic and anisotropy energies of their islands compared to thermal energies but as it may, kinetics can be extracted as shown for granular media [64,65] and structural glasses [66]. In the case of artificial spin ice systems, Nisoli *et al.* [56] have introduced in 2010 a method to ascribe an energy-based effective temperature using their arrested microstates. This approach uses the defects of the spin configurations to ascribe a temperature to any array. Relying on the 16-vertex model [67], it considers the four vertex types (shown in Fig.3-14), their corresponding degeneracy level ($q_1 = q_4 = 2$, $q_2 = 4$ and $q_3 = 8$) and energies. This formalism falls within a mean-field approximation therefore neglecting interactions among vertices. Assuming that we are close to thermal equilibrium, the fraction of vertices of type i is given by Boltzmann's law:

$$n_i = \frac{q_i e^{-\beta_{eff} E_i}}{Z}$$

with $Z = \sum_{i=1}^{4} q_i e^{-\beta_{eff} E_i}$ the partition function and $\beta_{eff} = (k_B T_{eff})^{-1}$. With this expression, the vertex populations are equal at the degeneracy levels at infinite temperature. The vertex energy of then system is therefore expressed as:

$$E_{tot} = \sum_{i=1}^{4} n_i \, E_i$$

The question now arises about how to compute the energy of each vertex type and subsequently the energy of the system. Nisoli *et al.* have chosen to use the "dumbbell" model (Ref. [51]) which well described their field-demagnetized configurations. However this approximation was later contradicted by Morgan and collaborators in their work on as-grown system [62]. Achieving a lower effective temperature ($\beta_{eff} E_3 \sim 7$) than the ones of in Ref. [56] ($\beta_{eff} E_3 < 3$), they have shown that the point-dipole approach is a better fit to describe low-temperature systems. We choose to adopt the same method as Morgan *et al.* so we compute the vertex energies according to (Eq.3) to (Eq.6).

Rather than plotting all vertex the vertex populations of all our tilted arrays, we choose to find a match using the total energy (Fig.3-20). We choose to use the computed values of vertex energies, unlike Refs. [56,62].

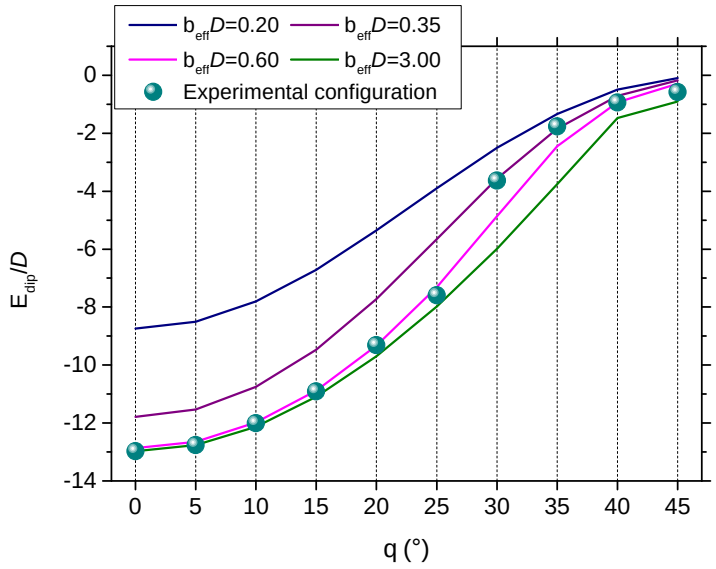

Fig.3-20: Experimental and computed dipolar energy with four values for $\beta_{eff}D$ within the 16-vertex model.

For the values of $\beta_{eff}D$ chosen, we find that our system lies with low effective temperatures and as hoped a good match is found for the entire rotated system –except for the 30°- and 35°tilted arrays- with $\beta_{eff}D = 0.60$. This rather low temperature value describes our system from 0° to 25° and then 40° and 45° with a good accuracy and is close the energy of the 30° and 35°. To verify this value, we compare now the experimental vertex population and expected ones, results are plotted in Fig.3-21.

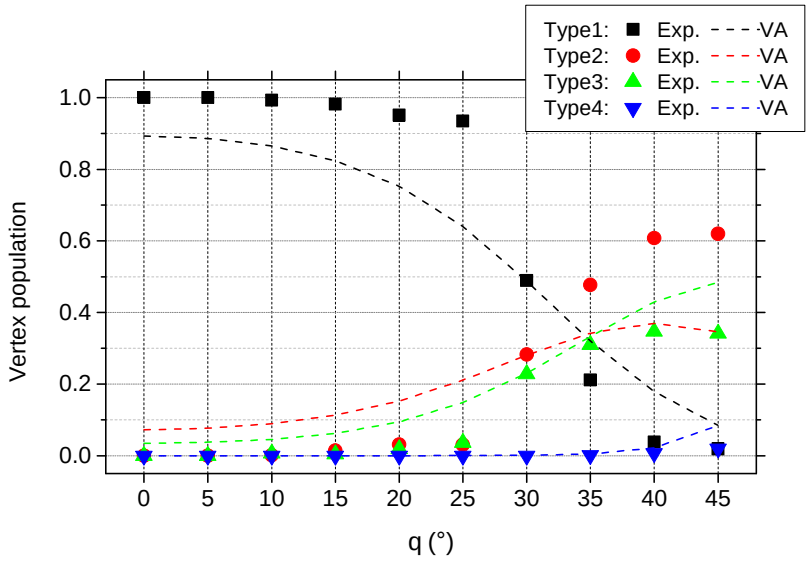

Fig.3-21: Experimental and computed vertex populations using a vertex approach (VA) with $\beta_{eff}D = 0.60$

We observe high discrepancies between the experimental and computed vertex populations on all levels. Higher values of temperatures have been tried but results were not conclusive. Thereupon, we conclude that match the energy is not sufficient to ascribe an effective temperature but both energies and vertex

populations are to be described. Furthermore, this approach fails to describe our tuning of the energies with a unique temperature unlike the Monte Carlo simulations that we will show in the next section.

Beyond the computations, we can make one more comment about how inappropriate seems to be the 16-vertex model. Vertex energies predict a change in ground state from Type1 to Type2 vertices with increasing rotation angle, hence any arrangement of Type2 vertices can be expected after the transition. For instance, if one computes the energies of an array arranged in ferromagnetic order and a Manhattan order, both would be of same energy. However, it does not correspond to the experimental observations which show a clear preference for a ferromagnetic order. Therefore, the very fact that all arrangements of Type2 are not of same energy advocates for taking into account interactions between vertices.

3.4.2. All-interaction approach

We now focus on the thermodynamics of our system using Monte Carlo simulations and show that a precise definition of its effective temperature is possible within an all-interactions approach.

3.4.2.1. Phase Diagram

We now take an interest in the thermodynamics using a spin Hamiltonian taking into account all interactions of the array. The goal is to describe our system with the means of statistical mechanics like in Ref. [68]. Assuming only dipolar interactions are at play, we adopt a similar approach to the one used by Macêdo *et al.* [47] and Silva *et al.* [53]. The difference lies in the boundary conditions used for the Monte Carlo simulations (using Metropolis algorithm [69]) that are periodic in their works and finite in ours. We compute the most probable configuration according to temperature using 10^5 Monte Carlo steps (1000 single-spin flips and energy average on 100 configurations) enough to reach thermodynamic equilibrium. All interactions are taken into account to compute the specific heat capacities defined as:

$$c = \frac{\langle E^2 \rangle - \langle E \rangle^2}{k_B T}$$

where E is the total energy of the system that we choose to compute with the dipolar approximation and the dipolar Hamiltonian in (Eq.2). We add that between our computations and the ones of Macêdo and co-workers, the size array considered is different. Silva *et al.* have shown that modifying this way the computations does not change the position of the specific heat capacity, only slightly its intensity. Specific heat capacities and corresponding vertex populations for three tilings of our system are given in Fig.3-22.

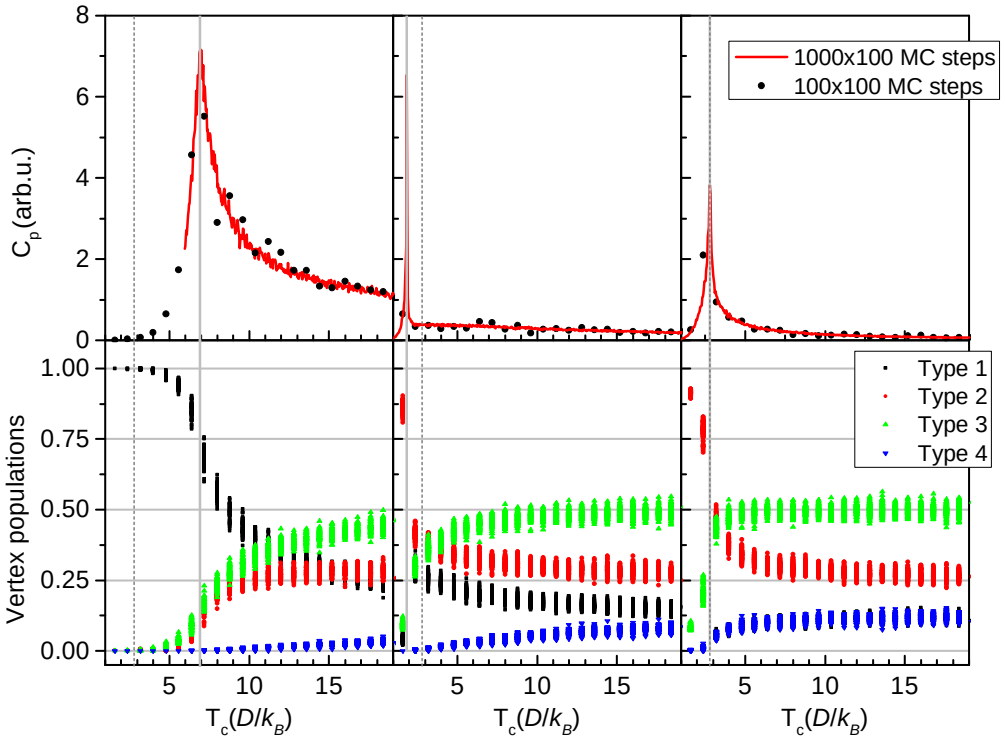

Fig.3-22: Specific heat computed by Monte Carlo simulations for square, 35°- and 45°-tilted networks with finite boundary conditions, same size as our experimental arrays (square array with 1800 spins).

The null-temperature configurations for all three tilings 0°, 35° and 45° give the ground state found with dipolar computations: Type1 vertices exclusively for the square array or perfect antiferromagnetic order and Type2 vertices of perfect ferromagnetic orders for the 35°- and 45°-tilted arrays. We remind here that the population of Type2 vertices translates in one Type2 vertex repeated all over the array and does *not* correspond to a Manhattan order.
Monte Carlo simulations return a specific heat capacity around $7.0D/k_B$ for which the configuration has a transition from antiferromagnetic phase to paramagnetic phase. This value of transition temperature is consistent with the $7.2D/k_B$ value found by Silva *et al.*'s [53] and Macêdo *et al.*'s [47] although they worked with periodic boundary conditions. It has already been shown by Silva *et al.* that when the lattice size is increased, the intensity of the peak only changes and very slowly. Finding a close result between periodic and finite boundary conditions is a first proof that such a change has little consequences on the specific heat capacity peak. Increasing the rotation angle, we find that the sharp peak of specific heat is located at lower temperatures than the square lattice. The 35°- and 45°-tilted lattices show a transition from ferromagnetic to paramagnetic phase at $1.9\,D/k_B$ and $T_c \approx 2.8D/k_B$ respectively. We also note for the pinwheel lattice that Type1 and Type4 vertices are of same proportion on vertex population which is consistent with the observations made in section 3.2.

In the previous sections, we have shown that our system exhibited a high proportion of Type3 vertices (from 30° rotation angle up to 45° as shown in Fig.3-12) which prevented us from asserting the order the arrays belonged to. We find that for all presented tilings, the paramagnetic phase is characterised by vertex populations with a majority of Type3 vertices. Being the next vertex type in line after the ground state one, the change occurs at lower temperature for the 35°- and 45° rotation angles than for the square array. This result strongly suggests that we are witnessing in our experimental system features of the paramagnetic phase.

We perform the same Monte Carlo simulations for each rotation angle of our system. The results are summarised in the phase diagram in Fig.3-23 and also compared with the one obtained by Macêdo and collaborators.

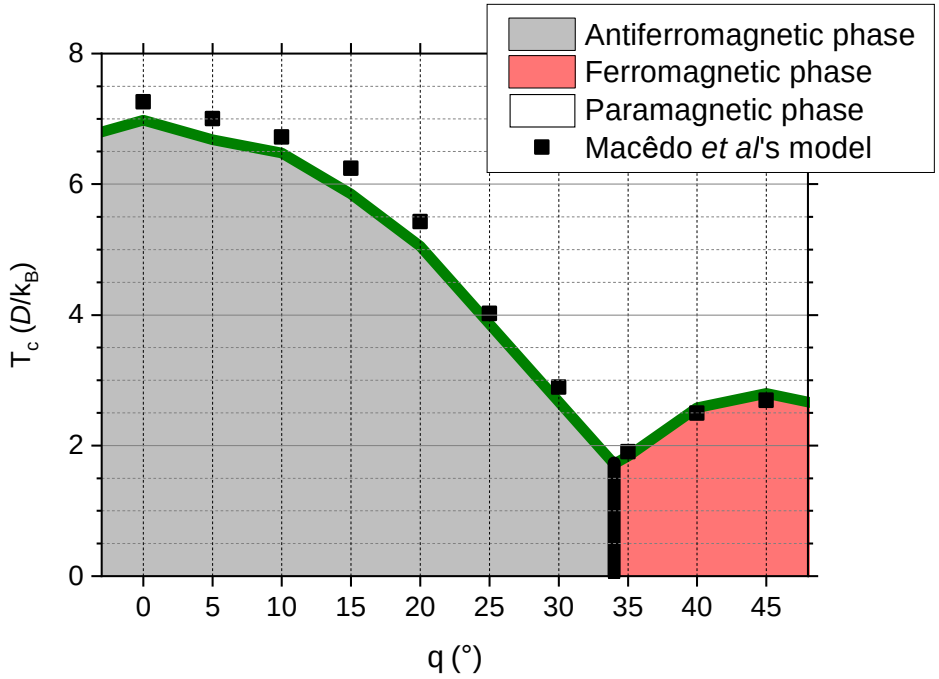

Fig.3-23: Phase diagram of our titled system determined by Monte Carlo simulations with finite boundary conditions in an all-interaction approach.

We confirm what was suggested before that deviations from periodic and finite boundary conditions are small. From the phase diagram, we find that up to ~34.9° the transition is from antiferromagnetic phase to paramagnetic phase with decreasing transition temperature with increasing rotation angle. Beyond this angle threshold, a transition from ferromagnetic to paramagnetic phases with increasing transition temperature as the rotation angle is increased.
As Macêdo *et al.* explained and our dipolar computations showed, the transition from antiferromagnetic to ferromagnetic phase (at low enough values of temperature) is due to the predominance of next-nearest interactions. Also, we observe that the transition temperature to paramagnetic phase is never zero. This is due to the fact that interactions beyond nearest neighbours are taken into account. Otherwise, the temperature would indeed be null at 45°. This stresses again the necessity to take all-interactions into account.

3.4.2.2. Comparison with our as-grown system

Now that we have characterised thoroughly the thermodynamics of our system, we can now try to find an effective temperature to our experimental as-grown system. We compare the energy of our system to energies computed using Monte Carlo simulations of three effective temperatures chosen using the phase diagram. Results are shown in Fig.3-24 along with the phase diagram.

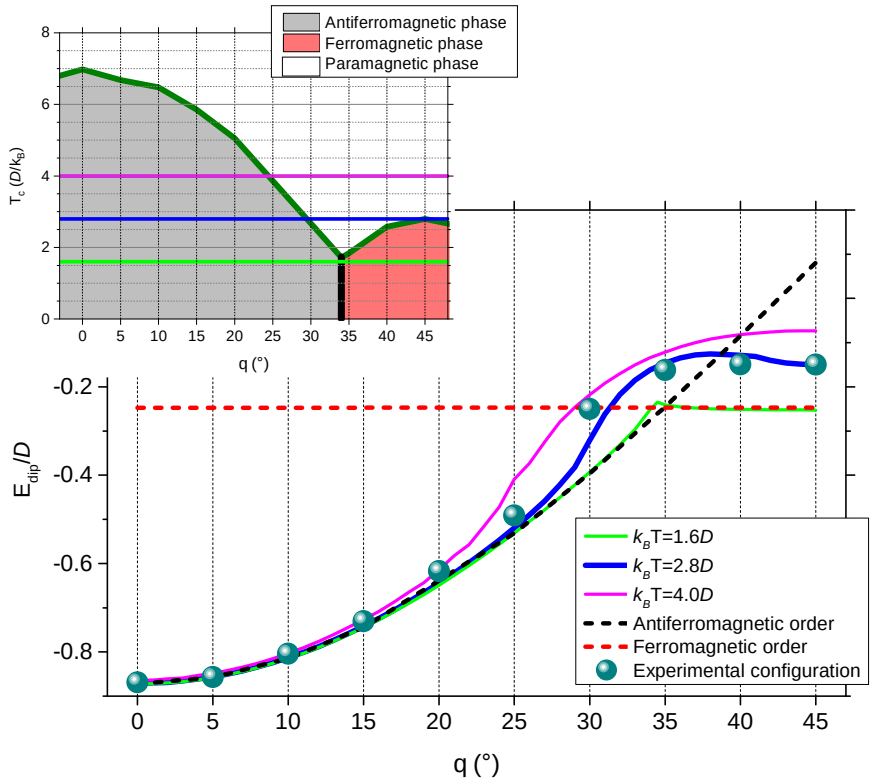

Fig.3-24: Dipolar energy of the as-grown system and computed effective temperatures determined by Monte Carlo simulations and in the inset, the phase diagram of our system and the effective temperatures.

All chosen temperatures -below the antiferromagnetic/paramagnetic transition (Fig.3-24 inset)- describe our system up to 20°. This result is therefore consistent with what has been seen up to now: vertex populations of perfect or almost prefect ground state and clear antiferromagnetic peaks on magnetic structure factor.

For the 25° rotation angle, we find a deviation between experimental and the $4.0D/k_B$ temperature but the other two are in good agreement. We see on the phase diagram that for $4.0D/k_B$, we are at the transition temperature meaning that we would start to see a drop in Type1 vertices. Keeping in mind that we have observed sharp antiferromagnetic (ground state) peaks on magnetic structure, we conclude that this tiling is not described by a high temperature. Therefore we conclude that the tiling is best described by $1.6D/k_B$ or $2.8D/k_B$.

Increasing the rotation angle, we start to see differences for the energies corresponding to the two low temperatures values. We find that the $1.6D/k_B$ effective temperature follows very closely the antiferromagnetic order up to the transition then closely the ferromagnetic one. We note a small deviation and a bump just before the transition around $\sim$34.8°. For the other value ($2.8D/k_B$), we find a deviation for the 30°-tilted array but for the higher rotation angles, a good agreement in energy. Reporting both temperatures on the phase diagram, we find very consistent results. On one hand, the lowest effective temperature value, $1.6D/k_B$, returns the ground state phase for all rotation angles except for 35° for which it draws near the transition temperature explaining the bump observed in energy. However, we have seen that our system is not in its ground state thus not matching the experimental vertex populations nor the features on magnetic structure factor. On the other hand, the higher value of effective temperature, $2.8D/k_B$, is slightly above the transition temperature from antiferromagnetic to paramagnetic phase for 30°-tilt. This result is consistent with the increased proportions of Type2 and Type3 vertices in vertex population and the features on magnetic structure not corresponding to the antiferromagnetic order. For the 35°-tilted array, the temperature is above the transition temperature from ferromagnetic to paramagnetic phase. According to the vertex populations determined by Monte

Carlo simulations (Fig.3-22), it corresponds to a temperature for which a clear drop in Type2 vertices can be expected to the benefit of Type3 vertices. This is what was observed experimentally with vertex population and features added to signature of ferromagnetic order on magnetic structure factor. Similar things are observed for the 40° rotation angle, also belonging to the paramagnetic phase at this temperature. This again is consistent with vertex populations but not as much with magnetic structure factor features which did exhibit ferromagnetic peaks. But we recall that the magnetic structure factor was not as clear as the ideal ferromagnetic order. For the 45°-tilt, this temperature value is slightly above the transition temperature from ferromagnetic to paramagnetic phase. Looking at the vertex population for this tiling expected from Monte Carlo simulations, this result is consistent with a spin configuration slightly off the ground state that needs a lower temperature to show an increased proportion in Type3 vertices which is according to experimental observations.

We can therefore conclude that there is a unique effective temperature describing our entire system energy and it is $2.8D/k_B$. But as we show for the 16-vertex model, one needs to verify that the effective matching the energy has to match the vertex populations for each tilted array of our system. Therefore, we compare in Fig.3-25 the experimental vertex populations to the ones computed with Monte Carlo simulations at the temperature of interest.

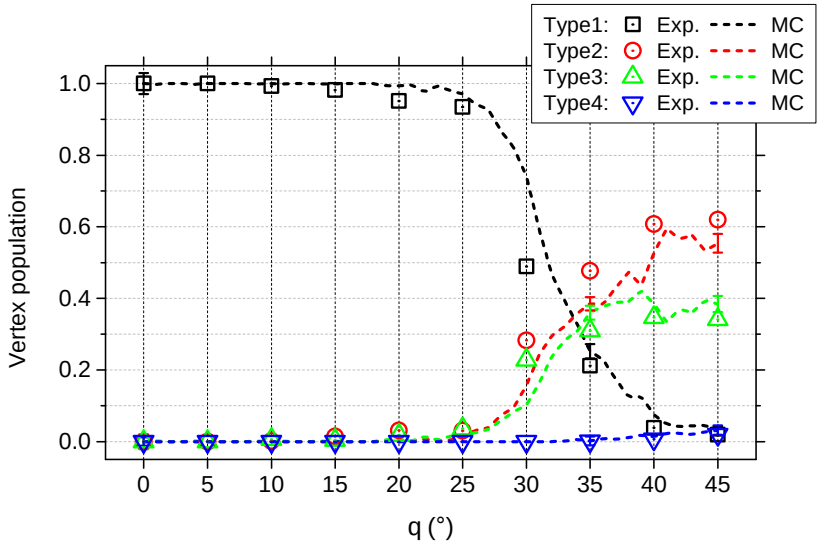

Fig.3-25: Comparison experimental and computed vertex populations with k_BT_{eff}=2.8D.

Consistent with what was stated before, we find an excellent agreement between experimental and computed vertex populations for low rotation angles. Very small observed deviations are observed for 20° and 25° which are most likely caused by the defects present. For higher rotation angles we find higher deviations although some are within or close to the error bars. This is particularly true for the 30°-tilted array for which Type1 vertices are not represented experimentally as in computations whereas Type2 and Type3 vertices are over-represented. For the 35°-tilted array, a difference is observed but only for the Type2 vertices. For the high rotation angles 40° and 45° however, experimental and computed vertex populations are close to one another. Results therefore show that experimental and computed vertex populations for the effective temperature of $2.8D/k_B$ are in good agreement for most of the tilings.

We conclude that our system is representative of thermodynamics at equilibrium since Monte Carlo simulations describe it quantitatively. We have also shown that the tuning of the interactions does affect

the thermodynamics of the sample because it is described by a unique energy-based effective temperature.

3.4.3. Conclusion

In this section, we have studied the thermodynamics of our tuned system by the means of two approaches: the 16-vertex model and all-interactions approach, both ascribing an effective temperature of arrested microstates.
We have shown throughout this chapter that, for multiple reasons, the vertex approach is not fit to describe our system with rotated elements. Although a temperature can be defined that describes dipolar energy, we could not ascribe a temperature to the vertex populations. Using Monte Carlo simulations and its spin Hamiltonian in an all-interactions approach, we have established the phase diagram of our tilted system. Consistent with literature. it has confirmed that the rotation changes the transition from antiferromagnetic-paramagnetic to ferromagnetic-paramagnetic phase. The phase diagram has shown the transition temperature changes with rotation angle due to the induced modification of the dipolar couplings.
We have compared the total energy of our experimental system with energies determined by Monte Carlo simulations at different temperature values. We have shown that a unique effective temperature describes all the tilted arrays of our system in both energies and vertex populations. The consequences of these observations are twofold. First, it means that our as-grown system is representative of thermodynamics at equilibrium because depicted by Monte Carlo simulations. Secondly, it would imply that the tuning of the interactions by rotation of the elements do not affect the thermodynamics of the system. This is not necessarily the case for other tuning for the interactions for instance lattice spacing [56,62].

3.5. Conclusion

We have chosen to tune the interactions of the original square ice by rotating its islands around their central point. Dipolar computations have shown that this modification of the square changes the couplings and the ground state from Type1 to Type2 vertex. While computing the energy of an array, we have seen that for the extreme rotation of the system, interaction between first-nearest neighbour becomes null, hence the choice of an all-interactions approach. It has revealed,, with the exploring of various ordered spin configuration, that the system is expected to undergo a transition from antiferromagnetic to ferromagnetic order. The latter is a specific arrangement of Type2 vertices.
Our ambition was to observe experimentally this transition. We chose to work with two samples: an as-grown –famous for reaching extremely low energy-state- and a field-demagnetized one –used since the very introduction of artificial spin ice but less efficient to reach low-energy state. We have studied both their vertex arrangements and populations and their total dipolar energy. From the observations made, we concluded that the as-grown state was the lowest-energy state thus the best candidate to observe the expected ground state evolution. We have seen that the as-grown was in an unambiguous antiferromagnetic state for the low-rotation angles. However, for higher rotation angles, we have observed that its ground state is not as clear. Although a majority of vertex type had been identified suggesting a specific order, we have seen that total energy is higher than both antiferromagnetic and ferromagnetic ideal orders. With vertices, we have seen that it was the result of arrangement in domains and a high proportion of Type3 vertices in their populations. The observations made, in need of description of disorder, were completed with magnetic structure factor. By comparing the experiments to reference orderings, we have concluded that our tuned system evolves from antiferromagnetic to ferromagnetic order. The transition is characterised by a coexistence of both orders.

The next step was the study of the thermodynamics of the system. We have shown that the 16-vertex model and the mean-field approximation it relies on could not describe the observables that are energy and vertex population. We then worked with Monte Carlo simulations to ascribe an effective temperature to our experimental system. The energy-based effective temperature has shown that our system evolves from antiferromagnetic to paramagnetic phase with increasing rotation angle. This result emphasised that we have bring our system at the thermodynamic equilibrium and that the tuning of our interactions is robust.

This study has proven that the rotation of the elements is a robust method to probe in or out-of equilibrium thermodynamics with the description of its energy and vertex populations by Monte Carlo simulations.

This work has been the result of a scientific publication [70] which was elaborated more or the less simultaneously with the papers mentioned previously. At the very same time of its publication, Macauley *et al.* [71] have published a very similar work also studying the rotation of the elements. Using thin thermally annealed Co arrays, they have shown the phase transition from antiferromagnetic to ferromagnetic order and also for rotation angles in between, a competition between phases.

Chapter 4. Domain wall propagation in an artificial spin system

"Because a magnetic Galton board is cute"
J. Grollier

In this chapter, we will present our study of an artificial spin system for applications of random number generation. The first part of this work focuses on the development of our artificial spin system in which we justify our choice for the connected geometry on small structures and study larger connected structures. This development will lead to an optimisation that exhibits mainly avalanche propagations throughout the structure. We will perform a thorough study of the domain wall propagation in terms of reversals and fields leading to the identification of the main propagation scenarios. Our system will then be compared to the Galton board and we will show that a mean value describes the system and no correlation between successive choices exists demonstrating that our system is magnetic nanoscale Galton board.

4.1. Motivations

Artificial spin ice systems have proven to be a fascinating playground for collective behaviour tuneable by geometry -as shown in the previous chapter- but also using magnetic field or spin torques. This flexibility has sparked applications for novel computation applications such as reservoir computing [23] or Hopfield networks [24] reported so far. The work we present here falls within this framework demonstrating that artificial spin systems can be tailored for applications of stochastic logic. In order to elaborate such a device, we rely on the properties of artificial spin ice in honeycomb lattice and the reversals induced by an external field.

Artificial spin ice in honeycomb lattice –where spins are located according to a kagomé arrangement- was first introduced as a remedy to the inequivalent interactions of the four-island vertex in square ice - between perpendicular and colinear spin pairs as shown in the previous chapter. Indeed, in this geometry the interactions into play at each vertex are equivalent yielding a highly degenerate ground state. A schematic of the geometry and the $2^3 = 8$ possible vertex configurations are shown in Fig.4-1.a) and b) respectively.

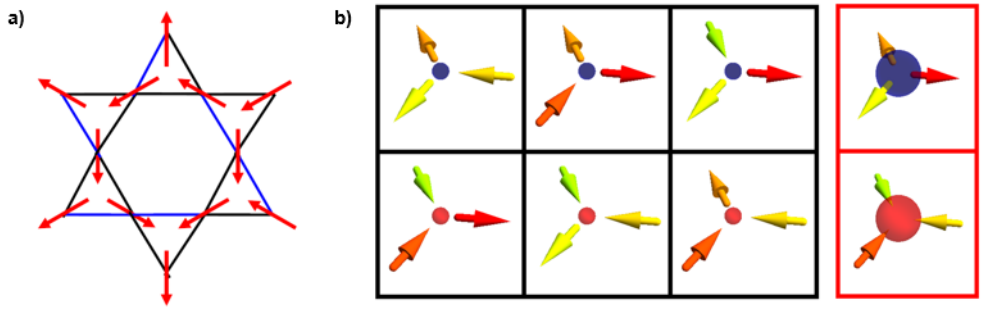

Fig.4-1: a) The honeycomb or kagomé lattice and b) the 8 possible configurations, 6 low-energy states with the spins arranged in 2-out/1-in and 2-in/1-out configurations (framed in black) and 2 high-energy states arranged in 3-out and 3-in configurations (framed in red).

Among the eight possible vertex configurations, there are six degenerate low-energy 2-in(out)/1-out(in) configurations and two degenerate high-energy 3-in(out) configurations. The low-energy configurations follow the *quasi*-ice rules, a translation of the 2-in/2-out ice rules configurations of the square lattice. The highly degenerate ground state configurations of the honeycomb lattice could find applications in logic computation and random number generation.

Two investigative methods have been considered to study these complex spin configurations: "low-energy" or "nearly equilibrium" configurations -similar to the approach of the previous chapter- and "out of equilibrium" configurations by controlling the reversal of elements. The second approach has been achieved by external field and other local modifications. We show in Fig.4-2, the most iconic results on reversals in honeycomb artificial spin systems for the study of magnetic monopoles from Refs. [16,17].

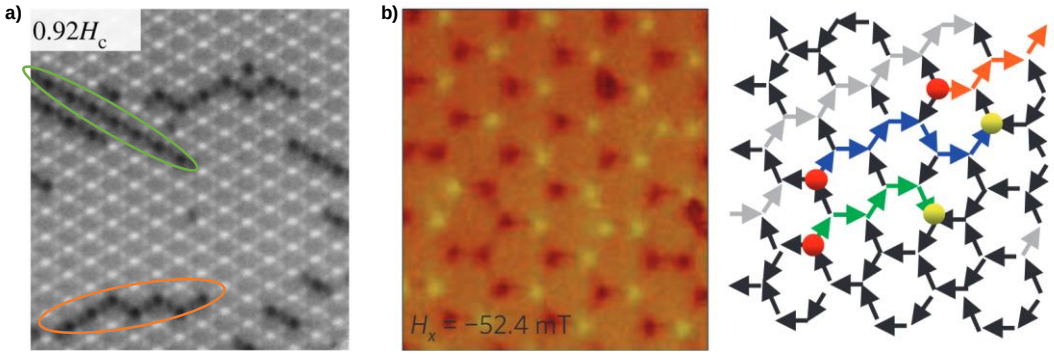

Fig.4-2: a) Adapted from Ref. [16], observation of Dirac strings in disconnected honeycomb artificial spin ice system under applied field, circled in green a unidirectional chain of reversals and in orange a chain of reversals with apparent stochastic choices and b) from Ref. [17], similar observation of connected systems.

This kind of reversasl has been studied in both disconnected systems [16,63,72,73], isolated nanoislands coupled by dipolar interaction, and connected systems [17,74–76], exchange coupled continuous material in which reversal is mediated by domain wall propagation. Despite their intrinsic difference, the two systems seem to share a common feature: the reversals occur mainly by unidimensional propagation. Reversals observed form chains (*c.f.* spin configurations in Fig.4-2.b)) without branching nor "backward" propagations (as will be defined in section 4.4.3), however several aspects have proven to be of importance. The first one is disorder either in the dispersion between the magnetic properties of individual elements or in specific nucleation and pinning sites for connected elements [77]. Another is

the coupling between isolated elements [73], systems with low coupling exhibit different reversal behaviour. One can add to the list the field alignment [75,77–80] and the geometry of the connected elements [34].
Of particular importance is the direction of the unidimensional propagation that is considering a vertex with one reversed element, which element will reverse next? If the first reversed element is oblique to the field (spins 2 or 3 in Fig.4-3.a)), the propagation will continue with the reversal of the element parallel to the field (spin 1). However, if spin 1 is reversed first, spins 2 or 3 can equivalently reverse raising the question which spin will then reverse? This question is rather open and is at the heart of the present work.

In the case of disconnected systems, the degeneracy between the two equivalent elements can be lifted by long range dipolar interactions leading to a deterministic propagation. More prosaically, any misalignment in the applied field would lift the degeneracy resulting in unidirectional propagation (example circled in green on Fig.4-2.a)). Local variations among the elements like magnetic properties or shape, could also lift the degeneracy. Theses variations can induce apparently stochastic propagations as in the orange example. This stochasticity is not intrinsic as it is linked to spatial inhomogeneity (and would be reproducible from switching to switching). But more complex magnetic configurations, like chirality of monopole, could also lift the degeneracy and induce stochastic propagation.
In the case of the connected systems, the physics is quite different as the degeneracy is lifted by the internal degrees of freedom of the propagating domain wall. Reported numerical and experimental studies have correlated the nature of the domain wall and the direction of propagation in simple systems with Y shape [18,76,81,82]. Concerning the propagation in a honeycomb lattice, in a simple picture of a constant domain wall nature, a unidirectional propagation is expected. However if the nature of the domain wall varies during its propagation due to defects or more intrinsically to Walker breakdown, the direction of propagation is expected to be stochastic.

Our ambition is to exploit the stochastic reversals with a control on the starting point of the propagation in a honeycomb artificial spin system. We emphasise that this work is a first exploration and characterisation, no computation was performed. We wish for the control of the first reversal as an input therefore, any other nucleations are not desirable and considered as parasitic. We will show that a fine optimisation of honeycomb-based artificial spin system, using as injection an elliptic nucleation pad to reverse the first element, leads to robust stochastic behaviour.
This work is divided in two parts: the elaboration of the artificial spin system and the characterisation of avalanche mechanisms of the optimised structure. In the first part, we explore the possible geometries (disconnected/connected and various connected shapes) that our experiments proved to be stochastic. We keep in mind to observe the propagation of our willingly injected domain wall for the first reversal and no other parasitic nucleations. This study will lead to the introduction of an optimised connected structure in which the reversals observed are induced by the domain wall injected by the pad. The second part will be focused on the stochastic behaviour of our system. We will show that its behaviour is very similar to the one of a nanoscale Galton board by extracting specific parameters such as weights to go left/right. A special interest will be taken in studying the correlation between successive choices. We will also show that this behaviour is robust at low temperature.

4.2. Preamble: stochastic and avalanche behaviour, experiment and injection

In this work, our goal is to develop a honeycomb artificial spin ice system, this is a novel approach to which several concepts need definition. In this section, we will explain where stochastic choice lies in

the honeycomb geometry and the unidimensional/avalanche scenarios we aim to get experimentally. We will also explain the experiment protocol and how we have chosen to induce the first reversal.

4.2.1. Stochastic choices and avalanche scenarios

Stochastic choices can be expected in the honeycomb geometry at each of its vertices. We explain our point with the spin configuration of one vertex shown in Fig.4-3.

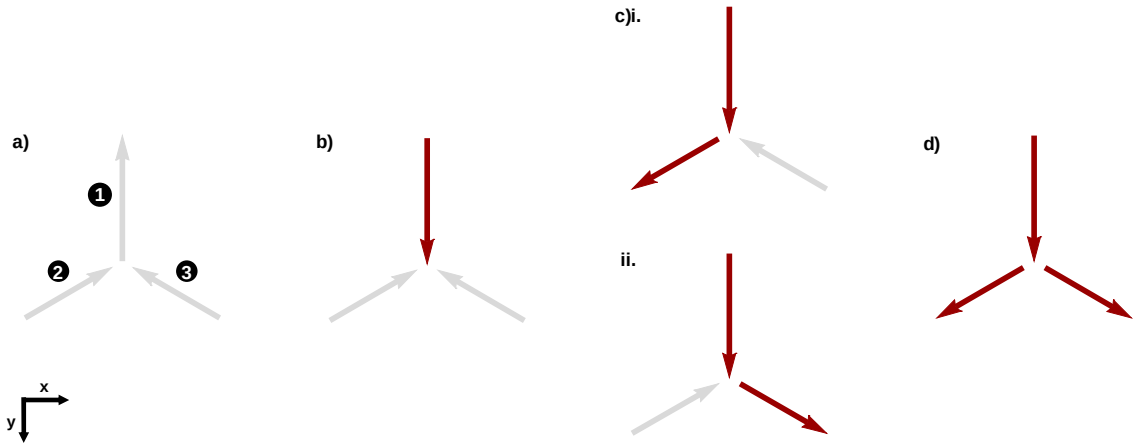

Fig.4-3: a) 3-spin vertex arbitrarily taken pointing upwards; b) injection of a domain wall with the pad into the element it is connected to (here spin labelled 1); c)i. and ii. the two possible paths of reversals and d) the reversal of the remaining element. One could also imagine reversing both elements simultaneously thus going from b) to d) without either of the c) configurations.

Starting from a configuration where all spins point in one direction (Fig.4-3.a) arbitrarily taken in the (-y direction), one can modify the spin configuration by applying a field along one of the three spins. If a field is then applied along the +y direction, spin 1 (as labelled in Fig.4-3.a)) reverses resulting in all spins pointing towards the vertex (Fig.4-3.b)). The vertex, in 3-in configuration, is in a high-energy state, in order to lower its energy, the system will tend to change its configuration with one respecting the *quasi*-ice rules (with a 2in(out)/1out(in) configuration). Taking into account that the direction of the applied field, two choices are offered: either reversing spin 2 or spin 3 (Fig.4-3.c)i. and ii.). In an ideal system, the choice between the two is *a priori* equivalent hence a 50%/50% chance to choose either side.
We mention that reversing both spins 2 and 3 yielding a 2-out/1-in vertex configuration (Fig.4-3.d)) would also lower the energy. For our work, this branching propagation scenario is not desired. In this chapter, we define a unidimensional propagation as reversal of spins with strictly increasing ordinate (+y in Fig.4-3)

In a honeycomb system, stochasticity lies in the shape of its vertices, so on larger systems, successive choices are expected. We take as an example the structure that will be studied experimentally in section 4.3.1.2 with a total of six vertices presented in Fig.4-4.a).

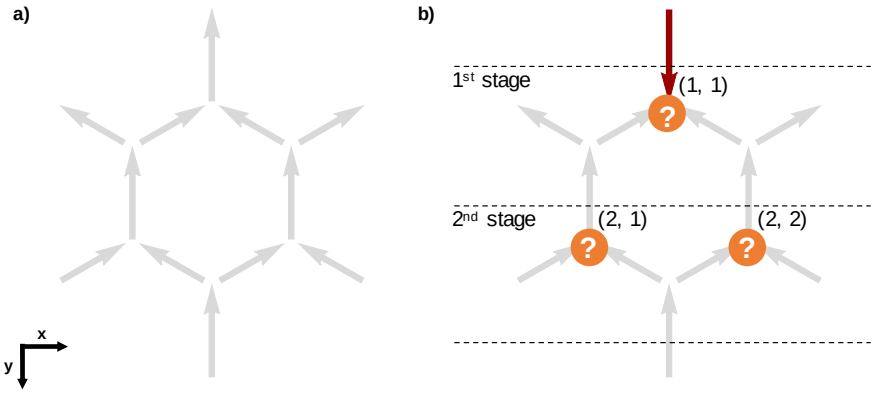

Fig.4-4: a) Spin configuration at saturation of a 2-stage structure and b) identification of the intersections (marked as '?') and their indexing.

Similarly to our previous example, we take as starting configuration the saturated one along the negative y direction (Fig.4-4.a)). This preparation of the magnetic configuration is essential for larger structures, this way the ice rules are obeyed with alternating positive and negative magnetic charges at the vertices (as shown on the MFM image in Fig.4-9.b)). Applying the field in the positive y direction, we take the first reversal to be the red spin in Fig.4-4.b) creating a high-energy state in the vertex labelled (1, 1). The situation at this vertex is similar to what was explained before: there is a choice to make, reverse the left or right spin. When it is realised, the reversals have made through -what we refer to as- the 1st stage arriving to either vertex (2, 1) or (2, 2) of the 2nd stage (Fig.4-4.b)). Therefore, in a unidimensional scenario or what we will also refer to as avalanche- or chain-like scenario, this 2-stage structure offers 4 possible paths shown in Fig.4-5.

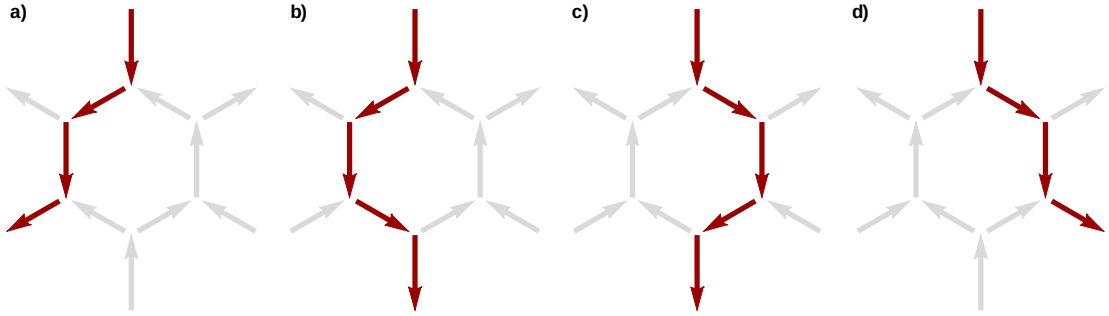

Fig.4-5: The four possible avalanche-like reversals in a 2-stage structure: a) left choices at (1, 1) and (2, 1) vertices; b) left and right choices: c) right and left at (1, 1) and (2, 2) vertices respectively and d) right and right.

In an ideal system, with 50% to go left or right at the vertices or intersections (marked as '?' in Fig.4-4.b)), each path is likely to be observed following a binomial distribution. Obviously, in a less perfect system, one could imagine other propagation scenarios but the ones presented in Fig.4-5 are the avalanche scenarios we would like our system to tend to.

Our approach is the same for 7-stage structure, shown as an example in Fig.4-6.

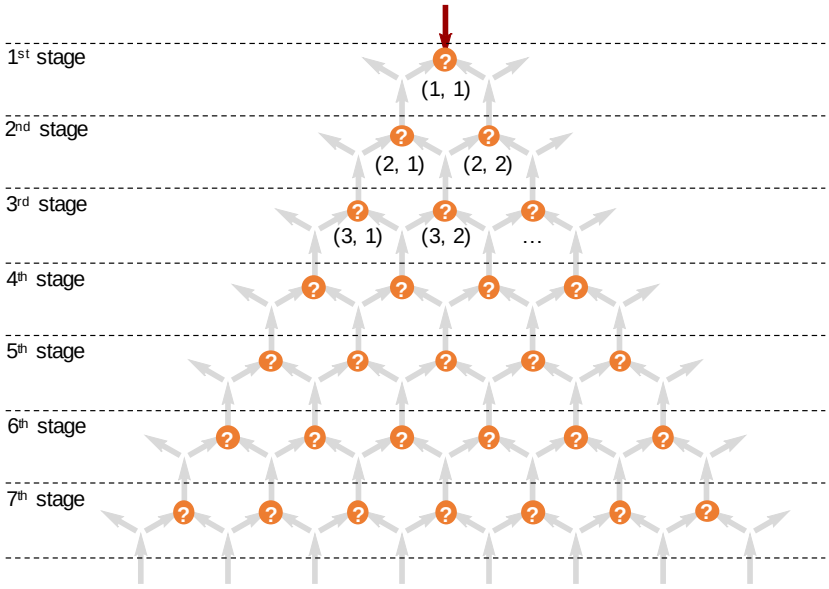

Fig.4-6: Schematics of our 7-stage structures, what we refer to as stages and identification of the intersections (marked as '?') and their indexing.

In what we have defined as avalanche scenario, with an equal probability to go left or right at the intersections, there are 128 possible paths. We show in Fig.4-7 two possible propagation scenarios that we refer to as avalanche with random choices and unidirectional propagation respectively.

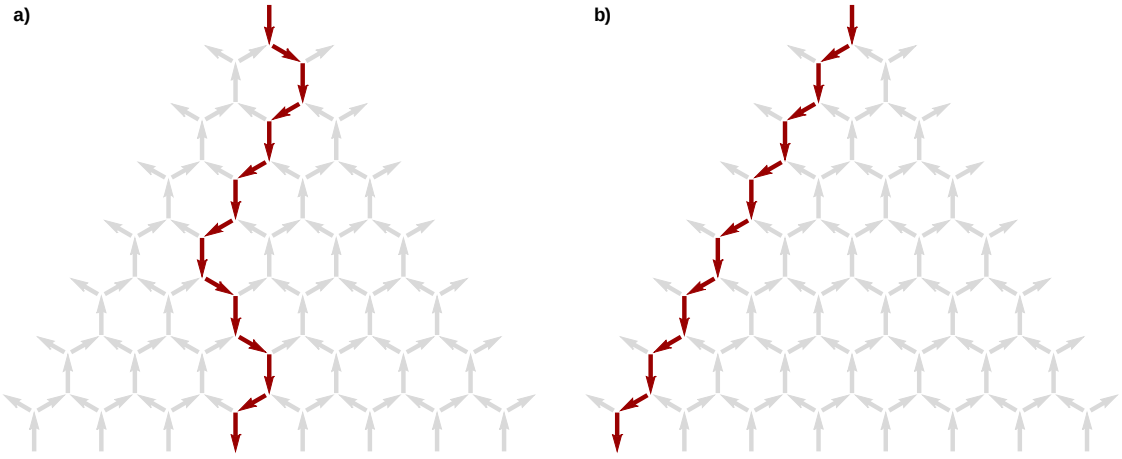

*Fig.4-7: **Examples** of a) avalanche or chain-like reversals with random choices at each intersection and b) unidirectional propagation with same choice made at each intersection.*

4.2.2. Field experiment and control of first reversal

In order to observe the reversals under applied field in our artificial spin systems, we use a field protocol explained in chapter Chapter 2 (shown again in Fig.4-8), similar to the ones used for the observation of magnetic monopoles [63,72,74]. We first saturate the sample by applying +1000 Oe along one of the sublattices of the system yielding spins along the defined direction. Then we apply a field in the opposite

direction (typically –200 Oe) and increment in steps of –12 Oe (±12 Oe), all images are acquired at remanence.

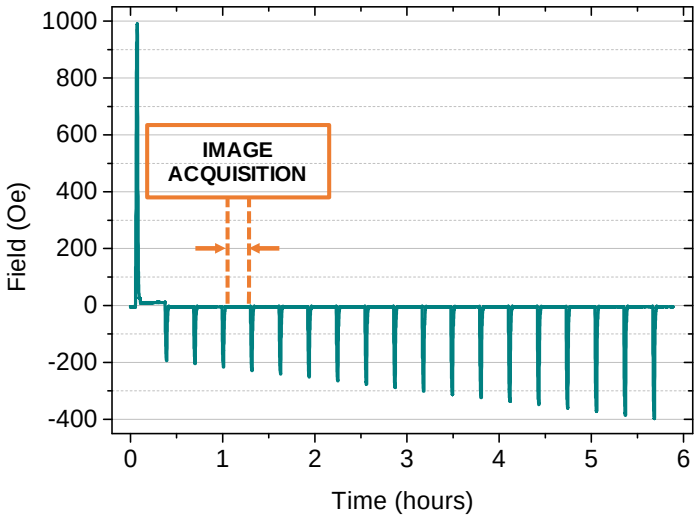

Fig.4-8: Field protocol of our experiments: first saturation by applying + 1000 Oe (±10 Oe), then starting at –200 Oe, the field is decreased in steps of 12 Oe (±2 Oe). Rise and fall times are of the order of the seconds.

For the magnetic characterisation of our artificial spin systems, we have performed the same field protocol on all our various structures and given great care to stay as much as possible in the same experimental conditions. We have identified two possible sources of variability specific to the setup of our magnetic force microscope: the field alignment and the field amplitude. On one hand, we do not have a fine control of the field alignment with our sample, our error being estimated to ±0.5° as explained in section 2.2.1. In the experiments presented, we consider that whenever removing the sample, the field alignment is different. On the other hand, the field strength is specific to the field protocol performed. Whenever relevant, we mention if the results shown have been acquired during a single field protocol or acquisition. However, we consider that any variation between them has no effect on the underlying phenomena of the observed reversals, the error on the field being set to a low value (±2 Oe).
In order to make sure that experiments on various structures are comparable thus with same field alignment, we perform -whenever possible- the acquisition on several structures simultaneously (as shown in Fig.4-9). This approach has the advantage of studying the variability from one structure to the other.

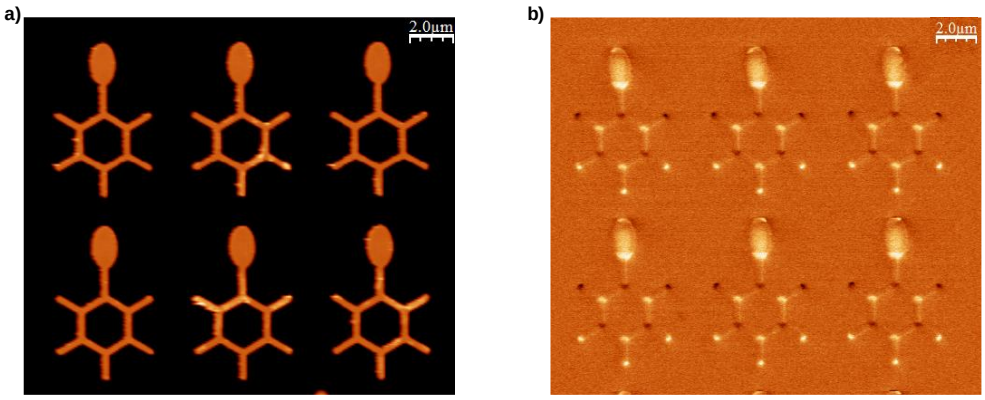

Fig.4-9: a) AFM image and b) MFM image (at saturation) of an acquisition performed simultaneously on six 2-stage connected structures.

We now move on to our method for the control of the first reversal. Reported works [16,18,19] have let the system nucleate domain walls by itself under external applied field. Nucleations started from the edges of the networks since nucleation field is lower there compared to the ones in the bulk array. Other works have presented control the nucleation locations with pads [74]. It has also been shown that the injected domain wall nature can be controlled with specific shapes acting as chirality filters [83] such as hook structure to inject a transverse domain wall [76], circular pad with longitudinal nanowire injecting a vortex anticlockwise or clockwise according to the applied field direction [34]. Propagations starting inside the bulk array have also been shown using a gold stripline to apply locally a magnetic field [84] and writing defect a high moment tip MFM [85]. More recently, control with strain-mediated multiferroic approach has been demonstrated [86].
In this work, we chose to inject a domain wall with an elliptic pad connected to an edge element to start the reversals as shown in our structures in Fig.4-9.

4.3. Development of an artificial spin system with stochastic behaviour

The goal of this section is to explain our optimisation of our honeycomb artificial spin system. In order for our device to undergo reversals due to a domain wall injected at a specified location, a few questions needed to be answered. The very first one concerns the choice of connected geometry over the disconnected one which will be explained in the first section on small structures. Then, we will show the issues to overcome specific of larger nanostructures.

4.3.1. Disconnected *vs.* connected structures

In disconnected honeycomb artificial spin ice, reversals are due to dipolar coupling whereas in connected geometries it is the result of domain wall propagation. Here, we demonstrate the stochastic behaviour of 1-stage structures for both geometries. We will justify our choice of the connected geometry for optimisation of wider structures with the study of 2-stage structures.

4.3.1.1. 1-stage structures

We first study the smallest structure with a unique vertex as in Fig.4-3 -that has one spin connected to the elliptic nucleation pad. We will show that both disconnected and connected geometries exhibit stochastic behaviour.

4.3.1.1.1. Disconnected structures

We first study experimentally 1-stage disconnected structures. The elements of the structure are 200 nm-wide, elements 2 and 3 as labelled in Fig.4-3.a) are 1.0 µm-long, the upper element labelled 1 in Fig.4-3.a), is 1.6 µm-long connected to the pad that whose short radius is 0.5 µm and large radius is 0.9 µm. A SEM image along with the dimensions are shown in Fig.4-10. The samples were fabricated using a lift-off process as detailed in section 2.1.1, the magnetic material deposited is 20 nm-thick Permalloy.

a)

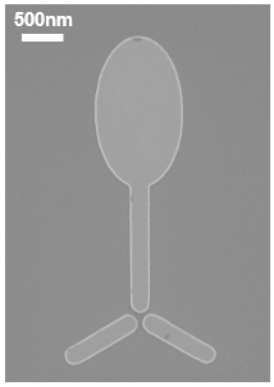

b)

	Width	Length
Ellipse	0.5µm	0.9µm
Vertical bar	0.2µm	1.6µm
Bars		1.0µm

Fig.4-10: a) SEM image of 1-stage disconnected structure with 20 nm-thick Permalloy; b) dimensions of the elements. The half diameters are given for the nucleation pad. The vertical bar length is taken from the edge of the pad to the end of the element.

We probe the reversals by MFM using the contrasts at the ends of the elements from which we deduce the spin configuration. We perform our field protocol on a few structures starting at –200 Oe with images are acquired at remanence (as in Fig.4-8). We start our study by presenting reversals of three different structures of one sample with same experimental conditions of field alignment acquired during the same field protocol. The first one is presented in Fig.4-11.

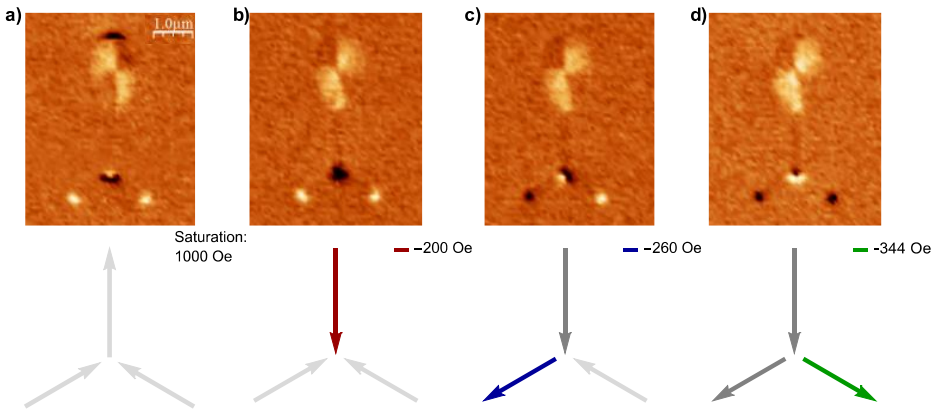

Fig.4-11: Reversals on a 1-stage disconnected structure with a left choice at the intersection: a) saturation of the system with +1000 Oe magnetic field in the upward direction; b) applying –200 Oe, observation of the reversal of the element connected the nucleation pad, coloured in red; c) applying –260 Oe, reversal of the left element of the vertex coloured in blue and d) applying –344 Oe, reversal of the last element coloured in green. Same colour code used for all this chapter. Spins in darker grey have reversed at lower fields.

After applying + 1000 Oe, all spins lie along the direction of the field, arbitrarily taken upwards, yielding a 2-in/1-out vertex configuration respecting the ice rules. When reversing the field at –200 Oe, a high-energy state with a vertex of 3-in configuration is observed. Applying a field of –260 Oe in the same direction, results in the reversal of the left spin of the intersection. The right spin, still in its initial orientation, reverses at –344 Oe. The presented structure follows one of the three expected scenarios in an avalanche behaviour with the reversal of the left element.

The other two possible scenarios have also been observed on two other structures, experiments are shown in Fig.4-12.

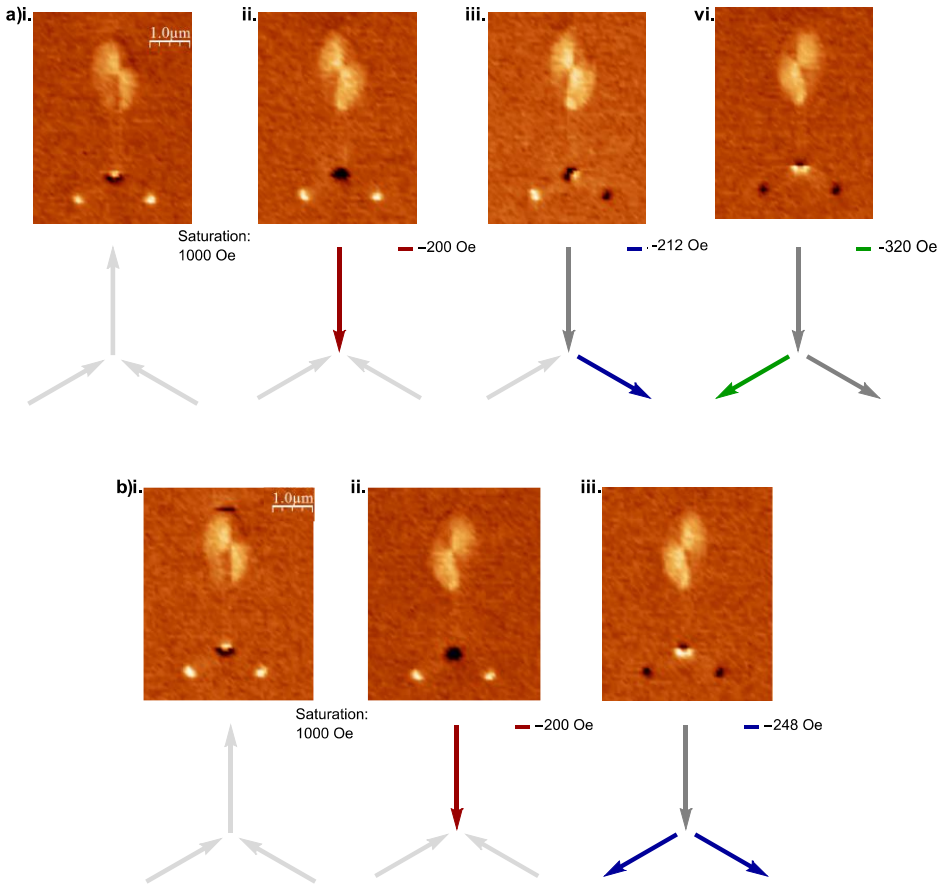

Fig.4-12: a) Reversals on a 1-stage disconnected structure with right choice at the intersection: i. saturation at +1000 Oe; ii. in red, first reversal observed at –200 Oe, element connected to the nucleation pad; iii. in blue, second reversal observed at –212 Oe, right element of the vertex; iv. in green, last reversal observed at –320 Oe, left element of the vertex and b) Reversals on another 1-stage disconnected structure exhibiting branching scenario: i. saturation at +1000 Oe; ii. in red, first reversal at –200 Oe, element connected to the pad; iii. in blue, last reversals at –248 Oe, both left and right elements of the intersection. Same colour code as before. Spins in darker grey have reversed at lower fields.

On another structure during the same acquisition or field protocol, we have observed an avalanche scenario with the reversal of the right element of the intersection (Fig.4-12.a)). The domain wall injection and propagation occurred at –200 Oe ,the reversal of the first element of the intersection at –212 Oe and the system saturated at –320 Oe. On a third structure always in the same acquisition, we observed the last expected scenario with reversals suggesting branching. Injection and propagation of the domain wall was observed at –200 Oe and the reversals of both elements of the intersection occurred at –248 Oe. We remark upon the contrasts observed in the pad forming vortices of different chiralities (Fig.4-11 and Fig.4-12). This is explained by the observation performed at remanence but it is also not always the case as we will show later (Fig.4-16). We have not studied further this behaviour.

Only the three experiments presented before prove that the behaviour under the same experimental conditions varies for different nanostructures. However this variability between structures could be viewed not as surprise as one could suspect different fabrication fluctuations (lithographic and deposition) on the considered structures. Now we study the behaviour of one structure if the experiment is performed several times in the same conditions. Results of a single structure -on a different sample- for 15 field experiments are summarised in Fig.4-13. Reversals are shown using trees whose colour are according how many times they have reversed. We divide them according to the changes in spin configurations as we have already done in Fig.4-11 and Fig.4-12 with the red, blue and green colours. We will now refer to the modifications of spin configuration as events. We have chosen this approach

because we have observed that similar modifications in the spin configuration (injection, reversal of one or both lower vertex elements, …) can occur at different field values depending on the experiment even within an acquisition. In order to emphasise these events, we keep the same colour introduced, red for the first spin reversal(s), blue for the second and green for the third one for both spin configurations and reversal fields.

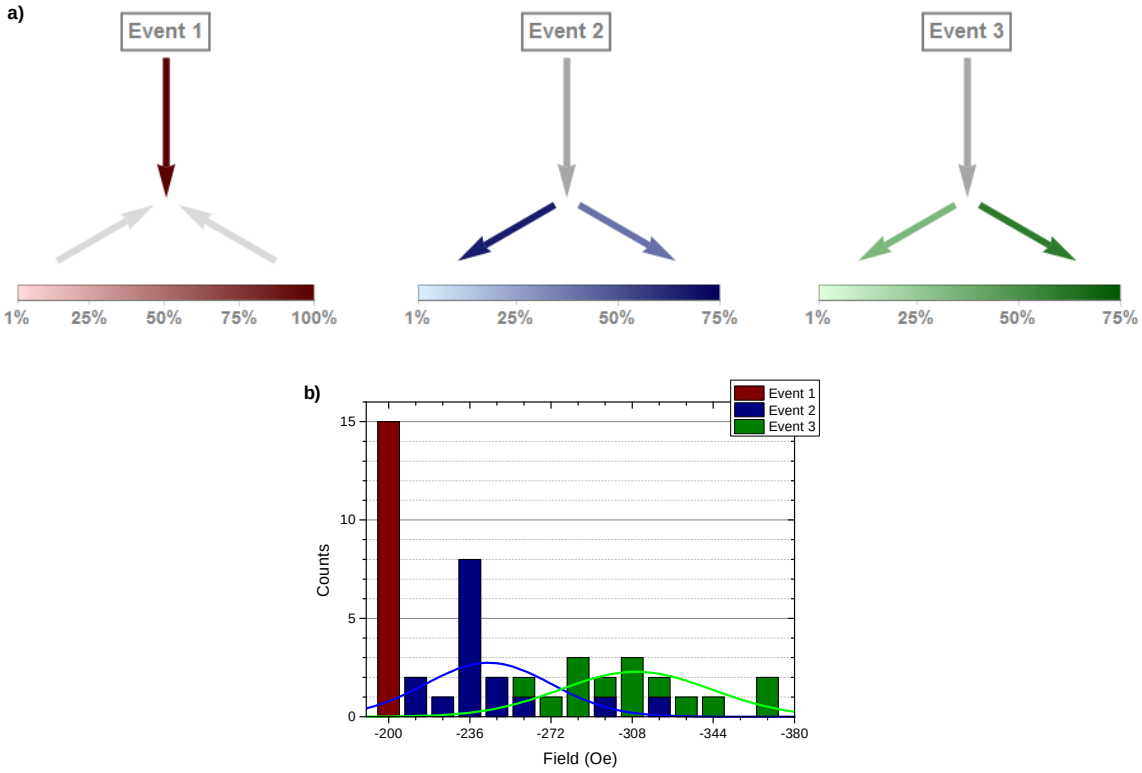

Fig.4-13: a) Observed reversals summarised in tree form on a single 1-stage disconnected structure for15 identical experiments with no regard of the propagation scenario, event 1: element connected to the pad has reversed first in all experiments, event 2: the next reversals observed are either the left or right elements of the vertex in 60% and 47% of the experiments respectively, event 3: last reversals are either left or right elements of the vertex, in 40% and 53% of the experiments respectively; when coloured in darker grey and reversed, the spins have reversed in one of the previous events in all experiments; b) counts of the reversals at each field step identified by their event.

Out of 15 field protocols performed, the first change in spin configuration is always the reversal of the element connected to the nucleation pad (Fig.4-13, Event 1). The second change in spin configuration (Fig.4-13, Event 2) is either the left or right element of the vertex: in eight experiments, we have observed exclusively the reversal of the left element, in six experiments exclusively the right element and in one experiment both left and right element at the same field step. In the blue colour scale, it translates in 60% and 47% proportions for the left and right elements respectively. We mention that the sum of the two proportions is not equal to one because we observe an experiment with branching scenario[5]. The third and last modification in spin configuration (Fig.4-13, Event 3) is again either the reversal of the left or right element of the intersection: in six experiments, we observe the reversal of the left element and in eight experiments the reversal of the right one. In the green colour scale, these results translate in 40% and 53% proportions of reversal of the left and right elements respectively.

[5] We mention that the sum of proportions of reversal of each element on all events is equal to 1 here since reversals from saturation in one direction up to the other is studied. Therefore if one should look for the total equal to 1 it would adding the proportions on all events for each element. I would like to emphasise that it was my choice to process this way the data and to define our trees and proportions.

Presented results show unambiguously the stochastic behaviour of a single structure if the field protocol is performed several times in the same conditions. From the 14 chain-like experiments, we can extract the probability to reverse the left element being of 8/14 ≈ 57% and therefore the probability to reverse the right one 6/14 ≈ 43%. The error on this statistical weight to go left/right can be estimated at $\sqrt{0.5^2/15} \approx 13\%$ (overrated value with 0.5). Obviously, it could have been decreased if more experiments were performed.
Studying the fields at which the events occur, we find that the domain wall is injected below –200 Oe (Event 1 values in red in Fig.4-13.b)). We mention that no images were taken at lower fields therefore we cannot assert the actual injection and propagation fields. The reversals of the lower diagonal elements of the intersection occur between –212 Oe and –368 Oe at events 2 and 3, where we observe the second and third change in spin configuration (Event 2 and 3 values in blue and green in Fig.4-13.b)). We find that both field events overlap (with the Gaussian fits shown in Fig.4-13.b)) showing that the induced reversal of the first element of the intersection is very close to the field that saturates the array.

In this section, we have shown a variability between structures characterised in the same acquisition (Fig.4-11 and Fig.4-12). We have also demonstrated that a single structure observed several times exhibits various reversals (Fig.4-13). These results prove unambiguously the stochastic behaviour of our 1-stage disconnected structures although we cannot conclude about the source of randomness at this point.
One possible explanation of the stochastic choices made at the intersection is the argument of chirality of the forbidden state put forward by Rougemaille *et al.* [73]. Using numerical simulations, they have reported that trajectory is mediated by the chirality of the monopole at remanence: the element reversing would be the one whose magnetisation bending is aligned with applied field. In our samples, we also observed bending of the magnetisation at the ends of the elements as shown in Fig.4-14.

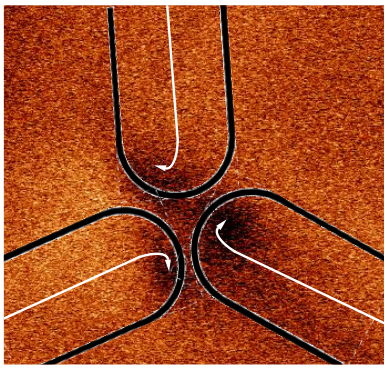

Fig.4-14: Experimental observation of the bending of magnetisation of the forbidden state.

In the experiment the monopole exhibits an anti-clockwise chirality and then the reversal of the right element whereas Ref. [73] predicts the reversal of left one. However, in this particular experiment (different that the others presented before) we suspect a large field misalignment probably biasing the result. We have not studied this behaviour in detail enough to be conclusive.

4.3.1.1.2. Connected structures

We perform the same characterisation on 1-stage connected structure where reversals are induced by domain wall propagation [36,87]. A SEM image and the dimensions of a typical structure are given in Fig.4-15.

a)

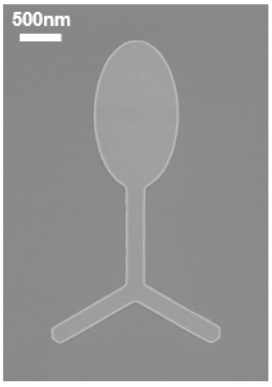

b)

	Width	Length
Ellipse	0.5µm	0.9µm
Vertical bar	0.2µm	1.3µm
Bars		1.2µm

Fig.4-15: a) SEM image of 1-stage connected structure with 20 nm-thick Permalloy; b) dimensions of the elements. The vertical bar length is taken from the edge of the pad to the centre of the vertex, diagonal bars lengths are taken from their "free" edge to the vertex centre.

We mention that the upper element is shorter than for the disconnected one but it is expected to be of little effect on the reversal mechanism. Same for the edges which, unlike our disconnected 1-stage structures, are not circular but triangular, shape added for the division of the patterning (*c.f.* designs for e-beam patterning in section 2.1.3.). Apart from that, dimensions are very similar to the 1-stage disconnected structures.

We proceed as we did for the disconnected one in order to see our 1-stage connected structures exhibit stochastic behaviour. We first determine if the behaviour varies from one structure to the other. As previously, the same field experiment on several structures and the two main scenarios have been identified. Experiments are shown in Fig.4-16, spin configurations are extracted using the method explained in section 2.2.2.2.

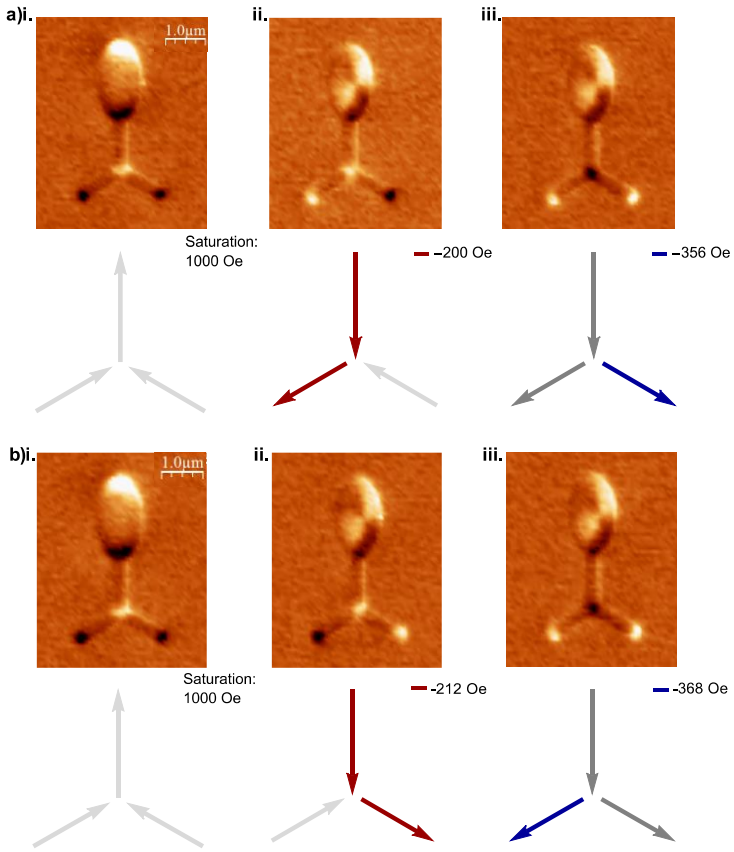

Fig.4-16: a) Reversals on a 1-stage connected structure with left choice at the intersection: i. saturation at +1000 Oe; ii. in red, first reversals observed at –200 Oe, element connected to the nucleation pad and left element of the intersection; iii. in blue, last reversal observed at –356 Oe, right element of the vertex and b) Reversals of another 1-stage connected structure with a right choice at the intersection: i. saturation at +1000 Oe; ii. in red, first reversals observed at –212 Oe, element connected to the nucleation pad and right element of the intersection; iii. in blue, last reversal observed at –368 Oe, left element of the vertex

The first experiment shows after saturation and application of –200 Oe reversal of the left element of the intersection. The system is then saturated at –356 Oe with the reversal of the right element of the intersection. The second experiment shows similar scenario only the reversal of the right element first at –212 Oe and the left one at –368 Oe. We remark that reversals take place in two steps with both upper and one diagonal elements at the low field and in a second step, the reversal of the remaining element at higher field. As for the disconnected geometry, the presented experiments show that the behaviour of the domain wall propagation is different on at least two structures in the same acquisition.

Now, we determine if the choices made at the intersection are stochastic if the same field experiment is performed more than once. Reversals observed on a single structure are summarised along with the fields at which events occur are shown in Fig.4-17.

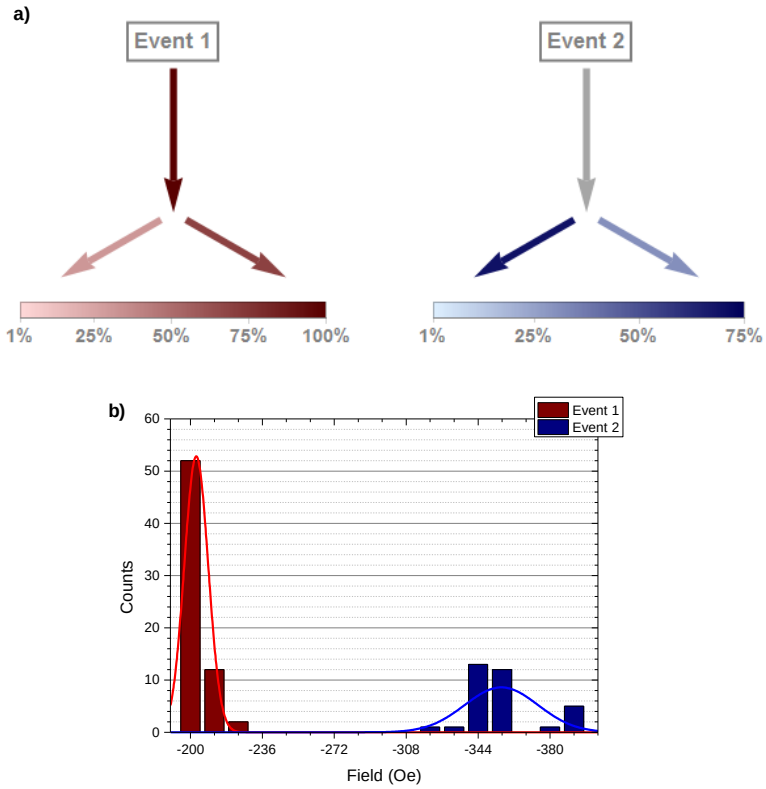

Fig.4-17: a) Observed reversals summarised in tree form on a single 1-stage disconnected structure for33 identical field protocols with no regard of the propagation scenario, event 1: element connected to the pad has reversed first in all experiments along with the left and right elements of the vertex in 30% and 70% of the experiments respectively, event 2: the next reversals observed are either the left or right elements of the vertex in 70% and 30% of the experiments respectively, when coloured in darker grey and reversed, the spins have reversed in one of the previous events in all experiments; b) counts of the reversals at each field step identified by their event.

We find that the first change in spin configuration (Event 1 in Fig.4-17.a)) is characterised by the reversal of the upper element along with one of the diagonal elements on all 33 experiments. The reversals of upper, left and right elements are observed in all, 10 and 23 experiments respectively. For the second and last change in spin configuration, we observed the reversal of the left and right elements in 23 and 10 experiments respectively (Event 2 in Fig.4-17.a)). As in the experiments shown in Fig.4-16, only two events allow to reach saturation. No branching scenario was observed in this experimental set. We also note that no high-energy state (3in(out) vertex configurations) was observed unlike reported work on Co samples [74].
Results show clear stochastic behaviour of the structure for the same field protocol performed 33 times. All of them are chain-like experiments and the probability to reverse the left element being of $10/33 \approx 30\%$ and therefore the probability to reverse the right one $23/33 \approx 70\%$ with an error is estimated at $\sqrt{0.5^2/33} \approx 9\%$.
With the study of field reversals (Fig.4-17.b)), we find that an applied field equal or lower than –224 Oe reverses the first two elements whereas the remaining spin requires an applied field of at least –320 Oe. A gap of 84 Oe separates the injection and propagation field distribution from the full saturation of the structure, thus no overlap between events 1 and 2 fields (see Gaussian fits on Fig.4-17.b)).

We have shown that there is a variability from one nanostructure to the other (Fig.4-16) but also within a unique structure (Fig.4-17). The connected geometry exhibits stochastic behaviour along with a large field gap between reversal of the first and the second element of the intersection. We emphasise that here we cannot assert that we are witnessing a propagation or the result of a nucleation from the edges

of the structure. A technique able to observe the dynamic of our system would be needed in order to know that our chain-like reversals are the result of a domain wall propagation. However, it seems reasonable to consider that the reversal of the first element of the intersection is the result of the domain propagation injected from the pad reversing the upper element.

Possible explanations of the source of randomness on the choice made by a domain wall at an intersection have been proposed in the literature. According to reported micromagnetic simulations [18,19,74,78,81,88], the choice at an interconnected vertex is mediated by the nature of the propagating domain wall. In the case of vortex domain walls, chirality determines the choice: vortex anticlockwise would go left whereas vortex clockwise right [19,81]. In the case of transverse domain walls, head-to-head up would go induce the reversal of the left element and head-to-head down right [18,82,84]. In our case, the stochasticity observed could be due either to the type of domain wall injected or to the propagation that somehow could be induce a source of randomness by evolution of the domain wall characteristic or position.

4.3.1.2. 2-stage structures

We have seen in the previous section that both geometries on 1-stage structures exhibit stochastic behaviour. Our goal here is to see if this behaviour is transposable when multiple choices are available. The specifications are the same: identify an avalanche from the pad and stochastic choices at intersections. We now present another set of experiments comparing 2-stage structures in both disconnected and connected geometries. SEM images of the typical 2-stage structures in Fig.4-18. Dimensions follow the ones presented in Fig.4-10 and Fig.4-15.

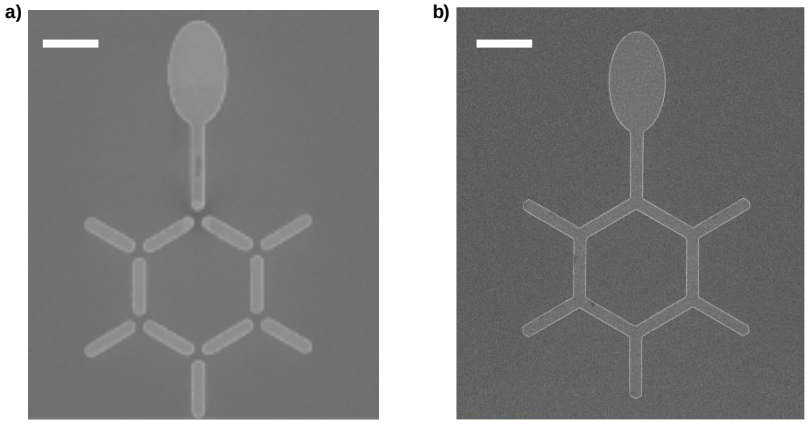

Fig.4-18: SEM images of a) 2-stage disconnected structures and b) 2-stage connected structures. Scale bars are 1um.

We perform the exact same field protocol as before: saturation at +1000 Oe, and then starting at –200 Oe field is decreased by steps of –12 Oe in order to see the steps in the reversal process. Images are acquired with MFM at remanence. Dedicated samples were fabricated and characterised for these designs.

4.3.1.2.1. Disconnected 2-stage structures

We present here our characterisation of 2-stage disconnected structures (Fig.4-18.a)). In this experimental set, we have observed simultaneously two structures on a single sample. Example of observed spin configurations for the structures are given in Fig.4-19.

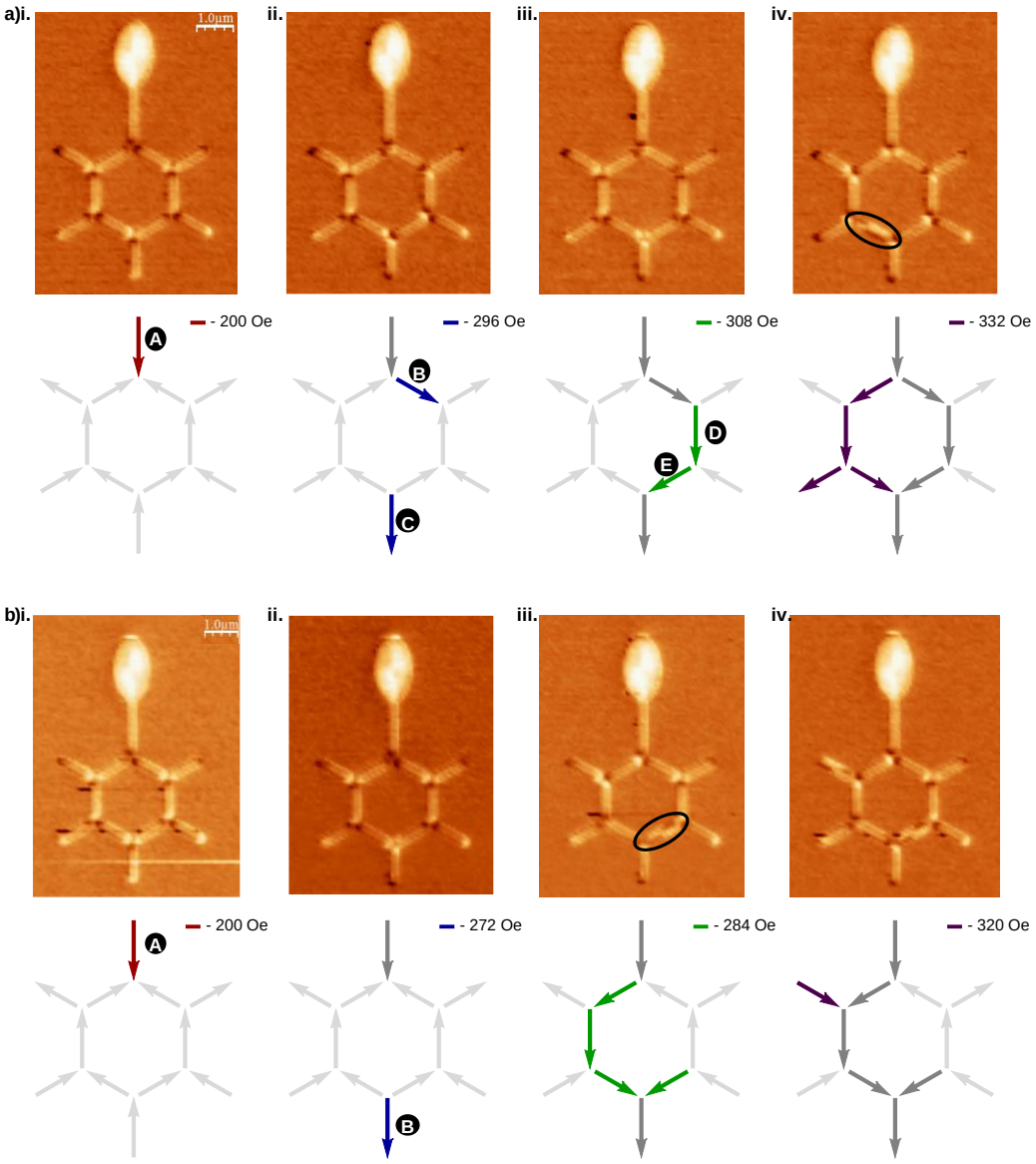

Fig.4-19: a) Reversals on a 2-stage disconnected structure: i. in red, first reversal observed at –200 Oe, element connected to the nucleation pad, labelled A; ii. in blue, next reversals observed at –296 Oe of spins labelled B and C; iii. in green, next reversals observed at –308 Oe, spins labelled D and E; iv. in purple, following reversals of left-sided spins and b) Reversals on another 2-stage disconnected structure: i. in red, first reversal observed at –200 Oe, element connected to the nucleation pad, labelled A; ii. in blue, next reversal observed at –272 Oe of spin labelled B; iii. in green, next reversals observed at –384 Oe, four spins located between spins A and B; iv. in purple, reversal of upper left spin of the first stage. Here saturation is not shown. Only first four spin changes are shown.

In the first experiment, the domain injection and propagation though the element connected to the pad (labelled spin A in Fig.4-19.a)i.) is observed when –200 Oe is applied. Then when applying –296 Oe, the right element of the intersection (spin B) along with the lowest element reverse (spin C). Adding one field increment, applying –308 Oe, elements vertical and on its lower left side return (D and E). The structure has most of its elements reversed at –332 Oe. Here we conclude that at the same field we observe reversal by coupling of one element of the intersection and nucleation on the low part of the structure. The next reversals, very close in field, somehow make them join. This experiment suggests the absence of avalanche behaviour due to, most-likely, a nucleation at the end of the system.

In the second experiment shown, another structure observed in the same conditions (same field alignment) during another acquisition, we observe similar features. The injection and propagation of the domain wall from the pad is observed at –200 Oe. Then at –272 Oe (spin A in Fig.4-19.b)i.), we observe low vertical element reversing (spin B). When applying –284 Oe, most of the elements are reversed on the left side of the structure but not following chain-like reversals. The next reversal is observed at –320 Oe with the upper left side element, located next to the spins reversed at the previous event.
We mention that we observe reversals through multi-domains (circled in MFM images in Fig.4-19.a)iv., b).iii. and iv.) at fields higher than the ones of the first reversals. We do not explain this feature.
Using both examples, we conclude that the issues of the design are the reversal of the lower free element (spin B) most likely induced by domain wall nucleation along with the absence of avalanche behaviour.

We now present the characterisation of a single disconnected 2-stage structure shown in Fig.4-19.a) and its behaviour over 11 field experiments. Results are summarised in tree form along with the event fields in Fig.4-20. Only four events out of the eight in total are considered for simplicity purposes.

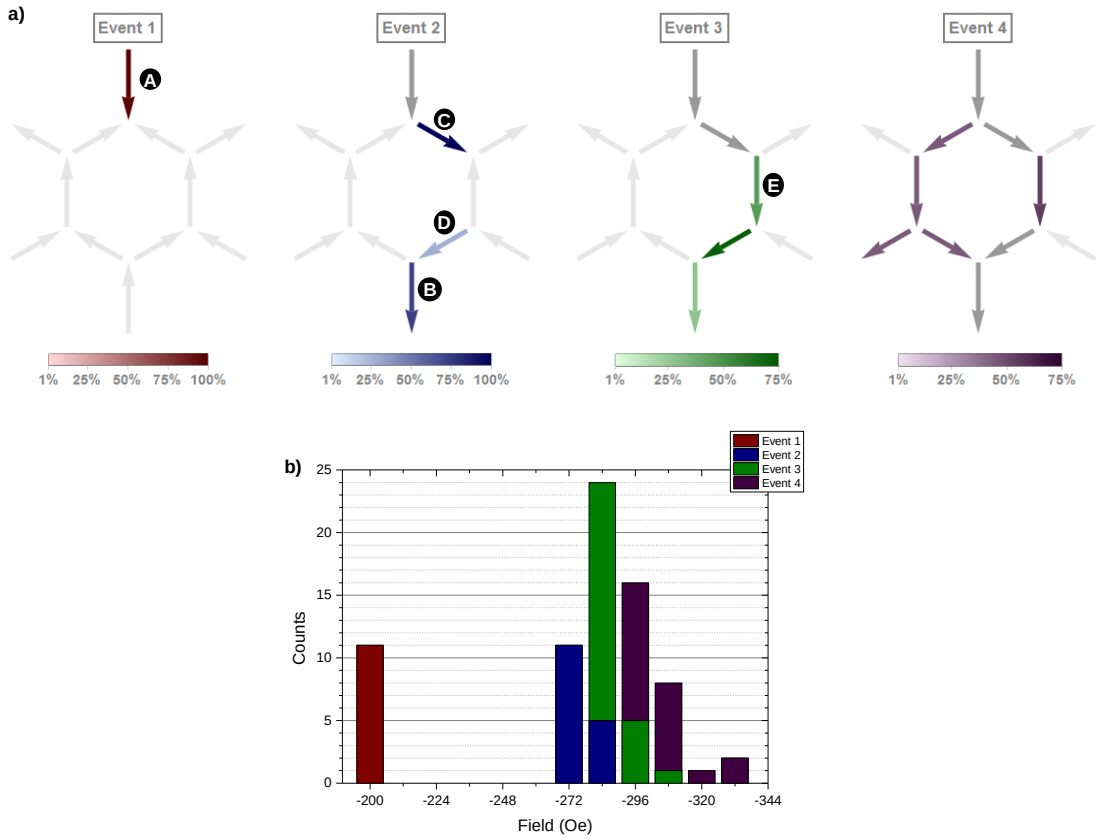

Fig.4-20: a) Observed reversals summarised in tree form on 11 identical experiments on a 2-stage disconnected structure, event 1; b) the fields at which reversals occur. When coloured in darker grey and reversed, the spins have reversed in one of the previous events in all experiments. Only first four events are considered.

First, we observe the reversal of the element connected to the pad (labelled A in Fig.4-20.a)) at or below –200 Oe (Fig.4-20.b)). The next modification in spin configuration is characterised by three features: the reversal of the lowest spin (labelled B) in 72% of the experiments, the systematic reversal of one element of the first intersection (identified as C); and finally the reversal of the left element connected to the vertex containing spin C (spin labelled D) in 27% of the set. These reversals are observed for images acquired between –272 Oe and –284 Oe. The following event shows the reversals of spins labelled C, D and E between –284 Oe and –308 Oe, therefore only 1-3 field increment with respect to

the previous modification. Experiments in which spins C and D have not reversed with the first intersection flip here, in 27% and 72% of the set respectively. The additional reversal is now spin E in between previously or presently reversed spins in 46% of the experiments. The last presented event shows the reversal of most remaining spins within a field range between –296 Oe and –332 Oe.

We have found that after the domain wall injection from the pad and its propagation, the right element of the first intersection (spin B) reverses most likely by coupling. Compared to the 1-stage disconnected structures, the choices here are deterministic. This feature of this specific structure can be explained either by the geometry since the elements of the intersections are not "free" or by defects specific to the sample and/or structure. Adding only a few field increments, we observe the reversal of the lowest element (spin C) sometimes along with one diagonal element sharing its vertex. As mentioned before, the most reasonable explanation is that we are actually witnessing a nucleation from the vertical free element that is accompanied with the reversal of spin D only simultaneously or within one to three field increments. We mention that exclusively the right element of the vertex is reversing yielding yet again a deterministic choice. The next observed reversal is spin E that form a chain linking the previously reversed elements. This last reversal does not create any high-energy state but neither would other elements of the intersections. This observation is quite surprising but we do not have an explanation reasonable enough to justify it. If we try to compare the fields of both the 1- and 2-stage structures (Fig.4-13.b) and Fig.4-20.b) respectively), we find that there is not much correlation but we emphasise that the two set of experiments were realised completely separately and as we suspect, could the source of variability.

The main conclusion with this particular disconnected structure is that it does not exhibit an avalanche behaviour nor stochastic choices at the intersections. The promising behaviour observed for the 1-stage structure is clearly not transferable to the 2-stage structure.
We mention that the reversals over the 11 field experiments for the other 2-stage structure (Fig.4-19.b)) are very similar. In 82% of the 11 experiments, we observe the reversal of element C during the second event. No avalanche strictly speaking were observed but the order of the reversals is different from the other structure.
Comparing the two structures, observed on the same sample during the same acquisitions, suggests a strong variability between structures but if we may say so, a certain consistency of their defaults. It also shows that this deterministic behaviour is not due to field misalignment since each structure exhibits reversals on only one and different side.

We take this opportunity to remark that studying the steps of the reversals is absolutely essential to assert if the reversals form a propagation from the pad. In this particular case, applying a field between –284 Oe and –308 Oe would lead, in about half of the experiments, chain-like reversals (spins A, B, E, D and C) without knowing in which order spins have reversed. This is why, in most experiments shown in this chapter, we have taken the necessary time (and images) to characterise thoroughly the steps of the reversals.

4.3.1.2.2. Connected 2-stage structures

We perform a very similar characterisation of 2-stage connected structures (Fig.4-18.b)). In this experimental set, we observe six structures on a single sample during the same acquisition. A dedicated sample was fabricated and characterised. Examples of observed spin configuration evolutions for two structures are given in Fig.4-21.

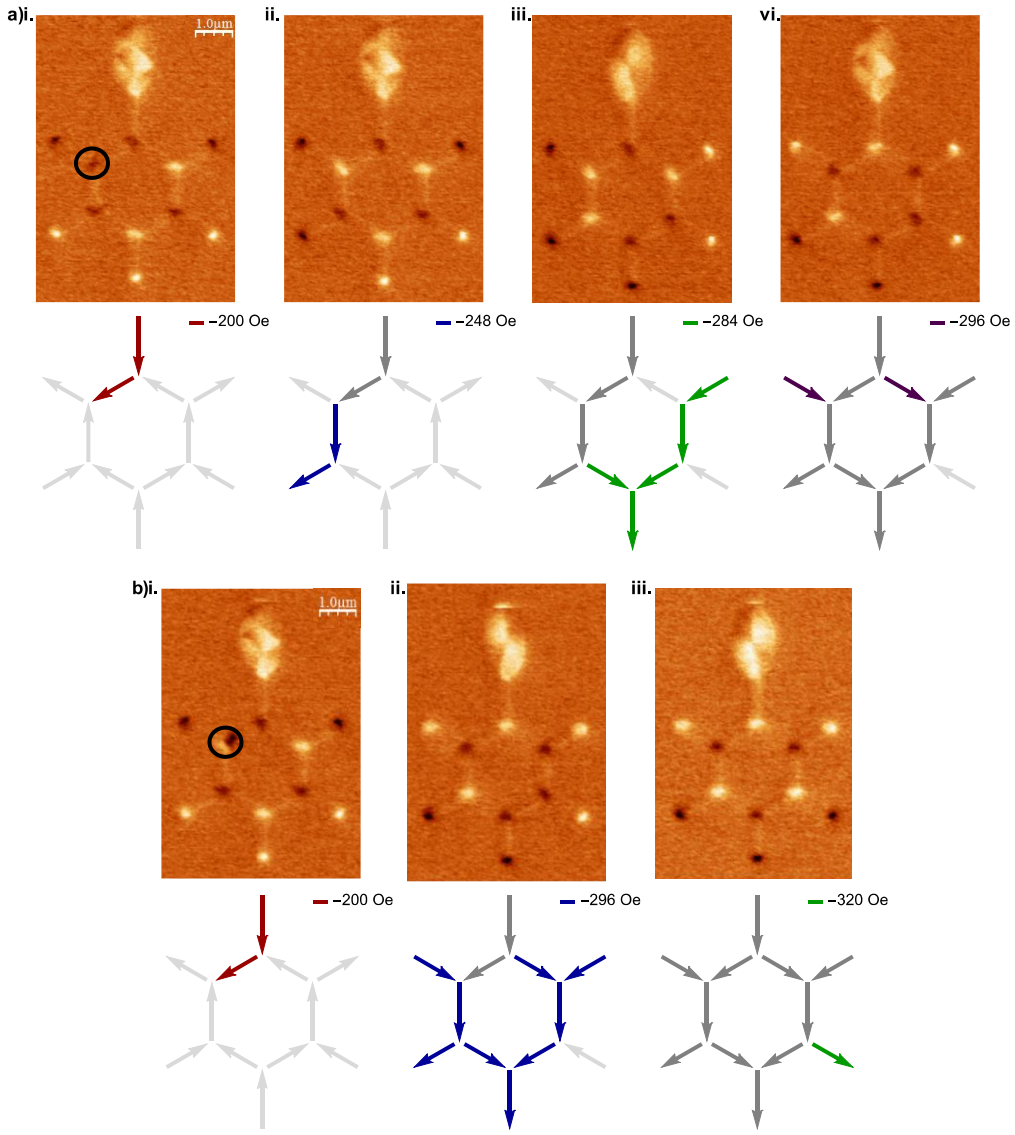

Fig.4-21: a) Reversals on a 2-stage connected structure: i. in red, first reversal observed at –200 Oe, element connected to the nucleation pad and left element of the first intersection; ii. in blue, next reversals observed at –248 Oe; iii. in green, next reversals observed at –284 Oe; iv. in purple, following reversals at –296 Oe and b) Reversals on another 2-stage connected structure: i. in red, first reversal observed at –200 Oe; ii. in blue, next reversal observed at –296 Oe; iii. in green, last reversal observed at –320 Oe.

In the first experiment (Fig.4-21.a)), we observe the propagation of the domain wall injected from the pad at –200 Oe. Then when applying –248 Oe, the domain wall gets depinned and the following reversals form a chain up to the outer left element of the structure. The next modifications in spin configuration occur when three and four field increments are added with the reversals of the edge elements on the right side of the structure.
In the second experiment shown (Fig.4-21.b)), we find that injection and domain wall propagation up to the left element of the first intersection occur at –200 Oe. The domain wall stays pinned there for six field increments. When –296 Oe is applied, nine out the remaining non-flipped elements reverse and the last one within an additional field increment. We remark on this specific structure that when the domain wall is pinned at the first intersection, the contrast (circled in Fig.4-21.b)i.) is divided in two, we do not explain this feature observed in several of our 2-stage structures.

With the presented experiments, we find that the structures exhibit pinning sites (circled in the MFM images of Fig.4-21.a)i. and b)i.). Depending on the experiment or the structure, high fields are required to depin the domain wall (–296 Oe in the first experiment and –248 Oe in the second). We conclude that these pinning sites have a different behaviour compared to the intersections and therefore in our system, not all vertices are equivalent. In the spin configurations obtained after injection and domain wall propagation, the ice rules are respected yielding a low-energy state configuration.

We now study the reversals over seven field experiments of one structure, the one shown in Fig.4-21.a). Results are presented in Fig.4-22, same as before reversals are presented in tree form along with the fields at which the events are observed.

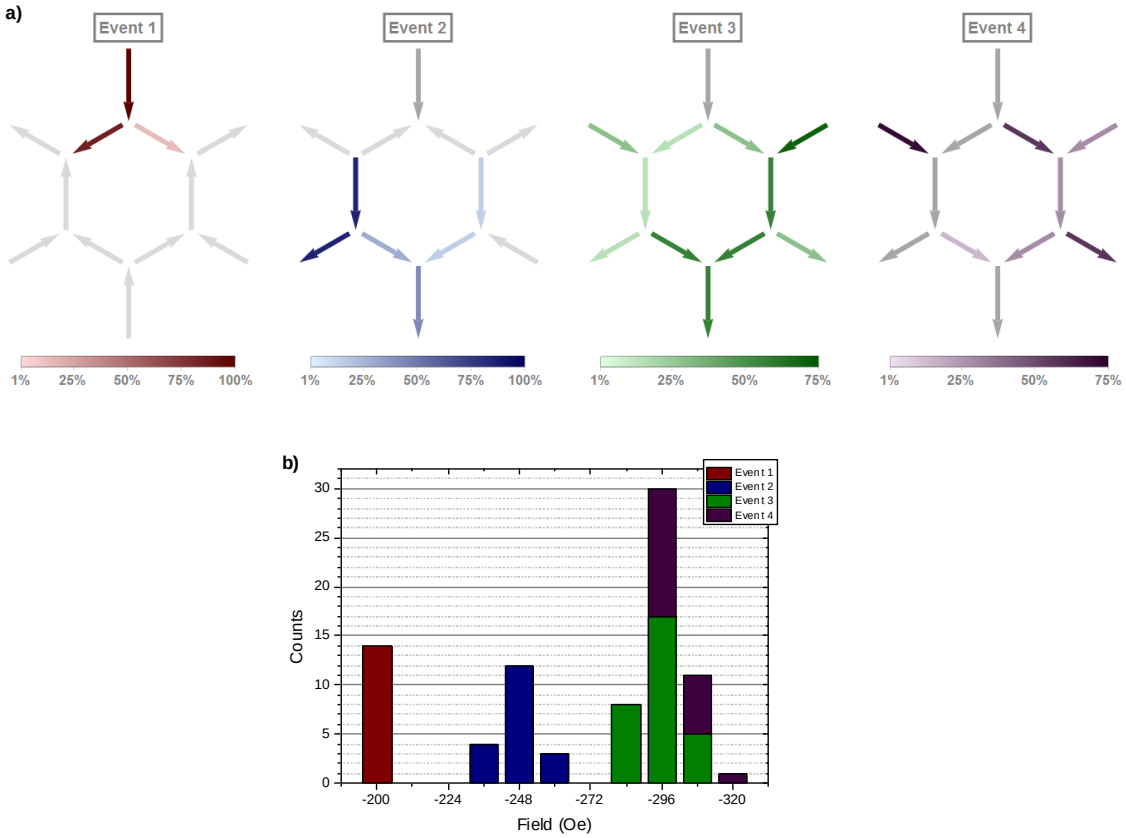

Fig.4-22: a) Observed reversals summarised in tree form on 7 identical experiments on a single 2-stage connected structure; b) the fields at which reversals occur. When coloured in darker grey and reversed, the spins have reversed in one of the previous events in all experiments. Only first four events are considered.

Over the seven field experiments performed on one structure, we observe the reversal of the upper element along reversal of one of the elements of the first intersection at or below –200 Oe (Event 1, Fig.4-22.a) and b)). We find that in six out of the seven experiments (86% probability to go left with an overrated error estimated at $\sqrt{0.5^2/6} \approx 20\%$), the left element of the first intersection reverses suggesting biased but stochastic choice. The next reversals observed on this structure between –236 Oe to –260 Oe are the next vertical elements up the ends of the structure part from the right output (Event 2, Fig.4-22.a) and b)). Avalanche path joining the left output seems to be preferred compared to all others. This apparent bias could be due to intrinsic variations or to the number of experiments performed (here the error is estimated to $1/\sqrt{7} \approx 38\%$). Increasing the field between –284 Oe and –320 Oe almost saturate the array.

For this structure, filtering the chain-like reversals showed that 71% of the experiments can be qualified as such. In the five avalanche experiments, we find that four follow a path to activate the outer left output and the other two the central output. In proportions it translates in 80%/20%/0% therefore suggesting stochastic behaviour that will be discussed in section 4.3.2.

Our observations show that this structure actually enables avalanche-like reversals and does exhibit stochastic choices. All other five structures observed in the same acquisition show similar observations: from 57% to 100% of the experiments are avalanches and stochastic choices are made at the intersections.
We emphasise that it is a first encouraging result for our applications of avalanche of honeycomb artificial spin system. Deviations from a binomial law with probability equal to 50% cannot be excluded due to the low statistics (only seven field experiments performed on six structures).
However for this geometry, we cannot conclude if the reversals reaching the end of the structure are the result of the injected domain wall or parasitic nucleations. We have little doubt that the reversals observed during the first event at the very first intersection are due to the injected domain wall. For the other reversals, the only way to be sure would be to observe experimentally the dynamics of the structure. But we will show in the following sections that larger structure give the answer.

4.3.1.3. Comparison small structures disconnected/connected geometries for our applications

We have studied on various sets of experiments the behaviour of 1- and 2-stage structures in both disconnected and connected geometries. In this section, we will justify our choice of the connected geometry as a better fit to our device specifications.

For the 1-stage structures, we have shown that both disconnected and connected geometries show stochastic choices at the intersection (Fig.4-13.a) and Fig.4-17.a)) promising for avalanche mechanism. We have also seen that they have distinct field behaviour, we study further these features by comparing the reversal fields for each element of the system in Fig.4-23.

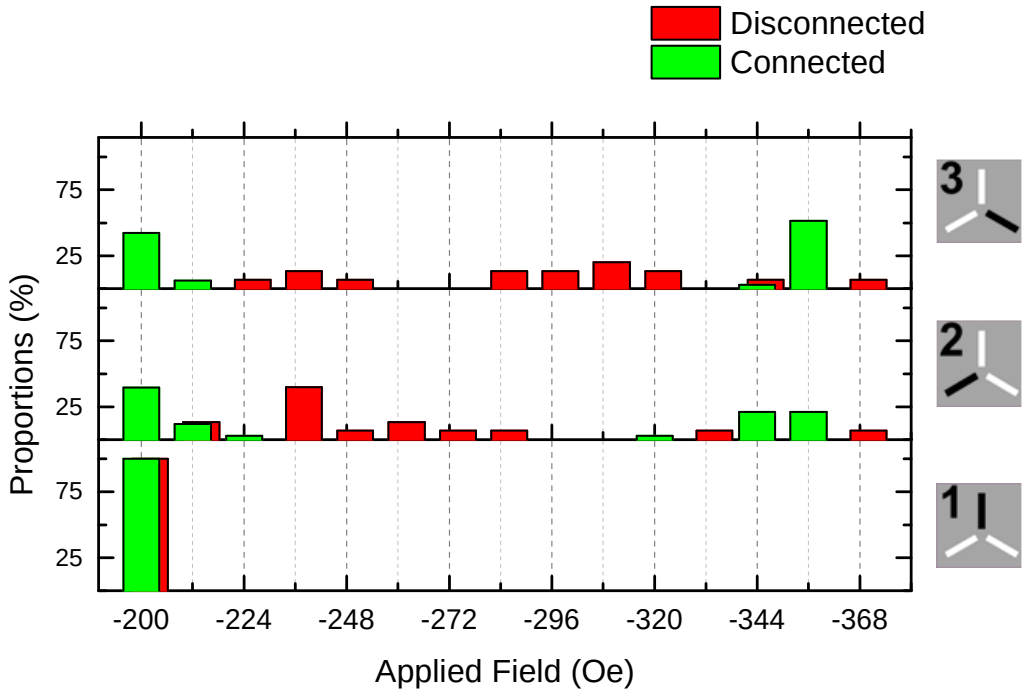

Fig.4-23: Comparison of reversal fields of elements of the disconnected (red) and connected (green) 1-stage structures shown in Fig.4-17 and Fig.4-13 respectively. Data of the disconnected structure is plotted with a slight offset for better readability.

For both geometries, the element connected to the nucleation pad reverses at or below –200 Oe (spin 1 in Fig.4-23) due to domain wall injection and propagation. We find that elements of the intersection (spins 2 and 3 in Fig.4-23) do not have a defined coercive field. This result emphasises that the reversal occurs by coupling for the disconnected geometry and by domain wall propagation for the connected one. This feature could be an asset for our application behaviour if it is indeed transferable on larger structures.
The other observation is the distribution of reversal fields for both geometries. In the case of the 1-stage disconnected structure, fields are scattered from –212 Oe to –368 Oe for both elements. In the case of the connected structure, the two elements have defined field ranges: for first reversal it is between –200 Oe and –224 Oe and for the second reversal between –344 Oe and –360 Oe. If we suspect that the reversal of a diagonal element leads to reversals in avalanche, then it raises the question about how to identify the one caused by the pad. For this reason, the large field gap between the reversals of intersection elements is preferable.

Despite the avalanche behaviour of the 1-stage disconnected and connected structures, we have seen that increasing the number of stages introduces new issues. In the case of the disconnected geometry, we have seen that the 2-stage structure studied (Fig.4-20.a)) does not exhibit avalanche behaviour anymore. Studying the steps of the reversals suggested that nucleation occur at the lower vertical element of the structure. In the case of the 2-stage connected structure (Fig.4-22.a)), some of the experiments show avalanche behaviour, the remaining ones showed large depinning field close the saturation.
Similarly to the 1-stage structures, we compare the reversal fields of each element of our 2-stage structures in disconnected and connected geometries in Fig.4-24.

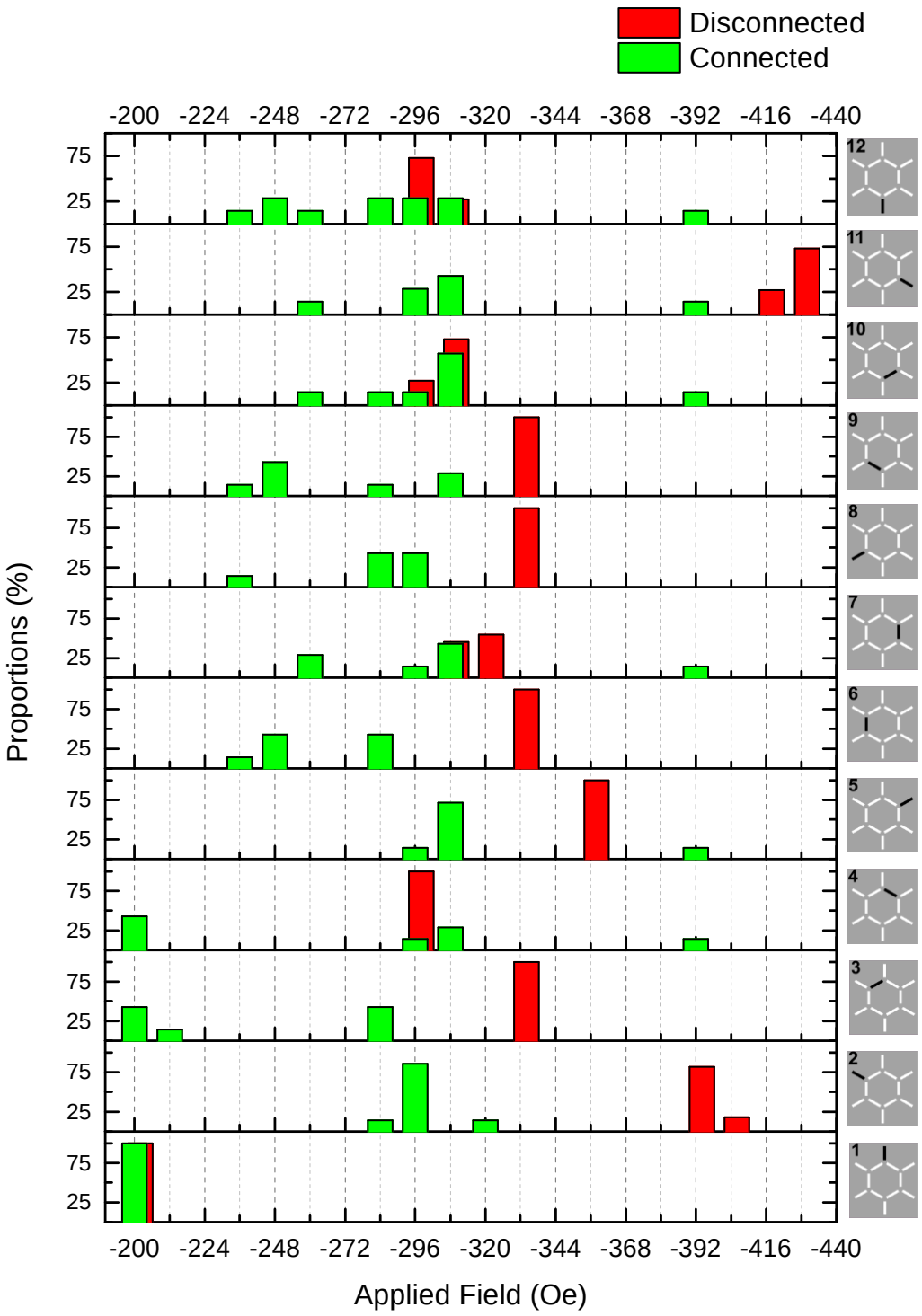

Fig.4-24: Reversal fields for all 12 elements of both disconnected (red) and connected (green) 2-stage structures. Data of the disconnected structure is plotted with a slight offset for better readability.

For the disconnected 2-stage structure, we find that reversals of element occur within at most one field increment for all experiments (Fig.4-24). This result strongly suggests that reversals are deterministic which is obviously an issue for both avalanche and stochastic behaviours.
For the connected structure, we find that reversal fields are very different. Indeed apart from the reversal field of the element connected to the pad, fields of all elements are scattered over at least three field

increments (36 Oe). However, looking at which element exhibit a high saturation field (–392 Oe), we count spins 4, 5, 7, 10, 11 and 12 (as labelled in Fig.4-24). All other elements apart from spins 3 and 4 (diagonal elements of the first intersection), reverse within –236 Oe and –320 Oe. This behaviour may be an issue for our avalanche behaviour since it could give doubt about the order of reversal.

We have seen that both geometries were stochastic in 1-stage structures but that only the connected geometry shows features that suggest avalanche-like reversals along with stochastic behaviour in 2-stage structures. Although it would be possible to optimise the disconnected structure by modifying for instance the gap between elements or the elements shape, we choose to continue with the connected geometry. We further characterise the 2-stage connected structure and its stochastic behaviour by comparing it a to binomial output distribution.

4.3.2. Stochastic behaviour of the 2-stage connected structure

Previously, we have seen that our 2-stage connected structures exhibit avalanche-like reversals in a majority of the experiments. We now try to determine if the behaviour observed is robust for several structures of the same sample with a few field alignments on another acquisition.

We study the output distribution, in which proportions the avalanche reaches left/middle/right outputs, for several structures. Here, we reassemble 21 structures observed during several acquisitions on a single sample making a total of 87 experiments that we consider independent. We filtered the avalanche-like scenarios. Proportions of activated outputs are shown in Fig.4-25.

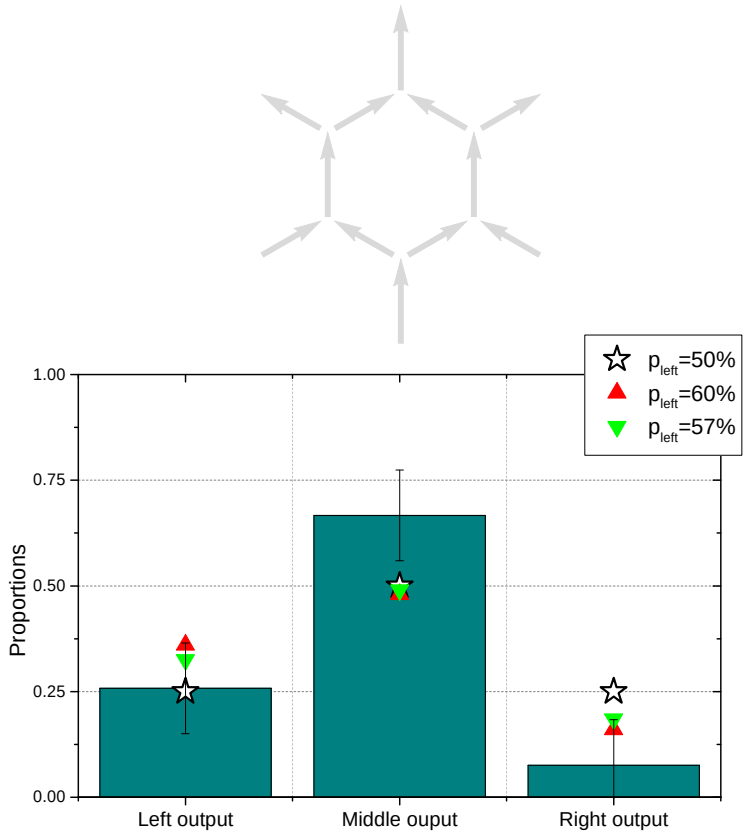

Fig.4-25: Observed activated outputs. Results are summarised over 21 structures (with a field alignment of ±0.5°) yielding 87 experiments considered independent, 76% of them form avalanche-like reversals and represented here.

Out of the 87 experiments considered, we find an output distribution of 25%/67%/8% for left/middle/right outputs respectively. Therefore the stochastic behaviour observed for the six previously presented structures is robust for additional one with same field alignment (±0.5°). In addition to this feature, 76% of the 21 experiments considered form chain-like reversals.
We observe that the output distribution is not following a binomial with equal probability to go left/right, 50%/50% yielding 25%/50%/25%. The computations are not within our estimated error ($\sqrt{87}/87 \approx 11\%$): our distribution is therefore biased. There is no probability describing the middle output and its uncertainty. However, the left and right outputs are both described by a probability to go left ranging from 57% to 60%.

One possible explanation for this slightly biased distribution is a field angle. We verify the effect of this parameter using two different acquisitions on several structures tilted at +3° and –7°. Activated output distributions are shown in Fig.4-26.

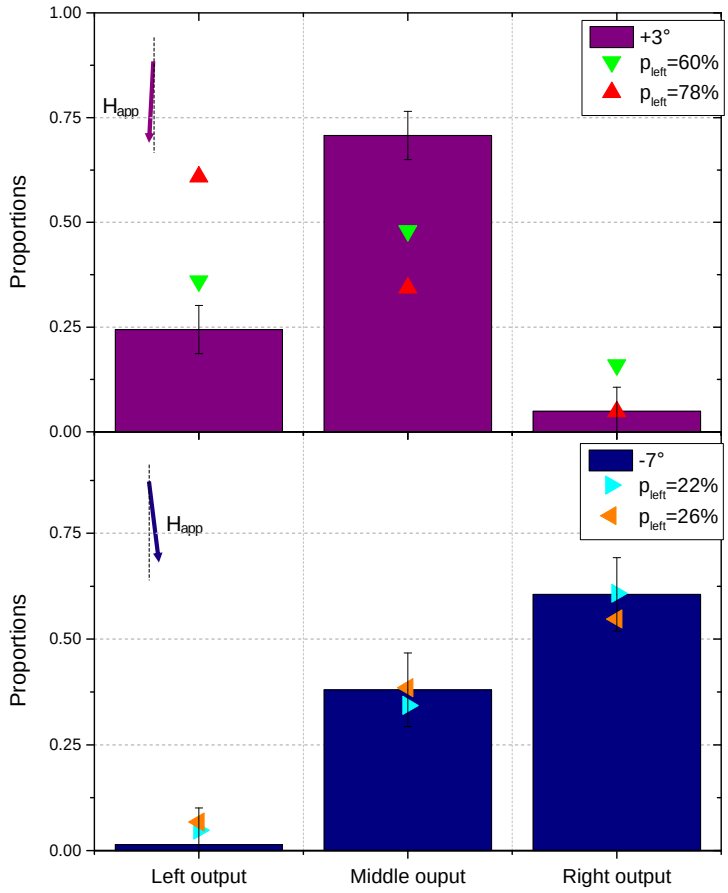

Fig.4-26: Observed activated outputs with a) +3° tilt, results over 50 structures observed 6 times yielding 300 experiments considered independent and b) –7° tilt, results over 12 structures observed 11 times yielding 132 experiments considered independent. Proportions of avalanches 68% and 54% for the +3° and –7° tilts respectively.

For set of +3°-tilted structures, 50 structures were observed on six acquisitions yielding 300 experiments that we consider independent. We have counted that 68% of the set exhibit avalanche behaviour which is a bit lower than for the previous set (Fig.4-25). Here we find that activated output proportions of 24%/74%/5% ($\pm\ 1/\sqrt{300} \approx 6\%$). We do not find a probability to go left matching our experimental results.
For the set of –7°-tilted structures, 12 structures were observed on 11 acquisition yielding 132 experiments that we consider independent. On this set, 54% of the experiments exhibit stochastic avalanche behaviour, and we see a clear difference in output distribution (1%/38%/61%). Trying to ascribe a probability to go left matching our results, we found that 22% to 26% yields a good description. This value is lower than the 60% found for the aligned results (Fig.4-25).

We conclude that the 2-stage connected design presented in Fig.4-18.b) exhibits robust stochastic behaviour and avalanche-like reversals in majority of the experiment (minimum of 54% of the set in Fig.4-26 exhibiting avalanche behaviour). The corresponding activated outputs of various tilted structures suggest that below ±3° field angle, the average probability to go left/right does not change drastically. However, increasing the field angle to 7° changes -drastically this time- the distribution with a maximum of activated outputs on the edge output. This feature can be translated on the average probability to go left/right that changes from 57-60% to 22-26%. This result shows that a misalignment in field changes the output distribution.

We have also seen that for the ±0.5° and +3° (Fig.4-25 and Fig.4-26.a)) there is a high proportion of activated middle output that cannot be described by any probability of a binomial law. This result already suggests what we will see in the next section that we are witnessing propagations starting from the lower vertical element of the structures.

4.3.3. Increasing the size of the connected structure

Our study now focuses on larger structures and if the stochastic behaviour observed in the 2-stage connected structures is transposable to 7-stage structures. We have designed an artificial spin system similar to the one of a Galton board[6] with seven stages thus eight outputs. The dimensions are like the ones of the connected structures presented previously (Fig.4-15.b)). A SEM image is given in Fig.4-27.a).

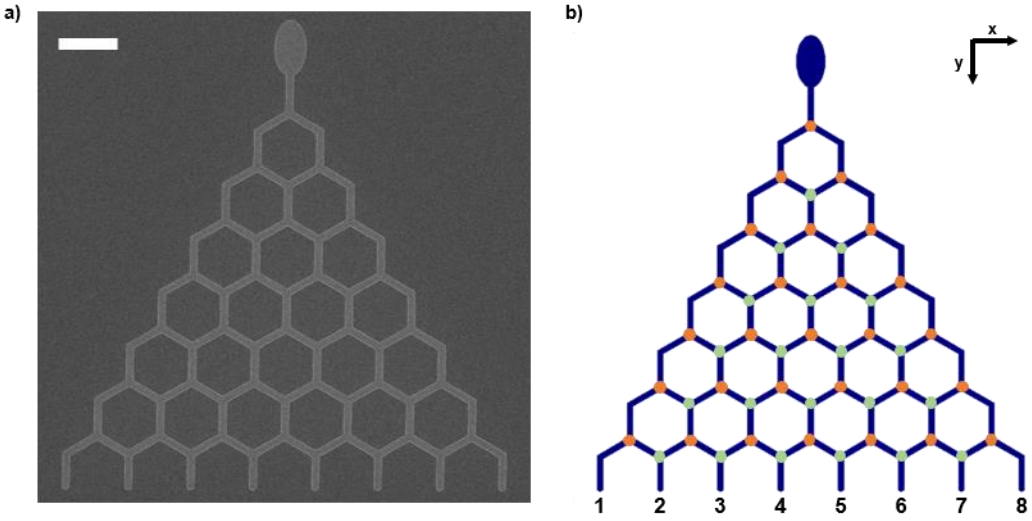

Fig.4-27: a) SEM image of the 7-stage structure, elements are 200 nm wide, elements are 1.2 µm-long, upper element connected to the pad is 1.3 µm-long; b) identification of the intersection (orange disks), pinning points (green disks) and the outputs of the structure (indexed from 1 to 8). Scale bar is 2µm.

This structure has 49 vertices, 28 intersections –where the domain wall has a choice to go left or right- (identified as orange disks in Fig.4-27.b)) and 21 other vertices that we have seen previously act like potential pinning points as we refer to as hereinafter[7] (identified as green disks in Fig.4-27.b)). From now on, each point type will be identified with a couple of indexes: (n, m) where n is the stage indexed in the ascending order (following the +y direction) and m the index in the ascending order (according to +x direction, see Fig.4-6). Outputs of the system are indexed from 1 to 8 along the +x direction.

In order to characterise the behaviour of our structure, we perform the same experiment as before, saturation and then smaller field in the opposite direction starting at –200 Oe and increment with –12 Oe. In an avalanche-like behaviour of the injected domain wall from the pad, the domain wall would pass by seven intersections and at maximum six potential pinning points. We summarise the reversals in the same way as before using trees and reversals fields for each modification of the spin configuration.

[6] The behaviour of a Galton board will be further explained in section 4.5.1 while studying the stochastic behaviour of our optimised structure.
[7] Whenever referring to pinning point, we will mean potential pinning point.

Results are shown in Fig.4-28, we have limited the study up to the event where an output is activated which is enough to determine if an avalanche takes place.

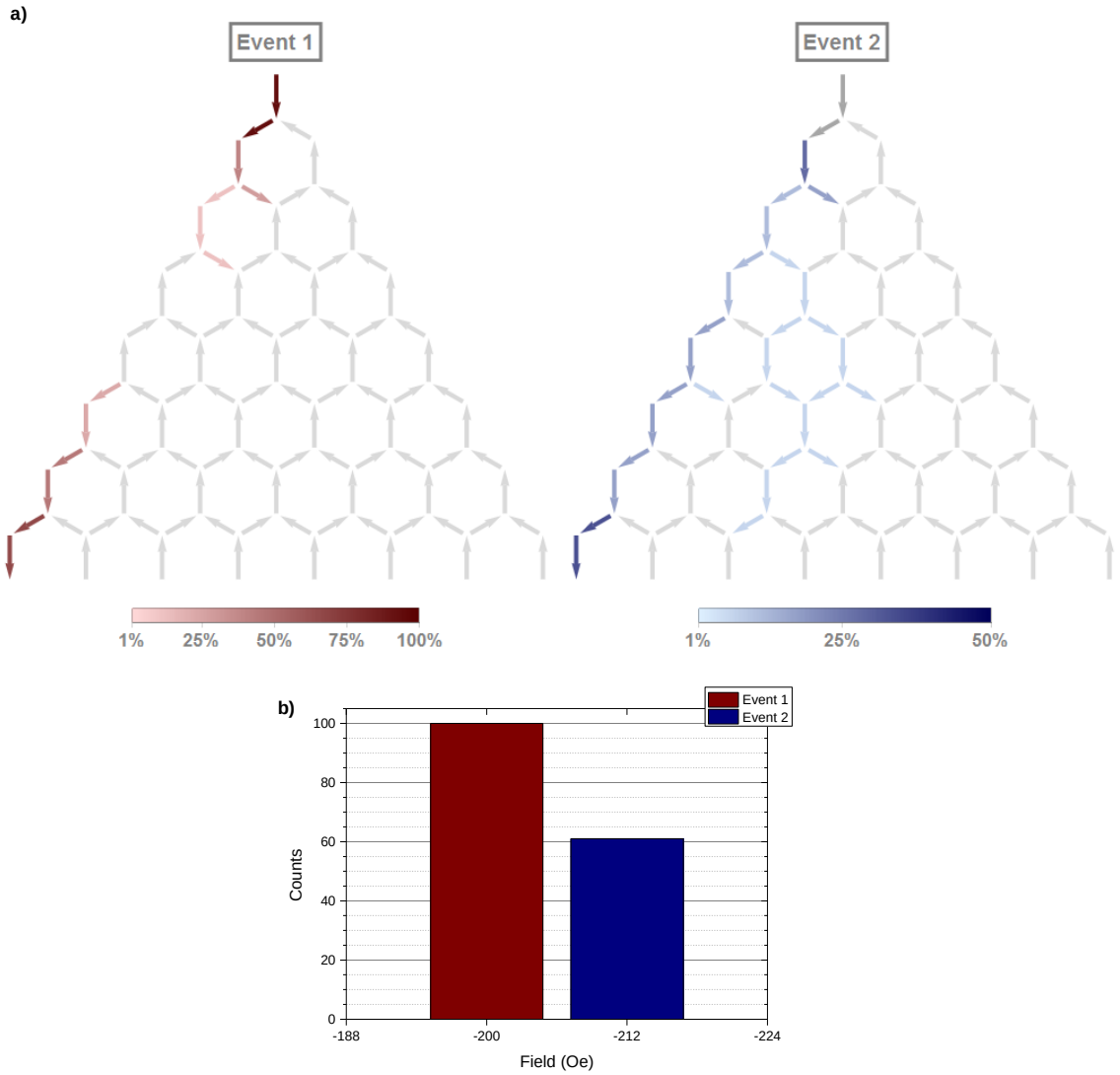

Fig.4-28: a) Observed reversals summarised in tree form on 18 identical experiments on a 7-stage connected structure resembling a Galton board; b) the fields at which reversals occur. When coloured in darker grey and reversed, the spins have reversed in one of the previous events in all experiments.

For this 7-stage structure observed 16 times in the same conditions, we observe a clear tendency of the elements on the left part of the system to reverse with no avalanche-like behaviour. We find that the domain wall is injected and gets pinned in the upper part of the structure at –200 Oe or –212 Oe. Along with these reversals, exclusively the first output is activated in all experiments considered. This result shows a nucleation on the first output that happens at the same field step as the injection. Two typical experiments are presented in Fig.4-29.

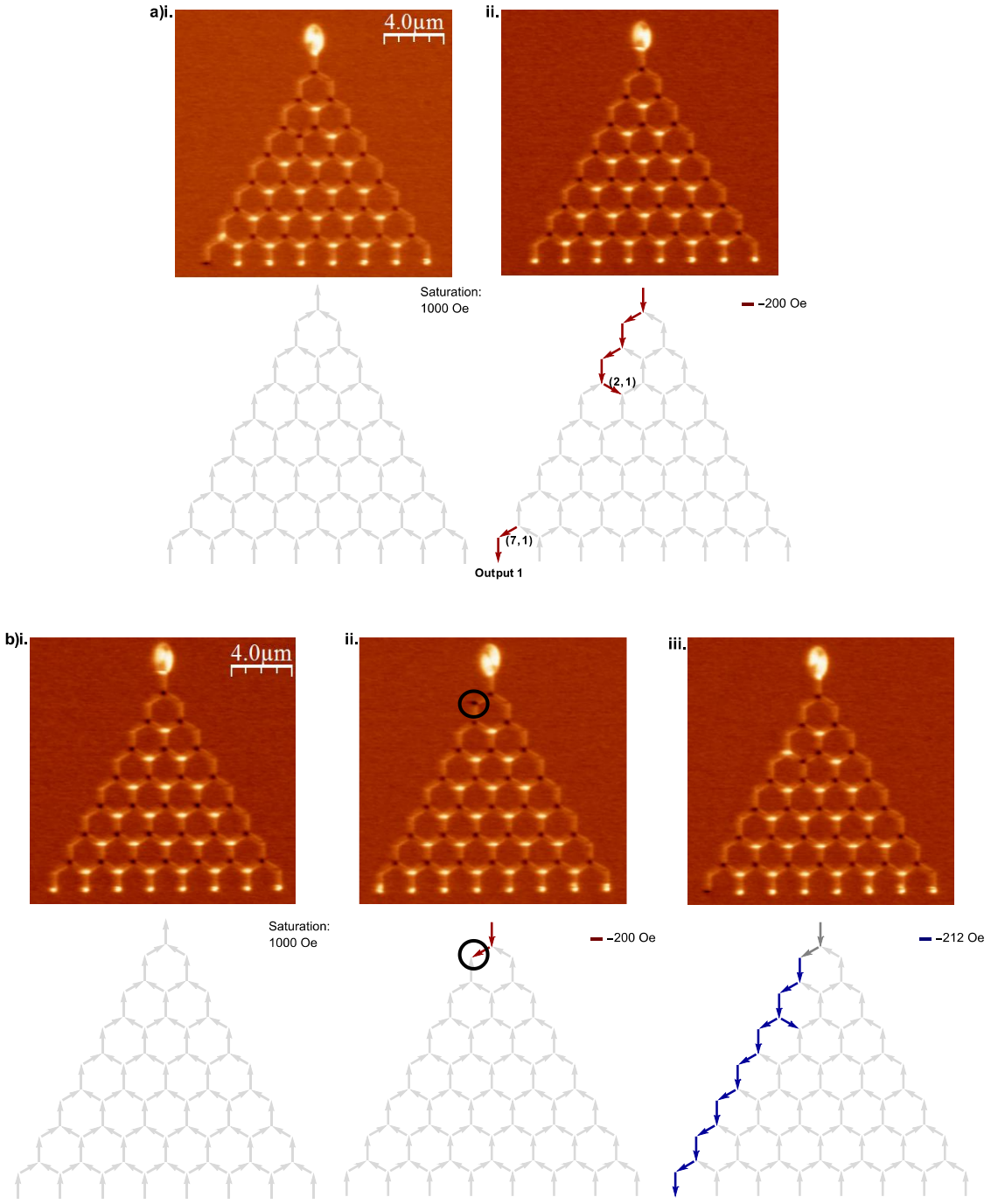

Fig.4-29: a) Typical scenario where domain wall has been injected and has propagated in the upper part of the structure and before reaching a field high enough to depin another domain has nucleated and propagated in the lower part of the structure; b) unique experiment with an avalanche-like behaviour, here the first pinning has occurred at the left edge of the structure.

In Fig.4-29.a), we show a typical scenario where after saturation (Fig.4-29.a).i.), the injected domain wall is pinned at pinning point (2, 1) and a nucleation either coming from the first output or intersection (7, 1) propagating to the other (Fig.4-29.a).ii.). This scenario with injection and propagation of a domain wall going in hand with a parasitic nucleation activating output 1 represent 89% of the experiments. We mention that in this structure, as well as for all experiments with an event observed at –200 Oe, the spin configuration could have changed at lower fields. However, we know for a fact that the field at which

the parasitic nucleation is observed is lower than the depinning field. Only one experiment exhibit avalanche-like reversals, shown in Fig.4-29.b). We find the first pinning (circled in clack in Fig.4-29.b)ii.) occurs at the edge after the first intersection. Taking into account the observations made in 94% of the experiments we can suspect a nucleation in the lower part of the structure joining the avalanche of the upper part.

One possible explanation for this biased behaviour could be a high field angle during the experiment However other structures were observed along with the one presented in Fig.4-28 (same acquisitions). Only activated outputs were surveyed, results are summarised in Fig.4-30.

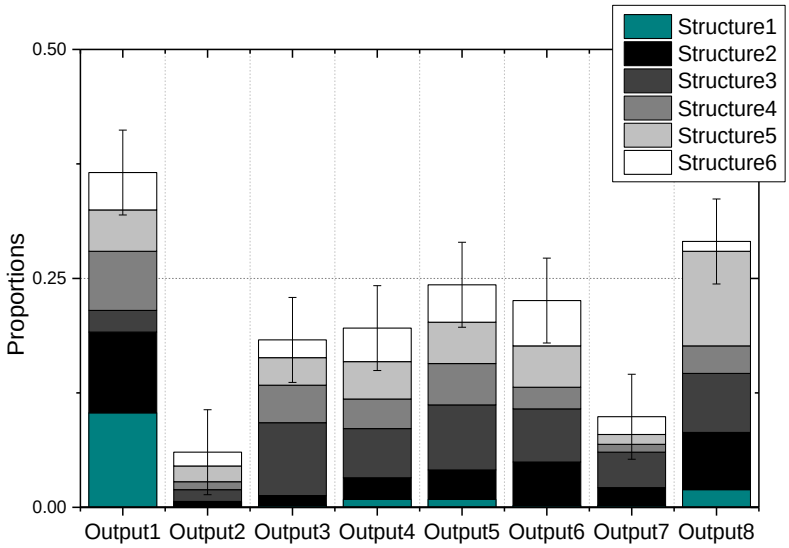

Fig.4-30: Activated outputs of six Galton-like design structures yielding a total of 465 experiments considered independent. Structure 1 has been detailed before. No filter has been applied for the reversal scenarios.

We have studied the output distributions of six structures observed in the same conditions of field alignment without filtering any of the reversal scenarios. The structure presented in the trees (Fig.4-28) is referred to as Structure1 shows clear bias on the outer left output. We find that out of the six structures, Structures2-6 show activations of outputs 2 to 6 but are also responsible for the biasing on the edges. Stucture2 exhibits a clear bias on both outputs 1 and 8, Structure3 on the output 1 and Structure5 on output 8. Only Structure4 and Structure6 do not exhibit a large bias on the outer outputs. This result also indicates that there is no reproducibility from one system to the other.

We find that the overall output distribution is far from a binomial clearly biased on the outer outputs. We can exclude the field angle since in the same experimental conditions and field alignment, outputs 1 and 8 are activated. This feature is due to a behaviour similar to the one presented before: nucleation on the edges of the structure either from output or edge. Inner outputs are also activated but are found to not be the result of avalanche behaviour in most of the experiments.

We conclude that, apart from the tendency of some structures to reverse edge elements, the main drawback of this design is the parasitic nucleations occurring at lower fields than the depinning field of the upper part. We can only strongly suspect that it occurs from the outputs using the trees (Fig.4-28.a)) but we cannot exclude nucleations from the edges taking into account the unusual behaviour observed (circled in Fig.4-29.b).ii).

We improve our design by stabilising its edges with the addition of elements so that all vertices are composed by three spins. We now introduce a novel design for our 7-stage connected structure with 14 elements on the edges of the structure compared to the previous one. A SEM image and schematic of our “stabilised” structure is shown in Fig.4-31.

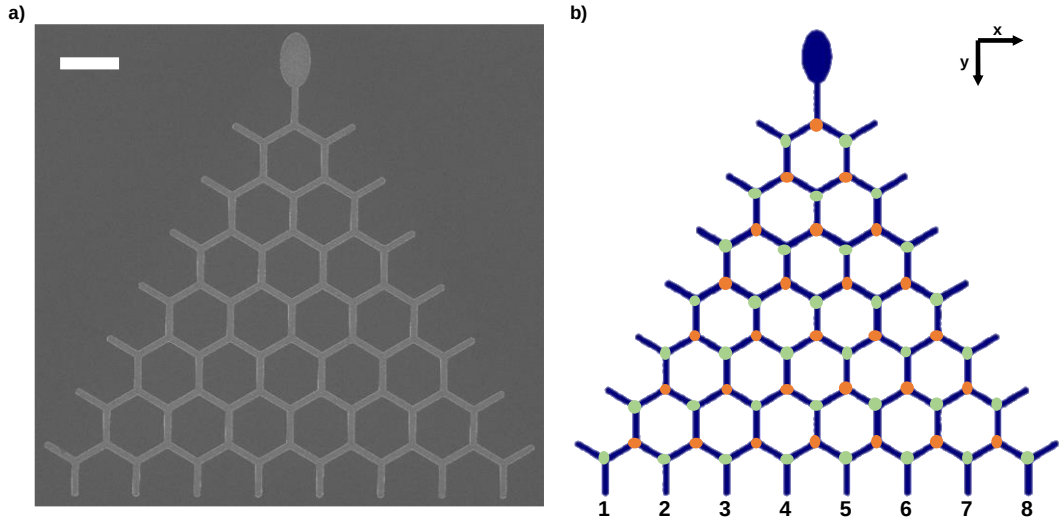

Fig.4-31: a) SEM image and b) design of the modified 7-stage connected structure with stabilised edges. Intersections and pinning points are identified as orange and green disks respectively, outputs are indexed from 1 to 8 as before. Scale bar is 2 µm.

This structure is composed by 63 vertices with 28 intersections (orange disks in Fig.4-31) as before but now there are 35 potential pinning points (green disks in Fig.4-31). We perform 16 times the field protocols on a single structure, reversals and event fields are shown in Fig.4-32.

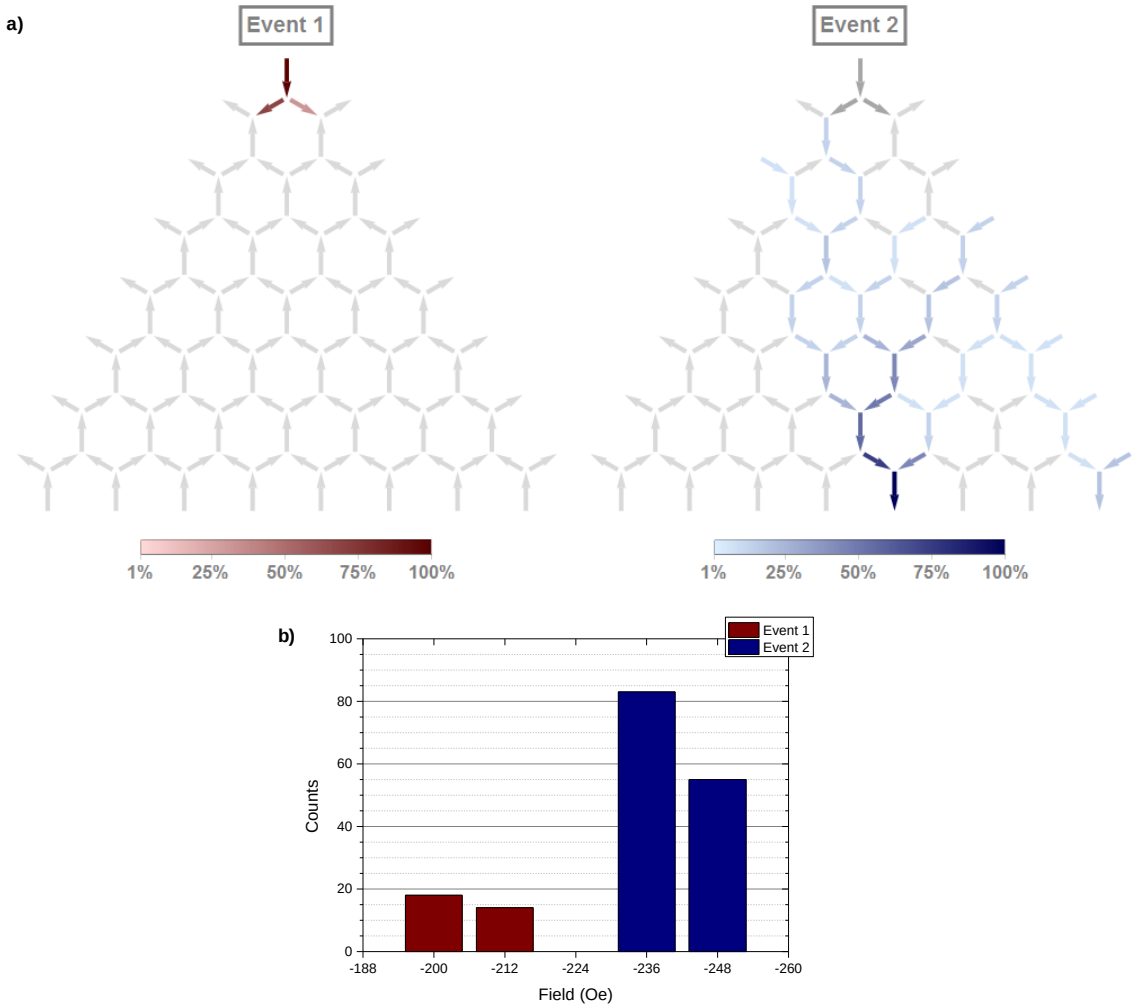

Fig.4-32: a) Observed reversals summarised in tree form on 16 identical experiments on a 7-stage disconnected structure with stabilised edges; b) the fields at which reversals occur. When coloured in darker grey and reversed, the spins have reversed in one of the previous events in all experiments.

Studying the reversal of our stabilised system on 16 acquisitions, we find there is no apparent avalanche behaviour in the reversals. First, we observe the injection of the domain wall from the pad that gets pinned either at pinning point (1, 1) or (1, 2) between –200 Oe and –212 Oe. Then applying a field from –236 Oe to –248 Oe, we observe the systematic reversal of the element of output 5 along with reversals located at output 8 and deeper into the structure. In only a few experiments, reversals from the first pinning join the end of the structure. Typical experiments are presented in Fig.4-33.

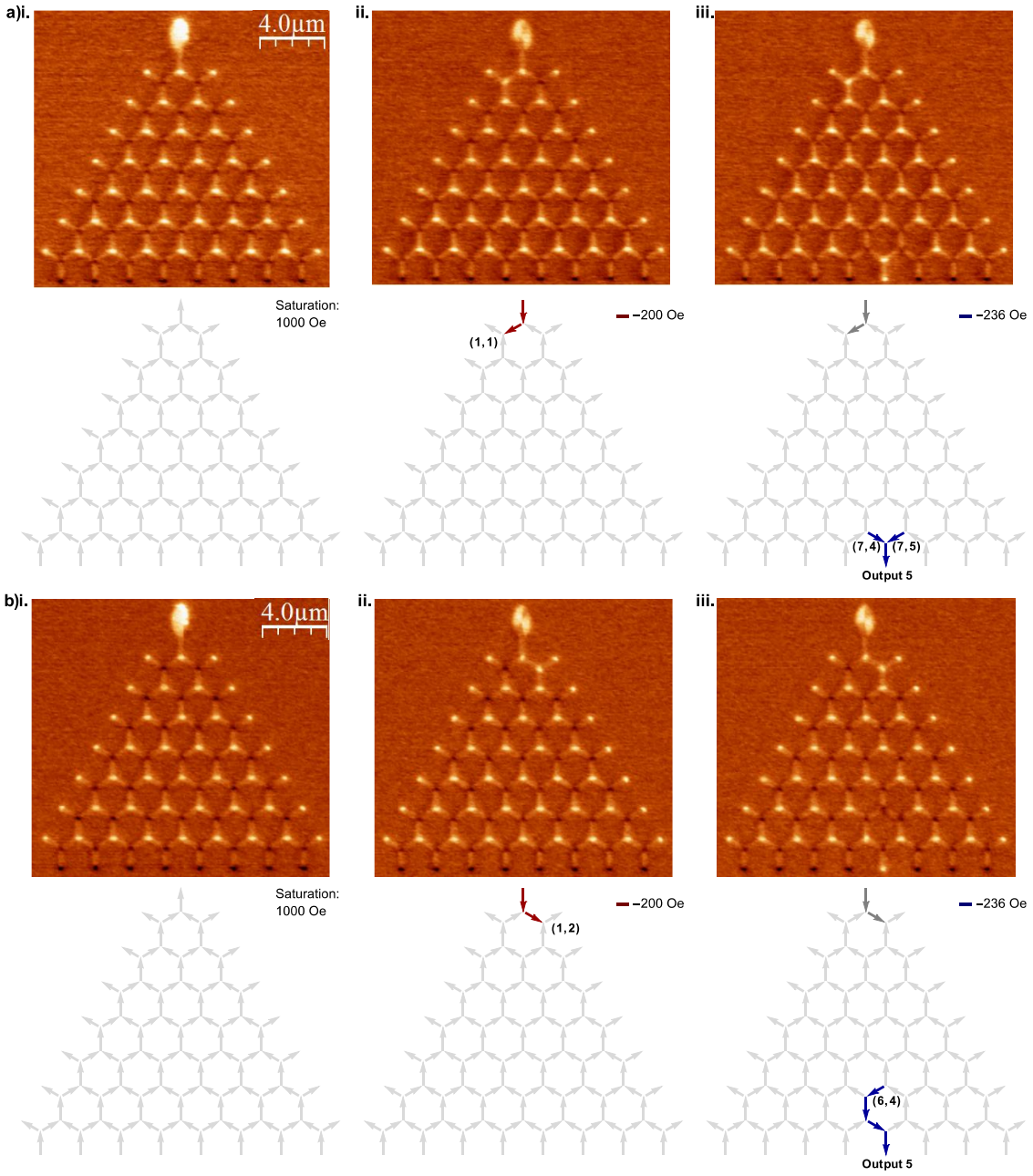

Fig.4-33: Typical scenarios observed in our stabilised 7-stage structure: a)i. saturation at +1000 Oe, ii. injection of the domain wall getting pinned at pinning point (1, 1) observed at –200 Oe, iii. reversal of the 5th output and both upper diagonal elements of the vertex at –236 Oe; b)i. saturation at +1000 Oe, ii. injection of the domain wall getting pinned at pinning point (1, 2) observed at –200 Oe, iii. reversal of the 5th output and three spins forming a chain at –236 Oe.

In the first experiment (Fig.4-33.a)), we observe that after having saturated the array and having applied –200 Oe, the domain wall injected by the pad propagates through the first intersection (1, 1) and stays pinned right after. Applying –236 Oe then nucleates a domain wall from output 5 that propagates to intersection (7, 4) and (7, 5) through a branching scenario. Here, –236 Oe is a field high enough to nucleate a domain wall from the end of the structure but not high enough to depin the domain wall injected by the pad.

In the second experiment shown (Fig.4-33.b)), we observe a similar scenario with pinning after the first intersection at pinning point (1, 2). We remark here that this a proof that stochastic choice as observed for the 1- and 2-stage structures is also present in this geometry. Then applying –236 Oe does not allow

depinning of the injected domain wall but does induce a nucleation starting from output 5 to intersection (6, 4) in an avalanche scenario.
We mention that all results shown for our stabilised structures strongly suggests a nucleation from output 5 propagating inside the structure. This hypothesis indeed seems more reasonable than a nucleation inside the structure propagating to its end.

This argument is underpinned by the observations made on another structure studied in the exact same experimental conditions (same sample and same acquisitions). The reversals are very similar: pinning of the injected domain wall in (1, 1) or (1, 2) and then for 94% of the experiments the reversal of the second output. The issue stated before has therefore being translated been transposed to another output. This behaviour translates in the output distributions summarised for both structures observed simultaneously shown in Fig.4-34.

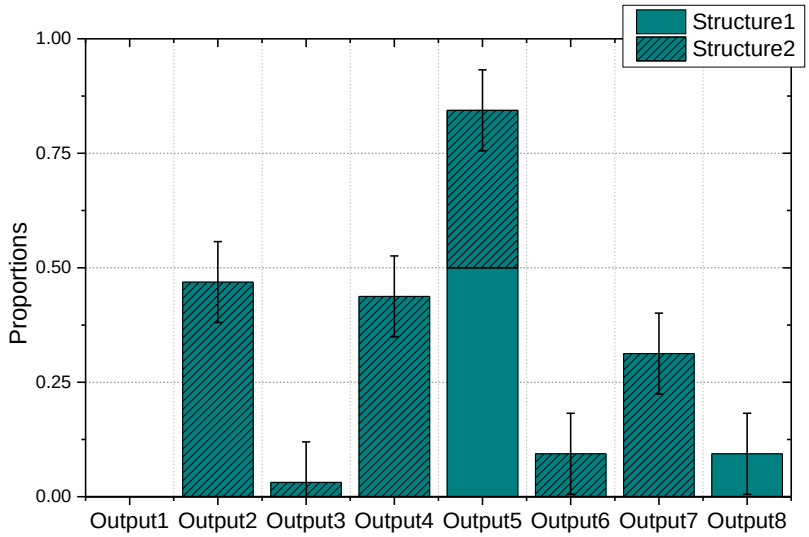

Fig.4-34: Activated outputs of 2 stabilised design structures observed each 16 times in the same conditions yielding a total of 32 experiments considered independent. Structure 1 has been detailed before. No filter has been applied for the reversal scenarios.

We find that the proportions of activated outputs summarised over our two structures is not even close to a binomial distribution. This observation is the result of intrinsic nucleation fields from some outputs of the structures. The fact that the two identical structures behaves so differently can be explained by fabrication fluctuations yielding differences in coercive fields of the elements.

We note that the bias on the outer outputs is not present in the Galton-like design (Fig.4-30) is not present anymore on our stabilised structure. This result shows that the additional elements on the edge of the structure are required to observe reversals within the structure and not mostly following a unidirectional path (where the choice is the same at all passed intersections as shown in Fig.4-7.b)). The comparison between the two designs have clarified that parasitic nucleations happen at the outputs of the structure and not at its sides.

We have highlighted with our 7-stage honeycomb artificial spin systems the main issue to overcome on wide structures: the right trade-off between depinning field of the upper part of the structure and nucleation fields of the outputs. The former should be lower than the latter in order to observe

propagation-like reversals of the injected domain wall from the pad. Therefore, for an adequate optimisation of our 7-stage structure design we need to carefully adjust these two parameters.

4.3.4. Conclusions

In this section, we have presented a study of various honeycomb artificial spin systems and the issues raised by both disconnected and connected geometries for small and large structures.
We have first shown on 1-stage structures (Fig.4-10.a) and Fig.4-18.a)) that both geometries exhibit injection and propagation of a nucleated domain wall by the pad. In the case of the disconnected structures, the first reversal induces by coupling the reversal of one of the diagonal elements and in some cases, both simultaneously. In the case of the connected structure, we observe the reversal of one diagonal element. For both geometries, the reversals are stochastic meaning that we reverse either one or the other element of the intersection. The main difference between the two geometries is the field ranges at which first and last diagonal elements reverse: in the disconnected 1-stage structure, field ranges overlap whereas for the 1-stage connected structure, field ranges are separated by a large gap.
We have then studied 2-stage structures in both geometries (Fig.4-10.a) and Fig.4-18.a)). On one hand, the 2-stage disconnected structures showed reversal of the element connected to the pad by domain wall propagation. The following reversals included in most of our experiments the lower element of the structure. This feature is responsible for no avalanche-like reversals due to parasitic nucleations. This result was underpinned by the study of reversal fields of the elements that showed almost fixed coercive fields. The 2-stage connected geometry on the other hand, showed in a majority of experiments avalanche-like reversals from nucleation pad to one of the three outputs of the structures. Although the promising characteristics of this geometry, we were not able to assert that the observation were indeed the result of domain wall propagation of the injected domain wall. However, we have made the choice to proceed our development with only the connected geometry and rather than optimise the disconnected structures. We have then shown that the output distribution of our 2-stage connected structures of avalanche-like reversals follow quite closely a binomial distribution. We have also demonstrated that the distribution is biased by a field angle.

Increasing the size of our connected systems to seven stages, we have shown that in the case of simple "Galton board -like" design (Fig.4-27), the injection and propagation of the domain wall from the pad is stopped after the very first intersection at low fields. Before reaching a field high enough to depin the domain wall, it appeared that parasitic nucleations were occurring on the side of the structure. We have also shown a high variability from one structure to the other with both parasitic nucleations from either the outputs or the sides.
Because we could not exclude that the nucleations were not starting from the sides of the structures, we have studied another design of 7-stage with all vertices of the structure being composed by three spins (stabilised shown in Fig.4-31). In these structures, we have seen that injection and propagation of the injected domain wall by the pad happens and then gets pinned after the first intersection. The choices made at this intersection were stochastic. The next modification in spin configuration was on a specific structure systematically one output element along with a few others. On another, the issue was similar only on other output elements yielding completely biased output distributions due to defined coercive of output elements. In terms of fields, the nucleation field of the output elements is lower than the depinning field from the upper part of the structure.

The combination of both 7-stage designs has highlighted the main issue to overcome: in order to observe avalanche-like reversals, we need to find the right trade-off between depinning field and nucleation field. We will show in the next section that this can be overcome by tailoring our connected honeycomb artificial spin system.

4.4. Domain wall propagation in our optimised artificial spin system: observed phenomena

In this section, we will first present our optimised artificial spin system that allows the right trade-off between depinning field from the upper part and nucleation field from the outputs. Then we will characterise the domain wall propagations scenarios observed. We will show that our optimised system allows avalanche-like reversals qualified, as single-cascade scenario, in a majority of experiments, the remaining ones being multi-cascades. We will show that another type of reversal appears due to the shape of some intersections on the opposite direction of the applied field that we qualified as backward propagations. We will also present a characterisation of the pinning sites of our structure and show that there is not "hard" point and show experimentally that the depinning process depends on temperature.
The characterisation presented in this section is mainly the result of an acquisition of 229 field experiments performed on a single optimised structure by MFM. This is an acquisition of about 2 months during which the sample was not moved from the microscope. We completed our study with scanning transmission x-ray microscopy on another sample, with a different field module. The experiments were performed at the synchrotron Soleil on the Hermes Beamline with Dr. K. Ait Oukaci (Institut Jean Lamour/ Synchrotron Soleil), Prof. F. Montaigne (Institut Jean Lamour), Dr. R. Belkbou (beamline manager) and I, also with the help of Dr. D. Sanz-Hernandez (CNRS/Thalès). Magnetic Force Microscopy at low temperature was also performed thanks to Dr. K. Bouzehouane (CNRS/Thalès).

4.4.1. Optimised artificial spin system

We have shown previously that the main issue on 7-stage structures is not the injection of the domain wall but its propagation throughout the structure. Indeed the nucleated domain wall propagates through the first intersection and gets pinned after either the left or right diagonal element. Before we reached a field high enough to depin it, we have seen that a domain wall nucleates from the outputs and propagates inside the structure. To overcome the parasitic nucleations observed, we have performed several tests on 2-stage structures with various optimisations with and without nucleation pads: widen the vertical elements, taper the ends of outer elements both diagonal and the outputs (like in Ref. [84]) adding various rounding shapes to the intersections and potential pinning sites. Experiments will not be presented here. We have concluded that in order to avoid nucleations from the outputs, tapered ends are indeed efficient and to decrease the depinning field at the intersections, a simple funnel shape at the potential pinning points is needed. The final optimisation with both funnel shapes (Fig.4-35.b)) and tapered outputs (Fig.4-35.c)) on the 7-stage structure is shown in Fig.4-35.a).

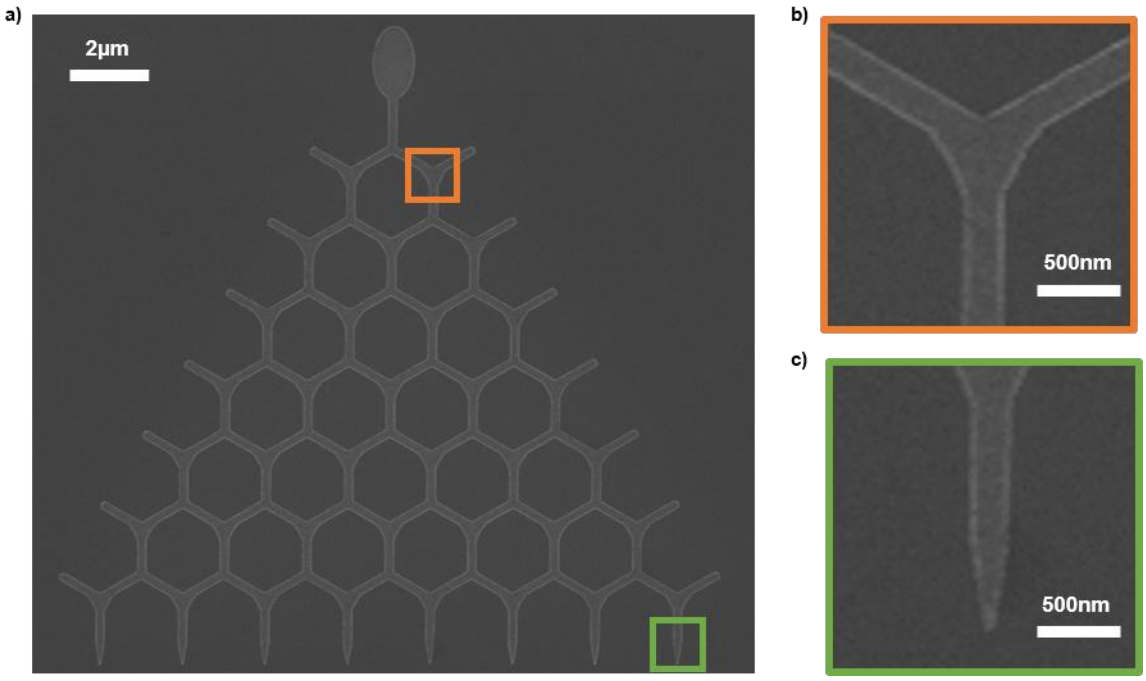

Fig.4-35: SEM images of a) our optimised 7-stage structure; b) with rounded pinning points and c) sharpen outputs.

We will show in the next section that this optimisation in indeed efficient for avalanche-like reversals with stochastic choices at the intersections with the characterisation of the reversals observed on a larger experimental set than presented up to now.

4.4.2. Propagation scenarios

This section is dedicated to the reversals observed in our structure and its relevant scenarios: single cascades (or avalanche-like reversals) and the various multi-cascades scenarios. We will show that the optimisation made is indeed a success for both avalanche and stochastic behaviours. All experiments presented are the result of a similar field protocol as before (shown in Fig.4-8): saturation at +1000 Oe, then starting at –164 Oe, we increment the field in steps of –12 Oe. We have made this choice based on our previous observations that at –200 Oe, the domain wall nucleated from the pad is already injected. This way, we will have an accurate field value for its injection and propagation.

4.4.2.1. Single Cascade scenario

We have shown previously that obtaining the hoped avalanche behaviour with a control of its starting point is actually complex and needed an adequate optimisation. Out of the 229 experiments performed on a unique structure, we have found that 120 experiments (52% of the set) exhibit avalanche behaviour with various paths taken to activated 1 of the 8 outputs of the system. Two experiments are shown in Fig.4-36.

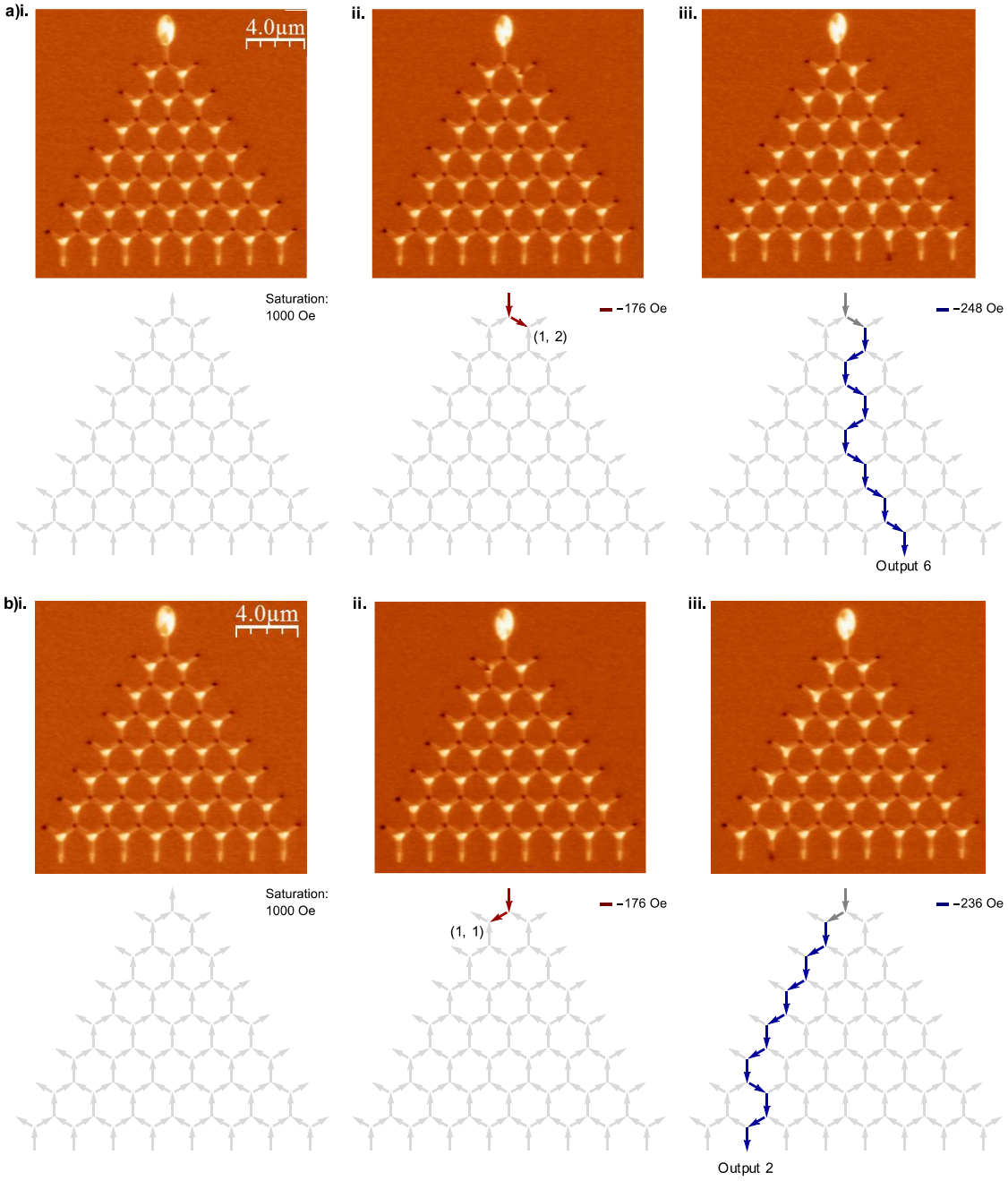

Fig.4-36: Examples of chain-like reversals forming a cascade reaching one output of the structure: a)i. after having saturated the array, ii. red spins reverse at –176 Oe: the domain wall is injected and propagates through the first intersection and gets pinned at pinning point (1, 2), iii. blue spins reverse at –248 Oe: the domain wall gets depinned and propagates throughout the structure to output 6; b)i. after having saturated the array, ii. red spins reverse at –176 Oe: the domain wall is injected and propagates through the first intersection and gets pinned at pinning point (1, 1), iii. blue spins reverse at –236 Oe: the domain wall gets depinned and propagates throughout the structure to output 2. In darker grey are represented the spins that have flipped at lower fields.

The first experiment shows that after saturation (Fig.4-36.a)i.), when applying –176 Oe, the domain wall nucleated from the pad is injected and has propagated through the first intersection. The domain gets trapped at pinning point (1, 2) thus having made a right choice (red spins in Fig.4-36.a)ii.). This pinning is overcome when a field of –248 Oe is applied, the domain wall follows its course up throughout the structure to output 6 (blue spins in Fig.4-36.a)iii.).

In the second experiment, the steps are similar: after having saturated the array (Fig.4-36.b)i.), when applying –176 Oe, the domain has made a left choice at the first intersection and gets pinned right after (red spins in Fig.4-36.b)ii.); then, it is depinned when applying –236 Oe and an avalanche activating output 2 is observed (blue spins in Fig.4-36.b)iii.).
Both experiments show that the behaviour on a single structure is indeed stochastic with two different paths taken to activate an output. The experiment presented show reversals in two steps: pinning after the first intersection (pinning points (1, 1) and (1, 2)) and then chain-like reversals activating an output. Similar avalanche scenarios were observed with more pinnings as shown in Fig.4-37.

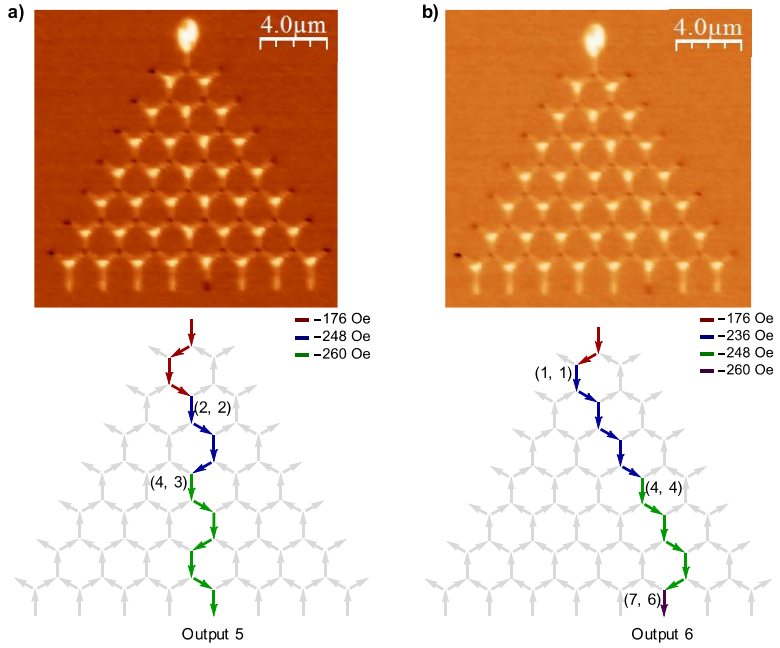

Fig.4-37: a) Experiment with chain-like reversals in 3 events: at –176 Oe, injection and propagation of the nucleated domain wall in the pad up to pinning point (2, 2); at –248 Oe, depinning and propagation of the domain wall up to pinning point (4, 3); at –260 Oe, depinning and domain wall propagation up to output 5. b) Experiment with chain-like reversals in 4 events: at –176 Oe, injection and pinning of the domain at intersection (1, 1); at –236 Oe, depinning and propagation up to pinning point (4, 4); at –248 Oe, depinning and propagation up to pinning point (7, 6) and at –260 Oe depinning and activation of output 6.

The experiment presented in Fig.4-37.a) shows chain-like reversals in three steps. The first one is observed at –176 Oe that is injection of the domain wall form the pad and propagation up to pinning point (2, 2) (identified as red spins). Then, when applying –248 Oe, the domain gets depinned and passes two stages up to pinning point (4, 3) (identified as blue spins). The domain wall gets depinned and an output is finally activated when –260 Oe is applied (green spins). All steps together form and avalanche from the pad to output 5.
In Fig.4-37.b), we present a four-step process observed also forming a chain-like propagation. The domain wall is injected and propagates through the first intersection at –176 Oe (red spins). It gets depinned from pinning point (1, 1) and propagates to pinning point (4, 4) (blue spins). Applying –248 Oe allows the avalanche to resume up to pinning point (7, 6) (green spins) and another field increment is required to depin the domain wall and activate output 6 (purple spin).

Experiments presented here demonstrate avalanche behaviour therefore suggesting that the optimisation made on our 7-stage structure is actually efficient. We have also shown that choices at the intersections are stochastic within the same structure in the same conditions. The avalanche process can occur in two to four events that is from one to three pinnings. This specific feature strongly suggest that we are

witnessing a propagation of the domain wall injected from the pad to the end of the structure. Although we cannot say with certainty that it is the case, looking at the events after the output is activated underpins the propagation argument. Two examples are shown in Fig.4-38.

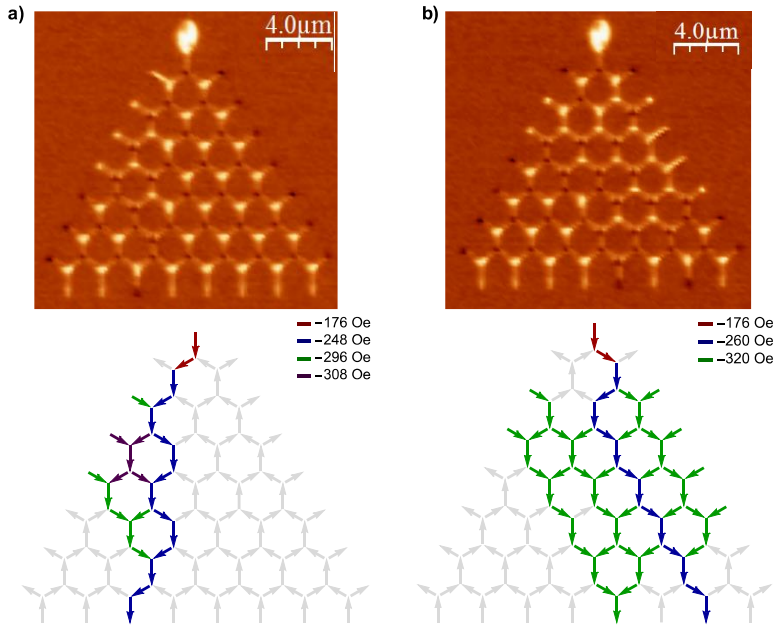

Fig.4-38: Examples of experiments with chain-like reversals and the reversals after the output is reached: a) output 2 is activated after a 2-step avalanche at –176 Oe and –248 Oe, then at –296 Oe green spins reverse starting from pinning point (6, 3) along with outer second left diagonal element and at –308 Oe, purple spins reverse from pinning points (4, 1 and 2) up to both upper elements of pinning point (3, 1).

In the two-step avalanche scenario showed in Fig.4-38.a), output 3 is activated after having applied –248 Oe. The spin configuration with its avalanche does not evolve for another 4 field increments that is –296 Oe. At this field, we observe reversals at two locations: between pinning point (6, 3) up to intersection (5, 2) and the fourth edge element on the left side and between pinning point (2, 1) and second edge element also on the left side (green spins). Adding one field increment we observe supplementary reversals between pinning points (4, 1) and (4, 2) up to both upper elements of pinning point (3, 1) (purple spins).
In the other avalanche scenario of Fig.4-38.b), the avalanche activating output 6 is complete after applying –260 Oe. Another 5 field increments are required to modify the spin configuration that is applying –320 Oe. We find that numerous spins have reversed on the sides of the avalanche up to output 5 in this case.
With both examples, we find that further reversals after the avalanche are connected to the ones that have reached the output. Although reversals can reach an output (Fig.4-38.b)), we find that there is always more than one field increment after further reversals.

In this section, we have shown that some experiments exhibit avalanche behaviour, that will be referred to as Single Cascades from now on, and that the choices at the intersections are stochastic. The presented experiments show avalanches in at least two events and up to three or four events (Fig.4-36.a) and b), Fig.4-38.a) and b) respectively). We cannot assert if we are witnessing a propagation induced by the injected domain wall by the pad by it seems a -more than- reasonable assumption. Studying the reversals after an output is activated show that reversals observed after are most of the time connected to the cascade but can also include outputs. We note that there is a field gap to observe any further modifications of the spin configuration suggesting that an adequate filtering in field can allow to extract only the cascade in at least most of the cases.

4.4.2.2. Multi-Cascades scenarios

We have seen that our optimised 7-stage structure exhibits, in a majority of the set, avalanche behaviour with stochastic path choices. However, as its predecessor the 2-stage structure, it is not perfect since other propagation scenarios were observed. We present here the other scenarios where several cascades are observed.

4.4.2.2.1. Two Activated Outputs

In 10 out of our 229 experiments (4%), we observe that two outputs were activated at the same field step, referred to as Two Activated Outputs scenario. An example is shown in Fig.4-39.

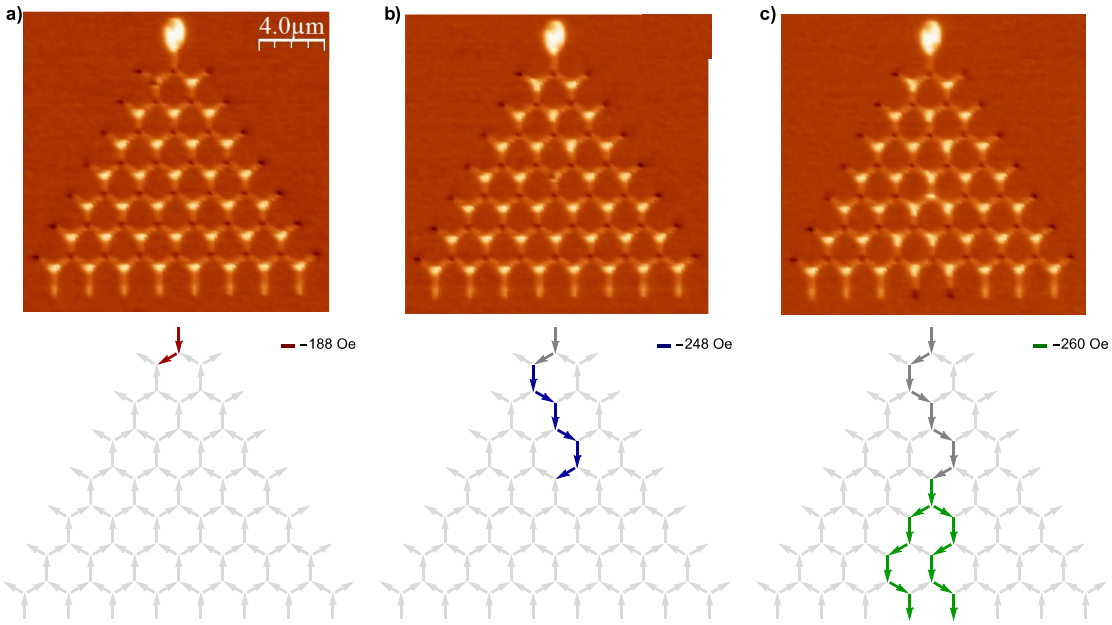

Fig.4-39: Experiment with a domain propagation in three events: a) at –188 Oe, injection and propagation of the nucleated domain wall up to pinning point (1, 1); b) at –248 Oe, depinning and propagation of the domain wall up to pinning point (4, 3); c) at –260 Oe, depinning and propagation with intersection (5, 3) being a splitting point. Spins in darker grey have reversed at lower fields.

The first event occurs when applying –188 Oe the domain wall is injected and stays pinned at pinning point (1, 1) after having passed the first intersection (Fig.4-39.a)). The second event is observed after applying –248 Oe, the propagations resumes up to pinning point (4, 3) (Fig.4-39.b)). Then, applying –260 Oe, we find a branching scenario -with the activation of both elements of the intersection- at the following intersection, that is intersection (5, 3) (Fig.4-39.c)). Each diagonal reversal result in avalanche of their own activating output 4 and output 5. The branching scenario is the most reasonable assumption since whenever observing both diagonal elements activated, it was always at the same field step.

This propagation scenario takes 1 to 3 events or up to 2 pinnings to reach two outputs. We remark upon that whenever pinnings are observed in this propagation scenario, it is always before the propagation splits its course.

4.4.2.2.2. Lost propagation

We describe here the last propagation type observed in four of our 229 experiments what will hereinafter referred to as Lost propagation scenario. A typical example is shown in Fig.4-40.

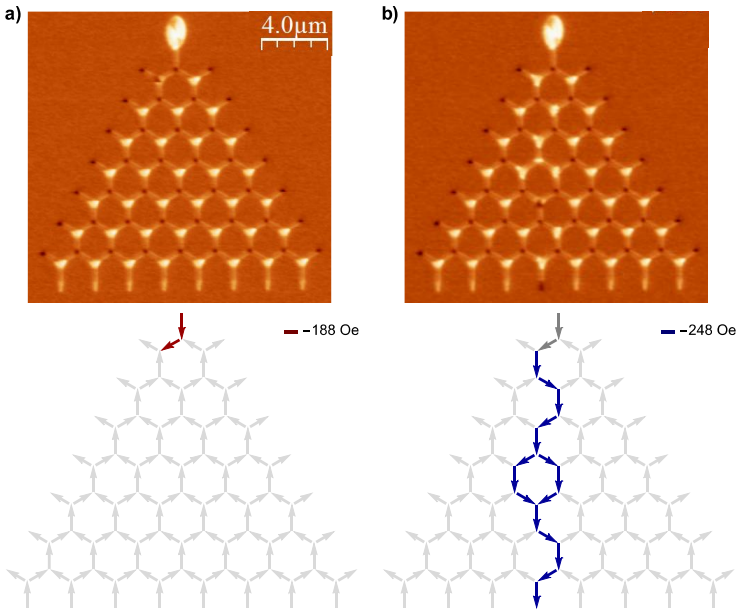

Fig.4-40: Example of ambiguous path to reach the end of the structure: a) at –188 Oe, injection and domain wall propagation from the pad to pinning point (1, 1); b) at –248 Oe, depinning and chain-like reversals up to intersection (4, 2) at which both diagonal elements have reversed, following reversals join at pinning point (5, 3) then activate output 4. Spins in darker grey have reversed at lower field.

The experiment presented in Fig.4-40 is a two-step propagation. First, after having saturated the array, when applying –188 Oe, the domain wall is injected and propagates through the left side of the first intersection. Applying –248 Oe depins the domain wall and reversals occurred up to output 4. Successive reversals are observed up to intersection (4, 2), at the following stage, both intersections (5, 2) and (5, 3) are activated on right and left sides respectively. The reversals then join at pinning point (5, 3), then a single cascade activates output 4.

Here, we cannot assert about how the reversals occurred between intersection (4, 2) and pinning point (5, 3), the propagation is kind of lost. It could be that at intersection (4, 2) a splitting of the avalanche like in a Two Activated Outputs scenario. It could also be a backward propagation (defined in section 4.4.3) starting from pinning point (5, 3) up to intersection (4, 2). We note that no pinnings were observed in these experiments in between the points where propagation is lost and the output is activated, as it was for the Two Activated Outputs scenario.

4.4.2.2.3. The puzzling ones

In our study of the reversals induced by the nucleated domain wall from the pad, three experiments were left with no match with any of the proposed scenarios (Single Cascades, Two Activated Outputs and Lost Propagations). The experiments are shown in Fig.4-41.

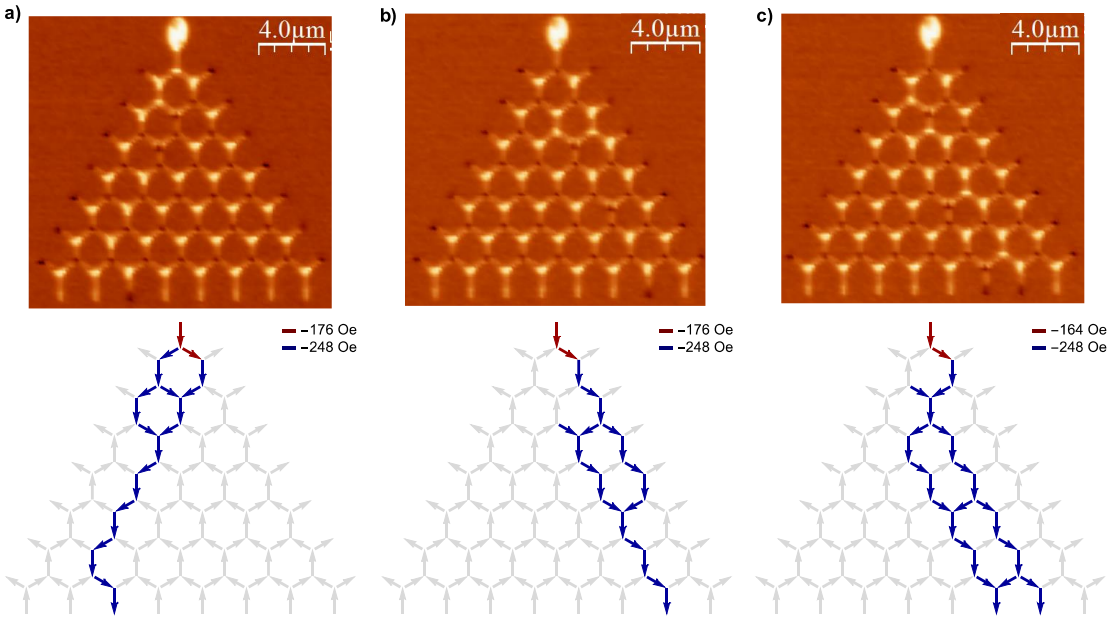

Fig.4-41: The only three experiments with unexpected reversals.

The experiments of Fig.4-41 are a two-step process with pinning at (1, 2) after having applied –176 Oe (Fig.4-41.a) and b)) and –164 Oe (Fig.4-41.c)). Then, applying –248 Oe (Fig.4-41.a)-c)), we observe multiple splitting points (as shown in Fig.4-39.c)) and points where propagations are joined (as in Fig.4-40.b)). As can be seen, it is difficult to relate to any of the previously defined propagation scenarios.

We emphasise that these are the only three experiments that we could not explain representing only 1% of the experimental set.

4.4.3. Backward propagations

We have just presented the typical scenarios observed in our experimental set, however, one might have noted that we have left out 92 experiments. These experiments belong to the scenarios presented before if additional reversals are taken into account. We qualify these reversals as backward propagations that are most likely induced by the funnel shape of our optimised structure. These backward propagations are displayed in various forms that will be presented here.

4.4.3.1. Additional reversals observed

On the remaining experiments, we have observed an unexpected feature that seems to be specific of the shape of our system. A first example is shown in Fig.4-42.

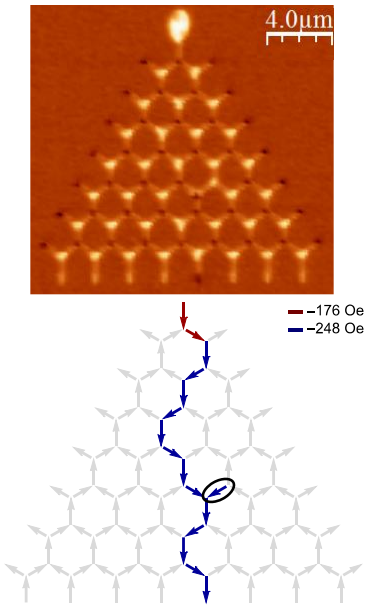

Fig.4-42: Experiment exhibiting a Single Cascade propagation with an additional reversal at pinning point (5, 4) (circled in black).

The experiment is a propagation in two steps: first pinning at (1, 2) after having applied –176 Oe then 14 reversals reaching output 5 after applying –248 Oe. We notice in the second event an avalanche with an additional reversal next to it between pinning point (5, 4) and intersection (5, 4). This reversal (circled in black in Fig.4-42) does not create a high-energy state since the vertex (pinning point (5, 4)) is in a 2-in/1-out configuration. This additional reversal makes the avalanche two-dimensional.

This type of additional reversal has been observed in various forms: as a single reversal at a unique location (as in Fig.4-42) but also at more than one location as shown in Fig.4-43.

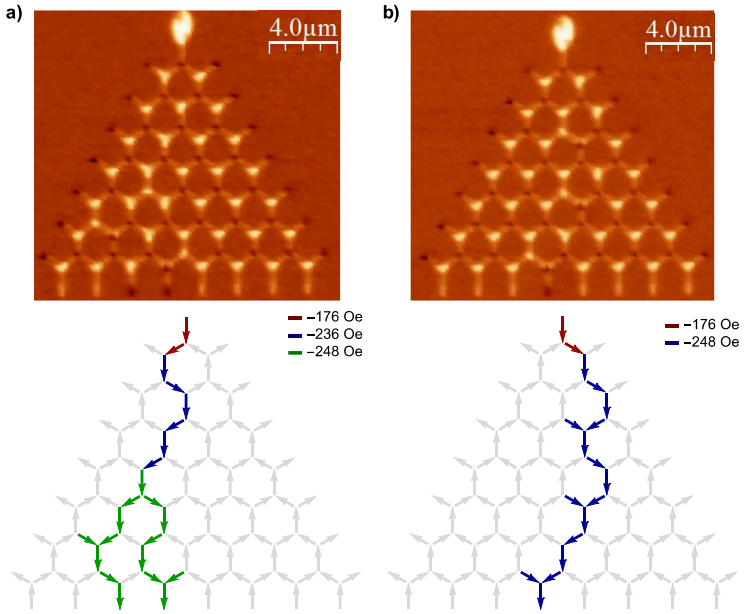

Fig.4-43: Examples of single backward propagation (one additional spin reversed) at multiple locations in a) within a Two Activated Output propagation, at 2 locations pinning points (6, 2) and (7, 4) and b) within a Single Cascade at 3 locations pinning points (3, 3), (5, 4) and (7, 4).

In Fig.4-43.a), we present a propagation in three steps resembling a Two Activated Outputs scenario (as defined in section 4.4.2.2.1). At –176 Oe, the domain wall is injected by the pad and propagates through the first intersection and gets trapped at pinning point (1, 1). Then, applying –236 Oe, the domain wall further propagates and gets pinned at pinning point (4, 2). At –248 Oe, outputs 3 and 4 are activated through two avalanches with additional reversals at pinning points (6, 2) and (7, 4). Here we have observed a Two Activated Outputs scenario with two additional reversals. We emphasise that these reversals are observed at the same field as the reversals belonging to the main avalanche they are connected to although we cannot assert exactly at which field they appear.
In Fig.4-43.b), we observe a single cascade-like scenario with three additional reversals observed connected to the avalanche reaching output 4 at pinning points (3, 3), (5, 4) and (7, 4).

We qualify the additional reversals detailed in the three examples shown in Fig.4-42 and Fig.4-43 as backward propagations because connected to a known propagation scenario and on the opposite direction of the applied field. These backward propagations have been observed in the form of a single flip at 1, 2 and 3 locations on the main avalanche(s) were observed in 65, 12 and 2 experiments respectively. We present in Fig.4-44, the other types of backward propagations observed.

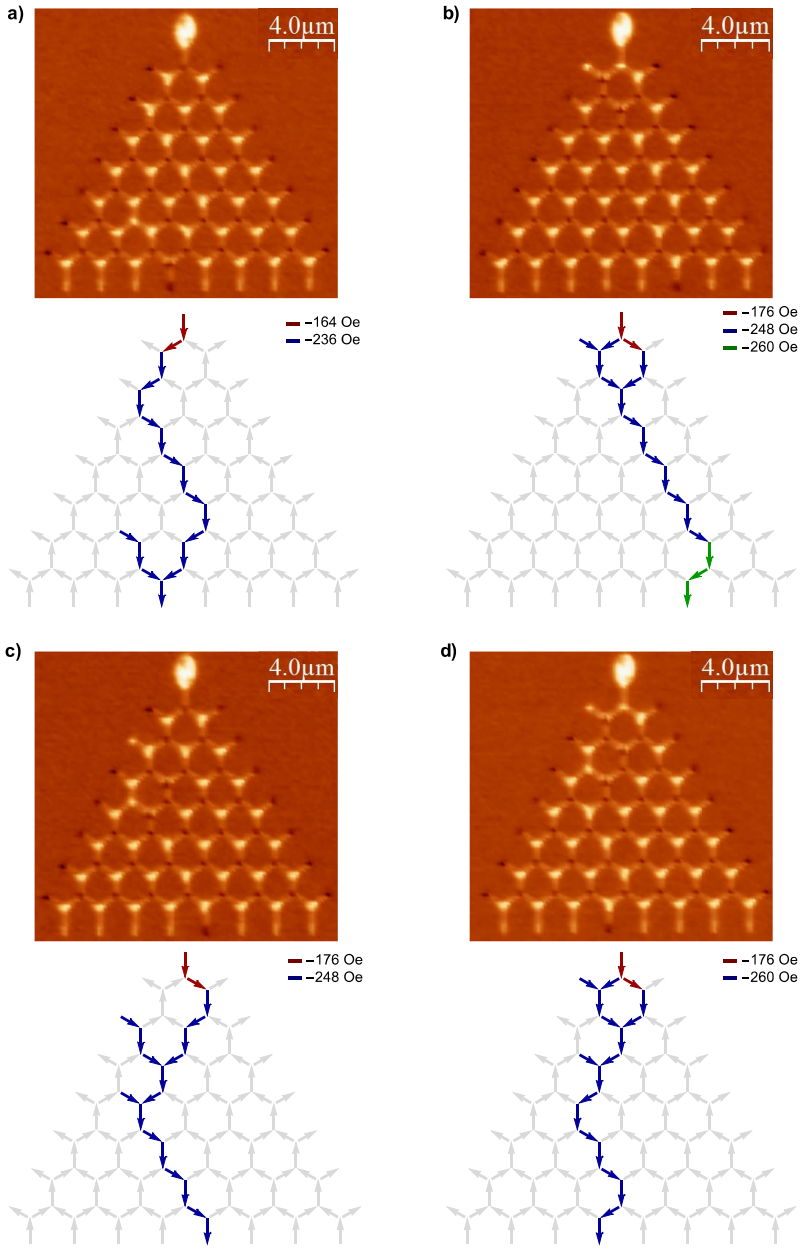

Fig.4-44: Experiments with multiple backward propagations within Single Cascades: a) 3-element-long backward propagation at pinning point (7, 4); b) 4-element backward propagation starting at pinning point (2, 2); c) 3-element and single backward propagations starting at pinning points (3, 2) and (5, 2) respectively and d) 4-element and single backward propagations at pinning points (2 2) and ((3, 2) respectively.

In Fig.4-44.a) and b), we show examples of backward propagations of 3- and 4-element long. The first one exhibits a main single cascade reaching output 4 in which three additional reversals starting from pinning point (7, 4) up to intersection (6, 2) are observed. The second example has a main single cascade with four additional reversals starting from pinning point (2, 2) up to both upper elements of pinning point (1, 1). Here, the backward propagation was effectively observed at the second event but reaches reversals of the first event belonging to the main cascade.

We now present two typical experiments with multiple backward propagations. The first experiment (Fig.4-44.c)) exhibits two backward propagations: a 3-element long starting at pinning point (3, 2) up the second element on the side and a single one starting at pinning (4, 2). The second experiment (Fig.4-44.d)) also exhibits two backward propagations: one that is 4-element long starting at pinning

point (2, 2) and the second one a single reversal starting from pinning point (3, 2). We mention that whenever 4-element backward propagations are observed, they are always located pinning point (2, 2) up to both sides of pinning point (1, 1) as in Fig.4-44.b) and d). The presented backward propagations are all connected to the main propagation scenario that is in the cases of Fig.4-44 single cascades.

We observed in five experiments 3-element long backward propagation (as in Fig.4-43.a)); 4-element long backward propagation (as in Fig.4-43.b)) was observed only in twi experiments on the set. The 3-and-1 backward propagation (as in Fig.4-43.c)) was observed in five experiments and the 4-and-1 backward propagation (as in Fig.4-43.d)) only once.

We take this opportunity to comment about our choice to make the Lost Propagation scenario (presented in section 4.4.2.2.2) and the puzzles (presented in section 4.4.2.2.3), propagation scenarios of their own. In the case of Lost Propagation scenario (Fig.4-40), we cannot assert with the spin configurations if we are witnessing is the domain wall propagation splitting its course like a Two Activated Outputs scenario and then the two created propagations joining or if it is a 3-element backward propagation starting from the pinning point to the intersection above. Similar reasoning can be applied to the puzzles, although some reversals can be considered as backward propagation, we cannot conclude about their nature.

The backward propagations, observed in 92 experiments, cover all propagation scenarios presented in the previous section (we do not consider the puzzling ones). Therefore, over our entire experimental set, we have observed a total of 145 reversals summarised in Fig.4-45 according to their location on the array along with their starting points.

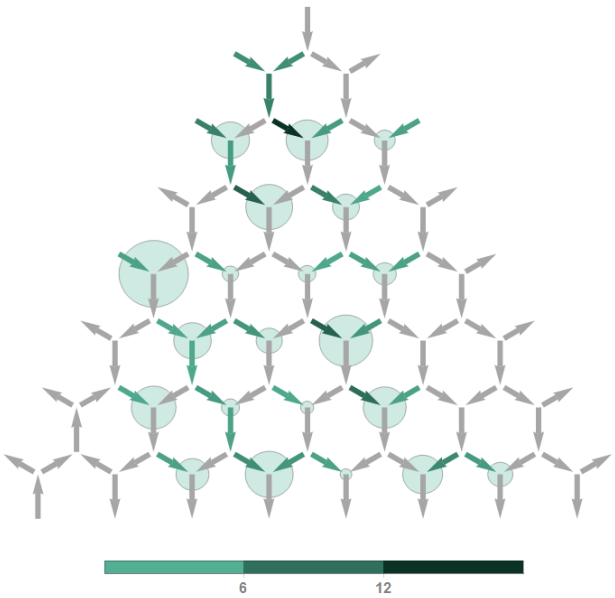

Fig.4-45: Summary of the backward propagations. Disks represent ratio starting point of backward propagation out of the number of domain walls passing by in the entire set. Spins belonging to backward propagations are coloured in green levelled in their occurrence. Spins that flipped at least once over the entire set are drawn pointing down.

We remark upon that an even number of successive reversals composes the backward propagations observed that do not create any high-energy state whereas an odd number of reversals would. The 4-element backward propagation always occurring at the same location does not create either a forbidden state since both upper elements of the pinning point reverse. No more than four elements compose the observed backward propagations. We also observe that all 3-element long backward propagations are always one-dimensional chains and flip always the elements on the left side. We find a clear tendency

to flip the upper left spin of the pinning point (89 on the left side and 26 on the right out of 145). We find that out of the 145 backward propagations, no more than 19 times a given spin reverses due to this phenomenon (see scale in Fig.4-45).
Studying the starting point of the backward propagations, we find that some potential pinning points of the structure are more subject to backward propagations. Indeed, looking at stages of pinning points, at stages 2, 3, 5 and 7, a greater number of backward propagations (in proportions compared to how many domain walls have passed by) are observed starting from there than at stages 4 or 6. However considering the finite –and quite small- size of our experimental set, we cannot conclude if specific potential pinning points are more subject to backward propagations than others.

We have observed 142 spins starting backward propagations (that can be 1-, 3- or 4-element long), we can compare it to the number of pinning points passed over the entire set. Overestimating it at $7 * 229$ (in the case multi-cascade scenarios more than 7 pinning points are passed through), we find that $142/(7 * 229) \approx 8\%$. We conclude that whenever a domain wall passes at a potential pinning point, it has 8% chance to induce a backward propagation. Therefore, although we observed a large amount of these backward propagations, it is not a feature that is likely to appear a lot at the pinning points of our structure.

4.4.3.2. Discussion

We have presented the different types of backward propagations observed in 40% of the set (92 experiments) connected to cascades of the typical single- or multi-cascade scenarios (Fig.4-42 and Fig.4-43). We want to determine whether this phenomenon is the result of a supplementary nucleation (as shown in Fig.4-38.a) after the output is reached) or occurs during the crossing of the domain wall by the funnel shape.

Using magnetic force microscopy, the only information about the timing of these additional reversals is at which field they are observed. However, we find that whenever there is a backward propagation, it is connected to the portion of main propagation observed, even if the propagation takes several events as shown in Fig.4-46.

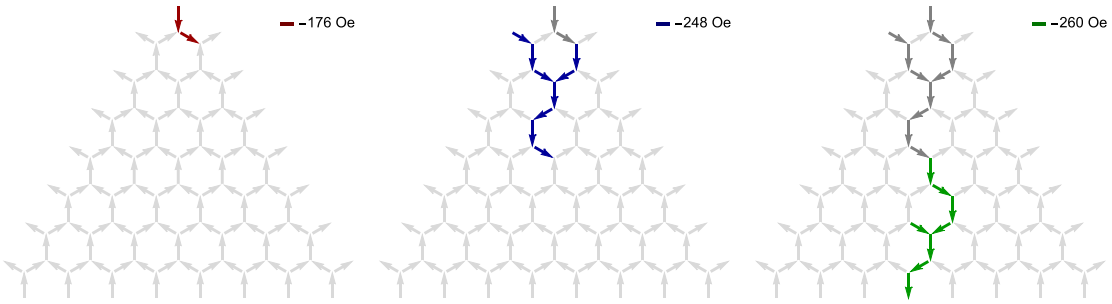

Fig.4-46: Spin configuration of a single cascade with at the second event 3-element backward propagation starting at pinning point (2, 2) and at the third event a single backward propagation starting at pinning point (6, 4).

This observation suggests that the backward propagation occurs on the course of the domain wall at potential pinning points and a few evidences support this theory. We propose in Fig.4-47, two possible scenarios for single backward propagations connected to a single cascade (with the aim of simplifying) that were *never* observed.

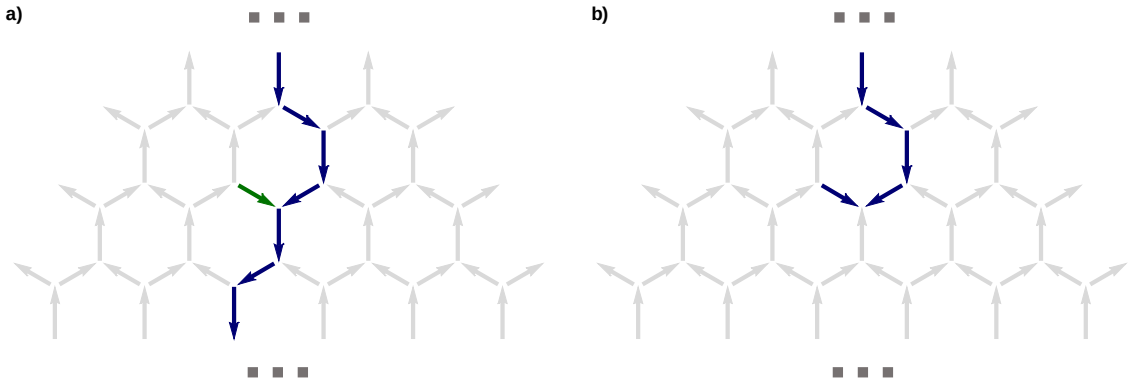

*Fig.4-47: **Never** observed scenarios of backward propagation.*

In Fig.4-47.a), we show a portion of single cascade within the structure occurring at an event (arbitrarily the second one), and a backward propagation appearing at the following event (arbitrarily at the third one). This peculiar possible scenario would suggest that the backward propagation could occur after the domain wall has made its course throughout the structure and being the result of an additional nucleation. In Fig.4-47.b), we show a similar single cascade where the domain wall gets pinned and at this very point a single backward propagation, all happening during the same event. This time, this possible scenario would suggest that the backward propagation could happen without the domain wall passing through the pinning point of interest, indicating that the crossing of domain wall has no consequence on the additional reversal. This scenario creates a 3-in configuration at the pinning point which was never observed in the experimental set.

These two hypothetical scenarios were never observed in any of our experiments. This result strongly suggests that they are due to the domain wall passing the pinning points as a dynamic effect in a transitory regime most likely due to their funnel shape.

Experiments performed by scanning transmission x-ray microscopy (STXM) have allowed us insight about the magnetisation that underpinned our suspicion. These experiments -that we will not describe in detail in this manuscript- were performed at the synchrotron Soleil at the Hermes Beamline. A typical experiment is shown in Fig.4-48.

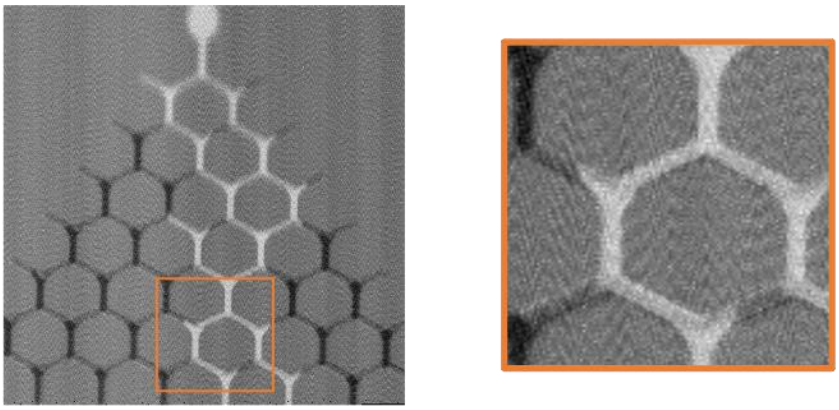

Fig.4-48: Observation of reversals using STXM of a propagation on another structure and close-up view of the framed part. White contrasts correspond to the reversed elements of the structure. Experiments performed by Dr. K. Ait Oukaci, Prof. F. Montaigne, Dr. R. Belkou and me.

Using the Two Activated Outputs scenario presented, we have observed that when having passed the potential pinning point, the domain wall enters significantly into the funnel shape and the non-reversed element. We can thus easily imagine that in some cases, the domain wall enters and reverses entirely the element inducing our backward propagation.

4.4.4. Summary of the reversals and domain wall propagating

Previously, we have shown that our optimised 7-stage structure exhibits avalanche-like reversals consistent with stochastic domain wall propagation from the pad throughout the structure. The reversals observed could be sorted in specific propagation (Single Cascade, Two Activated Outputs and Lost propagation) scenarios and backward propagations (1-, 3- or 4-element long at a unique or multiple locations). We have also seen in the experiments presented that propagation can occur in two to three steps with each time a pinning in the upper part of the structure (at low fields) and then propagation in the structure.

We summarise the reversals of our entire experimental set along with field events in tree forms -as done for the other structures- in Fig.4-49.

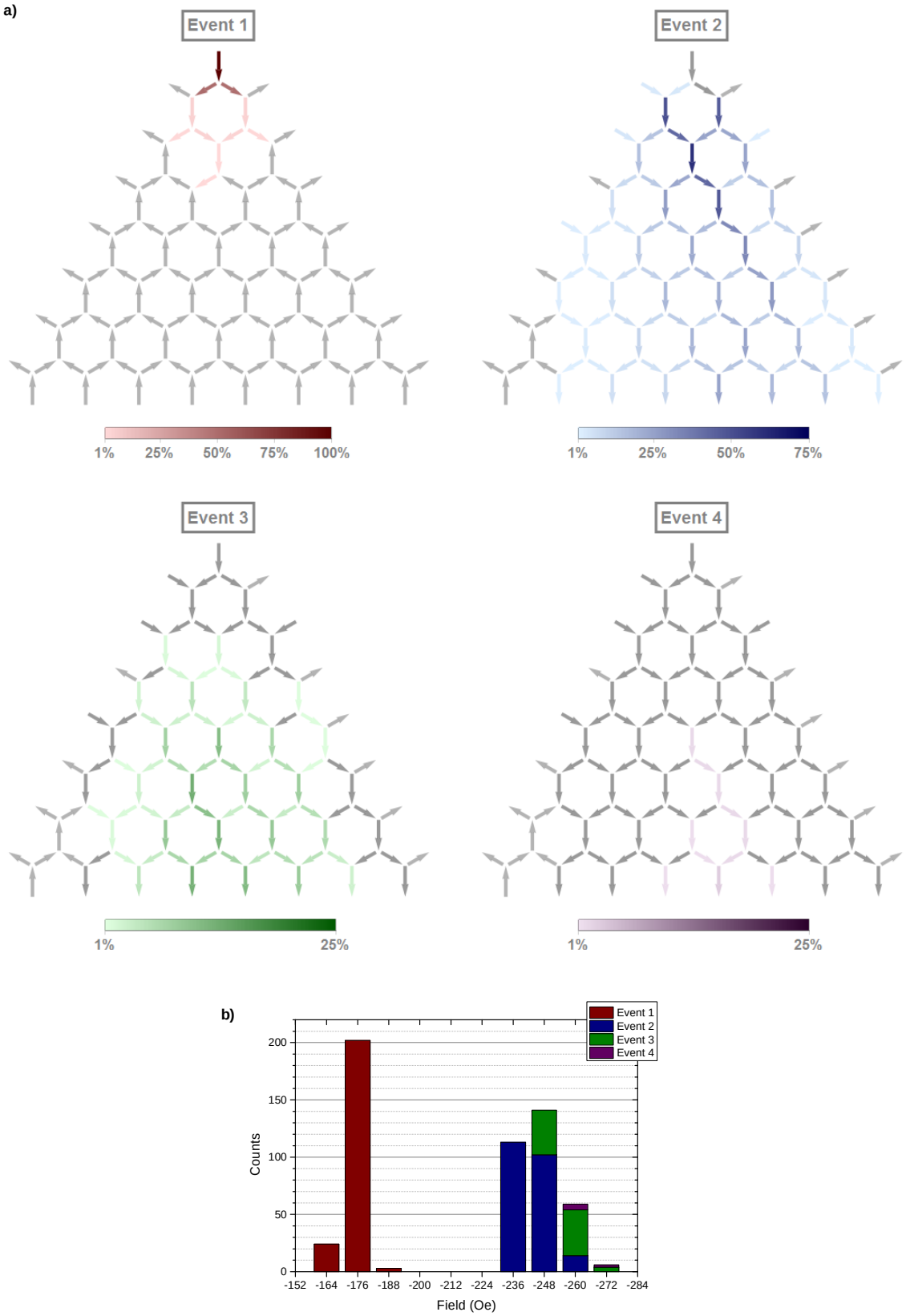

Fig.4-49: a) Reversals observed on 229 same field experiment on a single structure on four events and b) fields at which events are observed.

We observe that for all propagations, the first event is characterised by the injection and propagation in the upper part of the structure where the domain wall gets pinned. We find that in a small proportion of experiments (7% of the set), the domain wall passes the second and third stages of pinning points in 16 and one experiments respectively. In terms of field, this event takes place when applying from –164 Oe (or below) to –188 Oe.
Then the propagation inside the structure is observed from –236 Oe and up to –260 Oe, the field range to depin the domain wall from the upper part of the structure. In 142 experiments (62% of the set), this field range is enough to activate one or two outputs, thus no need of a third event. For this event, we find that most of the spins of the system have reversed over the entire set of experiments. We also observe reversals of some edge elements of the structure due to backward propagations. Outputs 2 to 8 are activated in this event.
In 90 experiments (39% of the set), a third event with an applied field from –248 Oe to –272 Oe is necessary to reach the end of the structure. At this event, reversals start from the second stage of the structure to reach outputs 3 to 8.
The rest of the set (seven experiments) needs a fourth event with a –260 Oe to –272 Oe applied field is required to finally reach the output. Reversals start from the 4^{th} stage to outputs 3 to 6.

The reversals observed show clear stochastic and avalanche-like propagations on the entire array, with no regard to the propagation scenario. This shows that our optimisation of the structure indeed has achieved the right trade-off between depinning field from the first stages of the structure and nucleation fields from the outputs. The process occurs in two steps: injection and propagation in the upper part of the structure of the nucleated domain wall in the pad at low field (between –164 Oe and –188 Oe) and then depinning and propagation in the structure (from –236 Oe and –272 Oe).

Using transmission x-ray microscopy, we have identified the type of domain walls at play in our system. Images of the same experiment as previously (Fig.4-48) are shown in Fig.4-50.

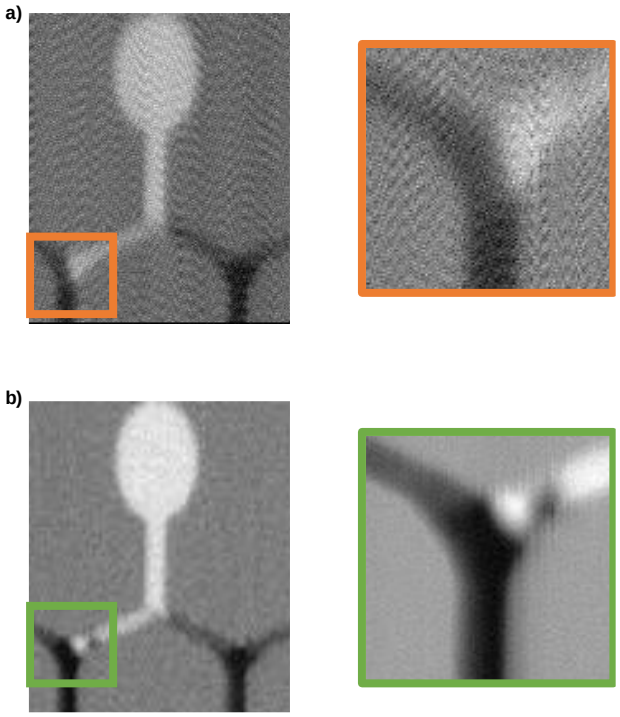

Fig.4-50: Images using STXM of two experiments with pinnings at (1, 1) on the same structure; observation of a) transverse domain wall and b) vortex domain wall.

Contrasts show that the domain wall pinned at the first pinning point is either a transverse domain wall (Fig.4-50.a)) or vortex domain wall (Fig.4-50.b)) as it can be expected with our system dimensions [89]. We mention that the vortex domain wall was observed only once out of about a dozen of experiments.

The fact that we observe at least two types of domain walls can be the source of randomness of the domain wall propagation in our system as reported by micromagnetic simulations [18,19,74,78,81,88]. The clear stochastic behaviour observed could also be due to the propagation itself between intersections. Indeed, we saw that depinning and propagation through the structure occurs at high fields, beyond Walker breakdown in the turbulent regime [90]. We can suspect that during the propagation between intersections -where choices are to be made-, changes the nature of the domain wall and therefore the choice to go left/right at the intersection.

4.4.5. Intermediate propagations

We have seen that reversals observed in our experiments are consistent with a propagation from the pad to the outputs in a process in two to four steps that is with one to three pinnings. We have summarised the pinnings observed according to their position in the structure and compare it to the number of times the potential pinning point has been passed by in Fig.4-51.

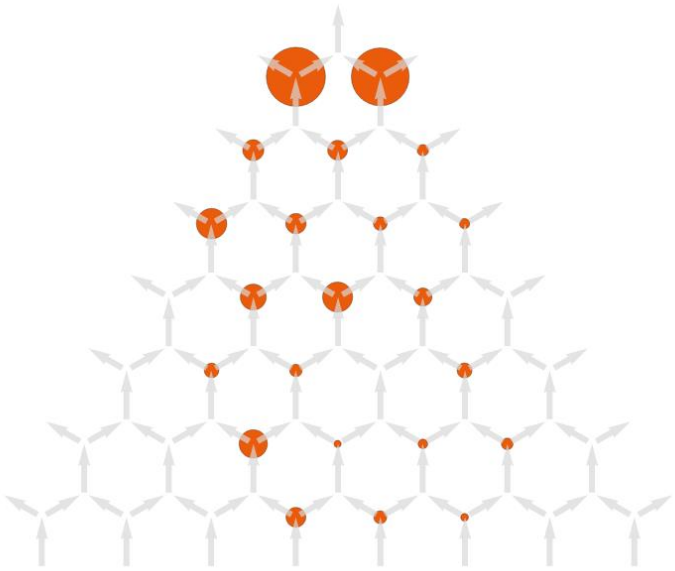

Fig.4-51:Locations of the pinnings observed in the structure. Disk size are proportional to the ratio number of domain walls pinned over the total number of domain walls having passed by the pinning point.

We find that the first stage of the structure is the major "obstacle" to pass with a total of 212 pinnings out of the 229. As mentioned before, 17 experiments in the set do not get pinned at the first stage of the structure (as the one shown in Fig.4-38.a)) demonstrating that there is non-zero probability to pass the first stage after injection.
Studying the following stages, we find much lower ratios pinned *vs.* passed ranging from 1% to 25% with a mean value 9% and standard deviation at 8%. The highest one is pinning point (3, 1) with a proportion of 25% (out of 16 domain walls in total having passed by), then pinning point (4, 3) with 21% (out of 78) and pinning point (6, 3) with 21% (out of 37). Then we have pinning point (4, 2), with 18% (out of 44) and pinning points (2, 1), (2, 2), (3, 2) and (7, 4) that are between 11% and 12% (out of 33, 142, 71, 47 domain walls having passed by respectively). The remaining are comprised between 1 and 9%.

The two aspects presented before need to be considered differently because when reaching the first stages, the field is lower than when propagating inside the structure (see field events in Fig.4-49.b)). Therefore, two phases are identified: the first one below –224 Oe where we depin from the pad and the second one, when we depin from a pinning point inside the structure.

During the first phase, we find that in 93% of the experiments, the domain wall gets pinned at the first stage, in 7% at the second stage and in less than 1% the domain wall gets pinned at the third stage. This result suggests dynamical pinning [35,91,92] with 92% chance to get pinned at each stage.
During the second phase, the field to overcome the first pinning is enough to reach the end of the structure in 62% of the experiments. In the other cases, the domain walls get pinning in maximum 25% of the cases at a handful of intersections. We have also observed that not all of our potential pinning points are actual ones as can be seen with pinning point (5, 4). In this second phase with six stages of potential pinning points to overcome, we observed a total of 97 pinnings over the set. We therefore estimate a chance of $97/(6 * 229) \approx 7\%$ for the propagating domain wall to get pinned. Although we cannot assert about how much "harder" are some points compared to others due the finite size of our experimental set, but we can assert that no potential pinning point pins systematically the domain walls passing by and the probability to observe a pinning during the propagation is actually quite low.

We have performed an observation under applied field of the depinning process using STXM. Images for pinnings at the first and fifth stages are shown in Fig.4-52.

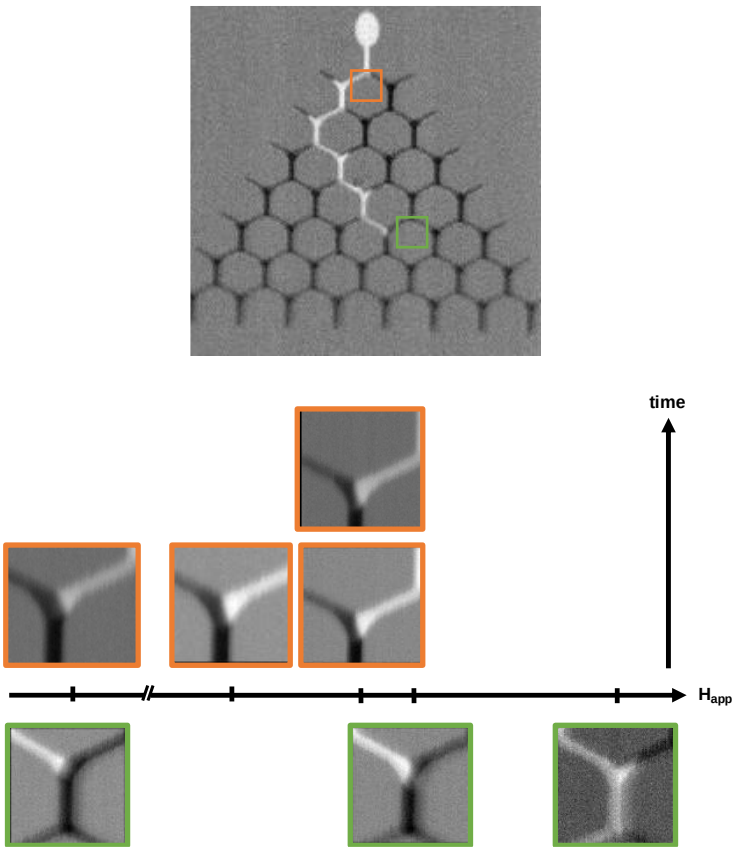

Fig.4-52: Images using STXM of depinnings at (1, 2) (orange square) and (5, 4) (green square) with increasing field and time.

We find similar behaviour for the two positions: as the field is increased, the domain wall enters progressively into the funnel shape until it reverses the next vertical element. We have also observed depinning without modifying the field only by waiting a few minutes. This last result shows that thermal activation plays an important role in the depinning process.

4.4.6. Conclusions

Domain wall propagation is a complex phenomenon and our honeycomb artificial spin system is no exception to the rule as we have shown in this section. We have presented the reversals observed in our tailored artificial spin system with funnel shapes and sharpened outputs on 229 experiments. We have shown that the propagation observed can be divided in three scenarios: the Single Cascade in which unidimensional reversals activate a single output; the Two Activated Outputs in which an avalanche at some point divides its course and activates two outputs and finally, the Lost Propagation in which reversals are unidimensional, at some point both elements of an intersection are reversed and seem to rejoin and activate a single output. Our study has also shown additional reversals in the opposite direction of the applied field taking various lengths that we have referred to as backward propagations. The proportions of each scenarios taking into account the backward propagations are shown in the pie chart in Fig.4-53.

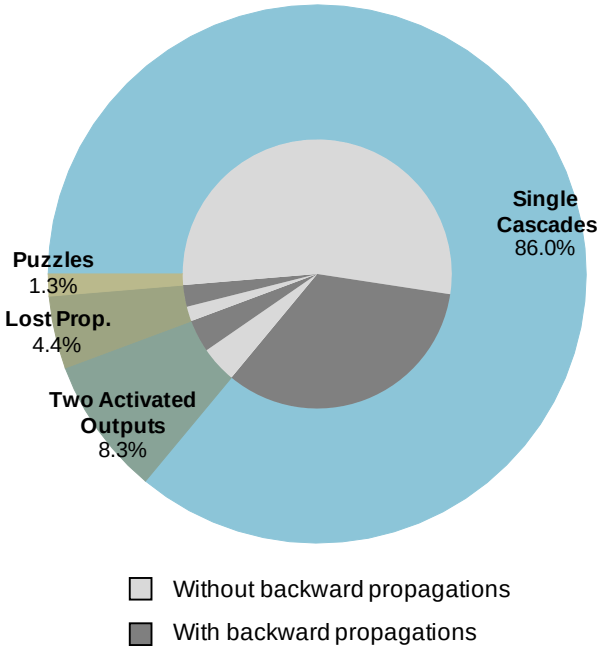

Fig.4-53: Pie chart of the propagation scenarios observed with or without backward propagations

Our exhaustive characterisation of the reversals has shown that we are witnessing the propagation of the nucleated domain wall from the pad through the structure with at low fields, injection and propagation in the upper part of the structure and at high fields, depinning and propagation. Our study has left out only three experiments unexplained. We have also shown that the domain wall induces our backward propagation because of the funnel shapes at our potential pinning points. In our study of occurrences of both backward propagations and pinning sites, we have said that although they are observed, these features of the propagation are not preponderant.
All enunciated observations demonstrate the efficiency of our optimisation for the trade-off between depinning and nucleation fields. They have also shown mainly Single Cascade propagation with or without backpropagations along with clear stochastic behaviour.
Possible explanations for the stochastic behaviour have been proposed as the nature of the domain wall passing through the intersections. But we mainly suspect the regime at which propagations occur beyond Walker breakdown introducing non-periodic evolutions of the domain wall during its propagation in between intersections.

4.5. Characterisation of our artificial spin system randomness

In the previous section, we have studied the reversals in our 7-stage optimised and shown that they are consistent with a stochastic domain propagation from the pad throughout the structure. We have seen that about half of the experiments exhibit Single Cascade scenario in which only one intersection at each stage is passed. These experiments can be easily combined with Single Cascades with backward propagations since main cascade and therefore choices at the intersections can be identified.
The topic of this section is the stochasticity of the structure by studying the choices made at the intersections. To do so, we will compare our system to the prime example of random device: the bean machine also called the quincunx machine or the Galton board.

4.5.1. Analogy with a Galton board

Named after its inventor, the Galton board is a vertical board with interleaved rows of identical pegs on top of which beads are dropped, schematics is shown in Fig.4-54.a). The beads, collected at the end of the board, have made random choice at each peg according to Bernoulli's law. Our honeycomb artificial spin system, with its 7 stages of intersections and 8 outputs, is very similar to a Galton board only with domain walls as shown in Fig.4-54.b).

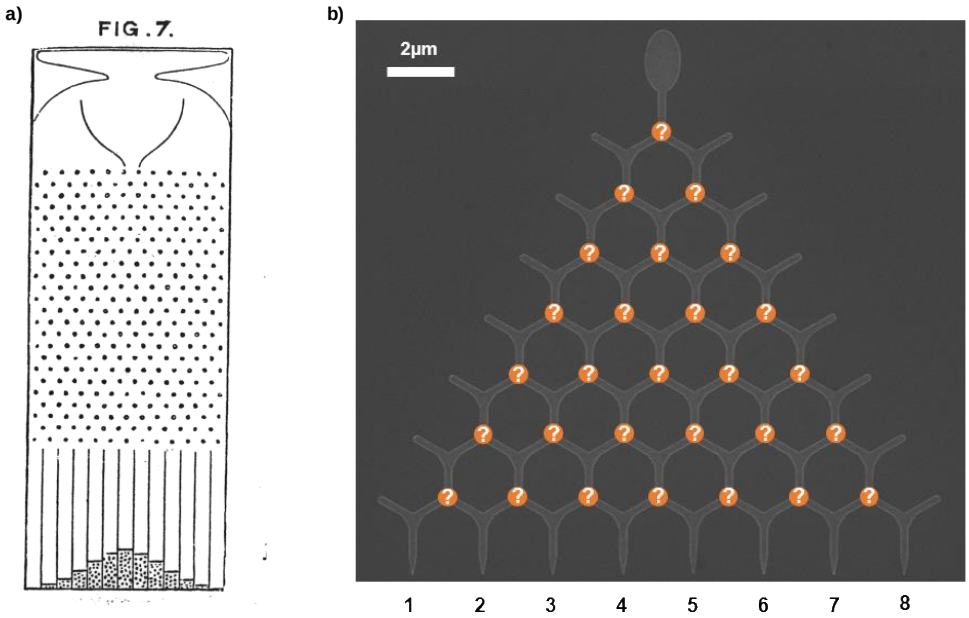

Fig.4-54: a) Schematic of the Galton Board or Quincunx machine as drawn by Sir. F. Galton [93] and b) SEM image of the nanostructure studied, marked '?' the points where the domain wall has a choice to go left or right.

If the pegs are not biased, there is a 50%/50% chance to go on one side of the peg or the other. This device is the experimental demonstration of the central limit theorem showing the convergence between binomial and normal distributions. The convergence is met only if enough experiments are performed. We show in Fig.4-55 distributions for 50, 10,000 and 197 variates.

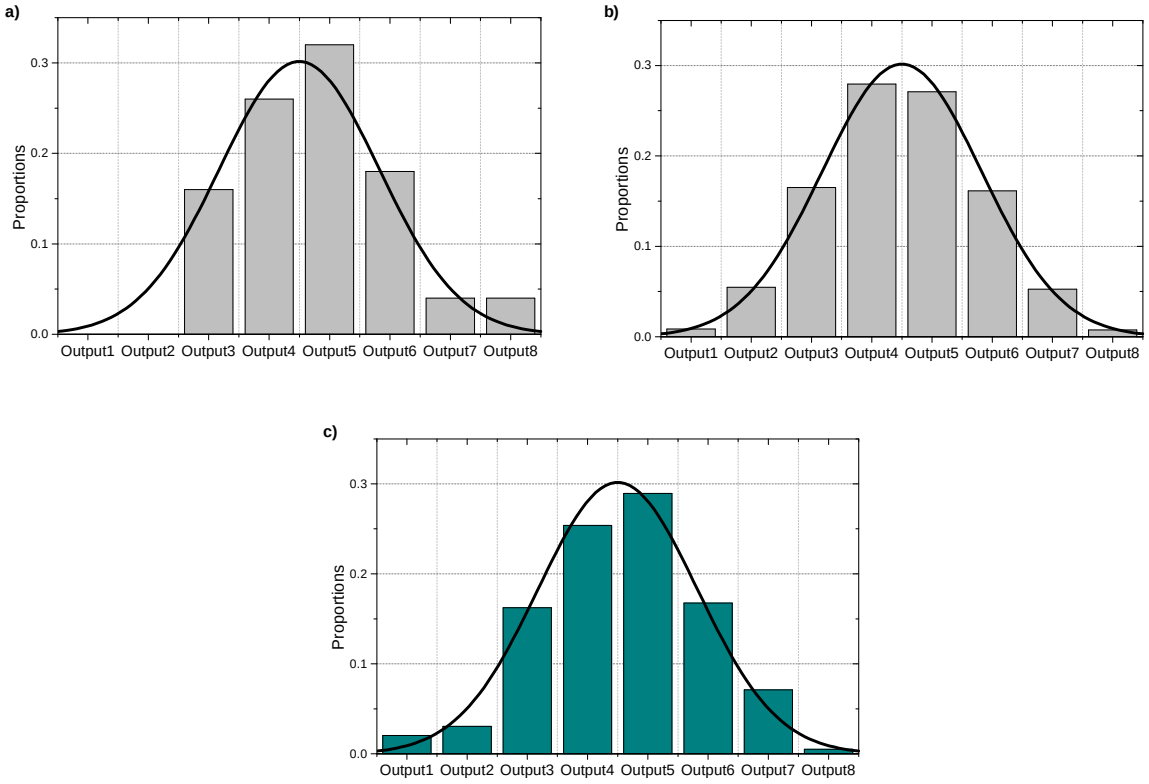

Fig.4-55: random generations of a binomial distribution with p=50% and 7 choices computed with b) 50, c) 10 000 and d) 197 variates. The latter is the size of our experimental set. Gaussian fits have mean value of 3.5 and σ^2 = 7/4.SEM image of the nanostructure studied, marked '?' the points where the domain wall has a choice to go left or right.

In our examples, the random distribution of 50 variates (Fig.4-55.a)) is far from a normal distribution (with mean value of 3.5 and σ^2 of 7/4) compared to the one with 10 000 variates (Fig.4-55.b)) as predicted by the central limit theorem. In the case of 197 variates, that is the size of our experimental set (Fig.4-55.c)), the distribution approaches indeed the one of a binomial distribution.

The goal of this section is to determine if our system is stochastic as a Galton board, biased or not, therefore two requirements to meet:

(i) all intersections have same probability to go left/right;

(ii) choices at the intersections are independent.

In order to study the stochastic behaviour of our 7-stage optimised structure, we filter the propagation scenarios resembling a bead falling into a mechanical Galton board and keep only the Single Cascades (with or without backward propagations). This shrinks our experimental set to 197 experiments which is enough for a good characterisation of its stochastic behaviour.

4.5.2. Experimental weights and output distribution

In order to ascribe a unique probability to go left/right to our system, we use all our Single Cascade scenarios without and with backward propagations. In this study, we focus exclusively on the paths taken to reach the end of the structure and especially the choices made at the intersections by the domain wall propagation. In our MFM images, we now study the paths taken using the method presented in section 2.2.2.2. We first determine the statistical weights to go left/right for each intersection by proceeding as shown with the two Single Cascades one without and the second with backward propagations in Fig.4-56.

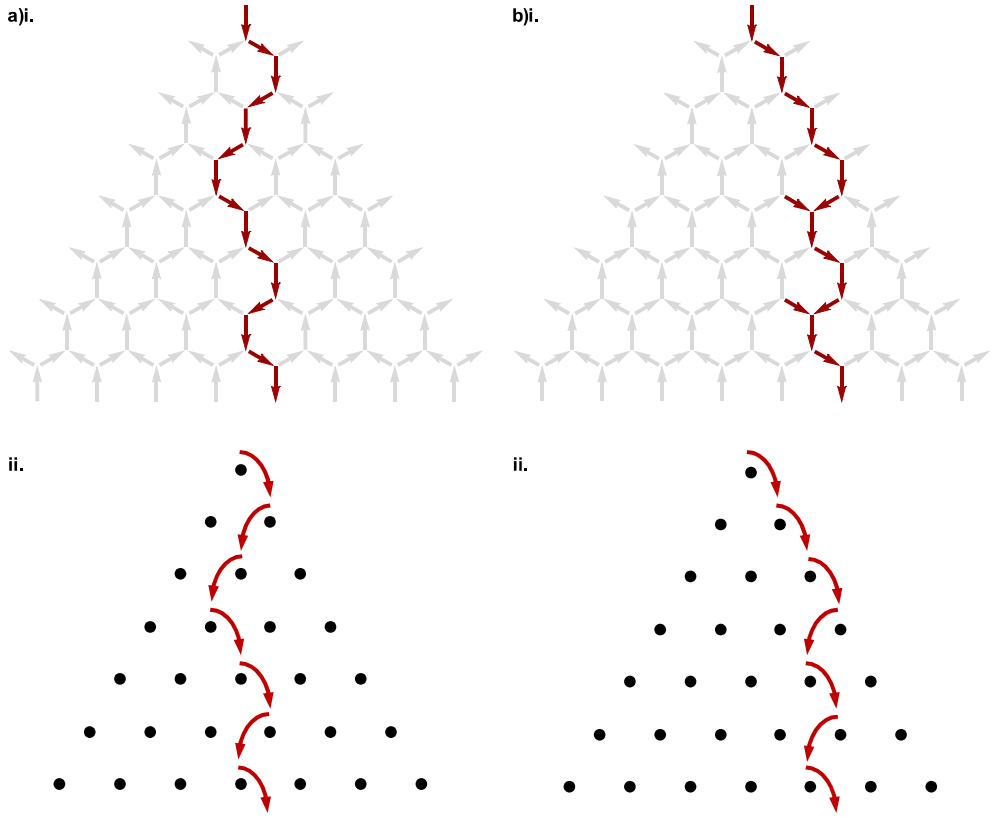

Fig.4-56: Two Single Cascade propagations a) without and b) with backward propagations and ii. how choices at the intersections (black dots) are counted both the two propagations.

On a plain Single Cascade (Fig.4-56.a)) the choices and therefore the analogy with the Galton board is straightforward. On a Single Cascade with backward propagations (with two single backward propagations in Fig.4-56.b)), the choices are identified by focusing only on the intersections. We see that it is possible to perform the same analysis as already mentioned before.
We have performed the same characterisation for each of our 197 Single Cascades. We summarise our results by counting the total number of times the domain wall has passed left or right reported to the total number wall passing for each intersection. The ratios for all our experimental set are shown in Fig.4-57.

Fig.4-57: Statistical weights at each intersection (black dots) over our 197 Single Cascade propagations with and without backward propagations: a) in ratios with absolute numbers and b) in percentage. In green, the proportion of domain walls going left and in orange going right. The ratios are to be read as in the denominator the domain walls having arrived at the intersection, the numerator in green the number of domain walls having chosen to go left and in orange having chosen to go right. On the first three intersections, out of the 197 domain walls, 103 chose to go left and 94 right; out of the 103 having arrived at intersection (2, 1), 31 chose to go left and out of the 94 arriving at intersection (2, 2), 45 of them went right. Same reasoning for the others.

We find using Fig.4-57.a), that all 197 injected domain walls in the system considered have taken various paths to reach the end of the structure. We present the data using both ratios with absolute numbers and percentages in order to evaluate the statistics, indeed some intersections have undergone more domain walls crossing than others. For example, intersection (1, 1) 197 domain walls out of the 197 injected have passed by and at intersection (6, 2) only two and therefore the former should be more representative than the latter. Combining both approaches is therefore essential for an accurate description since the statistical uncertainty varies.
We find that the experimental weights in percentages are ranging from 8% (92%) to 80% (20%) go left (right). We also observe that one intersection (7, 1) has never been reached. Computing a simple mean value of our statistical weights, we find a value of 38% to go left with a standard deviation of 11%. We observe that some intersections of our system deviate from this mean value. This can be explained by the low statistics in the case of intersections (5, 5), (6, 2) and (7, 7) where only 20, 13 and 5 (less than 10%) out of the 197 injected domain walls have reached them respectively. In the case of intersections (1, 1), (5, 3), (5, 4) and (7, 5) it has to be explained differently since more than 25% of the domain walls have reached them. In the case of intersection (1, 1), we have seen in the previous section that its propagation mechanism is different since occurring at low fields as the result of a depinning from the pad.

This simple characterisation and comparison to a standard mean value has its flaws. First, as we have mentioned previously, some intersections are computed with more domain walls than some others for which we get more accurate statistical weights. Therefore, we can think that giving the same "weight" to all intersections in the mean value is not adequate. To remedy this, we propose an alternative method to compute the mean value by making the ratio of all domain walls having chosen to go left out of the passing by all the intersections. This value that we define as the mean value on events is computed as follow:

$$\frac{11_{left} + 21_{left} + 22_{left} + 31_{left} + \cdots + 77_{left}}{11 + 21 + 22 + 31 + \cdots + 77}$$

(Eq.7)

where nm_{left} refers to the domain walls going left at intersection (n, m) and nm the total of domain walls passing by the intersection. This approach allows to compare intersections that do not have same statistics. It could also be viewed as an alternative to a weighted mean value.
Second, we have mentioned that the first intersection undergoes a different propagation mechanism since it is the result of the depinning from the pad. In opposition to the other intersections where the choice is the result of either a propagation or depinning from a potential pinning of the structure.
We compare all statistical weights to mean values on events computed with and without the first intersection in Fig.4-58.

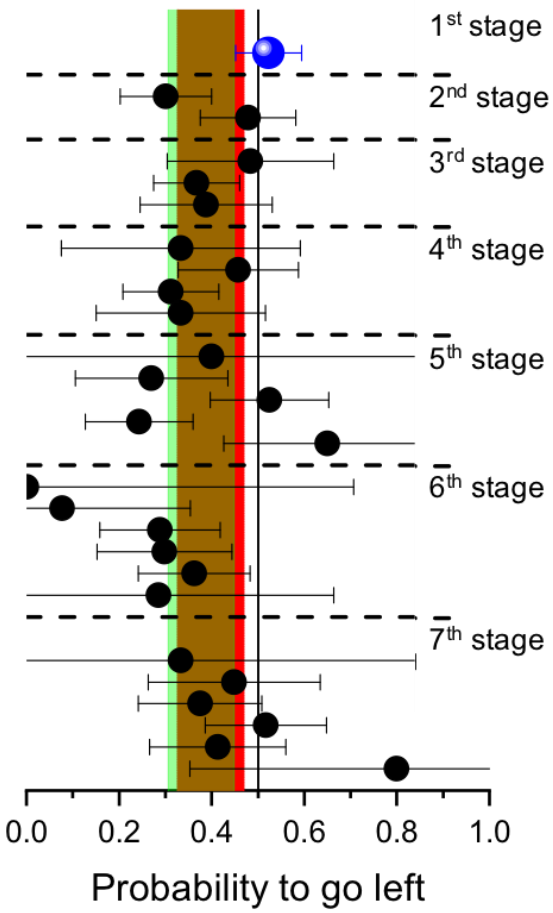

Fig.4-58: Probabilities to go left at the intersections divided by stages (dashed lines), within each stage, the upper point is the intersection on the left-most one thus points are to be reported on the structure from left to right. Mean weight values (vertical lines) computed as mean value on the events with (in red) and without (in green) the first intersection. Error is computed with 95% confidence interval as $\sqrt{p(1-p)/N}$ overrated with $p = 0.5$ with N the total number of domain walls passing by the intersection. Errors on the mean values are according to thickness of the lines. The black line 0.5 is a guide to the eye.

Here, the error on each intersection is computed with 95% confidence interval by $\sqrt{p(1-p)/N}$ overrated with $p = 0.5$ with N the total number of domain walls passing by the intersection. The mean value on the weights is computed as the total number of domain walls going left out of the total of domain walls having crossed all intersections (Eq.7).
For our system, the mean weight value on the events computed for all intersections is 40% ± 8% (red value in Fig.4-58) and without the first intersection is 38% ± 8% (green value) to go left. Both values

translate a bias towards the right side of the board. We note that there is only a 5% deviation between our mean values with and without the first intersection.

We find that the mean value computed for all intersections (first intersection included) describes all experimental weights whereas the mean value without the first intersection describes all beside intersection (1, 1). This last value describes quite closely the weights of stages 2 to 4, but starting from stage 5 we see different features. We observe that for intersections (6, 1-2), the domain walls that have passed by do not have the same tendency toward the right as for the other intersections. However, for these intersections, the statistics is low and therefore the uncertainty is large so we cannot conclude. For intersections on the other side of the structure (5, 5) and (7, 7) we also observe a different tendency towards the left side. But again, for these intersections, due to the low statistics we cannot conclude. However, as they are located are on right side of the system so we would expect them to follow the overall bias ($p_{left} \approx 38 - 40\%$) but it is not the case. This result shows that the intersections located on the edges of the structure have not the same behaviour as the ones inside which is could be due to the absence of neighbouring spins.

We now compare the experimental output distribution to binomial distributions with the ideal case (50%/50% to go left/ right) and the two mean values computed using the events approach. Results are shown in Fig.4-59.

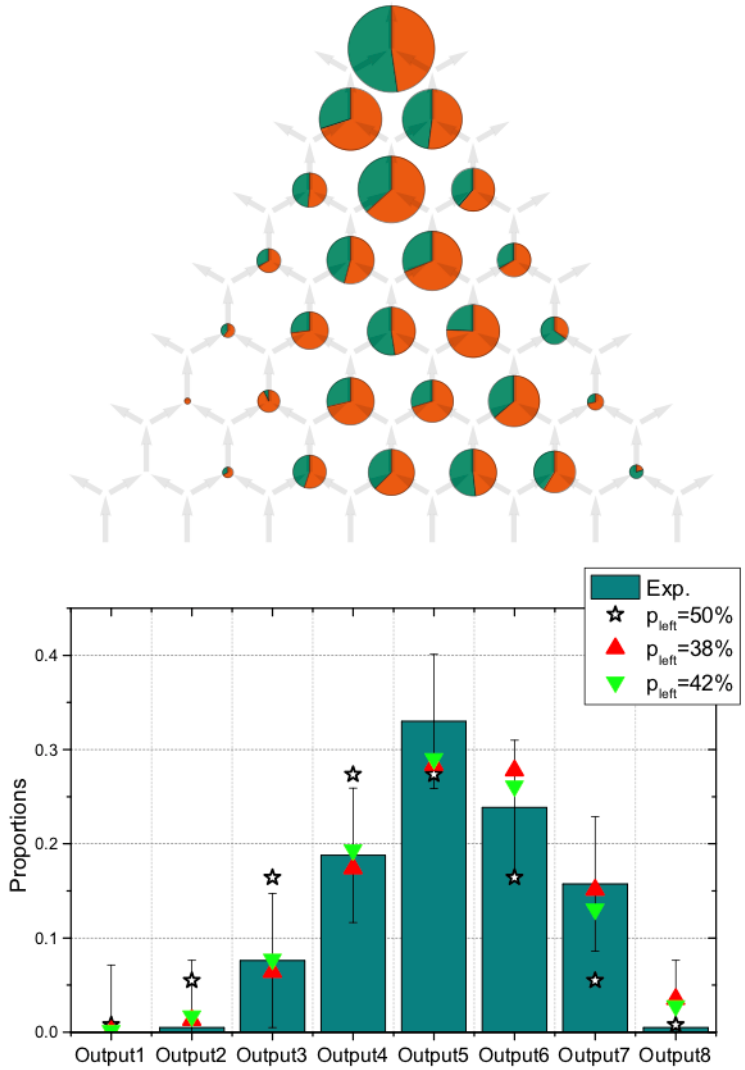

Fig.4-59: Experimental weights represented as pie charts whose sizes are proportional to the number of domain walls having passed by the intersection and green and orange proportions the domain walls having gone left and right respectively along with output distribution compared to binomial distribution with p=50%, 38% and 40%.

Using Fig.4-59, we find that the proportions of activated outputs are equal to 0%/0.5%/8%/19%/33%/24%/16%/0.5% for outputs 1 to 8 respectively. Comparing our experimental output distribution to binomial law with equal chance to go left/right at each intersection (p_{left} = 50%), we confirm that our system does not match an ideal Galton board. Our system is indeed biased towards the right as expected from the mean values of 38% and 40% computed before. The corresponding binomial distributions are well within the uncertainty (estimated at $1/\sqrt{197} \approx 7\%$) therefore describing our system.

We observe that outputs 5, 6 and 8 are less well estimated that the others. We do not have an explanation for this observation except for the outer one (as seen on the weights in our representation with pie charts in Fig.4-59). As mentioned before, we suspect that the behaviour of the edge intersections is somehow different than inner ones due to the lack of elements surrounding them. Maybe the addition of (more than a single element just stabilising the vertices) dummies elements could have change this.

Here as before, both mean values with and without the first intersection describe our experimental results. Our low statistics does not allow any conclusion on which approach of the mean value either on plain mean value or events based ones.

Field angle study performed by colleagues on same structures [94,95] has shown that field alignment is critical parameter for the weight value of the system. Their results show that our mean weight value of 38-40% actually corresponds to a field angle of less than 0.5°. This study has also shown stochastic and avalanche behaviour for various structures of same design demonstrating reproducibility from one structure to the other.

We have shown here that our system fulfils the first criterion of a Galton board that is all intersections can be described by a mean value whose binomial distribution matches the output distribution. We have also seen that we cannot identify if some intersections can be considered different due our low statistics. The next step is to study the correlation between successive choices.

4.5.3. Correlation between successive choices

We have seen in the previous section that our system can be described by an mean weight slightly biased on the right (about 40%(60%) to go left (right)). In this section, we will investigate the correlation between the successive choices made by the domain wall in its course from the pad to the outputs.

Here, we compare choices made by the domain walls at one intersection according to the choice made at the previous one. Our goal is to differentiate if the same choice is made twice or on the contrary opposite choices are made. We have chosen to define the correlation between successive choices by a correlation factor between – 1 and + 1 for exclusively opposite and exact same choices respectively and null if the choices are evenly distributed. For each intersection, we count out the number of domain walls that have made a right(left) choice at the previous intersection and how many have made the same choice to go right(left) or the opposite choice to go left(right). We define the choices as shown in Fig.4-60.

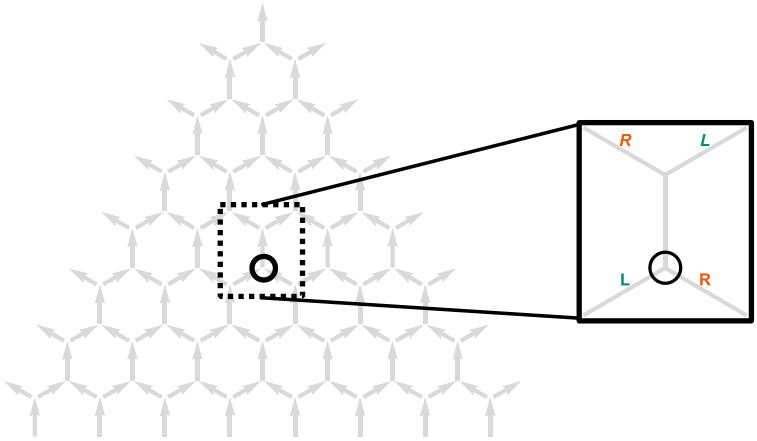

Fig.4-60: Intersection of interest (taken arbitrarily), domain walls having chosen to go right/left (R/L) then left/right (L/R).

We have to compare on two successive intersections the number of domain walls that made same choices -either right then right (labelled RR) or left then left (LL)- to the number of domain walls having made opposite choices -either right then left (labelled RL) or left then right (LR). We have thought of two ways to express the correlation factor of our intersections.
The first approach, referred to as on events, is to consider all domain walls and their choices altogether using the following expression:

$$C_{events} = \frac{RR + LL - RL - LR}{RR + LL + RL + LR}$$
(Eq.8)

This expression, similar to the one presented on the mean value on weights (Eq.7), can be applied to all intersections even the ones located at the edges of the structure. It has the advantage of putting at the same level the choices made by the domain walls coming from both sides and avoids any weighting.
The second approach, referred to as mean value, is to compute the mean value of correlation factors of both sides, as expressed in the following expression:

$$C_{mean} = \frac{1}{2}(\alpha_R + \alpha_L)$$
(Eq.9)

Where $\alpha_R = \frac{RR-RL}{RR+RL}$ and $\alpha_L = \frac{LL-LR}{LL+LR}$ .This approach cannot be applied to edge intersections and puts on the same level both sides. The latter point may be an issue if the number of domain walls arriving from both sides are very different.
Results for both methods on our experimental set are shown in Fig.4-61.

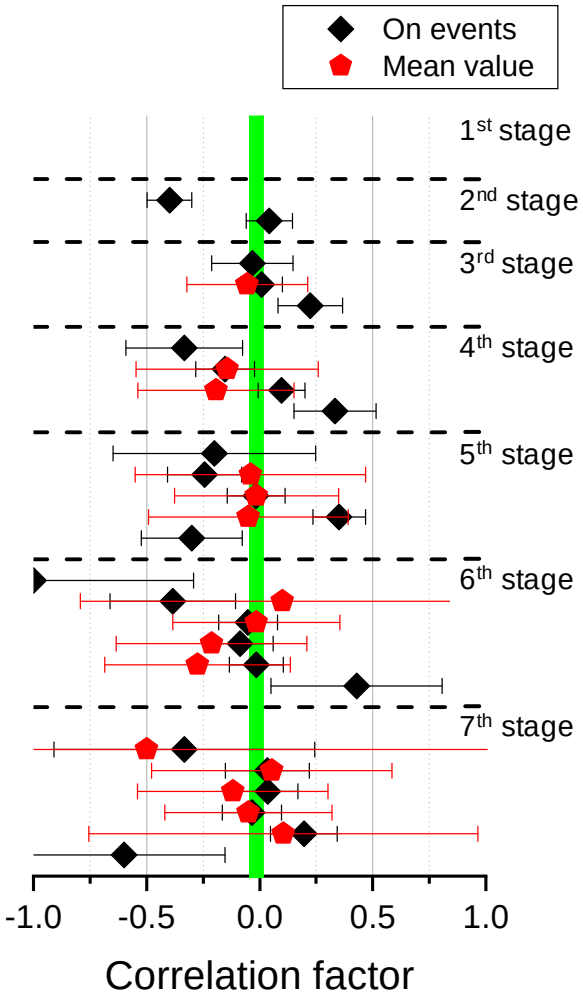

Fig.4-61: Correlation factor on the intersections using (Eq.8) and (Eq.9) in black and red respectively. Values are divided by stage (dashed lines), within each stage, the upper point is the intersection on the left-most one thus are to be read from left to right. Mean value (vertical green line) is computed using method on events.

Both methods yield similar results or at least their errors overlap. We find that the correlation factors are, for 90% the intersections, comprised between -0.5 and +0.5, the only exceptions being intersections (6, 1) and (7, 7). We also observe that 60% of the intersections (all except the edge intersections) have correlation factors are between -0.25 and +0.25. Considering this simple threshold, it seems that none of the intersections in our system is completely biased in terms of correlation between successive events.

In order to extract a mean value of correlation factor, we compute the mean value of both methods. For the method on the events, we find an overall correlation factor of -9% (median at -3% and σ = 31%). For the mean value method, we also find a correlation factor of -9% (median at -5% and σ = 16%). We also tried to compute the correlation of the entire structure using the method on the events with the total number of domain walls and their choices. This approach gives a correlation factor of -2%.
These results suggest that the choices made at one intersection do not strongly depend on the choices made before. Therefore, correlation is not a major feature of our system and exhibits a slight preference towards opposite choices to the extent of the two approaches proposed.

From the computations performed, we cannot extract any tendency of the choices to go either left or right although we have seen that our system exhibits an overall bias towards the right. We propose a last

approach to study the correlation factors of our intersections that is to examine α_R and α_L in a two-dimensional plot. Results are shown in Fig.4-62.

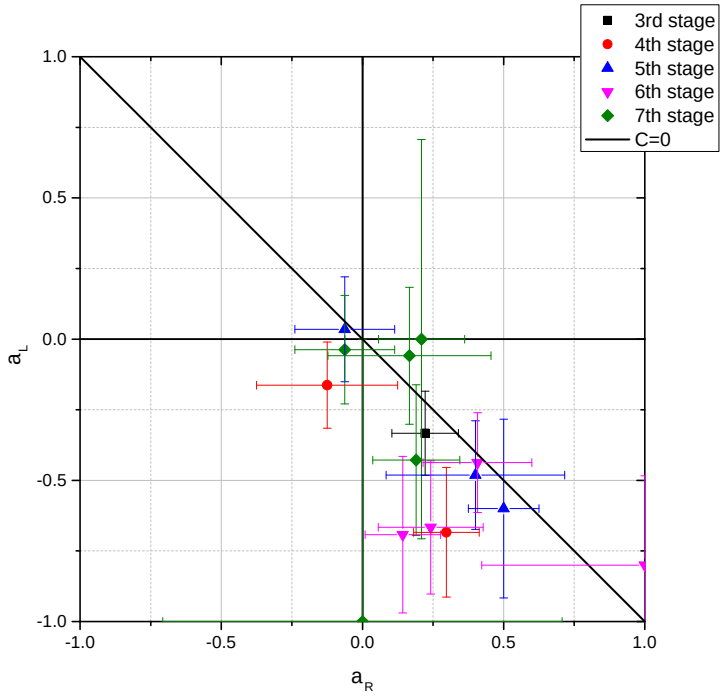

Fig.4-62: α_L vs. α_R for inner intersections of our structure.

We see that all (α_R, α_L) points are close to the $\alpha_R = -\alpha_L$ (C_{mean}=0) expect for two points (0, -1) and (1, 0.8) which are intersections (6, 2) and (7, 2). This result emphasises that the correlation between successive choices is low. We find a mean value of α_R at 24% (median at 31% and σ = 28%) and a mean value of α_L at -42% (median at 44% and σ = 28%). Studying the values of α_L and α_R individually, we find that most of the former are positive and most of the former negative. This result is twofold: most of the domain walls having made a right choice then make a left and the domains walls having made a left choice make a left choice.

We conclude that our system shows low or no correlation between successive choices which fulfils the second criterion for our system to be qualified as a Galton board.
However, these observations raise the question about how to consider memory effect in the domain wall propagation. But as mentioned before, we have seen in our study of the weights that our system is biased towards its right side. Are the results studying the correlation only a consequence of this slight bias or is there a contribution of a memory in the successive choices? In the following section, we introduce a novel approach to our study of correlation taking into account both weight and memory effect.

4.5.4. Choices at the intersections as a function of both weight and memory effect

One can consider that the domain wall propagation throughout the structure depends on two features: (intrinsic) weight of the intersection and memory effect. Ideally, we would expect no bias on the weight

nor on the correlation on successive choices. But as we demonstrated previously, there is a global bias towards the right part of the structure that could be due to either weight or memory.

We define correlation between successive events as a function of η and δ the biases on weight and memory respectively. The two quantities are therefore between -1/2 and +1/2 translating in weight biased completely to the left and to right respectively and in memory effect biased completely towards the opposite and same direction respectively or no contribution if they are null.

$$\begin{pmatrix} RL+LL \\ LR+RR \end{pmatrix} = \begin{pmatrix} \frac{1}{2}-\eta-\delta & \frac{1}{2}-\eta+\delta \\ \frac{1}{2}+\eta+\delta & \frac{1}{2}+\eta-\delta \end{pmatrix} \begin{pmatrix} RR+RL \\ LL+LR \end{pmatrix}$$

where RR, LL, RL and LR are defined as in Fig.4-60; if there is no contribution on the "intrinsic" weight if the intersection η is null, $\eta > 0$ means that the right direction is favoured; if there is no memory effect, δ is null, $\delta > 0$ means that the propagation tends to keep the same direction. This approach is only another way to describe the parameters introduced before and could probably have been handled differently. We mention that this approach cannot be used for outer intersections. Results for inner intersections of each stage are plotted in Fig.4-63.

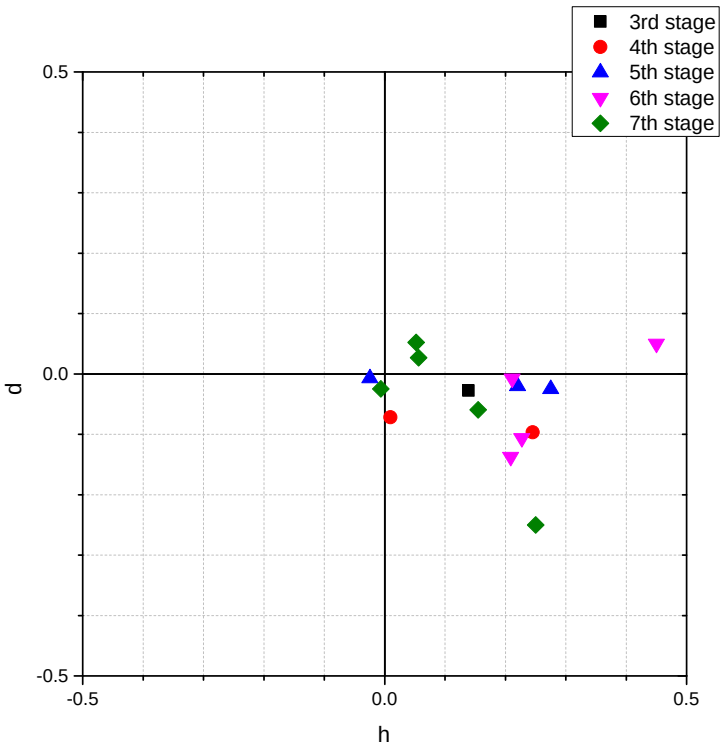

Fig.4-63: Correlation between successive choices by differentiating the contribution of δ memory effect and η intrinsic bias of the intersection.

We find that the bias on weight (η) is comprised between -10% and +50% and that 14 of the 15 intersections are between -5% and +30%. The overall bias on weight has a mean value of +16% (median at 21% and σ = 13%). This positive mean value on intrinsic bias shows that right choice is favoured.
We observe that the bias on memory effect (δ) of the intersections is comprised between +10% and -30% and 12 of the intersections are comprised between +10% and -10%. We find a mean value at -5%

(median at -3% and σ = 8%). This negative mean value of δ shows that there is small memory effect resulting in a tendency towards same choices.

We conclude that the domain wall propagation in our system is not mediated by memory effect with a contribution estimated at -5% suggesting a slight tendency to keep the choices in the same direction. The overall bias observed on weights has been translated with our defined η value estimated at +16%. This result translating in a tendency towards right choices is most likely the result of our field angle.

4.5.5. Behaviour at low temperature

We have seen that our structure, which can be qualified as a biased Galton board, exhibits stochastic choices in the domain wall propagations. We seek to determine if this behaviour is robust at low temperature.

On the structure thoroughly studied in this section and the previous one, we have performed similar field experiments using magnetic force microscopy at 77 K. We compare them to experiments in the same conditions of field alignment at 300 K. These experiments were carried out using an Attocube MFM with application of *in situ* in-plane magnetic field. These experiments were performed thanks to Dr. K. Bouzehouane (CNRS/Thalès). Two experiments are shown in Fig.4-64.

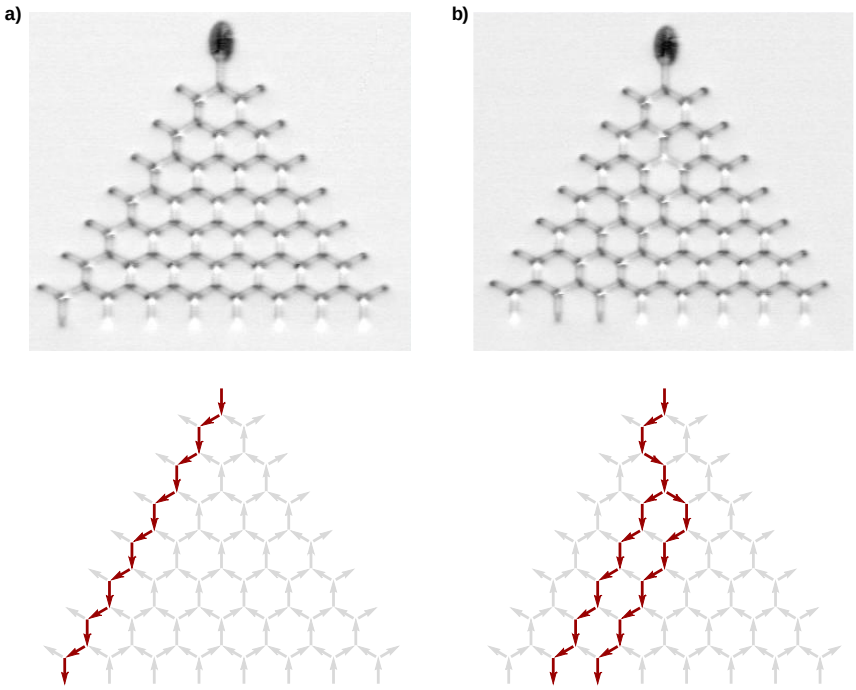

Fig.4-64: Examples of reversals observed a) single cascade reaching output 1 and b) two activated outputs 2 and 3.

On the two examples shown, we find that one exhibits a Single Cascade reaching output 1 and the other follows a two activated outputs scenario reaching outputs 2 and 3. These results indicate that the propagation is still stochastic at 77 K.

We now compare the output distributions for the same field angle (±0.5°) at 77 K and 300 K for 20 and 51 experiments for both temperatures respectively. Output distributions are shown in Fig.4-65.

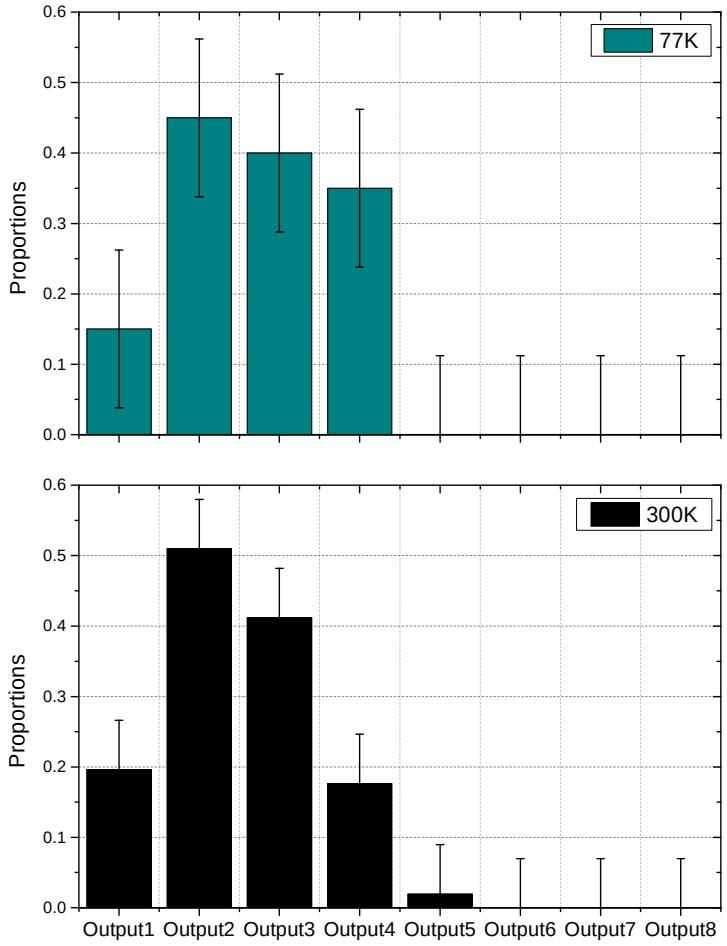

Fig.4-65: Output distributions at 77 K for 20 experiments and 300 K for 51 experiments. Measurements performed mainly by Dr. K. Bouzehouane (CNRS/Thalès).

We observe that outputs 1 to 5 are activated at both 77 K and 300 K, therefore demonstrating the same stochastic behaviour. The spatial distribution of the outputs suggests that there is no path preferred at low temperatures compared to room temperature for the same field angle.
We note that the distributions are shifted compared to the ones presented before (Fig.4-59). The difference is due to the field alignment which is quite challenging in this particular microscope since the sample is "hidden" inside the cryostat. Due to the allocated time, we did not look for a better field alignment since in order to demonstrate to stochastic choices, only a field alignment "good enough" meaning not completely biased was sufficient.

We conclude that the stochastic behaviour of our structure is preserved at 77 K. To be conclusive about the influence on temperature on the domain wall propagations in our system, experiments at 4 K are needed. These experiments were schedules but could not be realised due to technical issues.

4.5.6. Conclusions

In this section, we have compared our artificial spin system optimised for avalanche-like reversals that clearly exhibits stochastic behaviour similar to a Galton board. Our goal was to determine if our structure fulfilling the two criteria of this prime example of device for random generation: average weight

describing all the intersections points and no correlation between successive choices at the intersections.

We have studied the propagations of all our Single Cascades with and without backward propagations from which we have extracted the choices made at the intersections. We have proposed several approaches to describe accurately the statistical weights of our structure. The average weight value of our system ranges from 38%-40% (±8%) probability to go left. This result, translating in a bias towards the right part of the structure, has been shown by colleagues to be due a field angle of about 0.5°. Both values reasonably described the experimental output distribution of the system. Due to the finite size of our experimental set, we were not able to identify intersections with drastically different behaviour. However we suspect that intersections on the sides were biased because of the absence of surrounding elements and that the first intersection that we have shown undergoes propagation at much lower fields because of the domain wall injection. But again, results are not conclusive because our -quite large- statistical error. These results showed that our system fulfils the first criterion of the Galton board.
We have also studied the correlation between successive events by counting at each intersection how many times the domain walls made same or opposite choices compared to the choice made before. A first approach has shown that the origin of the domain walls has little effect on the choice made at a given intersection, with an overall correlation factor below 10%. However, studying the choices made individually has shown that no matter the choice made before, the domain walls show a tendency to go towards the right with little regard to the choice made previously. This result, in hand with our overall bias in weights towards the right, has raised the question about how to quantify the influence of intersection "intrinsically" with the external parameter that is the field alignment. We have come up with a novel approach that discriminate the contribution of the intersection from the one of memory effect. This rearranging of the presented parameters has highlighted the presence of a bias due to the intersection of about 16% and a contribution of memory effect no greater than 5%. The overall contribution of the intersection being due to field misalignment. These results have shown that our system fulfils the second criterion of the Galton board.
We have completed our study with an observation at low temperature (77 K) on the same structure. We have found that the choices made by the domain walls in our structure are still stochastic. Experiments at 4 K were planned in order to be conclusive about the influence of temperature on the domain wall propagation but could not be performed due to technical difficulties.

We can therefore qualify our system as a magnetic nanoscale Galton board with robust stochastic behaviour at both room temperature and 77 K.

4.6. Conclusion

In this chapter, we have presented the development and study of a honeycomb artificial spin ice system for applications of stochastic logic or random number generation. We have chosen to develop a system exhibiting avalanche-like reversals induced by a nucleated domain wall from a nucleation pad throughout the system. Such ambition has proven to be difficult and in need for a precise optimisation.

We have first studied the behaviour on small structures (1- and 2-stage structures) of both disconnected and connected geometries. Observations on one intersection have shown that the nucleation and injection of a domain wall using our elliptic pad is efficient with the reversal of the element connected to it. In both geometries, the next reversal is either one of the diagonal elements of the intersection demonstrating stochastic behaviour and therefore validating our concept. Increasing the number of stages has shown that imposing several choices to the injected domain wall is not as straightforward. We have seen in the disconnected geometry that although the injection along with the reversal of an element of the first intersection, we witness parasitic nucleation from the other of the structure. In addition, the experiments exhibit mainly deterministic reversals and important variability from one

structure to the other. We mention that the behaviour of these structures could probably have been modified by an optimisation of gap between element and/or shape of the elements. Rather than that, we have chosen to continue with connected geometry which suggested chain-like reversals along with stochastic choices at its two stages of intersections resembling binomial distributions. For these structures, we have also demonstrated reproducibility from one structure to the other and a first glimpse of influence of field angle.
We have continued our study with two 7-stage connected designs. We have seen that a design resembling a Galton board is not suitable since reversals are not following a domain wall propagation from pad to the other end of the structure. These structures have shown reversals consistent a pinning at the upper part of the structure of the injected domain wall along with nucleations from either the outputs or the sides of the structure since some structures showed a large bias on the outer outputs. We have therefore tried to stabilise the edges of the structure by adding elements on the side so all vertices on the possible paths of the domain walls would be composed by three-spin vertices. On this design, reversals observed were divided in two steps: injection and propagation of the domain wall from the pad in the upper part of the structure and nucleation from outputs propagating inside the structure. The parasitic nucleations observed varied from one structure to the other, suggesting that the dispersion in coercive fields does allow for depinning of the structure from the upper part of the structure. This last design has shed the light on the main issue to overcome that is the right trade-off between depinning field in the upper part of the structure and nucleation fields from the outputs. In order to observe avalanche behaviour, we needed to ensure that the domain wall injected by the pad would propagate inside the structure at lower fields than the ones to nucleate a domain wall from the outputs.

These observations have led to the final optimisation of our 7-stage structure with stabilised edges in which we added funnel shapes at the potential pinning points and sharpened the outputs. The study of the reversals has shown that observations are consistent with propagation of the nucleated domain wall from the pad to the outputs of the system. This first result proved that our optimisation was indeed efficient for avalanche-like reversals. In our experimental set, we have identified three main propagation scenarios: Single Cascades (chain-like reversals), Two Activated Outputs and Lost Propagations, leaving only three out of 229 experiments unexplained.
This structure has revealed an unexpected feature that is additional reversals connected to the propagation, that we have referred to as backward propagations. These backward propagations do not follow the direction of the applied field, can occur at several locations on the propagation and can be one- to three-elements long. Observations, and the absence of some evidences, suggest that these reversals are a dynamic result of complex passing through the funnel shapes of our system. In our small experimental set, we could not identify any spatial fluctuations in the structure for this phenomenon but also showing that there is no place in the structure where it is observed systematically.
The study of all reversals and their fields have shown that the propagation takes place in two phases: the injection and domain wall propagation into the upper part of the structure where it gets pinned and the propagation inside the structure than can also take a few steps to come through. The study of the depinning field has shown two main features. The first one about the first systematic pinning of the propagation at low fields has suggested dynamical pinning. We have observed a non-null proportion of domain walls pass the first stage of the structure. The second feature that is pinning inside the structure has shown that there is only a small chance for the domain wall to get pinned. Here again, we could identify any “harder” point probably due to the finite size of our experimental set but also that there is no “actual” pinning point where the domain wall would get pinned systematically.

The summary of the reversals clearly showed an aspect in trees with stochastic choices at the intersections. The question then was how random our structure is. In order to study its stochasticity, we have compared it to the prime example of random devices that is the Galton board. Our goal was to determine if our structure fulfils the two criteria to be a Galton board: intersections than could be considered identical and independent choices between successive intersections. We have therefore taken an interest at the paths taken in our Single Cascades without or with backward propagations. We made this choice first to increase our statistics and second because the backward propagations do not “affect” the main propagation. Using several parameters, we have shown that our intersections can be described

by a unique mean weight value whose binomial distribution matches the experimental output distribution. Our artificial spin system fulfils the first criterion of the Galton board and that our system is slightly bias towards the right side. We have then shown that our propagations do no exhibit major correlation between successive choices using also several approaches. A study with the contributions of both intersection bias and memory has shown that there is a contribution of the intersection and a very small contribution of memory effect. The intrinsic bias is attributed to our bias towards the right and is suspected to be due to the field misalignment of our experiments. This robust stochastic has proven to be also present at 77 K, although to be conclusive about the effect of temperature on the domain wall propagation, experiments at 4 K are necessary. Colleagues have shown that the observed behaviour is reproducible from on structure to the other on different samples.

However, the question remains about the origin of the robust stochastic behaviour. As already mentioned, reported works on micromagnetic simulations showed that the choice at an intersection depends on the characteristics of the domain wall propagating. We have seen experimentally that indeed both transverse and vortex domain walls get pinned inside the structure. However, it does not explain the propagations and the random choices made. Our best guess is on the regime at which propagations occur. We have seen that propagation fields inside the structure are way beyond Walker breakdown. This specific regime is expected to make the domain wall propagation undergo several changes and therefore modify the domain wall nature. Indeed if the domain wall changes -more or less- randomly in between intersections, then the choices would be random as well. However, this aspect of the behaviour of our system needs to be further investigate.

We conclude that we have successfully developed an artificial spin system with stochastic behaviour similar to a Galton board. This magnetic device is therefore clearly suitable for random number generation. We can easily imagine that these properties could be of great potential for stochastic computing, but this lead could not be explored during the time allocated. As one might have noticed, the development of the artificial spin system has proven to be more difficult than anticipated.

Chapter 5. Conclusions and perspectives

"On peut faire du calcul avec ça"
D. Querlioz

For 15 years now, the interest in arrays of nano-magnets in interaction that can be tailored at will, known as artificial spin ice has not dried up. In this PhD work, we have continued this exploration by showing that artificial spin systems are indeed a fascinating playground to study complex phenomena and can also be used as device for computing applications. We have first shown that through a simple modification of the geometry, it is possible to determine with precision the thermodynamics established during material deposition using only frozen states. We have then shown that exploiting domain wall propagation in these systems and a fine optimisation of their shape, it is possible to develop a device for random number generation.

In the second chapter, we have detailed and compared the fabrication processes of artificial spin ice systems that could be either lift-off or etching processes. We have also taken a special interest at the lithography step and particularly the patterning strategies in order to obtain the designed structures. We have shown that a specific patterning strategy is required to obtain symmetric and smooth structures. Then, we have presented our use of the main characterisation tool used for this work that is magnetic force microscopy with *in situ* magnetic field. We have also shown through various examples how the magnetic force microscopy images are to be understood as a guide for the reader. We have also detailed the time-issues imposed by our acquisition of large sets of images and presented our method to decrease reasonably the acquisition time.

In the third chapter, we have focused on a simple geometrical modification, that is rotation angle, to tune the dipolar interactions taking place into artificial spin ice systems. We have described the dipolar interactions considering the elements as punctual magnetic moments in both a vertex and all-interactions approaches. We have studied various ordered spin configurations taking into account all interactions at play in order to have an accurate description of the total dipolar energy. Our computations have shown that the ground state of the system evolves from antiferromagnetic to ferromagnetic ordering while increasing rotation angle. Then, we have tested the two main preparation protocols documented in order to observe the transition experimentally. We have chosen to work on as-grown state and a field-demagnetized state. We have characterised our experimental systems in terms of vertex populations and total dipolar energy. We concluded that the as-grown state leads our system into a low energy state compared to the field-demagnetized one. However, by comparing its energy to antiferromagnetic and ferromagnetic ground states we have seen that our as-grown state does not lie in the lowest possible energy state. Then, by comparing computed dipolar energy and magnetic structure factors to the one extract from direct imaging experiments we have shown that: for low rotation angles, the system follows an antiferromagnetic order and further increase of the rotation angle leads to a progressive ferromagnetic

order appearance. Taking an interest in the thermodynamics of the system, we have established the phase diagram of our tilted system using Monte Carlo simulations taking into account all interactions (*i.e.* both short and long range). Both the energy of tuned systems and their vertex populations as function of the rotation angles are successfully described by a unique effective temperature! Therefore, we have shown that varying the rotation angle is a robust way to get insight into the thermodynamic properties of such systems. Moreover, through this work we have also demonstrated that taking into account long-range interactions is essential to a precise definition of the ground state effective temperature.

In the fourth chapter, we have presented our development of a honeycomb artificial spin system for random number generation. With the study of small disconnected and connected structures, we have seen that 2-stage connected structures exhibit avalanche-like reversals along with stochastic choices at the intersections. We have seen that increasing the stage number of connected structures leads to the appearance of parasitic nucleation sites at the array edges. Therefore, we have optimised our magnetic devices rounding the potential pinning points and sharpening the outputs elements. An exhaustive study of the reversals has shown that they are consistent with a propagation from the pad towards the outputs of the system. The reversals follow mainly unidimensional propagation process that is the desired behaviour. Nevertheless, our experiments showed additional reversals referred to as backward propagations. These occasional events were ascribed to domain walls splitting at the potential pinning points.
Finally, this work has shown successful development of an artificial spin system based on domain wall propagation for random number generation. Indeed, we reported a stochastic behaviour in the reversal process. By comparing our system to a Galton board, we have shown that our artificial spin system fulfils the two required criteria to be considered as a nano-scaled one: all intersections are equivalent and no correlation between choices exists nor memory effect. A mean weight value describes the experimental output distribution. Unfortunately, no computing could be performed due to the allocated time for this work.

Having established the basic principle of the magnetic Galton board is of course a first important step leading to new perspectives but also leaves open questions.

Concerning the comprehension of the propagation phenomena, many aspects remain uncertain but some of them can be addressed with better statistics. Larger amounts of data can be obtained with Kerr microscopy (note that in that case the number of experiments can be limited by the amount of raw image data!). Information concerning the pinning-depinning process might be "easily" obtained by dynamic measurements in the microsecond to second time range. However experimental investigation of the propagation itself, its turbulent dynamic and the random choice of the domain wall seem out of reach with available techniques (pump-probe techniques are rather appropriate to investigate reproducible phenomena).
On the matter of the application of our structures to stochastic computing, there are numerous perspectives. Beyond the algorithmic and design issues related to the stochastic scheme itself, we can mention the three following aspects:

- Generation of "static" arbitrary random distribution

Although we were interested in demonstrating a probability distribution close to the binomial law, generating other distributions can be of interest. This can be achieved by tuning individually the probability at the intersections. For the sake of demonstration, we have chosen a more drastic approach by simply removing one element from the original design. This has proven to be an efficient way to tune the distributions.

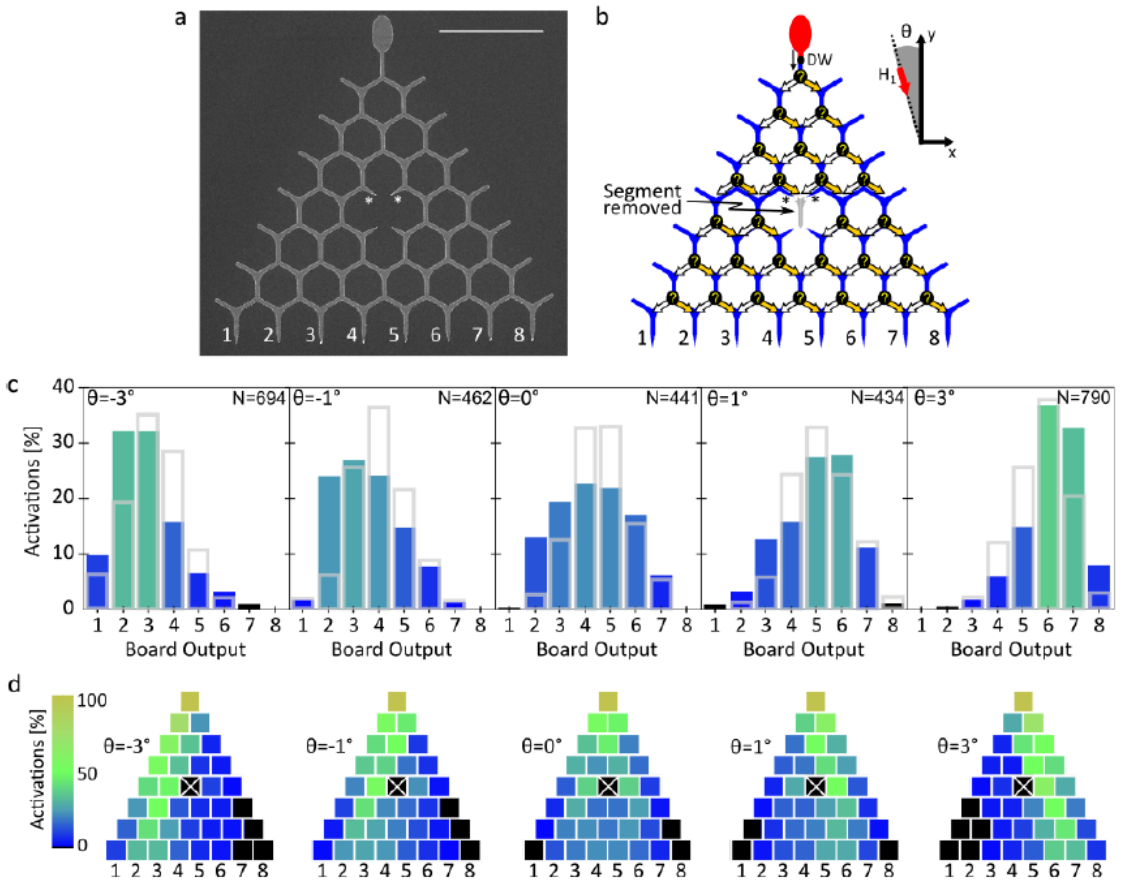

Fig.5-1: From Refs. [94,95], a) SEM of an optimised 7-stage structure with missing element (marked with ''); b) schematic of the missing element structure: c) output distributions according to field angle and d) trees of the activations.*

- Control of individual weight

Beyond the static control, reconfigurable properties are highly desirable either to generate different statistics distributions or -for a more elaborate stochastic device- to improve the device response by training. Many options could be considered for this purpose. We envision to control electrically the probability by local injection of electrical current which would impact the domain wall propagation either by local heating or by local spin or spin-orbit torques. To experimentally study such an impact, we have developed simplified structures with electrical contacts (see Fig.5-2). Up to now, we have demonstrated the possibility to detect electrically the direction of bifurcation with conventional anisotropy of magnetoresistance. The effect of current injection is yet to be studied.

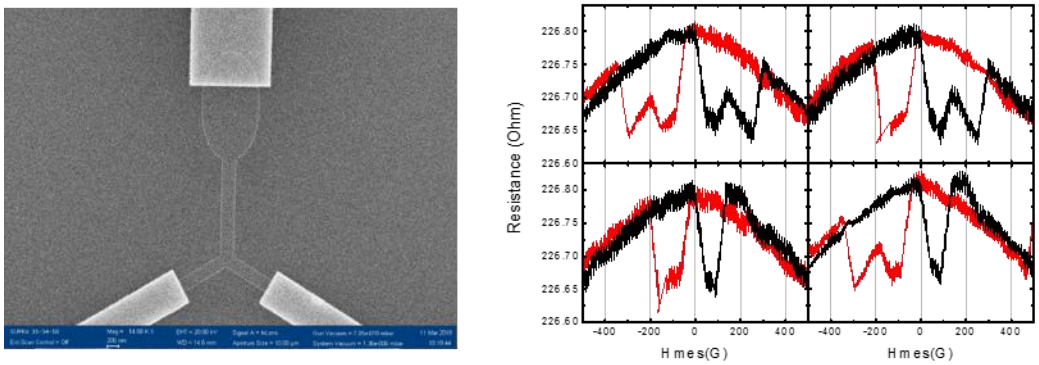

Fig.5-2: Electrical experiments on a 1-stage structure (performed by Dr. I. Cinar).

- Multiple domain wall injections

In order to process more complex information, it can also be interesting to inject several domain walls into the system. This has to be achieved by implementing several nucleation pads. The design we used allow us to simply generate different random input configurations. The image in Fig.5-3, obtained by STXM, shows that domain wall can propagate independently within the structure. On the other hand, when a path meets an already reversed path, its propagation is (of course) stopped.

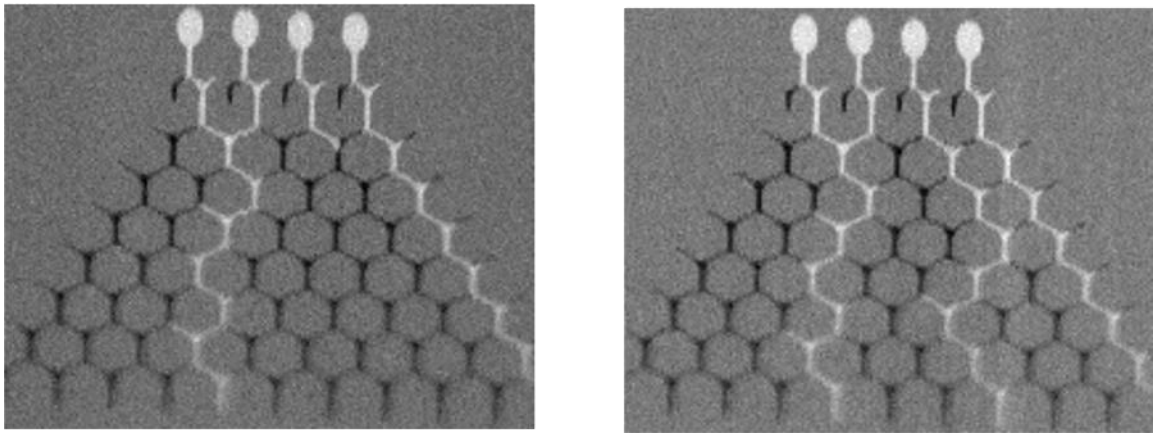

Fig.5-3: STXM images of a structure with 4 pads.

References

[1] C. Nisoli, R. Moessner, and P. Schiffer, *Colloquium: Artificial Spin Ice: Designing and Imaging Magnetic Frustration*, Rev. Mod. Phys. **85**, 1473 (2013).

[2] C. Marrows, *Experimental Studies of Artificial Spin Ice*, ArXiv161100744 Cond-Mat (2016).

[3] S. H. Skjærvø, C. H. Marrows, R. L. Stamps, and L. J. Heyderman, *Advances in Artificial Spin Ice*, Nat. Rev. Phys. **2**, 1 (2020).

[4] W. F. Giauque and M. F. Ashley, *Molecular Rotation in Ice at 10°K. Free Energy of Formation and Entropy of Water*, Phys. Rev. **43**, 81 (1933).

[5] L. Pauling, *The Structure and Entropy of Ice and of Other Crystals with Some Randomness of Atomic Arrangement*, J. Am. Chem. Soc. **57**, 2680 (1935).

[6] S. T. Bramwell and M. J.-P. Gingras, *Spin Ice State in Frustrated Magnetic Pyrochlore Materials*, Science **294**, 1495 (2001).

[7] M. J. Harris, S. T. Bramwell, D. F. McMorrow, T. Zeiske, and K. W. Godfrey, *Geometrical Frustration in the Ferromagnetic Pyrochlore $Ho_2Ti_2O_7$*, Phys. Rev. Lett. **79**, 2554 (1997).

[8] A. P. Ramirez, A. Hayashi, R. J. Cava, R. Siddharthan, and B. S. Shastry, *Zero-Point Entropy in 'Spin Ice,'* Nature **399**, 333 (1999).

[9] R. F. Wang, C. Nisoli, R. S. Freitas, J. Li, W. McConville, B. J. Cooley, M. S. Lund, N. Samarth, C. Leighton, V. H. Crespi, and P. Schiffer, *Artificial "Spin Ice" in a Geometrically Frustrated Lattice of Nanoscale Ferromagnetic Islands*, Nature **439**, 303 (2006).

[10] R. F. Wang, J. Li, W. McConville, C. Nisoli, X. Ke, J. W. Freeland, V. Rose, M. Grimsditch, P. Lammert, V. H. Crespi, and P. Schiffer, *Demagnetization Protocols for Frustrated Interacting Nanomagnet Arrays*, J. Appl. Phys. **101**, 09J104 (2007).

[11] J. P. Morgan, A. Stein, S. Langridge, and C. H. Marrows, *Thermal Ground-State Ordering and Elementary Excitations in Artificial Magnetic Square Ice*, Nat. Phys. **7**, 75 (2011).

[12] M. Tanaka, E. Saitoh, H. Miyajima, T. Yamaoka, and Y. Iye, *Magnetic Interactions in a Ferromagnetic Honeycomb Nanoscale Network*, Phys. Rev. B **73**, 052411 (2006).

[13] Y. Qi, T. Brintlinger, and J. Cumings, *Direct Observation of the Ice Rule in an Artificial Kagome Spin Ice*, Phys. Rev. B **77**, (2008).

[14] E. Mengotti, L. J. Heyderman, A. Fraile Rodríguez, A. Bisig, L. Le Guyader, F. Nolting, and H. B. Braun, *Building Blocks of an Artificial Kagome Spin Ice: Photoemission Electron Microscopy of Arrays of Ferromagnetic Islands*, Phys. Rev. B **78**, 144402 (2008).

[15] O. Sendetskyi, V. Scagnoli, N. Leo, L. Anghinolfi, A. Alberca, J. Lüning, U. Staub, P. M. Derlet, and L. J. Heyderman, *Continuous Magnetic Phase Transition in Artificial Square Ice*, Phys. Rev. B **99**, (2019).

[16] E. Mengotti, L. J. Heyderman, A. F. Rodríguez, F. Nolting, R. V. Hügli, and H.-B. Braun, *Real-Space Observation of Emergent Magnetic Monopoles and Associated Dirac Strings in Artificial Kagome Spin Ice*, Nat. Phys. **7**, 68 (2011).

[17] S. Ladak, D. E. Read, G. K. Perkins, L. F. Cohen, and W. R. Branford, *Direct Observation of Magnetic Monopole Defects in an Artificial Spin-Ice System*, Nat. Phys. **6**, 359 (2010).

[18] K. Zeissler, S. K. Walton, S. Ladak, D. E. Read, T. Tyliszczak, L. F. Cohen, and W. R. Branford, *The Non-Random Walk of Chiral Magnetic Charge Carriers in Artificial Spin Ice*, Sci. Rep. **3**, (2013).

[19] S. K. Walton, K. Zeissler, D. M. Burn, S. Ladak, D. E. Read, T. Tyliszczak, L. F. Cohen, and W. R. Branford, *Limitations in Artificial Spin Ice Path Selectivity: The Challenges beyond Topological Control*, New J. Phys. **17**, 013054 (2015).
[20] V. Kapaklis, U. B. Arnalds, A. Harman-Clarke, E. T. Papaioannou, Masoud Karimipour, P. Korelis, A. Taroni, P. C. W. Holdsworth, S. T. Bramwell, and Björgvin Hjörvarsson, *Melting Artificial Spin Ice*, New J. Phys. **14**, 035009 (2012).
[21] A. Farhan, P. M. Derlet, A. Kleibert, A. Balan, R. V. Chopdekar, M. Wyss, J. Perron, A. Scholl, F. Nolting, and L. J. Heyderman, *Direct Observation of Thermal Relaxation in Artificial Spin Ice*, Phys. Rev. Lett. **111**, 057204 (2013).
[22] A. Farhan, P. M. Derlet, A. Kleibert, A. Balan, R. V. Chopdekar, M. Wyss, L. Anghinolfi, F. Nolting, and L. J. Heyderman, *Exploring Hyper-Cubic Energy Landscapes in Thermally Active Finite Artificial Spin-Ice Systems*, Nat. Phys. **9**, 375 (2013).
[23] J. H. Jensen, E. Folven, and G. Tufte, *Computation in Artificial Spin Ice*, 2018 Conf. Artif. Life Hybrid Eur. Conf. Artif. Life ECAL Int. Conf. Synth. Simul. Living Syst. ALIFE 15 (2018).
[24] M. Hehn, F. Montaigne, D. Lacour, Y. Perrin, B. Canals, N. Rougemaille, J. Grollier, D. Querlioz, and A. Masseboeuf, *Bio-Inspired Computing Based on Artificial Spin Ices (Conference Presentation)*, in *Spintronics XI*, Vol. 10732 (International Society for Optics and Photonics, 2018), p. 107323D.
[25] A. Ortiz-Ambriz, C. Nisoli, C. Reichhardt, C. J. O. Reichhardt, and P. Tierno, *Colloquium: Ice Rule and Emergent Frustration in Particle Ice and Beyond*, Rev. Mod. Phys. **91**, 041003 (2019).
[26] A. Libál, C. J. O. Reichhardt, and C. Reichhardt, *Creating Artificial Ice States Using Vortices in Nanostructured Superconductors*, Phys. Rev. Lett. **102**, 237004 (2009).
[27] S. H. Kang, S. Shan, A. Košmrlj, W. L. Noorduin, S. Shian, J. C. Weaver, D. R. Clarke, and K. Bertoldi, *Complex Ordered Patterns in Mechanical Instability Induced Geometrically Frustrated Triangular Cellular Structures*, Phys. Rev. Lett. **112**, 098701 (2014).
[28] K. Ait Oukaci, Structures En Domaines Magnétiques Périodiques Pour La Propagation Guidée d'ondes de Spin., Thèse de doctorat, Université de Lorraine, 2021.
[29] C. Guillemard, Half-Metal Magnets Heusler Compounds for Spintronics, Thèse de doctorat, Université de Lorraine, 2019.
[30] D. Louis, A New Artificial Spin System : The Dipolar 4-State Potts Model, Thèse de doctorat, Université de Lorraine, 2016.
[31] S. Ladak, D. Read, T. Tyliszczak, W. R. Branford, and L. F. Cohen, *Monopole Defects and Magnetic Coulomb Blockade*, New J. Phys. **13**, 023023 (2011).
[32] J. Briones Hernandez, Anisotropie Magnétique Induite Par Modulation de Surface et Étude de La Propagation de Parois de Domaines Dans Des Nanostructures Magnétiques, These de doctorat, Nancy 1, 2008.
[33] F. Montaigne, Effet Tunnel Dépendant Du Spin : Des Simples Aux Doubles Jonctions, Thèse de doctorat, Paris 7, 1999.
[34] P. Sethi, C. Murapaka, S. Goolaup, Y. J. Chen, S. H. Leong, and W. S. Lew, *Direct Observation of Deterministic Domain Wall Trajectory in Magnetic Network Structures*, Sci. Rep. **6**, 1 (2016).
[35] X. Jiang, L. Thomas, R. Moriya, M. Hayashi, B. Bergman, C. Rettner, and S. S. P. Parkin, *Enhanced Stochasticity of Domain Wall Motion in Magnetic Racetracks Due to Dynamic Pinning*, Nat. Commun. **1**, 1 (2010).
[36] A. Thiaville and Y. Nakatani, *Domain-Wall Dynamics in Nanowiresand Nanostrips*, in *Spin Dynamics in Confined Magnetic Structures III*, edited by B. Hillebrands and A. Thiaville, Vol. 101 (Springer Berlin Heidelberg, 2006), pp. 161–205.
[37] O. Kazakova, R. Puttock, C. Barton, H. Corte-León, M. Jaafar, V. Neu, and A. Asenjo, *Frontiers of Magnetic Force Microscopy*, J. Appl. Phys. **125**, 060901 (2019).
[38] I. Horcas, R. Fernández, J. M. Gómez-Rodríguez, J. Colchero, J. Gómez-Herrero, and A. M. Baro, *WSXM: A Software for Scanning Probe Microscopy and a Tool for Nanotechnology*, Rev. Sci. Instrum. **78**, 013705 (2007).
[39] M. Hehn, Elaboration, Étude Des Propriétés Structurales et Magnétiques de Couches et Réseaux de Plots Submicroniques à Base de Cobalt, Thèse de doctorat, Strasbourg 1, 1997.

[40] M. J. Morrison, T. R. Nelson, and C. Nisoli, *Unhappy Vertices in Artificial Spin Ice: New Degeneracies from Vertex Frustration*, New J. Phys. **15**, 045009 (2013).
[41] S. Zhang, I. Gilbert, C. Nisoli, M. J. Erickson, L. O Brien, C. Leighton, P. E. Lammert, V. H. Crespi, and P. Schiffer, Crystallites of Magnetic Charges in Artificial Spin Ice, No. LA-UR-13-24128, 1083105, 2013.
[42] G.-W. Chern, M. J. Morrison, and C. Nisoli, *Degeneracy and Criticality from Emergent Frustration in Artificial Spin Ice*, Phys. Rev. Lett. **111**, 177201 (2013).
[43] I. Gilbert, G.-W. Chern, S. Zhang, L. O'Brien, B. Fore, C. Nisoli, and P. Schiffer, *Emergent Ice Rule and Magnetic Charge Screening from Vertex Frustration in Artificial Spin Ice*, Nat. Phys. **10**, 670 (2014).
[44] I. Gilbert, Y. Lao, I. Carrasquillo, L. O'Brien, J. D. Watts, M. Manno, C. Leighton, A. Scholl, C. Nisoli, and P. Schiffer, *Emergent Reduced Dimensionality by Vertex Frustration in Artificial Spin Ice*, Nat. Phys. **12**, 162 (2016).
[45] Y. Perrin, B. Canals, and N. Rougemaille, *Extensive Degeneracy, Coulomb Phase and Magnetic Monopoles in Artificial Square Ice*, Nature **540**, 410 (2016).
[46] S. Gliga, G. Hrkac, C. Donnelly, J. Büchi, A. Kleibert, J. Cui, A. Farhan, E. Kirk, R. V. Chopdekar, Y. Masaki, N. S. Bingham, A. Scholl, R. L. Stamps, and L. J. Heyderman, *Emergent Dynamic Chirality in a Thermally Driven Artificial Spin Ratchet*, Nat. Mater. **16**, 1106 (2017).
[47] R. Macêdo, G. M. Macauley, F. S. Nascimento, and R. L. Stamps, *Apparent Ferromagnetism in the Pinwheel Artificial Spin Ice*, Phys. Rev. B **98**, (2018).
[48] D. Louis, D. Lacour, M. Hehn, V. Lomakin, T. Hauet, and F. Montaigne, *A Tunable Magnetic Metamaterial Based on the Dipolar Four-State Potts Model*, Nat. Mater. **17**, 1076 (2018).
[49] M. Wyss, S. Gliga, D. Vasyukov, L. Ceccarelli, G. Romagnoli, J. Cui, A. Kleibert, R. L. Stamps, and M. Poggio, *Stray-Field Imaging of a Chiral Artificial Spin Ice during Magnetization Reversal*, ACS Nano **13**, 13910 (2019).
[50] Y. Li, G. W. Paterson, G. M. Macauley, F. S. Nascimento, C. Ferguson, S. A. Morley, M. C. Rosamond, D. A. MacLaren, R. Macedo, C. H. Marrows, S. McVitie, and R. L. Stamps, *Superferromagnetism and Domain-Wall Topologies in Artificial 'Pinwheel' Spin Ice*, 20 (n.d.).
[51] C. Castelnovo, R. Moessner, and S. L. Sondhi, *Magnetic Monopoles in Spin Ice*, Nature **451**, 7174 (2008).
[52] M. De Graef and M. Beleggia, *General Magnetostatic Shape–Shape Interaction Forces and Torques*, J. Magn. Magn. Mater. **321**, L45 (2009).
[53] R. C. Silva, F. S. Nascimento, L. A. S. Mól, W. A. Moura-Melo, and A. R. Pereira, *Thermodynamics of Elementary Excitations in Artificial Magnetic Square Ice*, New J. Phys. **14**, 015008 (2012).
[54] N. Rougemaille and B. Canals, *Cooperative Magnetic Phenomena in Artificial Spin Systems: Spin Liquids, Coulomb Phase and Fragmentation of Magnetism – a Colloquium*, Eur. Phys. J. B **92**, 62 (2019).
[55] Y. Perrin, Réseaux Artificiels à Frustration Géométrique, PhD Thesis, Université Grenoble Alpes, 2016.
[56] C. Nisoli, J. Li, X. Ke, D. Garand, P. Schiffer, and V. H. Crespi, *Effective Temperature in an Interacting Vertex System: Theory and Experiment on Artificial Spin Ice*, Phys. Rev. Lett. **105**, (2010).
[57] C. Nisoli, R. Wang, J. Li, W. F. McConville, P. E. Lammert, P. Schiffer, and V. H. Crespi, *Ground State Lost but Degeneracy Found: The Effective Thermodynamics of Artificial Spin Ice*, Phys. Rev. Lett. **98**, 217203 (2007).
[58] J. P. Morgan, A. Bellew, A. Stein, S. Langridge, and C. Marrows, *Linear Field Demagnetization of Artificial Magnetic Square Ice*, Front. Phys. **1**, (2013).
[59] J. M. Porro, A. Bedoya-Pinto, A. Berger, and P. Vavassori, *Exploring Thermally Induced States in Square Artificial Spin-Ice Arrays*, New J. Phys. **15**, 055012 (2013).
[60] J. Drisko, S. Daunheimer, and J. Cumings, *FePd3 as a Material for Studying Thermally Active Artificial Spin Ice Systems*, Phys. Rev. B **91**, 224406 (2015).
[61] C. Nisoli, *On Thermalization of Magnetic Nano-Arrays at Fabrication*, New J. Phys. **14**, 035017 (2012).

[62] J. P. Morgan, J. Akerman, A. Stein, C. Phatak, R. M. L. Evans, S. Langridge, and C. H. Marrows, *Real and Effective Thermal Equilibrium in Artificial Square Spin Ices*, Phys. Rev. B **87**, (2013).
[63] R. V. Hügli, G. Duff, B. O'Conchuir, E. Mengotti, A. F. Rodríguez, F. Nolting, L. J. Heyderman, and H. B. Braun, *Artificial Kagome Spin Ice: Dimensional Reduction, Avalanche Control and Emergent Magnetic Monopoles*, Phil Trans R Soc A **370**, 5767 (2012).
[64] R. Di Leonardo, L. Angelani, G. Parisi, and G. Ruocco, *Off-Equilibrium Effective Temperature in Monatomic Lennard-Jones Glass*, Phys. Rev. Lett. **84**, 6054 (2000).
[65] N. Greinert, T. Wood, and P. Bartlett, *Measurement of Effective Temperatures in an Aging Colloidal Glass*, Phys. Rev. Lett. **97**, 265702 (2006).
[66] A. Mehta and S. F. Edwards, *Statistical Mechanics of Powder Mixtures*, Phys. Stat. Mech. Its Appl. **157**, 1091 (1989).
[67] R. J. Baxter, *Exactly Solved Models in Statistical Mechanics* (Elsevier, 2016).
[68] I. A. Chioar, B. Canals, D. Lacour, M. Hehn, B. Santos Burgos, T. O. Menteș, A. Locatelli, F. Montaigne, and N. Rougemaille, *Kinetic Pathways to the Magnetic Charge Crystal in Artificial Dipolar Spin Ice*, Phys. Rev. B **90**, (2014).
[69] N. Metropolis, A. W. Rosenbluth, M. N. Rosenbluth, A. H. Teller, and E. Teller, *Equation of State Calculations by Fast Computing Machines*, 7 (n.d.).
[70] M. Massouras, D. Lacour, M. Hehn, and F. Montaigne, *Probing the Antiferromagnetic-Paramagnetic Transition in Artificial Spin Ice by Tuning Interactions*, Phys. Rev. B **101**, 174421 (2020).
[71] G. M. Macauley, G. W. Paterson, Y. Li, R. Macêdo, S. McVitie, and R. L. Stamps, *Tuning Magnetic Order with Geometry: Thermalization and Defects in Two-Dimensional Artificial Spin Ices*, Phys. Rev. B **101**, 144403 (2020).
[72] R. V. Hügli, G. Duff, B. O'Conchuir, E. Mengotti, L. J. Heyderman, A. F. Rodríguez, F. Nolting, and H. B. Braun, *Emergent Magnetic Monopoles, Disorder, and Avalanches in Artificial Kagome Spin Ice (Invited)*, J. Appl. Phys. **111**, 07E103 (2012).
[73] N. Rougemaille, F. Montaigne, B. Canals, M. Hehn, H. Riahi, D. Lacour, and J.-C. Toussaint, *Chiral Nature of Magnetic Monopoles in Artificial Spin Ice*, New J. Phys. **15**, 035026 (2013).
[74] S. Ladak, D. E. Read, W. R. Branford, and L. F. Cohen, *Direct Observation and Control of Magnetic Monopole Defects in an Artificial Spin-Ice Material*, New J. Phys. **13**, 063032 (2011).
[75] P. Mellado, O. Petrova, Y. Shen, and O. Tchernyshyov, *Dynamics of Magnetic Charges in Artificial Spin Ice*, Phys. Rev. Lett. **105**, 187206 (2010).
[76] D. M. Burn, M. Chadha, and W. R. Branford, *Dynamic Dependence to Domain Wall Propagation through Artificial Spin Ice*, Phys. Rev. B **95**, 104417 (2017).
[77] S. A. Daunheimer, O. Petrova, O. Tchernyshyov, and J. Cumings, *Reducing Disorder in Artificial Kagome Ice*, Phys. Rev. Lett. **107**, 167201 (2011).
[78] Y. Shen, O. Petrova, P. Mellado, S. Daunheimer, J. Cumings, and O. Tchernyshyov, *Dynamics of Artificial Spin Ice: A Continuous Honeycomb Network*, New J. Phys. **14**, 035022 (2012).
[79] D. M. Burn, M. Chadha, and W. R. Branford, *Angular-Dependent Magnetization Reversal Processes in Artificial Spin Ice*, Phys. Rev. B **92**, 214425 (2015).
[80] D. Shi, H. Chen, J. Xu, H. Xia, Y. Chen, and Y. Wu, *Kerr Microscopy Real-Time Imaging of the Magnetization Reversal Process in Kagome Artificial Spin Ice*, Phys. Rev. B **101**, 134428 (2020).
[81] A. Pushp, T. Phung, C. Rettner, B. P. Hughes, S.-H. Yang, L. Thomas, and S. S. P. Parkin, *Domain Wall Trajectory Determined by Its Fractional Topological Edge Defects*, Nat. Phys. **9**, 505 (2013).
[82] C. Murapaka, P. Sethi, S. Goolaup, R. Maddu, Y. Chen, S. Leong, and W. Siang Lew, *Direct Observation of Domain Wall Evolution at a Bifurcation in Magnetic Network Structures*, Appl. Phys. Express **7**, 113003 (2014).
[83] E. R. Lewis, D. Petit, A.-V. Jausovec, L. O'Brien, D. E. Read, H. T. Zeng, and R. P. Cowburn, *Measuring Domain Wall Fidelity Lengths Using a Chirality Filter*, Phys. Rev. Lett. **102**, 057209 (2009).
[84] D. M. Burn, M. Chadha, S. K. Walton, and W. R. Branford, *Dynamic Interaction between Domain Walls and Nanowire Vertices*, Phys. Rev. B **90**, (2014).

[85] J. C. Gartside, D. M. Arroo, D. M. Burn, V. L. Bemmer, A. Moskalenko, L. F. Cohen, and W. R. Branford, *Realization of Ground State in Artificial Kagome Spin Ice via Topological Defect-Driven Magnetic Writing*, Nat. Nanotechnol. **13**, 53 (2018).
[86] A. C. Chavez, A. Barra, and G. P. Carman, *Voltage Control of Magnetic Monopoles in Artificial Spin Ice*, J. Phys. Appl. Phys. **51**, 234001 (2018).
[87] M. Hayashi, L. Thomas, C. Rettner, R. Moriya, and S. S. P. Parkin, *Direct Observation of the Coherent Precession of Magnetic Domain Walls Propagating along Permalloy Nanowires*, Nat. Phys. **3**, 21 (2007).
[88] P. Mellado, O. Petrova, Y. Shen, and O. Tchernyshyov, *Dynamics of Magnetic Charges in Artificial Spin Ice*, Phys. Rev. Lett. **105**, (2010).
[89] Y. Nakatani, A. Thiaville, and J. Miltat, *Head-to-Head Domain Walls in Soft Nano-Strips: A Refined Phase Diagram*, J. Magn. Magn. Mater. **290**–**291**, 750 (2005).
[90] J.-Y. Lee, K.-S. Lee, S. Choi, K. Y. Guslienko, and S.-K. Kim, *Dynamic Transformations of the Internal Structure of a Moving Domain Wall in Magnetic Nanostripes*, Phys. Rev. B **76**, (2007).
[91] T. J. Broomhall and T. J. Hayward, *Suppression of Stochastic Domain Wall Pinning Through Control of Gilbert Damping*, Sci. Rep. **7**, (2017).
[92] T. J. Hayward and K. A. Omari, *Beyond the Quasi-Particle: Stochastic Domain Wall Dynamics in Soft Ferromagnetic Nanowires*, J. Phys. Appl. Phys. **50**, 084006 (2017).
[93] *"Natural Inheritance", Francis Galton, 1889*, (n.d.).
[94] D. Sanz-Hernández, M. Massouras, N. Reyren, N. Rougemaille, V. Schánilec, K. Bouzehouane, M. Hehn, B. Canals, D. Querlioz, J. Grollier, F. Montaigne, and D. Lacour, *A Nano-Magnetic Galton Board*, ArXiv201010389 Cond-Mat (2020).
[95] D. Sanz-Hernández, M. Massouras, N. Reyren, N. Rougemaille, V. Schánilec, K. Bouzehouane, M. Hehn, B. Canals, D. Querlioz, J. Grollier, F. Montaigne, and D. Lacour, *Tunable Stochasticity in an Artificial Spin Network*, Adv. Mater. **33**, 2008135 (2021).

Résumé

"On a déjà eu cette discussion"
F. Montaigne

Depuis leur introduction en 2006, les réseaux de nano-aimants en interaction, appelés spins artificiels, ont suscité un large intérêt autant pour leurs applications en tant que système modèle pour l'observation de phénomènes de frustration magnétique qu'en tant que dispositifs. A l'origine introduits en arrangement carré déconnecté pour leur similarité avec la glace d'eau, ces réseaux de nano-aimants fabriqués par des procédés de nanofabrication issus de la micro-électronique ont l'avantage d'être modifiables à volonté. La modification de leur géométrie entraînant une modification des interactions qui donnent lieu à des comportements physiques souvent qualifiés d'exotiques. Ces interactions vont de la simple interaction dipolaire en géométrie déconnectée à l'interaction d'échange en géométrie connectée. Ces deux géométries et les interactions associées sont exploitées dans ce travail de thèse pour une étude de leur thermodynamique et pour des applications de génération de nombres aléatoires. Dans un premier temps, nous nous sommes intéressés à la modification des interactions par une modification de la géométrie carrée classique par une rotation des aimants autour de leur centre. Ce changement de géométrie modifie les couplages dipolaires et donc l'énergie du système. Nous montrons que le changement d'état fondamental du système est prédit par des calculs dipolaires et que la thermodynamique de notre système expérimental est décrite grâce à des simulations Monte Carlo. Dans un second temps, nous nous intéresserons à ces réseaux de nano-aimants en géométrie connectée et montrons qu'une fine optimisation de ce système permet d'obtenir des propagations d'un bout à l'autre du système caractérisé par des trajets aléatoires.

Grâce aux progrès des nanotechnologies et de leurs procédés de nanofabrication, les systèmes de spins artificiels sont faciles à modeler : des géométries carrées et en nid d'abeilles ont été les premières introduites, beaucoup d'autres ont suivi telles que la géométrie carrée en trois dimensions, les mailles « tetris », « shakti », « santa fe » et bien d'autres. En 2017 -conjointement à nos travaux-, la maille baptisée « pinwheel » (moulinet en français), où les aimants de la géométrie carrée originelle sont tournés de 45° autour de leur point central, a été proposée. Cette géométrie est particulièrement intéressante car elle rend les interactions entre plus proches voisins nulles contrairement à la géométrie carrée où cette interaction est prépondérante. Nous nous proposons d'étudier l'évolution des interactions induite par cette rotation de 0° (géométrie carrée) à 45° (géométrie pinwheel). Par des calculs dipolaires entre premiers voisins, dite approche vertex, nous attendons une transition d'un couplage antiferromagnétique entre spins colinéaires pour des petits angles à un couplage ferromagnétique entre spins colinéaires pour de grands angles. Cette approche de premiers voisins donne l'évolution du couplage pour quatre spins mais dans notre cas, n'est pas adaptée au calcul de l'énergie dipolaire totale d'un réseau de grande taille. Comme nous l'avons mentionné précédemment, à 45° les interactions premiers voisins devient nulle donc les interactions deuxième et troisième voisins deviennent prépondérantes dans le calcul d'énergie totale. Nous décidons de considérer toutes les interactions soit toutes les paires de spins dans notre Hamiltonien dipolaire pour estimer l'énergie dipolaire totale du

système. Cette méthode est applicable à tous nos réseaux tournés de 0° à 45° quelles que soient les interactions et permet un calcul précis de l'énergie totale des configurations de spins.
Dans cette approche de considérer toutes les interactions, les calculs montrent que l'état fondamental évolue d'un couplage antiferromagnétique sur les spins colinéaires à un couplage ferromagnétique sur *tous* les spins colinéaires. Les calculs prédisent que la transition entre configuration antiferromagnétique et ferromagnétique se produit à 35°. Ces calculs prouvent que l'approche vertex n'est pas adaptée pour décrire les interactions de notre système. En effet, pour les petits angles, l'approche vertex et toutes interactions donnent le même résultat car il n'y a qu'une seule façon d'arranger des spins avec un couplage antiferromagnétique sur un réseau. L'information supplémentaire est sur le couplage ferromagnétique car il y a plusieurs façons de l'obtenir toutes décrites par l'approche vertex alors que l'approche sur toutes les interactions les différencie. Notre approche montre que la configuration ferromagnétique qui correspond à l'état fondamental est celle où toutes les lignes et colonnes de spins sont orientées dans la même direction.
Nous avons fabriqué un système de réseaux tournés de 0° à 45° par pas de 5° pour observer l'évolution de l'état fondamental en fonction de l'angle de rotation. Les systèmes de spins artificiels sont en général difficiles à amener dans un état de basse énergie mais plusieurs travaux publiés ont montré qu'il était possible d'atteindre un état de -relativement- basse énergie : la démagnétisation en champ et l'état brut de croissance. Nous avons testé ces deux approches sur nos réseaux dans le but de trouver le système de plus basse énergie. Dans un premier temps, nous avons regardé quelles étaient les proportions de vertex dans nos deux systèmes. Même s'il s'agit d'une approche qui ne décrit pas au mieux nos systèmes, elle n'en reste pas moins une caractérisation sans ambigüité de la configuration de spins. Nous observons dans l'état démagnétisé en champ que le réseau carré est arrangé en domaines de couplages antiferromagnétiques avec des parois à couplages ferromagnétiques. Dans le cas de l'état brut de croissance, la configuration de spins montre uniquement des couplages antiferromagnétiques. Ces deux observations suggèrent que l'état brut de croissance est de plus basse énergie. Augmenter l'angle de rotation ne contredit pas cette observation : de 0° à 25° l'état brut de croissance contient plus de 90% de couplage antiferromagnétique alors l'état démagnétisé environ 75% au maximum au profit de couplages ferromagnétiques ; au-delà, l'état brut de croissance montre une chute des couplages antiferromagnétiques et une nette hausse des ferromagnétiques alors que l'état démagnétisé à peine 25% de couplages ferromagnétiques. Ces observations sont confirmées par une comparaison de l'énergie dipolaire totale de chacun des réseaux tournés : l'état brut de croissance est celui de plus basse énergie.
Nous comparons à présent l'énergie de notre système dans l'état brut de croissance aux énergies de nos deux états fondamentaux antiferromagnétique et ferromagnétique. Nous trouvons que jusqu'à 25°, notre système suit l'énergie de l'état fondamental avec une très faible déviation qui est aisément expliqué par la présence de défauts dans nos configurations de spins (5% de couplages non-antiferromagnétiques). A partir de 30°, un écart plus important est observé entre les états calculés et expérimentaux. Ces résultats montrent que notre système est dans un état de basse énergie sans être dans l'état de plus basse énergie possible. Pour comprendre l'origine de cette différence, nous utilisons le facteur de structure magnétique, la transformée de Fourier de la fonction scalaire de corrélation entre spins. Cette caractérisation de l'ordre de notre système montre le passage d'un état clairement antiferromagnétique entre 0° et 25° à un état entre 40° et 45° dont la signature est celle d'un état ferromagnétique. Pour les réseaux de 30° et 35°, nous observons que le système est dans un état de coexistence d'états antiferromagnétique et ferromagnétique. L'observation de l'ordre de notre système nous permet de comprendre que la transition d'un état à un autre n'est pas abrupte comme le prédisent les calculs dipolaires mais continue, avec aux angles de rotation entre les deux, des configurations qui montrent à la fois des couplages antiferromagnétiques et ferromagnétiques.
Nous procédons ensuite à une étude de la thermodynamique de notre système dans l'état brut de croissance et cherchons à lui attribuer une température effective. Nous nous intéressons à deux approches qui ont fait l'objet de publications scientifiques : l'approche vertex (entre premiers voisins) et l'approche contenant toutes les interactions du réseau. Nous montrons qu'il est possible de décrire l'énergie de notre système tourné de 0° à 45° par une température effective unique dans une approche vertex, cependant cette température ne décrit pas les autres observables de notre système que sont les proportions des différents couplages. En revanche, avec une approche considérant toutes les interactions, nous sommes capables de décrire à la fois l'énergie dipolaire totale de notre système ainsi que les

proportions de couplages par une température effective unique. Cette température, calculée par simulations Monte Carlo, reportée sur un diagramme de phase établi par la même méthode avec des conditions de bords finies, montre que nous assistons à une transition de phase bien définie. Notre système expérimental passe d'une phase antiferromagnétique jusqu'à 25°, ensuite entre 30° et 35° à une phase paramagnétique et finit par une phase ferromagnétique à la limite de l'état paramagnétique entre 40° et 45°. Ces observations sont cohérentes avec l'écart en énergie observé à partir de 30° puisque le système est effectivement dans un état de plus haute énergie que l'état fondamental puisque proche de la phase paramagnétique. Nous précisons que l'étude du système tourné dans son ensemble permet cette conclusion, n'étudier qu'un angle de rotation aurait pu donner plusieurs valeurs de température effective et ainsi biaiser l'étude de la thermodynamique de notre système.
Ces travaux ont montré qu'à partir d'états bruts de croissance, il est possible de déterminer avec précision la thermodynamique de systèmes de glace de spins artificielle fixée pendant la croissance grâce à une simple modification de la géométrie. Cette étude montre une fois de plus, le potentiel des systèmes de spins artificiels en tant que systèmes modèles pour des études de phénomènes physiques complexes.

Comme nous l'avons mentionné précédemment, les systèmes de spins artificiels peuvent prendre la forme de réseaux en géométrie en nid d'abeilles, aussi appelée kagomé -les spins étant situés sur une maille composée de triangles et hexagones. Cette géométrie a été introduite en réponse à l'asymétrie des interactions de la géométrie déconnectée car les interactions entre premiers voisins (trois spins à 0°, 120° et 240°) sont égales puisque positionnés à distance égale. La configuration de basse énergie 2-entrants(sortants)/1-sortant(entrant) est complètement dégénérée ce qui peut être intéressant pour des applications de calcul ou de génération de nombres aléatoires. Nous nous intéressons à cette possible application avec l'élaboration d'un système de spins artificiels dans cette géométrie par le contrôle des modifications de configurations de spins. Le réseau kagomé est, par sa géométrie, un système aléatoire potentiel. En effet, si l'on considère trois spins dans cette géométrie en configuration de basse énergie 2-entrants/1-sortant, le reversement du spin sortant modifie la configuration en 3-entrants qui est énergétiquement peu favorable. Dans le but de retrouver un état de basse énergie, le système a trois possibilités -sans modifier celui retourné en premier- : reverser un des deux autres spins pour retrouver un arrangement 2-entrants/1-sortant ou renverser le deux simultanément pour un arrangement 2-sortants/1-entrant. Dans le premier cas, le choix du renversement d'un spin plutôt que l'autre dépend des paramètres appliqués ou intrinsèques mais dans des conditions sont idéales le choix entre les deux spins est équivalent.
Dans un système de spins artificiels en géométrie kagomé, la modification d'un spin peut entraîner des modifications sur un réseau complet à cause des configurations énergétiquement peu favorables crées. Comme nous l'avons mentionné précédemment, ces renversements peuvent être sur le principe aléatoires. Nous nous proposons de développer un tel système par la modification en un point sur le bord du réseau et par renversements successifs jusqu'à son autre bout. Le premier renversement se fait par nucléation et injection de paroi à l'aide d'un pad de nucléation. Par l'application d'un champ magnétique dans le plan et suivant la direction de l'élément à renverser en premier nous avons un contrôle précis de l'endroit du premier renversement. Nous commençons notre étude par la comparaison entre des géométries déconnectée et connectée kagomé sur des réseaux de petites tailles. Il s'agit ici de déterminer s'il est préférable d'utiliser des retournements par couplage dipolaire dans des réseaux déconnectés ou par propagation de paroi dans des réseaux connectés. Dans le cas de trois spins, les deux géométries montrent la bonne injection de paroi pour le premier renversement. Le renversement suivant est soit le spin de « gauche » soit le spin de « droite » selon l'expérience -si on regarde la structure avec le brin d'injection à la verticale- : les renversements sont donc stochastiques et notre concept validé. Augmenter la taille du réseau à douze spins impose aux retournements deux choix d'aller à gauche ou à droite. Nous observons que dans le cas de la géométrie déconnectée, l'injection est bien réalisée *ie* que le premier retournement est bien contrôlé. Cependant en augmentant l'intensité du champ magnétique, on observe le retournement d'un spin juxtaposé à celui de l'injection mais également le renversement du spin situé au bord de l'autre côté du réseau de manière reproductible. Ce résultat signifie que nous observons un retournement par couplage à la suite de l'injection et simultanément par nucléation à l'autre bout du réseau. Cette nucléation n'est pas souhaitée car pourrait induire une propagation à son tour à plus faible

champ que celle induite par la paroi injectée. A l'inverse, nous observons dans le cas de la géométrie connectée des renversements cohérents avec la propagation de la paroi injectée à un bord du réseau. Les renversements forment principalement des propagations unidimensionnelles et les choix sont stochastiques. Cette étude sur des réseaux de petites tailles montre que la géométrie connectée est plus adaptée que la déconnectée. Cette dernière pourrait certainement être optimisée mais nous choisissons de continuer uniquement avec la géométrie connectée. Nous avons approfondi l'étude de nos petits systèmes connectés en recensant le nombre d'expériences présentant des propagations unidimensionnelles de la paroi injectée jusqu'à l'autre extrémité du réseau ainsi que la proportion de choix gauche/droite sur plusieurs structures et plusieurs dizaines d'expériences. Nous observons que les renversements sont dans plus de la moitié de nos expériences il semble que les renversements forment une propagation et ce sur plusieurs systèmes. Les proportions de choix gauche/droite sont proches de 50%/50% et que ces systèmes peuvent être comparés à une loi binomiale avec une proportion moyenne d'aller d'un côté ou de l'autre. Ces proportions sont modulées par l'inclinaison du champ : de environ 50%/50% à 0°, le système passe à 60%/40% à +3° et à 20%/80% à -7°. Nous décidons de poursuivre notre étude sur des toujours en géométrie connectée mais de plus grande taille. Cette étape s'est avérée être cruciale pour l'élaboration de notre système de spins artificiels. Sur un réseau connecté où la propagation aurait sept intersections à passer, nous remarquons que les observations sur deux intersections (à 16 spins) ne se transposent pas. Nous trouvons que l'injection est réalisée avec une propagation qui passe uniquement la première intersection. Dans le but de la dépiéger, nous augmentons le champ et observons que le système nuclée une paroi de domaine à l'autre bout du réseau. Deux dessins de cette taille de structure ont été nécessaires pour déterminer l'obstacle à la propagation : il nous faut trouver le bon compromis entre champ de dépiégeage du haut de la structure -où la paroi est injectée- et champ de nucléation aux sorties -où la paroi injectée est censée finir sa course. Ces observations mènent une optimisation du système avec des entonnoirs aux potentiels points de piégeage ajoutés à notre structure ainsi que des sorties aiguisées. Nous avons réalisé une étude approfondie des renversements sur un grand nombre d'expériences sur une unique structure. Cette caractérisation montre que dans une grande majorité des cas, les renversements forment effectivement une propagation depuis le point d'injection jusqu'au bout de la structure. Ce résultat montre l'efficacité de l'optimisation de notre système de spins artificiels. Les expériences restantes montrent d'une part des propagations des fois en deux-dimensions et d'autre part des renversements supplémentaires dans la direction opposée au champ. Notre technique de microscopie ne nous donne pas accès la dynamique de la propagation par contre nos observations -et l'absence de certains indices- suggèrent que ces renversements dans la direction opposée au champ sont dus à la forme en entonnoir ajoutée et à la dynamique de la propagation de paroi à ces endroits. En d'autres termes, la paroi, en se propageant, retourne certains éléments sur son passage. Grâce à la caractérisation de ces signatures de la propagation de paroi dans notre système optimisé -qui explique 226 des 229 expériences menées-, nous trouvons que notre système permet la propagation majoritairement unidimensionnelle d'une paroi injectée au bord du réseau. Les renversements sont clairement stochastiques et ressemblent fortement au comportement d'une planche de Galton (planche de clous intercalés où sont lâchés un grand nombre de billes qui ont 50% d'aller à droite ou à gauche à chaque clou et dont la distribution finale forme un loi normale). Nous nous proposons de caractériser le comportement stochastique de notre système en étudiant les chemins empruntés par la paroi injectée sur notre ensemble d'expériences. Nous réalisons une étude statistique des choix réalisés à chacune des intersections : les proportions varient de 8% à 80% d'aller à gauche. La moyenne est de 38% (σ=11%) d'aller à gauche et la distribution de sorties activées -l'endroit où la paroi est arrivée- est cohérente avec une distribution binomiale. De plus, notre système et les propagations observées ne montrent aucune corrélation significative entre les choix successifs réalisés qui démontre l'absence d'effet mémoire de notre propagation de paroi de domaines. Notre système est donc une planche de Galton magnétique légèrement biaisée. Des expériences complémentaires sur de petits désalignements en champ ont montré que le biais observé dans nos expériences est dû à un désalignement en champ de 0.5°. Ce résultat est cohérent avec l'erreur de positionnement sur l'échantillon du microscope utilisé pour réaliser ces expériences. L'ébauche d'une étude en température de la propagation de paroi de notre système a quant à elle montré un comportement toujours stochastique à 77 K. Pour être conclusif sur l'influence de la température, nous avions prévu des expériences à 4 K qui n'ont malheureusement pas pu être réalisées à cause de problèmes techniques.

Par ce travail, nous montrons que notre système de spins artificiels en géométrie kagomé optimisé est stochastique mais la question sur l'origine de ce comportement demeure. En effet, des travaux publiés de simulations micromagnétiques montrent que le choix sur trois spins dépend des caractéristiques de la paroi : par exemple, une paroi vortex avec un chiralité horaire ira à droite alors qu'une chiralité antihoraire à gauche. Dans notre système, les choix ne sont pas périodiques donc le type de paroi arrivant à une intersection dépendent d'autre chose. Nous soupçonnons que ce comportement est dû à la propagation de la paroi entre les points de choix qui se font à fort champ. En effet, nos propagations sont observées bien au-delà du régime de Walker, des travaux publiés montrent que dans ce régime turbulent, ces évolutions de la paroi sont plus nombreuses et moins prévisibles que dans le régime de Walker où les modifications sont périodiques et bien décrites par les simulations micromagnétiques. Il reste donc un travail à effectuer pour expliquer le comportement clair et robuste de notre planche de Galton magnétique nanométrique.

Cette thèse a montré la versatilité des systèmes de spins artificiels en qualité de système modèle de glace de spin pour la compréhension de l'influence de la modification des interactions et la description de leur thermodynamique. Ce travail a également démontré leur potentiel pour une application grâce à la simple modulation de leur forme suite à la caractérisation de leur comportement aléatoire dans la propagation de parois. La deuxième partie de ce travail introduit des perspectives en matière de contrôle de distributions. En effet, des expériences démontrent qu'en enlevant un brin à l'intérieur du réseau, donc en imposant certains choix à deux intersections, la distribution de sorties est modifiée. Nous pouvons imaginer aussi de modifier la distribution par un contrôle électrique. Pour l'instant, nous n'avons montré que la détection des signaux liés aux renversements. Un autre perspective serait l'élaboration de systèmes plus complexes avec plusieurs points d'injection, des expériences préliminaires avec des systèmes à quatre pads montrent qu'il est possible d'utiliser ces systèmes et que nous pouvons nous attendre à des interactions entre les propagations. Ces perspectives variées montrent que les systèmes de spins artificiels sont d'excellents candidats pour des applications de calcul stochastique.